

## INTERFERENCE-FIT FASTENER INVESTIGATION

*BATTELLE  
COLUMBUS LABORATORIES  
505 KING AVENUE  
COLUMBUS, OHIO 43201*

SEPTEMBER, 1975

TECHNICAL REPORT AFFDL-TR-75-93  
FINAL REPORT FOR PERIOD MARCH, 1973 — JUNE, 1975  
CONTRACT NO. F33615-73-C-3121

Approved for public release; distribution unlimited

AIR FORCE FLIGHT DYNAMICS LABORATORY  
AIR FORCE WRIGHT AERONAUTICAL LABORATORIES  
Air Force Systems Command  
Wright-Patterson Air Force Base, Ohio 45433

Best Available Copy

20060921121

## NOTICE

When Government drawings, specifications, or other data are used for any purpose other than in connection with a definitely related Government procurement operation, the United States Government thereby incurs no responsibility nor any obligation whatsoever; and the fact that the government may have formulated, furnished, or in any way supplied the said drawings, specifications, or other data, is not to be regarded by implication or otherwise as in any manner licensing the holder or any other person or corporation, or conveying any rights or permission to manufacture, use, or sell any patented invention that may in any way be related thereto.

This report has been reviewed by the Information Office (IO) and is releasable to the National Technical Information Service (NTIS). At NTIS, it will be available to the general public, including foreign nations.

This report has been reviewed and is approved for publication.

*Frank D. Adams*

Frank D. Adams  
Project Engineer

*R. M. Bader*

ROBERT M. BADER, Chief  
Structural Integrity Branch  
Structures Division

FOR THE COMMANDER

*Gerald G. Leigh*

GERALD G. LEIGH, Lt Col, USAF  
Chief, Structures Division

Copies of this report should not be returned unless return is required by security considerations, contractual obligations, or notice on a specific document.

REPORT DOCUMENTATION PAGE		READ INSTRUCTIONS BEFORE COMPLETING FORM
1. REPORT NUMBER AFFDL-TR-75-93	2. GOVT ACCESSION NO.	3. RECIPIENT'S CATALOG NUMBER
4. TITLE (and Subtitle) Interference-Fit-Fastener Investigation		5. TYPE OF REPORT & PERIOD COVERED Final - March 26, 1973 - June 30, 1974
		6. PERFORMING ORG. REPORT NUMBER
7. AUTHOR(s) S. C. Ford, B. N. Leis, D. A. Utah, W. Griffith, S. G. Sampath and P. N. Mincer		8. CONTRACT OR GRANT NUMBER(s) F33615-73-C-3121
9. PERFORMING ORGANIZATION NAME AND ADDRESS Battelle's Columbus Laboratories 505 King Avenue Columbus, Ohio 43201		10. PROGRAM ELEMENT, PROJECT, TASK AREA & WORK UNIT NUMBERS Project No. - 1467 Task No. - 146702 Work Unit No. - 14670228
11. CONTROLLING OFFICE NAME AND ADDRESS Air Force Flight Dynamics Laboratory/FBR Wright-Patterson Air Force Base Ohio 45433		12. REPORT DATE September, 1975
		13. NUMBER OF PAGES 167 pages
14. MONITORING AGENCY NAME & ADDRESS (if different from Controlling Office) DCASO, Columbus Building 1, Section 1 Defense Construction Supply Agency Columbus, Ohio 43215		15. SECURITY CLASS. (of this report) Unclassified
		15a. DECLASSIFICATION/DOWNGRADING SCHEDULE
16. DISTRIBUTION STATEMENT (of this Report) Approved for public release, distribution unlimited.		
17. DISTRIBUTION STATEMENT (of the abstract entered in Block 20, if different from Report)		
18. SUPPLEMENTARY NOTES		
19. KEY WORDS (Continue on reverse side if necessary and identify by block number)		
Fastenings	Fatigue Prediction	Fe-3Si
Fatigue	Fatigue Improvement Fasteners	Speckle
Fatigue Life	Interference Fit Fasteners	Speckle Photography
Fatigue Tests	Hole Metrology	Stress Analysis
Fatigue (Mechanics)	Dislocation Etching Technique	Joints
20. ABSTRACT (Continue on reverse side if necessary and identify by block number) This report presents analytical and experimental techniques for defining the stress-strain and deformation states around holes filled with tapered shank interference fit fasteners. A prescription for fatigue-life analysis and prediction is developed wherein the above noted data are used. Stresses and plastic strains around fastener holes are determined analytically for two- and three-dimensional elastic and elastic-plastic cases using AXISOL and MARC computer codes. These results are evaluated based on data obtained from the dislocation etching technique, speckle photography experiments,		

19. Fastened Joints  
Finite Element Technique  
Experimental Stress Analysis

20. and electrical resistance strain gages.

A fatigue analysis technique is developed based on (1) a mechanics analysis to estimate local stress and strain and (2) a calculation of fatigue damage. This analysis provides a good estimate of life to crack initiation.

Fastener installation variables are studied and critical ones selected. Constant amplitude and spectrum loading fatigue tests are reported and the data used to verify fatigue life predictions.

## FOREWORD

The research reported herein was conducted by Battelle's Columbus Laboratories for the Structures Division, Air Force Flight Dynamics Laboratory, Wright-Patterson Air Force Base, Ohio, under Contract No. F33615-73-C-3121, Project No. 1467, Task No. 146702. Dr. Frank D. Adams of AFFL/FBR was the project engineer.

The study was conducted during the period from March 26, 1973, to June 30, 1975. The principal investigator was Stephen C. Ford, Structural Materials Section. Major contributors to the effort were - B. N. Leis and D. A. Utah, Structural Materials Section, W. Griffith and S. G. Sampath, Applied Solid Mechanics Section, and P. N. Mincer, Metal Sciences Section. This report was submitted by the authors on September 11, 1975.

## TABLE OF CONTENTS

	<u>Page</u>
1. INTRODUCTION . . . . .	1
2. FATIGUE ANALYSIS FOR FASTENER SYSTEMS . . . . .	3
2.1. Introduction . . . . .	3
2.2. Current Technology . . . . .	8
2.2.1. The Indirect Approach . . . . .	8
2.2.2. The Direct Approach . . . . .	10
2.2.2.1. Biaxiality . . . . .	11
2.2.2.2. Failure Criterion . . . . .	13
2.2.2.3. Inelasticity . . . . .	13
2.2.3. Essential Features of the Direct Approach . . . . .	16
2.2.4. Analysis Framework for No-Load-Transfer Specimens Subjected to Constant-Amplitude Loading . . . . .	19
2.3. Limitations of the Fatigue Analysis Procedure as Applied in this Report . . . . .	30
2.4. Discussion . . . . .	31
2.4.1. Use of Static Analyses in Fatigue Applications . . . . .	31
3. CONCLUSIONS AND RECOMMENDATIONS . . . . .	32
4. REFERENCES . . . . .	34
APPENDIX A	
HOLE PREPARATION AND METROLOGY . . . . .	37
APPENDIX B	
DISLOCATION ETCHING TECHNIQUE . . . . .	49
APPENDIX C	
SPECKLE PHOTOGRAPHY . . . . .	75
APPENDIX D	
FINITE ELEMENT METHODS . . . . .	109
APPENDIX E	
EXPERIMENTAL ASPECTS OF THE FATIGUE PROGRAM . . . . .	151

## LIST OF FIGURES

	<u>Page</u>
Figure 1. Breakdown of the Various Aspects of the Fatigue Life and Deformation Response of Cyclically Loaded Components . . .	6
Figure 2. Influence of Biaxiality (Reference 11) . . . . .	12
Figure 3. Influence of Failure Criterion (Reference 10) . . . . .	12
Figure 4. Influence of Plasticity (Reference 12) . . . . .	12
Figure 5. Comparison of Stable Notch-Root Strain With Smooth Specimen Strain at the Same Life to Crack Initiation (Reference 10) . . . . .	15
Figure 6. Histogram of the Values of the Ratios . . . . .	17
Figure 7. Essential Features in the Direct Fatigue Analysis Procedure . . . . .	18
Figure 8. Block Diagram of Fatigue Analysis Procedure During Crack Initiation . . . . .	20
Figure 9. Actual and Predicted Fatigue Life Behavior of Notched Open Hole Plates for 2024-T351 Aluminum (Reference 19) . . . . .	22
Figure 10. Gage 1 Strain Response With Cycles . . . . .	24
Figure 11. Fatigue Damage - Life Relationship for 7075-T6 Aluminum Alloy (Reference 23) . . . . .	29
Figure A-1. Microstop Drill Cage . . . . .	38
Figure A-2a. Taper-Lok Drill Reamer for Flush-Head-Type Fastener Holes . . . . .	40
Figure A-2b. Taper-Lok Drill Reamer for Protruding-Head-Type Fastener Holes . . . . .	41
Figure A-3. Typical Talyrand Trace of a Normal Round-Tapered Hole . .	43
Figure A-4. Typical Talyrand Trace of a Nonperpendicular-Tapered Hole . . . . .	44
Figure A-5. Typical Talyrand Trace of an Out-of-Round and Fluted Hole . . . . .	45
Figure A-6. Typical Talysurf Trace of Tapered Hole . . . . .	46
Figure B-1. Stress-Strain Characteristics for Fe-3Si Material . . . .	53

	<u>Page</u>
Figure B-2. Load-Deflection Characteristics for Fe-3Si Material . . .	54
Figure B-3. Load-Deflection Characteristics for Fe-3Si Material . . .	55
Figure B-4. Test Specimen Strained to 90 Percent of Yield Stress ( $\epsilon_p = 0$ ) . . . . .	56
Figure B-5. Test Specimen Strained Beyond Yield Stress, $\epsilon_p = 1$ Percent . . . . .	57
Figure B-6. Test Specimen Strained Beyond Yield Stress, $\epsilon_p = 2.5$ Percent . . . . .	58
Figure B-7. Test Specimen Strained Beyond Yield Stress, $\epsilon_p = 5$ Percent . . . . .	59
Figure B-8. Test Specimen Strained Beyond Yield Stress, $\epsilon_p = 7$ Percent . . . . .	60
Figure B-9. Test Specimen Strained Beyond Yield Stress, $\epsilon_p = 9$ Percent . . . . .	61
Figure B-10. Test Specimen Strained Beyond Yield Stress, $\epsilon_p = 14$ Percent . . . . .	62
Figure B-11. Etching Responses for Specimen Loaded to 90 Percent Yield ( $\epsilon_p = 0$ ) . . . . .	63
Figure B-12. Etching Response for $\epsilon_p = 1$ Percent . . . . .	63
Figure B-13. Etching Response for $\epsilon_p = 2.5$ Percent . . . . .	64
Figure B-14. Etching Response for $\epsilon_p = 5$ Percent . . . . .	64
Figure B-15. Etching Response for $\epsilon_p = 9$ Percent . . . . .	65
Figure B-16. Etching Response for $\epsilon_p = 14$ Percent . . . . .	65
Figure B-17. Top View of 2-Inch-Square x 1/2-Inch- Thick Coupon Specimen . . . . .	67
Figure B-18. Cross-Sectional View of 2-Inch-Square x 1/2-Inch-Thick Coupon Specimen . . . . .	67
Figure B-19. Top View of 2-Inch-Square x 1/2-Inch- Thick Coupon Specimen . . . . .	68
Figure B-20. Cross Sectional View of 2-Inch-Square x 1/2-Inch Thick Coupon Specimen . . . . .	69
Figure B-21. Top View of No-Load-Transfer Specimen . . . . .	70

	<u>Page</u>
Figure B-22. No-Load-Transfer Specimen — Sectioned Along Line A-B . . .	71
Figure B-23. Enlarged View of No-Load-Transfer Specimen — Sectioned Along Line A-B . . . . .	72
Figure C-1. Photograph of Model Aircraft Illuminated By Laser Light . . . . .	77
Figure C-2. Young's Fringes in the Diffraction Halo . . . . .	79
Figure C-3. Specklegram Recording Procedure . . . . .	82
Figure C-4. Photograph of the Loading Fixture and Camera . . . . .	83
Figure C-5. Cross Section of Camera . . . . .	85
Figure C-6. Data Acquisition Procedure . . . . .	86
Figure C-7. Photograph of the Data Acquisition Scanning Device . . . . .	88
Figure C-8. A Typical Plot of the Diffracted Halo With Young's Fringes . . . . .	89
Figure C-9. Radial Displacement Versus Radial Position for a 6 x 6 x 0.5-Inch 7075-T6 Aluminum Specimen With 0.00378-Inch Interference . . . . .	91
Figure C-10. Radial Displacement Versus Radial Position for a 6 x 6 x 0.5 Inch 7075-T6 Aluminum Specimen With 0.0026-Inch Interference . . . . .	92
Figure C-11. Metrological Data for an Aluminum Coupon Specimen . . . . .	93
Figure C-12. Radial Displacement Versus Radial Position for a 2 x 2 x 0.05-Inch Silicon-Iron Specimen With 0.00243-Inch Interference . . . . .	95
Figure C-13. Metrological Data for a Steel Coupon Specimen . . . . .	96
Figure C-14. Metrological Data for an Out-of-Round Aluminum Coupon Specimen . . . . .	98
Figure C-15. Radial Displacement Versus Radial Position for a 6 x 6 x 0.5-Inch Aluminum Specimen with a 0.5 Percent Out-of-Round Hole and 0.00366-Inch Interference . . . . .	99
Figure C-16. Strain Gage Locations on a 7075-T6 Aluminum No-Load Specimen . . . . .	101

	<u>Page</u>
Figure C-17. Radial Displacement Versus Radial Position For a No-Load 7075-T6 Aluminum Specimen With 0.00338-Inch Interference . . . . .	102
Figure C-18. Metrological Data for an Aluminum No-Load-Transfer Specimen . . . . .	103
Figure D-1. Linear Stiffness Elements and Frictional Forces Acting on Interface . . . . .	113
Figure D-2. Finite-Element Grid of One Quarter of a 2 x 2-Inch Plate . . . . .	115
Figure D-3. 3/8-Inch-Diameter Steel Fastener in 2 x 2 x 1/2-Inch Aluminum Plate . . . . .	117
Figure D-4. 3/8-Inch-Diameter Steel Fastener in 2 x 2 x 1/2-Inch Fe-3Si Plate . . . . .	118
Figure D-5. 3/8-Inch-Diameter Steel Fastener in 2 x 2 x 1/2-Inch Titanium Plate . . . . .	119
Figure D-6. 3/8-Inch-Diameter Steel Fastener in 6 x 6 x 1/2-Inch Titanium Plate — Edges Free . . . . .	120
Figure D-7. 3/8-Inch Diameter Steel Fastener in 6 x 6 x 1/2-Inch Titanium Plate — Edges Clamped . . . . .	121
Figure D-8. Finite-Element Grid Through the Thickness of Axisymmetric Disk . . . . .	123
Figure D-9. 3/8-Inch-Diameter Steel Fastener in 2-Inch- Diameter Aluminum Disk — Stress and Strain at Fastener at Hole Interface . . . . .	124
Figure D-10. 3/8-Inch-Diameter Steel Fastener in 2-Inch-Diameter Aluminum Disk — Stress and Strain Along Bottom Surface . . . . .	125
Figure D-11. 3/8-Inch-Diameter Steel Fastener in 2-Inch-Diameter Aluminum Disk — Stress and Strain at Mid-Thickness . . . . .	126
Figure D-12. 3/8-Inch-Diameter Steel Fastener in 2-Inch-Diameter Aluminum Disk — Stress and Strain Along Top Surface . . . . .	127
Figure D-13. 3/8-Inch-Diameter Steel Fastener in 2-Inch-Diameter Fe-3Si Disk — Stress and Strain at Fastener- Hole Innerface . . . . .	128
Figure D-14. 3/8-Inch-Diameter Steel Fastener in 2-Inch-Diameter Fe-3Si Disk — Stress and Strain Along Bottom Surface . . . . .	129

	<u>Page</u>
Figure D-15. 3/8-Inch-Diameter Steel Fastener in 2-Inch-Diameter Fe-3Si Disk - Stress and Strain at Mid-Thickness . . . . .	130
Figure D-16. 3/8-Inch-Diameter Steel Fastener in 2-Inch-Diameter Fe-3Si Disk - Stress and Strain Along Top Surface . . . . .	131
Figure D-17. 3/8-Inch-Diameter Steel Fastener in 2-Inch-Diameter Titanium Disk - Stress and Strain at Fastener-Hole Innerface . . . . .	132
Figure D-18. 3/8-Inch-Diameter Steel Fastener in 2-Inch-Diameter Titanium Disk - Stress and Strain Along Bottom Surface . . . . .	133
Figure D-19. 3/8-Inch-Diameter Steel Fastener in 2-Inch-Diameter Titanium Disk - Stress and Strain at Mid-Thickness . . . . .	134
Figure D-20. 3/8-Inch-Diameter Steel Fastener in 2-Inch-Diameter Titanium Disk - Stress and Strain Along Top Surface . . . . .	135
Figure D-21. 3/8-Inch-Diameter Steel Fastener in 4 x 4 x 3/8-Inch Aluminum Plate - 0.0025-Inch Interference . . . . .	137
Figure D-22. Contact Angle Achieved Between Fastener And Out-of-Round Hole Surfaces For Various Interferences . . . . .	138
Figure D-23. Radial Stress and Equivalent Plastic Strain Around Edge of Out-of-Round Hole . . . . .	139
Figure D-24. Geometry of Out-of-Roundness of Hole and Contact Stress Distribution Around the Edge for Interference Load Which Causes Initial Yield In Specimen; Diametral Interference = 0.00271 Inch . . . . .	141
Figure D-25. Stress and Plastic Strain Distribution Around the Edge of Out-of-Round Hole For Maximum Interference; Diametral Interference = 0.005 Inch . . . . .	142
Figure D-26. Finite-Element Grid of a Quarter Section of a No-Load-Transfer Specimen . . . . .	143
Figure D-27. 3/8-Inch-Diameter Steel Fastener in Aluminum No Load Transfer Specimen - Stress and Strain Parallel to Loading Direction Due to Fastener Installation . . . . .	145
Figure D-28. 3/8-Inch-Diameter Steel Fastener in Aluminum No Load Transfer Specimen - Stress and Strain Normal to Loading Direction Due to Fastener Installation . . . . .	146
Figure D-29. 3/8-Inch-Diameter Steel Fastener in Aluminum No Load Transfer Specimen - Stress and Strain Parallel to Loading Direction Due to Axial Load . . . . .	147

	<u>Page</u>
Figure D-30. 3/8-Inch-Diameter Steel Fastener in Aluminum No Load Transfer Specimen - Stress and Strain Normal to Loading Direction Due to Axial Load . . . . .	148
Figure D-31. Von Mises Stress and Equivalent Plastic Strain Around the Hole Edge: Comparison Between Sequential and Combined Load Analysis . . . . .	149
Figure E-1. No-Load-Transfer Joint Specimen . . . . .	152
Figure E-2. Specimen Detail, Reverse Dogbone - Low-Load-Transfer Test Specimen . . . . .	153
Figure E-3. Simple Lap Joint Specimen - Single Shear, 100 Percent Load Transfer . . . . .	154
Figure E-4. Structural Fatigue Laboratory . . . . .	156
Figure E-5. Strain Gaged Fatigue Specimen Mounted in Fatigue Machine Using Pin Grips . . . . .	158
Figure E-6. Fatigue Specimen Mounted in Fatigue Machine Using Wedge Grips . . . . .	159
Figure E-7. Failed No-Load-Transfer Specimen . . . . .	164
Figure E-8. Failed Low-Load-Transfer Specimen . . . . .	165
Figure E-9. Failed High-Load-Transfer Specimen . . . . .	166
Figure E-10. Surface Strain as a Function of Fastener Draw . . . . .	167

## LIST OF TABLES

	<u>Page</u>
Table 1. Details of Surface Strain Study . . . . .	25
Table C-1. Comparison of Strain Gage Readings With Strains Predicted by Finite-Element Analysis for an Interference Load of 0.00338 Inch in an Aluminum No-Load- Transfer Specimen . . . . .	105
Table C-2. Comparison of Strain Readings With Strains Predicted by Finite-Element Analysis for Axial Loads in an Aluminum No-Load-Transfer Specimen . . . . .	106
Table E-1. Aluminum No-Load Transfer Specimen Fatigue Results - 3/8-Inch-Diameter Steel Fasteners . . . . .	161
Table E-2. Aluminum High-Load Transfer Specimen Fatigue Results - 3/8-Inch-Diameter Protruding Head Steel Fasteners . . . . .	162
Table E-3. Aluminum Low-Load-Transfer Specimen Fatigue Results - 3/8-Inch-Diameter Protruding-Head Steel Fasteners . . . . .	163

## SUMMARY

This report presents the results of a multidisciplinary effort directed toward the development of a fatigue life prediction method for joints assembled with interference fit fasteners. The program objectives were as follows:

- Develop finite-element modeling techniques whereby stresses and strains at critical locations around fastener holes could be determined for optimum and normal production hole configurations.
- Develop the speckle photography techniques of surface displacement measurement and use data obtained by that method to verify finite-element results.
- Verify, by means of the dislocation etching technique, finite-element analytical predictions of through-thickness plastic strains.
- Develop fastened joint fatigue life data which can be used to verify fatigue life predictions.
- Using all of the above noted information, develop a fatigue-life-prediction technique.

The results of this effort can be summarized as follows:

- The finite-element modeling technique has been shown to be a viable tool for predicting stress and strains around interference-fit fastener holes in coupon specimens. Techniques have been developed that provide for elastic-plastic sequential simulation of the fastener insertion process, and modifications of the same computer code provide for the sequential application of external loads.

Based on electrical resistance strain gage data, it appears that additional work will be required in the area of element selection and modeling technique in order to more accurately predict stresses and strains for loaded specimens. This work should be extended to include stress-strain results after the completion of one loading cycle.

- The speckle photography technique has been shown to be a reliable tool for the measurement of in-plane surface

displacements. The use of this technique included development of a special camera, a twin-exposure technique for the measurement of incremental displacements, and a special data reduction technique and apparatus. It has been shown that the speckle photography technique as used in this effort is limited to coupon specimens only, as rigid body displacements due to the application of external loads reduce speckle correlation to unusable levels. However, an extension of this method to a two-plate technique has been shown to be workable.

- The dislocation etching technique has been shown to be applicable to the interference fit fastener problem. A method of coupon specimen preparation has been devised. Through-thickness plastic strains have been measured and used to verify analytical results. The application of the technique to fatigue problems has been found to be difficult, as the material ages at room temperature (during the fatigue test process) and hence becomes insensitive to the etching process.
- Fatigue life data have been developed for three joint configurations in several aluminum material thicknesses. These data reflect several fastener interference levels and hole conditions. Data were generated both for constant-amplitude and two simple spectra loadings. Much of these data were not used to verify fatigue predictions as the required stress-strain data were not available to make those predictions. Nevertheless, these data will be of great value to future investigators working on the fastened-joint fatigue-prediction problem.
- A mechanics-analysis/fatigue-damage-based fatigue analysis technique has been developed. This method uses critical local stress and strain information coupled with smooth-specimen damage-life relationships to predict fatigue life to crack initiation. It has been shown to be applicable for those cases where the necessary information is available and can be tested against other cases as information becomes available.

## 1. INTRODUCTION

The coming of the space age has brought about previously unimaginable technological advances. The aerospace industry has taken maximum advantage of these advances. In less than two decades, airplane designs have reflected major improvements in materials and manufacturing technology. Power plants have shown vast increases in size, power, and efficiency, while electronics systems have been designed in miniature with capabilities never before dreamed of. Efficiency has become the password in aerospace design practice. "Design to cost and design for life" have become major airplane design goals. It is a wondrous feeling to stand in awe of the giant, sleek, fast airplanes modern man has made.

But - what if we asked, "Is there one major problem common to today's aircraft, that wasn't so in past eras?" The probable answer would be "Fatigue". Aircraft designed to minimize weight and therefore reduce costs typically fight the problem of structural fatigue failures from the drawing board to the bone-yard. And what area is given major consideration when structural fatigue is discussed? None other than structural joints!

The vast majority of aircraft structural fatigue problems can be traced to fastened joints. Indeed, along with more sophisticated aircraft design practices, one finds new and more sophisticated fastener systems designed to improve joint fatigue life. These "fatigue improvement" fasteners typically use some form of the interference-fit principal. That is, sometime during the fastener installation process some form of interference between joint hole diameter and the fastener shank diameter is put to work to provide "beneficial" fatigue improving stresses.

Fatigue improvement fasteners can generally be placed in one of two classes

- Interference-Fit Fasteners (IFF) - where the fastener shank (tapered, straight, fluted, or lobed) is pressed into a hole smaller in diameter than the shank.
- Cold Work Fastening Systems (C/W) - sometimes called mandrelizing processes, whereby an oversized mandrel is pulled through a fastener hole and so cold working the hole in the process.

If one inquires why fatigue life is improved through the use of IFF and C/W systems, the answer, if one is given, is confusing at best. One is told that IFF's "prop" the hole and reduce the alternating stress around the hole when the structure is subjected to cyclic loads. On the other hand, it is conjectured that C/W systems leave beneficial residual compressive stresses that reduce the maximum stresses around the hole when the structure is subjected to cyclic loads. However, when one inquires into quantitative explanations that might be used for fatigue-resistant design criteria, he is confronted with much arm waving and illusions of black magic. He is told that the problem is too large and the number of variables too great to make quantitative joint fatigue design possible.

The objective of this program has been to investigate and obtain a basic understanding of the tapered-shank IFF as related to joint fatigue, including the development of a fatigue prediction method and verification of same with experimental data. The results of the program are not without shortcomings, but the findings reported herein will provide a sound baseline for the next investigator.

The approach was to develop the analytical tools whereby critical stress-strain states around IFF's could be defined. The initial effort dealt with the characterization of stress-strain states around optimum (round, properly tapered, smooth finished) holes. This effort was followed by a study of the effects of such hole variables as hole roundness, concentricity, taper, contact area, and surface finish. Where necessary, analytical results were verified experimentally via hole metrology, the dislocation-etching technique, speckle photography, or electrical resistance strain gages. These results were then used to develop a mechanics-analysis/fatigue-damage-based fatigue-prediction technique. Finally, the fatigue-prediction technique was verified with data from constant-amplitude and spectrum-fatigue evaluations.

The development of the fatigue prediction technique for joints assembled with IFF's is presented in the body of this report along with conclusions and recommendations. The individual analytical and experimental efforts required to accomplish the program objectives are documented in separate appendices, thus providing each element of the program with specific coverage.

Section 2 presents a brief review of fatigue-analysis methodologies followed by a discussion of the indirect and direct methods of fatigue analysis. The direct method was selected for application to the fastened joint problem,

expanded, and given detailed consideration. A fatigue-prediction technique was developed and applied to no-load transfer specimens subjected to constant amplitude and spectrum loading. Limitations of the analysis procedures are presented along with a discussion dealing with the use of static analyses in fatigue applications. Conclusions and recommendations are presented in Section 3.

Appendix A presents the hole drilling and measurement procedures used in this program. Examples are included to show round, out-of-round, nonperpendicular, and fluted holes. Methods of interference surface finish and contact area measurement are also discussed.

Appendix B describes the dislocation etching technique, as applied to the IFF problem. The physical basis for the technique, material preparation, calibration, and etching procedures are discussed. The results of the application of this technique to measure through-thickness plastic strain in IFF specimens are presented, discussed, and compared to analytical results.

Appendix C details the development of speckle-photography techniques as applied in this program. The basis for the technique is presented and then applied to the IFF problem. Experimental results are presented, discussed, and compared to analytical and other experimental results. A discussion of the application of the speckle-photography technique to axially loaded joint specimens is also presented.

Appendix D documents the results of the finite-element-analysis portion of effort. The finite-element computer programs used are described and the results are presented and discussed.

Appendix E deals with the experimental aspects of the fatigue program. Test specimens are described along with fatigue equipment and fatigue load levels. Fatigue life data is reported for all test specimens along with conclusions regarding the effects of hole quality and joint configuration.

## 2. FATIGUE ANALYSIS FOR FASTENER SYSTEMS

### 2.1. Introduction

The technology involved in the design and analysis of aircraft structures to resist a specific cyclic load history for an economically useful

lifetime is highly complex and often contains considerable uncertainty. In the recent past, such structures were sized, based on static load or deflection requirements, and then reanalyzed at specific locations where fatigue was considered a problem. This reanalysis frequently resulted in specific, detailed changes in configuration. With the development of fracture mechanics technology, there was often another design iteration at specific details to account for the potential reduction in structural residual strength from initiated and propagated fatigue cracks.

Fatigue analysis, as simply described above, usually involved nominal stress spectra for each "critical" location - curves relating stress to number of cycles to failure, modified Goodman diagrams, fatigue quality indexes, fatigue-crack-propagation-rate equations, and the assumption that Miner's cumulative-damage hypothesis applied to nominal stresses was a workable tool. Sufficient evidence has been built up over the past two decades to cast considerable doubt on predictive value of this approach (either over or under conservative with no assurance of which may be the more probable occurrence) when it is used for the analysis of complex structures subjected to variable amplitude load histories.

During this time period, two research developments have taken place which impact significantly on the design philosophies inherent in the simplified statements in the first paragraph. One of these was the development of fracture-mechanics technology which represents both a stress-analysis technique and a set of material behavioral descriptors using a far field parametric representation of crack-tip-deformation response and an experimentally calibrated crack-propagation-rate equation. Fracture-mechanics technology is useful in assessing both the crack-propagation life and remaining or residual strength of a structure and impacts not only on the design and test evaluation of aircraft structures but also on economic and safety considerations in maintenance and repair. The second research development relates to assessing fatigue life to crack initiation at a given notch or flaw. It involves a local stress-strain approach that deals with fatigue-crack initiation in a manner which directly reflects the fatigue process in the zone where the fatigue crack initiates as compared with past nominal stress approaches. Like fracture mechanics, both stress analysis and material behavioral descriptions are also required. Essentially, this approach closely parallels

that of fracture mechanics but uses different equations. It recognizes that, in highly localized areas, material strain hardening or softening can occur during cyclic stressing that modifies the cyclic stress-strain response of a material compared with monotonic stress-strain behavior. Thus, the applied-load transformation to stress-strain response at notch roots provides a more realistic description of damage cycles and usage of this approach has led to much more accurate predictions of fatigue-initiation life than in the past.<sup>(1)\*</sup>

Although most of the work directed toward developing methods for predicting life to crack initiation and duration of propagation has been accomplished on simple coupons, both the aforementioned methodologies appear to have the potential capability of providing a realistic means of estimating life of complex components and structures. The method of fastener fatigue analysis reported herein is based on these methodologies. Both methodologies represent an engineering approach to assessing the life of complex structures using local (notch root or crack tip) stress and strain. The local stress-strain approach was introduced into analysis in order to estimate crack initiation life by Smith<sup>(2)</sup> as early as 1963 and into analysis to estimate crack-propagation life by Paris, et al<sup>(3)</sup>, in 1961. Figure 1 indicates the role each of these technologies plays in examining the fatigue life resistance of a structure or complex component. The framework of this figure is based on recent observations (1) by Forysth<sup>(4)</sup> and others related to the mechanisms of fatigue-crack initiation and propagation in the material at a notch root or flaw and (2) by Topper and Morrow and their co-workers<sup>(5,6)</sup> related to the development of methods of fatigue life prediction.

Results obtained from both of these significant contributions have had a major impact of the design philosophies for complex structures such as in aircraft, pressure vessels, and ground transportation vehicles. Generally speaking, for these types of structures, fatigue life is made up of (1) a portion during which notches or flaws introduced during fabrication, or for functional reasons, initiate cracks of an engineering size, (2) a portion during which these initiated cracks grow in a manner which can be adequately described as a rate process, and (3) a portion during which rapid extension and static separation occur. For purposes of analytical convenience, the demarcation between crack initiation and propagation (or the definition of a crack of engineering size) is taken as that

---

\* References listed on page 34 of this report.

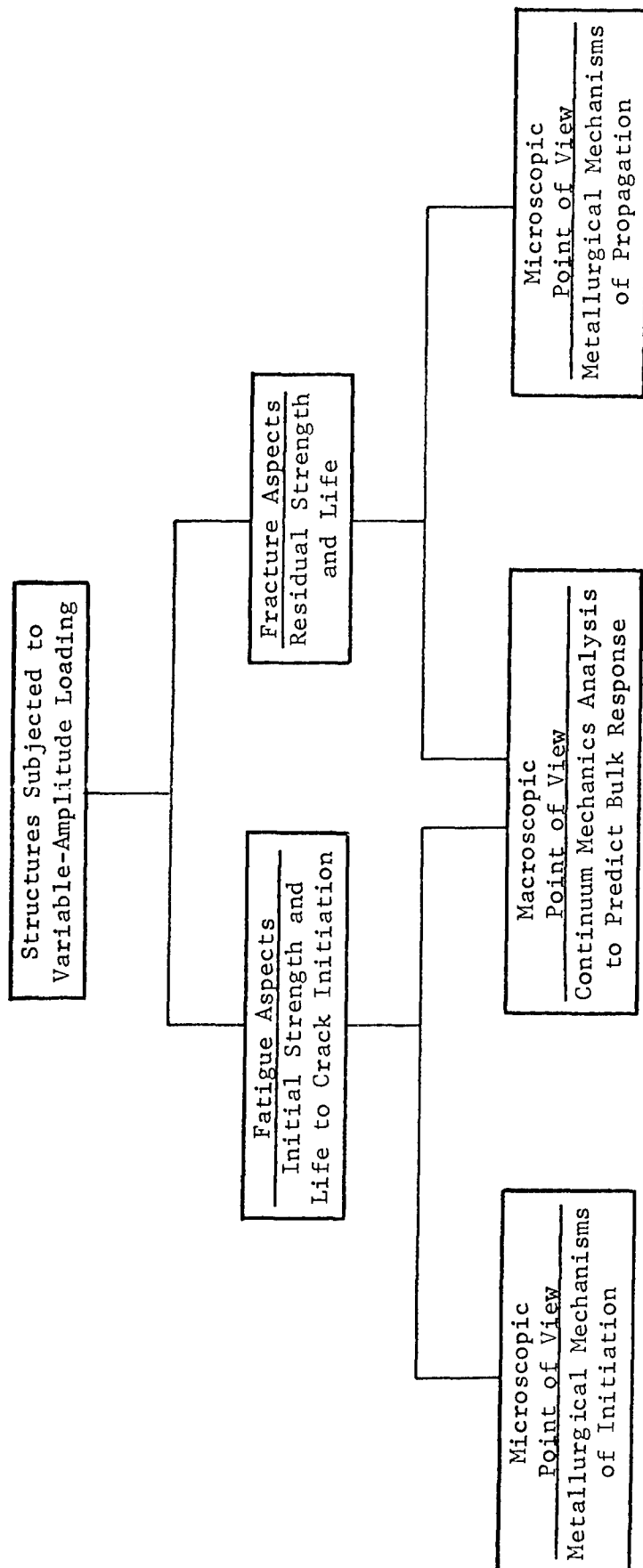


FIGURE 1. BREAKDOWN OF THE VARIOUS ASPECTS OF THE FATIGUE LIFE AND DEFORMATION RESPONSE OF CYCLICALLY LOADED COMPONENTS

crack length after which stable crack-propagation behavior can be satisfactorily modeled. Support for breaking the life to failure into these discrete stages comes from work whose purpose it was to characterize the mechanisms of fatigue failure. Although the many researchers involved have not agreed on the number of stages or to the fraction of life they govern, it is apparent that there are at least two distinct stages – life to crack initiation and the life expended in crack propagation. The total life is therefore considered as the sum of the life spent in each of these stages. Consequently, depending on the design/analysis philosophy, the life of a component may be equal to either the life-to-crack initiation,  $N_i$ , or the life (or some fraction of it) expended in crack propagation,  $N_p$ , or to their sum,  $N_t$ .

After Forsyth, there are two basic micromechanisms governing the fatigue behavior of cyclically loaded structures – one is operative during crack initiation, the other is operative during crack propagation. Each of these mechanisms is fundamentally different in the scale at which it operates; therefore, individual methods of analysis should be developed for each stage of life. The effects of both mechanisms can be viewed in two ways – in terms of the bulk response of the component (macroscopic) and in terms of the highly localized (microscopic) material behavior, as noted previously in Figure 1. Reviews of the microscopic aspects are numerous.<sup>(7)</sup> Details of the findings are, however, beyond the scope of this report. Suffice it to state that these studies have shown that reversed plastic flow is a necessary but not sufficient condition for fatigue failure in nonhostile environments. For the remainder of this report, only the macroscopic aspects are considered.

Even at the macroscopic level, fatigue failure is still difficult to predict even for simple laboratory samples. The design of realistic structures is therefore much more difficult. Designers of such structures must cope with the difficulties encountered in simple laboratory samples and at the same time account for structural interaction and the uncertainty of the service environment. While a number of studies have shown similarities in the fatigue resistances of complex components and structures and laboratory coupons<sup>(8)</sup>, several authors have pointed out that there are enough uncertainties to make designs based on this data extremely difficult. Work by other investigators<sup>(9)</sup> indicates that a major factor contributing to this uncertainty is that of the fastening of structural elements – the subject of the current report. To further pursue this aspect, a method of fatigue analysis for fastener systems based

on simple laboratory specimen data will be developed in this report. Current technologies which could form the basis for this analysis method are outlined and discussed in detail in the next section.

## 2.2. Current Technology

Current technology offers two basic approaches to the fatigue analysis of fastener systems.

- (1) The indirect approach, wherein attempts are made to predict fatigue life (assess and accumulate damage) on the basis of stresses and strains removed from the notch root or crack tip.
- (2) The direct approach, wherein attempts are made to predict fatigue life on the basis of actual or calculated stresses and strains at notch roots or crack tips (in lieu of actual or calculated stresses and strains, use would be made of measured or calculated variables which reflect the notch-root or crack-tip behavior).

### 2.2.1. The Indirect Approach

The indirect approach has been used extensively for correlating notched specimen fatigue life data and making fatigue life predictions. This is so largely because required deformation analyses and measurements are simple in comparison with those associated with the direct approach. Several authors have used nominal stress in notched components as a basis for correlating life to crack initiation of notched specimen fatigue life data. Alternately, other authors have suggested the use of the fracture-mechanics stress-intensity factor — a parameter based on elastic stresses remote to the notch root — as a basis for correlating notched specimen fatigue life to crack initiation data.

Generally, these indirect approaches provided reasonable consolidation of constant amplitude data. However, they lead to highly inaccurate and, depending on the overload direction, either conservative or unconservative predictions of notched specimen fatigue-life behavior under variable amplitude loading because they fail to account for the difference in sign of residual stress in the fatigue critical plastic zone as compared with the nominal stress

following overload cycles. Their use in situations where random or programmed loads are imposed is therefore not advisable. Similarly, these indirect approaches would lead to erroneous estimates of the influence of overload effects on the rate of crack propagation, unless the rate equation was modified through direct empirical calibration for overload effects. Such a modification is both time-consuming and expensive and usually does not afford the generality needed in dealing with the variety of load histories typical of those encountered in real structures.

Evidence for restricting the use of the indirect approach to the analysis of simple constant-amplitude load data comes from three sources -- analytical solutions for the deformation behavior of appropriate boundary value problems, measurements of local deformations in real and simplified components, and observed effects on life-to-crack initiation and crack-propagation behavior. The results of all available studies, both for initiation and propagation, point to the need for the direct approach if problems having variable-amplitude loading are to be satisfactorily dealt with. Unfortunately, this need has become evident only recently, largely because deformation analysis in the past was mathematically intractable and deformation and life measurements were very difficult or unreliable.

The recent widespread acceptance and success of the direct approach in dealing with the crack initiation portion of life results from three factors: (1) the limited applicability of the indirect approach, (2) the recent advances in analytical tools required for deformation analysis, and (3) the fairly recent instrumentation developments that permit experimentally following deformation behavior under cyclic stress. Unfortunately, such a direct approach has not been developed for dealing with the crack-propagation stage of life and empirical corrections applied to propagation rate equations are used.

Despite the popularity of the latter indirect approach combining crack-propagation-rate equations with empirical load interaction correction factors in the aerospace industry, data obtained in the present study do not justify its use in the present application as outlined in the following paragraph.

Throughout the experimental phase of this program, results indicated that only a very small fraction of a test specimen's life was spent propagating a crack from a notch or machining mark (flaw). Seldom could flaws (aside from that of the dominant notch) be traced as crack initiation sites. Indeed in some cases, cracks were found to initiate in the vicinity of machining

marks but not at them. Another factor considered in rejecting the use of fracture-mechanics concepts was the occurrence of specimens surviving several thousand cycles at gross stress levels for which fracture-mechanics calculations using a variety of assumed initial flaw shapes and sizes indicated the stress-intensity factor exceeded  $K_{Ic}$  for the material. In general, observations indicated that the experimental data were not compatible with current fracture-mechanics concepts. For this reason, the direct approach for predicting life to crack initiation is adopted for further development as the basis for the method of fatigue analysis for fastener systems presented in this report.

### 2.2.2. The Direct Approach

Essentially, this method consists of first utilizing a mechanics analysis to estimate local stress and strain as a function of nominal stress on a reversal-by-reversal basis, assuming that both deformation response and the fatigue-life behavior at the notch is identical to that of a smooth specimen forced through the same loading history. Thus, quantities which represent the local stress and strain ranges where the fatigue crack starts (at the root of the notch) in a notched specimen can be replaced by the corresponding quantities which are measured stress and strain ranges in a strain-controlled smooth specimen of the same metal and having the same fatigue life as the notched specimen.

Note that crack initiation is used in defining failure. In order to use fatigue data obtained from smooth specimens to predict the fatigue behavior of notch specimens, the crack length chosen to define the end of initiation should be small enough to have similitude between the stress states in the material surrounding the crack initiation locations in smooth and notched specimens. On the other hand, in order to make fatigue-life predictions, the crack length should be large enough to correspond to a large fraction of the fatigue life of the smooth specimen. Additionally, it is desirable in experimental work that the crack length chosen be easily detectable. Fortunately, crack sizes large enough to represent most of the life of smooth specimens at lives of practical interest are still small compared with the stress fields around most stress raisers. A crack length 0.005 inch has been previously suggested as a suitable length. These criteria must be satisfied by the definition of crack initiation in addition to the criterion for defining a crack of

engineering size discussed earlier. The criteria discussed here relate to the scientific validity of the definition. The criteria outlined earlier is necessary for the definition of failure to be consistent for both initiation and propagation analysis. The actual choice of failure criterion (crack length to define initiation) in the present work will not strongly influence life predictions because the fraction of life spent propagating fatigue cracks was usually quite small.

First generation attempts to incorporate the critical location approach into fatigue analysis have encountered several pitfalls, even when applied to simple open-hole notched coupons. The accuracy of life predictions for these coupons has been shown to depend on a number of diverse effects. Among these are the material response of the metal from which the coupon is manufactured, extent of local inelastic deformation, presence and degree of a local biaxial stress-strain field, and the definition of failure as reviewed in References 10 and 11 and described in the next several paragraphs.

Generally, the use of an inconsistent definition of failure (one which fails to account for differing fractions of life spent in crack propagation in smooth and notched specimens) will influence the value of the fatigue notch factor,  $K_f$ , over the entire life range. Similarly, the influence of biaxial stresses at notch roots, not accounted for in fatigue analysis based on two-dimensional deformation analysis, will influence  $K_f$  over the entire life range. But, the last factor, errors made by deformation solutions which fail to accurately determine inelastic notch-root strains, is important only over the range of life for which local stress-strain response is nonlinear.

Figures 2, 3, and 4, taken from References 11, 10, and 12, respectively, graphically depict variations in the value of  $K_f$  which are directly attributable to the above factors. In both Figures 2 and 3, the variation in  $K_f$  is shown directly in terms of the fatigue notch factor as defined in Reference 2, while Figure 4 uses this same measure normalized with respect to  $K_t$ .

2.2.2.1. Biaxiality. Figure 2 clearly indicates the influence of notch root biaxiality on the value of  $K_f$ . Note that as  $K_t$  increases, notch root radius decreases which, for the data from Vee-notched bars of constant minimum diameter shown in this figure, causes a local biaxial stress state that prevails for these data at values of  $K_t$  greater than about 2.5. Below 2.5, excellent predictions of  $K_f$  based on  $K_t$  are achieved; but at values greater than 2.5, the data fall on or slightly below a line with a slope of about 0.87. Such a slope is predicted when the notch root biaxial stress field is taken into account<sup>(11)</sup>.

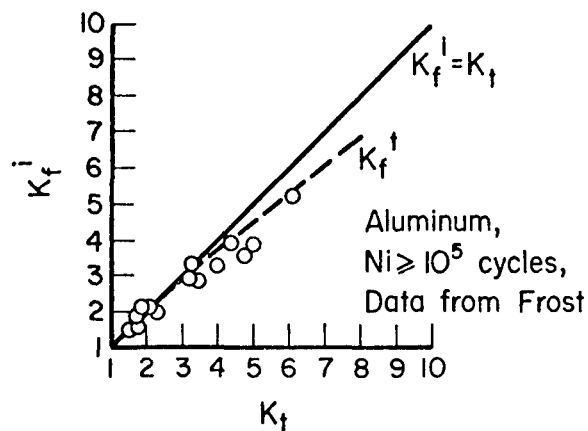


FIGURE 2. INFLUENCE OF BIAxIALITY (REFERENCE 11)

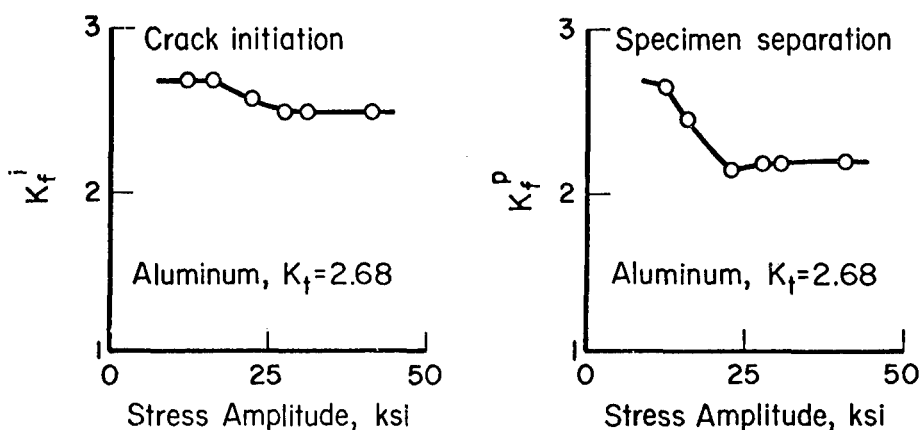


FIGURE 3. INFLUENCE OF FAILURE CRITERION (REFERENCE 10)

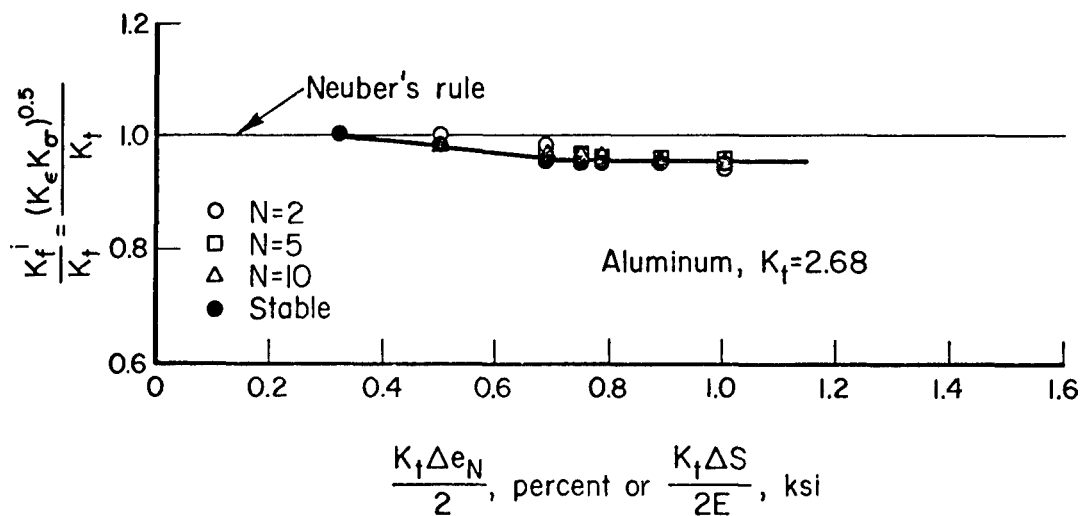


FIGURE 4. INFLUENCE OF PLASTICITY (REFERENCE 12)

2.2.2.2. Failure Criterion. Figure 3 indicates differences in the value of  $K_f$  attributable to the use of different failure criterion. When crack initiation (0.005-inch length) is used to define failure, there is a high degree of predictability of  $K_f$  based on  $K_t$  (left-hand graph of Figure 3). In contrast, when separation is used, only limited predictability is achieved (right-hand graph of Figure 3).

2.2.2.3. Inelasticity. Finally, the variability in  $K_f$  due to use of an inaccurate inelastic deformation analysis (Neuber's Rule in this case) is evident in Figure 4 as the difference between the line labeled Neuber's Rule and the data points at larger values of nominal stress. Recent studies on other materials and notch geometries<sup>(13,14)</sup> indicate this lack of correlation depends on both material and geometry. Furthermore, the lack of correlation was always greater than that shown in Figure 4.

It should be pointed out that the data in Figures 2, 3, and 4 are for fully reversed loading conditions. These factors need to be extended to and included in cases where mean stress is present. As yet, this aspect has not been examined in detail.

While demonstrating the need for both more refined deformation analyses for notches and a consistent definition of failure for smooth and notched specimens, data in Figures 2, 3, and 4, and that discussed in References 10-14 support the practice of predicting notched specimen fatigue life on the basis of smooth specimen data. Further, work reported in these and other references [for example, that of Morrow, et al<sup>(6)</sup>], supports the practice of damage assessment and accumulation during crack initiation in terms of notch root stress and strain rather than nominal stress used in the more conventional fatigue analyses procedures.

A number of authors proposed empirical formulations suitable for assessing the combined influence of the above noted effects and justified them in terms of a "material size effect". This "material size effect" was hypothesized to cause the small amount of material at a notch root to exhibit a greater fatigue resistance than the much larger amount of material in a smooth specimen. In other words, rather than having the same life-to-crack initiation as a smooth specimen at a given strain level, the metal at the notch root would have a longer life. Other authors have rationalized this observed fatigue-life

behavior through the hypothesis that failure initiates at some critical depth below the surface at a stress level reduced through the gradient to some value less than the peak (surface) value. This size (depth) effect therefore causes a reduction in the stress level causing fatigue as compared with the maximum principal stress or its ratio to nominal stress. It is important to point out here that measurements on which "material size effects" were predicted consisted of measured nominal stresses in notched specimens and stresses and strains in a smooth specimen. While these measurements showed that the fatigue notch strength reduction factor was less than  $K_t$ , they could not determine whether an increased fatigue resistance for the metal at a notch root or an erroneous deformation solution was responsible.

Resolution of which factor is responsible for this behavior has come recently when accurate direct measurements of cyclic strains at notch roots allowed a direct comparison of the deformations at the critical locations of smooth and notched samples corresponding to the same life to crack initiation. Since notch root stress in fatigue applications must be determined on the basis that material in this location exhibits the same stress-strain response as a uniaxial sample, an experimental evaluation of the degree to which "material size effect" alters the fatigue resistance of the material at the root of sharp stress raisers from that of the same material in a smooth sample can only be based on measured local strains.

A comparison of strains at the critical locations of smooth and notched specimens corresponding to the same life to crack initiation shown in Figure 5 indicates that smooth and notched samples form cracks at the same life when identical strain histories are imposed at their respective critical locations. There is no evidence of a material size effect. It should be noted that in determining the "lives" corresponding to measured strain histories in smooth and notched samples, "crack initiation" was used as the definition of failure. Other studies of the local-strain life-to-crack-initiation behavior of smooth- and notched-laboratory fatigue samples have produced more extensive data. A comparison of the equivalent strains corresponding to the same life-to-crack initiation at the fatigue-critical locations of smooth and notched specimens made using these data also fails to indicate any evidence of a material size effect. Values of the ratio of equivalent notch root strain,  $\bar{\epsilon}^P$  and  $\bar{\epsilon}^T$  (plastic and total strain components, respectively), to the corresponding equivalent smooth specimen strain,  $\bar{\epsilon}^P$  and  $\bar{\epsilon}^T$ , at the same life-to-crack initiation were used as the

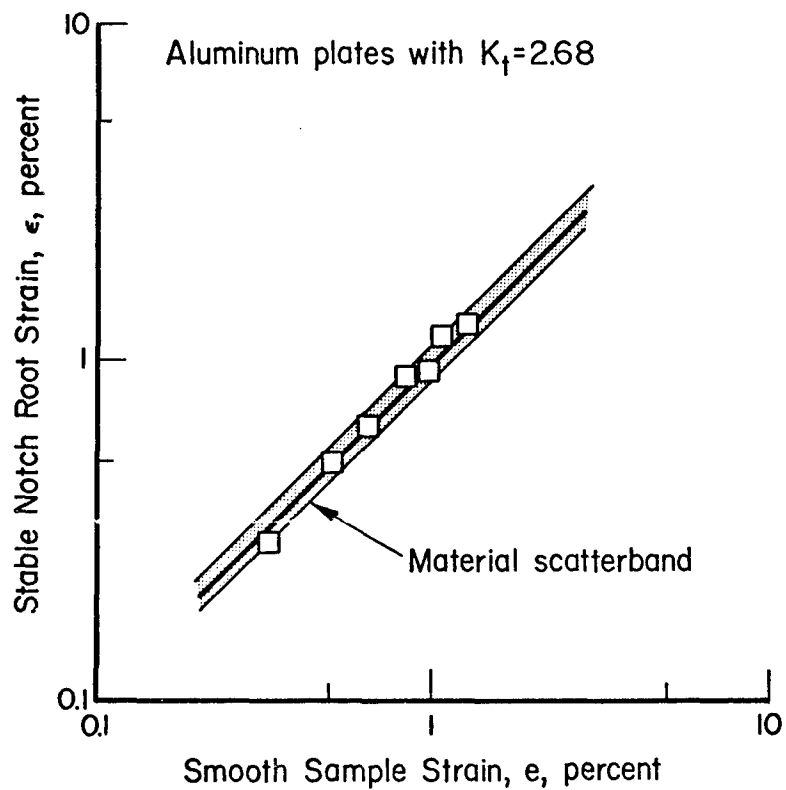


FIGURE 5. COMPARISON OF STABLE NOTCH-ROOT STRAIN WITH SMOOTH SPECIMEN STRAIN AT THE SAME LIFE TO CRACK INITIATION (REFERENCE 10)

basis for comparison. Although the data were limited for any given value of  $K_t$ , values of these ratios did not appear to depend on  $K_t$ . Similarly, values of these ratios did not show any marked dependence on life to crack initiation. A histogram of the data pooled with respect to both life-to-crack initiation and elastic stress-concentration factor representing 117 comparisons is shown in Figure 6. A statistical evaluation of these data, grouped as shown in the histogram, indicates that values of the ratios  $\bar{\epsilon}^P/\bar{\epsilon}^P|_{N_i}$  and  $\bar{\epsilon}^T/\bar{\epsilon}^T|_{N_i}$  are normally distributed (with 99 percent confidence) about a sample mean of 1.014 with a standard deviation of 0.218. In summary, it was concluded that these data do not show evidence of any significant "material size effect" in fatigue. This conclusion means that when fatigue critical strain (and stress) values are used in damage assessment and life prediction, accurate predictions can be made without resorting to a fudge factor empirically determined from size effect considerations.

Since the above results (which are independent of the deformation analysis) showed no evidence of a "material size effect", an explanation for the results of the many studies which have indicated that  $K_f$  differs from  $K_t$  (and, in addition, varies with stress level) must be sought elsewhere. Recent experimental and analytical results reviewed in References 10 and 12 suggest that three main factors, (a) the definition of failure, (b) local biaxial stress, and (c) inaccuracy in inelastic deformation theories, are responsible for discrepancies between the value of the notch-strength-reduction factor and the theoretical stress-concentration factor. This report accounts for factors (b) and (c) through the use of accurate measured and analytically determined strains. The definition of failure, as previously discussed, will not have a significant influence in the present context.

### 2.2.3. Essential Features of the Direct Approach

The essential features of the direct approach to fatigue analysis of fastener systems are shown schematically in Figure 7. Included are: (1) a knowledge of typical input load histories, (2) material monotonic and cyclic stress-strain response, (3) a mechanics analysis to transform nominal stress into fatigue critical strain and stress that includes fastener installation effects, (4) a means of assessing fatigue damage including a cycle counting routine and a damage

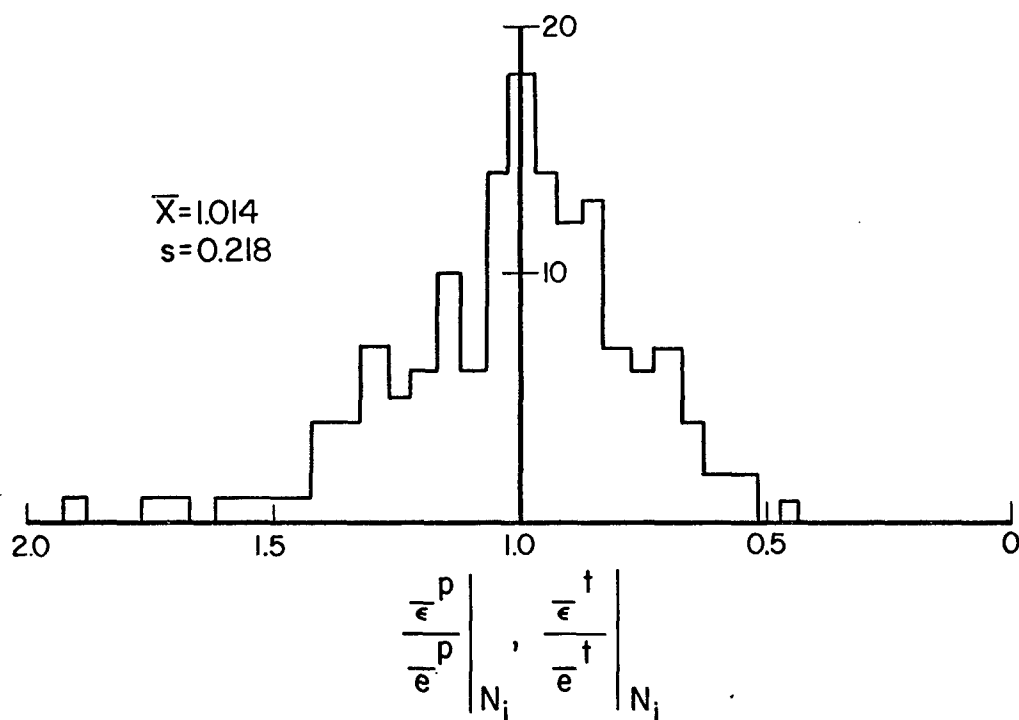


FIGURE 6. HISTOGRAM OF THE VALUES OF THE RATIOS

$$\frac{\left. \frac{\bar{\epsilon}^p}{\bar{e}^p} \right|_{N_i}}{\left. \frac{\bar{\epsilon}^t}{\bar{e}^t} \right|_{N_i}}, \frac{\left. \frac{\bar{\epsilon}^t}{\bar{e}^t} \right|_{N_i}}{\left. \frac{\bar{\epsilon}^p}{\bar{e}^p} \right|_{N_i}}, \text{ FROM REFERENCE 10.}$$

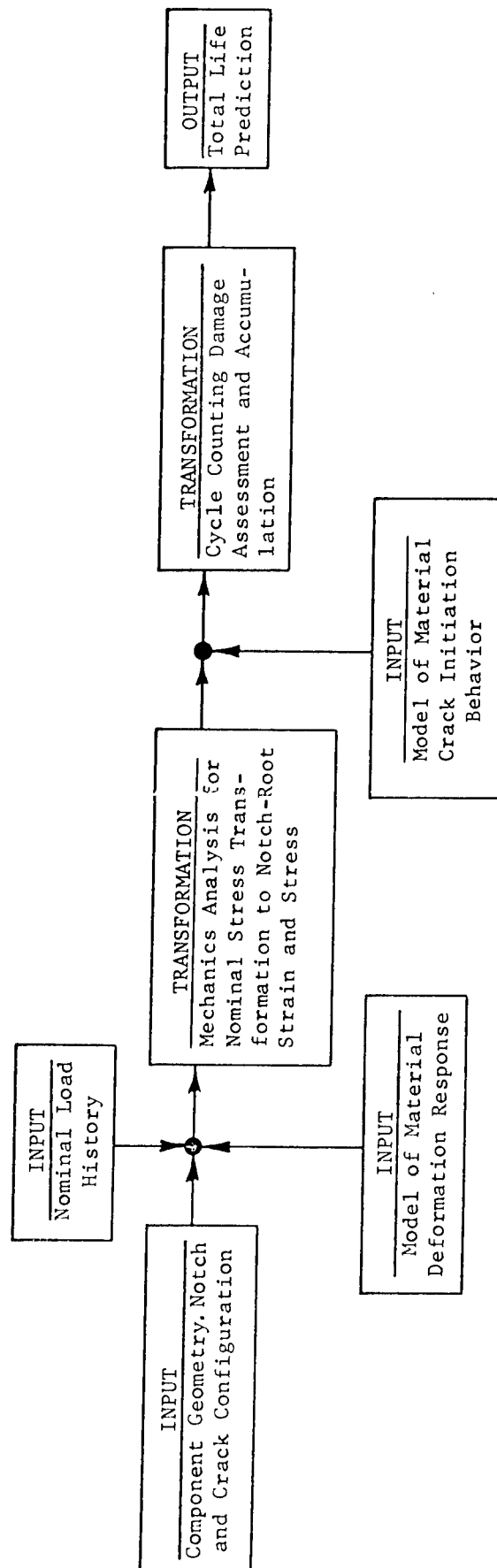


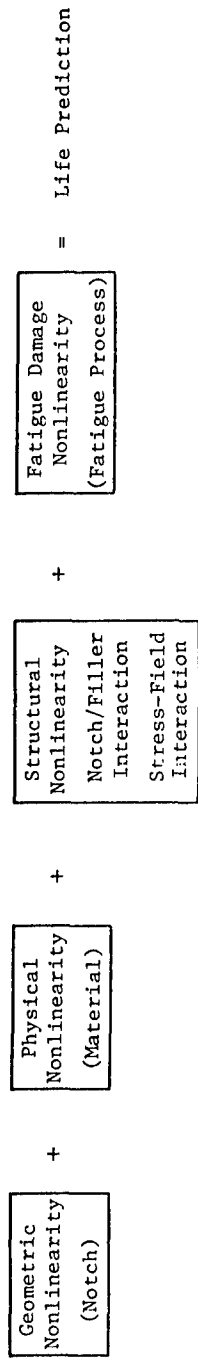
FIGURE 7. ESSENTIAL FEATURES IN THE DIRECT FATIGUE ANALYSIS PROCEDURE.

parameter, and (5) a routine for accumulating damage assessed on a reversal-by-reversal basis. Each of these essential features is expanded on in Figure 8 which outlines the nonlinear transformations encountered in the analysis procedure (part a) and outlines in detail the aspects involved with each of the features when dealing with general variable-amplitude load histories (part b). Each of these is much simpler when dealing with constant-amplitude and spectrum loading consisting of repeated blocks of constant-amplitude cycles. In the following section, examples of how the direct approach to fatigue analysis can be applied are presented and discussed and references from which further information can be found will be noted. It is believed that by dealing with these simplified problems first, the approach can be better demonstrated. Thereafter, the complexities introduced by fastener systems will be discussed and the approach will be modified to account for these effects.

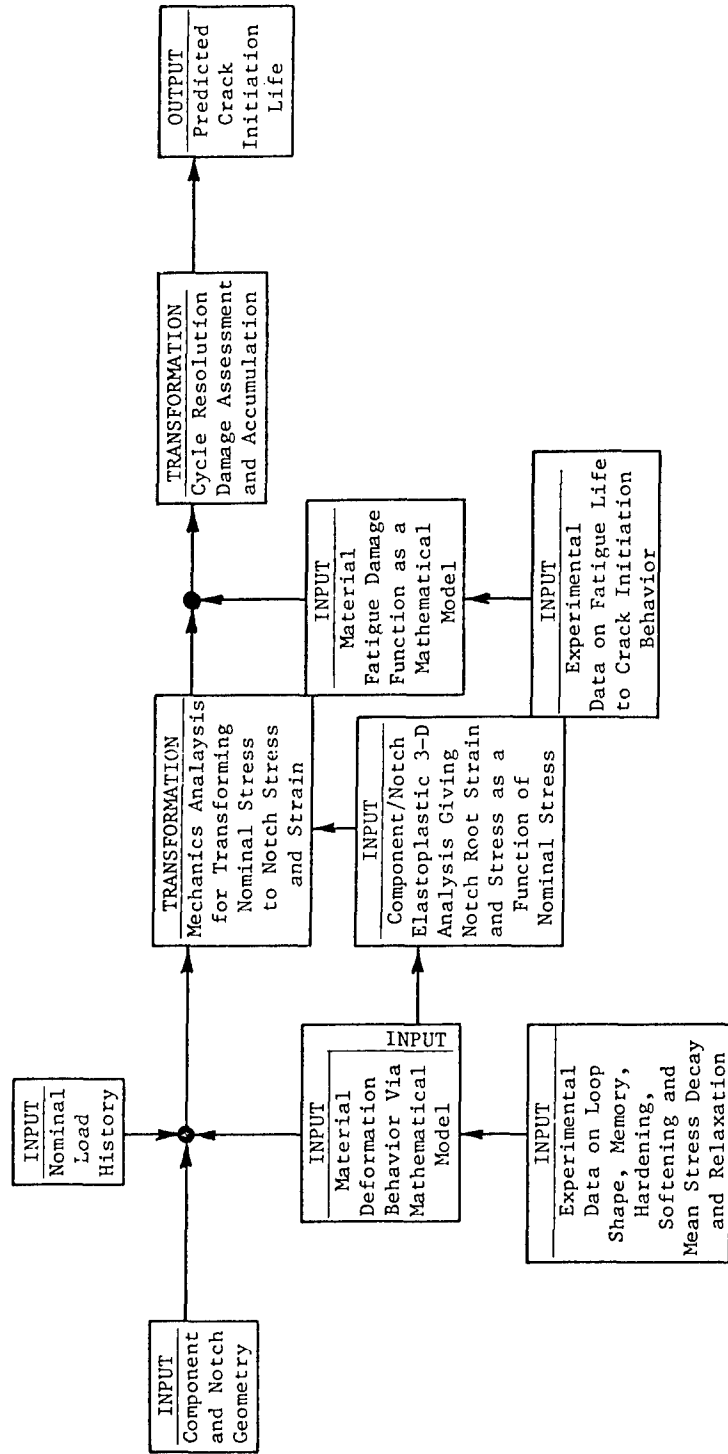
#### 2.2.4. Analysis Framework for No-Load-Transfer Specimens Subjected to Constant-Amplitude Loading

Since its introduction into fatigue analysis by Smith<sup>(2)</sup> in 1963, the direct approach has found wide application. Generally, either the Hardrath-Ohman modification of Stowell's notch analysis<sup>(15,16)</sup> or some form of Neuber's rule<sup>(17)</sup> have been used to transform nominal stress to local strain. But as might be expected, the use of notch analysis obtained through the solution of a specific boundary value problem as a "general notch analysis" led to numerous difficulties — the majority of which were often manifest in differences in the value of the fatigue-notch factor (FNF) determined by these analyses and the value of  $K_t$ , the elastic stress-concentration factor. Some measure of the magnitude of the problem of estimating the FNF is evident in Reference 18 devoted to this subject. In this review, a total of nine different fatigue concentration factors are defined, none of which were found to be constant with life. In addition, consistent values of these factors could not be found in systematic variations in material only or notch geometry only.

Until recently, the inability to predict this notch factor was the only major problem remaining in making consistent life predictions of simple notched coupons<sup>(10)</sup>. However, it has been shown that this problem can be resolved by the use of either accurate notch analysis or measured notch root strains to "calibrate" these analyses for application to a specific problem<sup>(10)</sup>. An



(a) Nonlinear Transformations Involved in Determining Crack Initiation Life, For a Prescribed Input Load History



(b) Block Diagram of Procedure

FIGURE 8. BLOCK DIAGRAM OF FATIGUE ANALYSIS PROCEDURE DURING CRACK INITIATION

example of life prediction will be given next for open-hole notched specimens subjected to constant-amplitude loading. Predictions made using measured notch root strains for notched aluminum plates in the manner outlined in References 10 and 19 are shown in Figure 9. Corresponding predictions based on accurate notch analysis are also shown in this figure. In such applications, fatigue resistance is plotted on axes where the ordinate is given by  $(\Delta s \cdot \Delta e \cdot E)^{\frac{1}{2}}$  for smooth specimens and  $(\Delta S \cdot \Delta e_N \cdot E)^{\frac{1}{2}}$  or  $\Delta S$  for notched specimens and the abscissa is life (to crack initiation). The symbols  $S$  and  $e_N$  and  $s$  and  $e$  refer to nominal stress and strain, respectively, in notched and smooth samples;  $E$  is the modulus of elasticity; and  $\Delta$  indicates peak-to-peak changes in the corresponding quantities. In this example, smooth specimen data are shown as the solid line. Experimentally determined data for notched plates are shown as open symbols whereas the corresponding predicted values calculated from the smooth specimen data are shown as broken lines. The close correspondence between actual and predicted behavior shown in this figure is typical of that for a variety of data obtained from the literature<sup>(19)</sup>.

In each of the previous applications of the direct approach, only simple open-hole notched plates or Vee-notched bars have been examined. In the present application, the added complexity caused by the presence of an IFF must be accounted for in the transformation from nominal stress to local strain and stress. But, accounting for this added complexity in no way requires modification of the basic prescription for fatigue analysis that was used in making life predictions of simple notched specimens. It does, however, require significantly more sophisticated and complex stress analysis and experimental measurements in that cyclic, rather than monotonic, loading data are needed. The analytical developments which formed a part of this effort are reported in detail in Appendix D. Unfortunately, difficulties encountered with the development of three-dimensional elastic-plastic finite-element models precluded the extension of the technique to include cyclic loading. However, measurements of fastener installation strains and then of cyclic strains in the vicinity of the fastener proved successful. Details of the complexities associated with the use of electrical resistance strain gages to measure cyclic inelastic strains are reported in detail in Reference 20. Results of the fastener installation strains are included in Appendix E. They will, however, be discussed later in

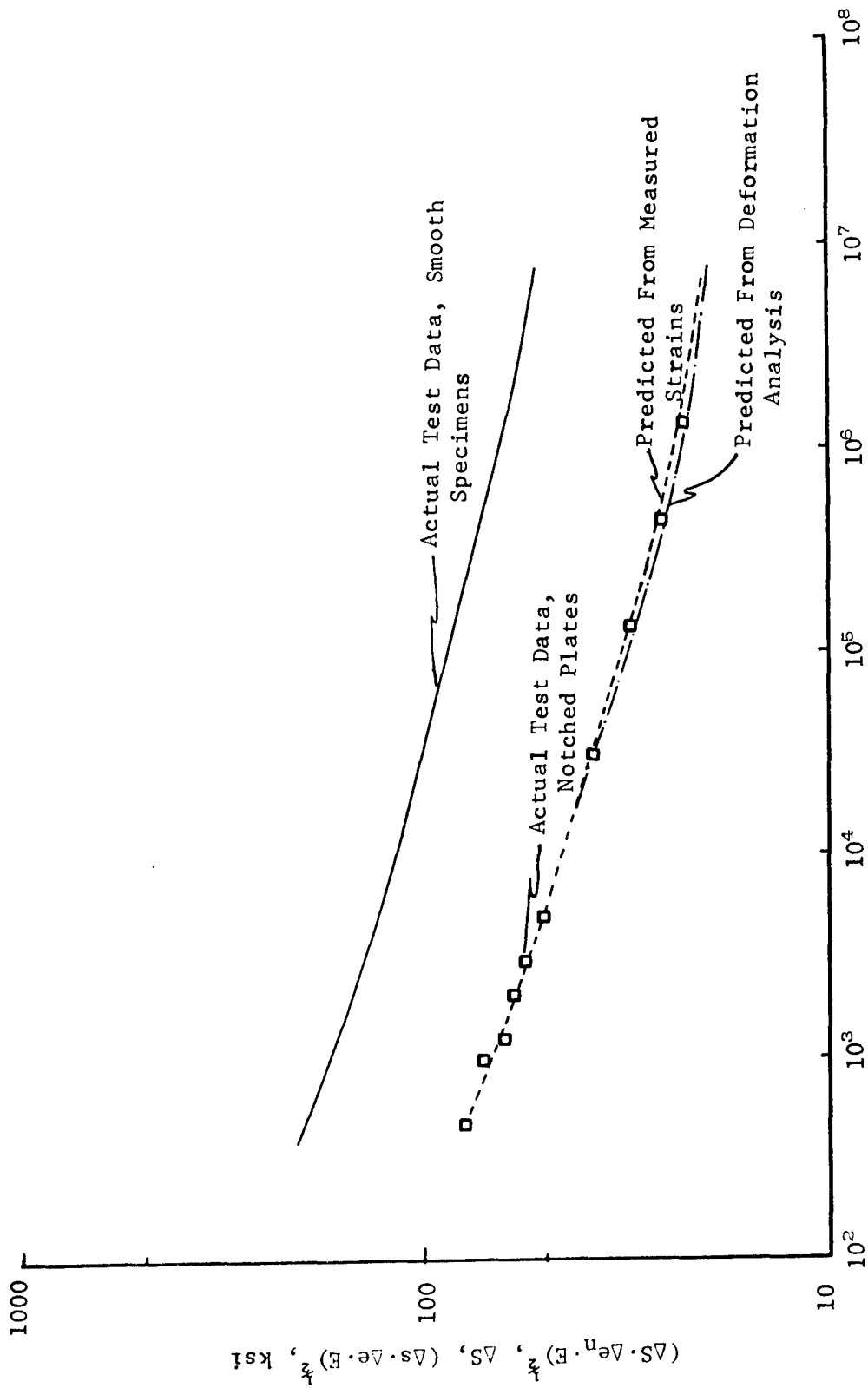


FIGURE 9. ACTUAL AND PREDICTED FATIGUE LIFE BEHAVIOR OF NOTCHED OPEN HOLE PLATES FOR 2024-T351 ALUMINUM (REFERENCE 19)

this section as they impact significantly on understanding the behavior of the IFF during subsequent load cycling.

Results obtained as a part of this strain-gage study are shown in Figure 10. (The aluminum specimen configuration is shown in Figure E-1.) Note that only results obtained from the strain gage nearest the hole are shown and that only data from the first several reversals are included. Details of the gage type, size, and position are shown in Table 1 along with the corresponding values of the stable cyclic strains recorded by each gage. After the first reversal, the waveform of all three gages on a given specimen were comparable and exactly in phase. Because the gage waveform both away from the hole in the elastic stress field and near the hole was comparable, deformation after the first reversal was linear elastic. A total of five no-load-transfer specimens were allocated to this investigation. One specimen was tested in static tension whereas a second was used as a reference (open hole) to tie in the results of this study to previous investigations. Three specimens were used to investigate the effect of interference. To accent this effect, these specimens were tested at 70 percent of material yield stress load level ( $R = 0$ ), a nominal stress level sufficiently high to cause significant local inelastic flow. Below optimum, optimum, and above optimum interference levels of 0.002 inch, 0.004 inch, and 0.005 inch, respectively, were considered. Finally, to examine the influence of load, one specimen was tested at 35 percent load level ( $R = 0$ ) using the fastener manufacturer's recommended optimum interference of 0.004 inch.

A number of trends are evident in these data which have a significant impact on life predictions and add greatly to the understanding of fatigue improvement IFF's. In comparing cases A, B, C, and D of Figure 10, the influence of interference is apparent.

- (1) Propping, as evidenced by an increase in the mean strain during steady load cycling and indirectly in the decrease in the cyclic strain amplitude, increases with increasing interference. It is this decreased strain amplitude which is primarily responsible for the increased fatigue life when IFF's are used. Note that the strain ratio,  $R_e$  (the algebraic ratio of minimum to maximum local strain), is directly proportional to the extent of this propping. Also note that a number of investigators have shown that small






Gage Response	Case	Load, % Yield	Interference, inch	Propping, %	$R_{\epsilon}$	$\frac{\epsilon_{peak}}{\epsilon_{a peak}}$
	A	70	Open Hole	0	0	1.0
	B	70	0.002	4	0.04	0.85
	C	70	0.004	20	0.20	0.65
	D	70	0.005	45	0.45	0.95
	E	70	0.004	0	0	NA

FIGURE 10. GAGE 1 STRAIN RESPONSE WITH CYCLES

TABLE 1. DETAILS OF SURFACE STRAIN STUDY

Specimen Number	Gage Position <sup>(a,b)</sup> and Stable Strain Range <sup>(c)</sup>		
	1 Position/Strain	2 Position/Strain	3 Position/Strain
8DP6SB2-8	0.029/0.21	0.090/0.19	0.395/0.19
8DP6SB2-12	0.022/0.59	0.082/0.45	0.381/0.395
8DP6SB2-14	0.026/0.72	0.093/0.42	0.431/0.385
8DP6SB2-16	0.027/0.36	(d)	(d)
8DP6SB2-20	0.023/0.42	0.086/0.38	0.391/0.36

(a) Distance from edge of hole to center line of gage gird, gage mounted along transverse minimum section — all dimensions in inches.

(b) Gage type: (1) 0.015 x 0.015 grid, backing trimmed along grid edge in strain measuring direction, (2) 120 $\Omega$  resistance; metal foil was a stabilized constantan alloy, and (3) AE type epoxy; cure in accordance with manufacturers instructions.

(c) Strain shown in percent; value shown is the stable cyclic strain.

(d) No gage was used.

mean strains have little influence on life. However, the presence of mean stress can significantly alter life.

Because the deformation after the first reversal was linear elastic, there is no driving force for cycle-dependent transient response in the plate material ( $\epsilon_p = 0$ ). Consequently, the local stress ratio,  $R_\sigma$  (the algebraic ratio of local minimum to maximum stress), is equal to  $R_\epsilon$ . The maximum local stress must, therefore, lie on the monotonic stress-strain curve of the material.

- (2) At all levels of interference, there was an initial tendency for the mean strain to increase indicating a "seating" of the fastener which causes an increase in interference level. This effect was most evident at the higher interference level.
- (3) The value of peak strain achieved on the first reversal decreases from about 0.72 percent strain for the open hole to about 0.60 percent strain for 0.002-inch interference to a low of about 0.46 percent at the optimum interference level of 0.004 inch. But at the higher interference level, 0.005 inch, the value of this peak strain rises to about 0.68 percent strain. At 70 percent load level and 0.005-inch interference, the plastic zone size is considerably larger than for those of the lower interference levels. Because of this, the effective interference defined by the product of interference and the ratio of hole diameter to plastic zone size is approximately equal to imposed interference at interference levels less than or equal to the optimum value. But, at large interference levels and correspondingly larger zone sizes, the effective interference is reduced. Note that this implies that, at lower load levels, the effective optimum interference level is greater than that at higher load levels. The effective interference would be a function of (1) the ratio of the elastic moduli for the fastener and plate materials and (2) the rate of strain hardening in the plate material.

In comparing cases C and E, the influence of load level at optimum interference can be assessed as follows.

- (1) The range of the stable cyclic strain is directly proportional to load, at least for loads not exceeding the 70 percent load level.
- (2) The magnitude of the peak strain attained on the first reversal is not directly proportional to load, or the influence of propping is not directly proportional to load, or some combination of these two is not proportional to load. The dependence of the peak strain on propping and load level cannot be isolated using the available data.

Other observations can be made concerning fastener installation for data generated for cases B, C, D, and E, which is detailed in Appendices C and E for strain gages and in Appendix B for the dislocation etching technique.

- (1) There was often a significant lag between interference as measured by surface strains and interference as measured by fastener draw and by installation torque which showed an essentially linear relationship with draw. This lag was measured on a total of five different no-load-transfer coupons, four of which were used subsequently to measure cyclic strains and one used during the speckle photography portion of the work. In all cases, the measured strains compared well with each other at a given value of interference. There was, however, significant discrepancies between measured and analytically predicted near-fastener strains as shown by comparing data in Appendices C, D, and E.
- (2) Measurements on the four subsequently fatigue-cycled specimens also showed that after an initial lag, the fastener draw, measured strain, and torque were linearly related to each other, at least during the first 0.002-inch to 0.003-inch interference. In drawing to 0.004-inch and 0.005-inch interference levels, there were discontinuities in the measured strain-fastener draw relationship. These steps are associated with the slip of

the fastener with respect to the wall as static friction between them was overcome. These steps occurred as flow of the plate material in the direction of the draw caused by friction reached a limiting state (restrained from deforming by the nut) and, by slip, unloaded elastically to begin the process again. At most, two steps were observed. Note that dislocation etching technique measurements reported in Appendix B indicate compressive plastic strains under the nut of as much as 14 percent. They also indicate the through-thickness strain distribution away from the nut and bolt head is uniform, possibly because it is dominated by the large plastic flow occurring during installations. Note that in "thick" plates for which conditions of plane strain prevail, this distribution of through-thickness strain is also uniform. Which of these factors is responsible cannot be isolated using presently available data.

Having completely outlined the influence of an IFF in an ideally round, tapered, nonfluted hole on the local stress-strain field, we are in a position to make life predictions for the no-load-transfer coupons loaded at 70 percent and 35 percent load level ( $R = 0$ ) and containing fasteners installed at 0.004-inch interference. This limitation as to what life predictions can be made is due to the limited availability of local stress and strains for this and the other joint configurations. It is not due to limitations in the fatigue analysis procedure. Observed fatigue lives for these two cases are: for 35 percent,  $N_f = 1,566,690$  and  $N_f = 432,715$ , giving an average of about  $10^6$  cycles; and for 70 percent,  $N_f = 25,833$  cycles to failure. Fatigue life predictions for these two cases are straightforward.

- (1) Using available data from Appendix D and in Reference 21, the peak strain at the fatigue critical location due to interference only was estimated as 1 percent strain. Thus, the peak strains at 35 percent and 70 percent loads were 1.21 and 1.43 percent, respectively. Since the stress-strain response must follow the monotonic curve, the peak local stress can be calculated using materials data from

Reference 22. These peak stresses are 72 ksi and 73.5 ksi, respectively, for 35 and 70 percent load levels. Because cycling is elastic following the first reversal, these values do not change with cycles.

- (2) Using measured strain data, the strain ranges are 0.21 and 0.43 percent, respectively, for the 35 and 70 percent load levels.
- (3) Fatigue damage has been hypothesized<sup>(23)</sup> and more recently analytically derived using energy considerations<sup>(24)</sup> as a function of maximum stress and strain amplitude (or range) in the vicinity of the fatigue-crack initiation site. Data for the aluminum alloy Clad 7075-T6\* are available in the form of this parameter in Reference 23. Using the above data, the values of this damage parameter are 29 ksi and 41 ksi, respectively, for the 35 and 70 percent load levels.
- (4) Using the relationship between damage life given in Figure 11, the predicted lives at 35 and 70 percent load levels are  $N_f = 950,000$  and  $N_f = 38,000$  cycles, respectively.

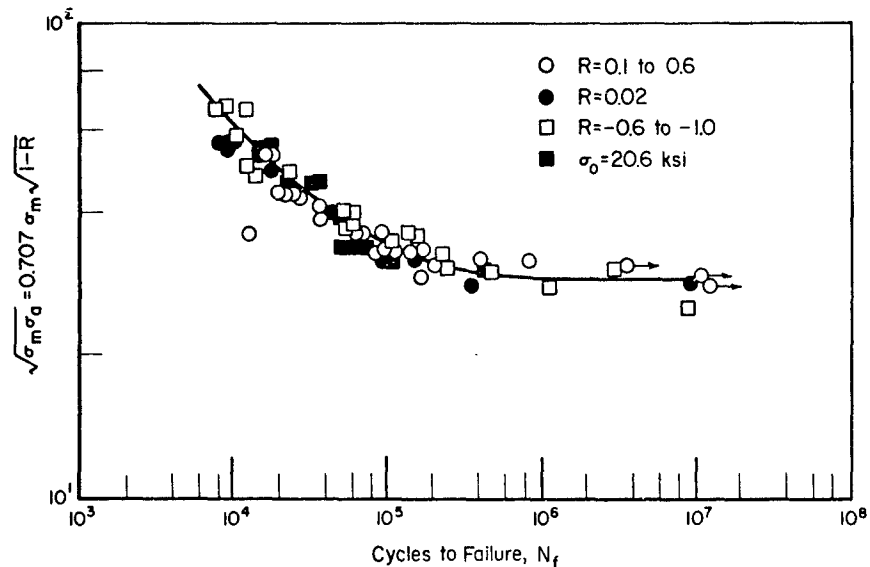


FIGURE 11. FATIGUE DAMAGE - LIFE RELATIONSHIP FOR 7075-T6 ALUMINUM ALLOY (REFERENCE 23)

\* The aluminum alloy material used in this program was 7075-T6 and T651 sheet and plate, clad on both sides. In the interest of brevity, the material will be referred to as 7075-T6 in this report.

These values are in unusually close correspondence with those obtained experimentally. Following these same four steps, life predictions for each of the combinations of interference and load level could be made if a knowledge of the local stress-strain field determined by accurate measurements or analyses were available. The information provided above can also be used to make life predictions of this same type of no-load transfer specimen loaded by Spectrum 1 (see Appendix E for spectrum definition). Assuming the validity of a linear-damage-summation rule applied to fatigue critical location damage, the damage per block of Spectrum 1 is equal to

$$D_B = \frac{2,000}{38,000} + \frac{6,000}{950,000} = 0.0589$$

Therefore, the number of blocks to failure is  $1/D_B$  or 16.98 blocks. Since each block was composed of 8,000 cycles, the predicted cycles to failure are 135,823 which corresponds reasonably well with the experimental result of 301,630 cycles. Note that since there is no significant plastic strain after the first reversal, there is no need to account for interaction effects because the driving force for transient response (plastic strain) is zero.

### 2.3. Limitations of the Fatigue Analysis Procedure as Applied in this Report

Ideally, fatigue-life predictions for fastener systems would be made with a more complete knowledge of the stress-strain field at the fatigue critical location. Because fatigue failure is strongly influenced by the multiaxial nature of both the stress and the strain, knowledge of the local stress-strain field is generally required in each of the three principal axes. In this regard, there are numerous shortcomings in the presently available information. The analysis procedure is, however, capable of dealing with the added complexity of this three-dimensional aspect.

In dealing with real fastener systems, fastener installation defects may also influence the local stress-strain field. As with all previous complexities associated with IFF's, this difficulty is manifest in the stage of estimating fatigue critical stresses and strains. It does not complicate the fatigue analysis prescription.

One final aspect which must be considered in this section is the added complexity of the fatigue analysis procedure when variable-amplitude load histories must be dealt with. Conceptually, this problem is no different from that of constant-amplitude loading. However, computationally, it is much more complex in that as many as three sets of nonlinear equations must be solved on every reversal (half-cycle) of loading. For this reason, the concepts have been cast into computation logic for use in such applications<sup>(25)</sup>. Because of the general nature of the concepts involved, these computer codes offer a great deal of potential and versatility in the prediction of life-to-crack initiation in realistic components and structures. The technique is, however, limited to predicting crack initiation and is therefore useful only in applications for which crack initiation occupies a significant fraction of a component's or structure's useful life.

## 2.4. Discussion

Throughout the preceding section discussing fatigue analysis for IFF's, the importance of the transformation from nominal stress to local strain in making accurate predictions was reiterated several times. It is this feature which is the essential difference between the direct and indirect approaches to analyses discussed previously. For this reason, a major goal of this effort was the accurate characterization of the three-dimensional stress-strain field at the fatigue critical location as influenced by a variety of IFF-related variables and the loading. Because of the importance of this step, this stress-strain field was to be determined by the numerical technique of finite elements and by a number of experimental techniques which included electrical resistance strain gages, speckle photography, and the dislocation etching technique.

### 2.4.1. Use of Static Analyses in Fatigue Applications

Results of each of these approaches are summarized in the appendices. For the most part, results of the electrical resistance strain gages provided the most useful results because their use is amenable to measuring cyclic strains. Any technique which cannot measure conveniently these cyclic strains is of little merit in making fatigue predictions because information relating to strains

obtained during the monotonic loading does not reflect the distribution of strains during fatigue. Indeed, strains obtained from the finite-element model for monotonic loadings suggest that IFF's are detrimental to fatigue because they increase rather than decrease the fatigue critical stresses and strains. Only after the finite-element model can tolerate "unloading" and "reloading" will its results be useful in fatigue applications. In this respect, its usefulness and ability to unload and reload should be demonstrated for simple no-load-transfer specimens or open-hole coupons before attempts to model joints are undertaken. In dealing with these simple coupons, the finite-element analysis should be, as a minimum, a three-dimensional representation of the coupon with the ability to model local inelastic response on a reversal by reversal basis. This model should be verified by extensive experimental work. After successfully modeling the above ideal components, installation effects can be considered as can the more complex joint configurations. If rather than IFF, cold work techniques which induce residual stresses are considered, the role of transient material response must also be included in the finite-element model. Only after these models are sufficiently accurate can their results be useful in making fatigue life predictions using the direct approach. In the meantime, the results of carefully performed experiments in which the interaction of strain fields in the more complex joint configurations, as well as the local strain field are examined could be used as the basis for fatigue analysis of these joints.

### 3. CONCLUSIONS AND RECOMMENDATIONS

An analytical method for fatigue-life prediction has been developed for joints assembled with tapered shank IFF's. This method requires either analytical or experimental information regarding fatigue critical stresses and strains at the point of interest. The following can be concluded from the results of this program.

- Fatigue predictions can be made for fastened joints using the local stress-strain procedures developed herein.
- Two- and three-dimensional elastic and elastic-plastic finite-element-analysis techniques are viable tools for obtaining the required local stress-strain data for fatigue analysis.

- Confirmatory experiment data are required for finite-element analysis results as all numerical modeling techniques are not as yet perfected.
- The dislocation etching technique provides a tool whereby finite-element results can be correlated.
- The speckle photography technique is a viable experimental tool for determining in-plane surface displacements for finite-element correlation and fatigue analysis.
- Until finite-element techniques are fully developed and verified, electrical resistance strain gage data can be used to estimate fatigue critical strains, as well as finite-element correlation.

The recommendations listed below for further work reflect careful consideration of the results of this effort and the necessary order of priorities needed to most efficiently develop a workable prescription for fatigue analysis of fastened joints.

- Based on the limited findings and on conceptual generality of the approach developed herein, additional work should be initiated to further develop and evaluate this fatigue-analysis technique.
- Efforts should be directed to develop extensive experimental and numerical data characterizing fatigue critical stress-strain data relating to interference-fit-fastener variables and loads. Emphasis should be placed on the experimental effort, the results of which can be used to both confirm the results of numerical techniques and make fatigue life predictions.
- A natural extension of the work noted above leads to the investigation of cold-work hole-fastening systems.

#### 4. REFERENCES

- (1) Topper, T. H., and Morrow, JoDean, editors, "Simulation of the Fatigue Behavior of the Notch Root in Spectrum Loaded Notched Members", T&AM Report No. 333, Department of Theoretical and Applied Mechanics, University of Illinois (January 1970).
- (2) Smith, C. R., "Small Specimen Data for Predicting Life of Full-Scale Structures", Fatigue Testing of Aircraft Structures, ASTM STP 338, pp 241-250 (1962).
- (3) Paris, P. C., Gomez, M. P., and Anderson, W. E., "A Rational Analytic Theory of Fatigue", Trend in Engineering, University of Washington, Vol 13, No. 1, pp 9-14 (1961).
- (4) Forsythe, P. J. E., "A Two-State Process of Fatigue-Crack Growth", Proceedings of the Crack Propagation Symposium, Cranfield (England), p 76 (1961).
- (5) Topper, T. H., Wetzel, R. M., and Morrow, JoDean, "Neuber's Rule Applied to Fatigue of Notched Specimens", JMLSA, ASTM, Vol 4, No. 1, pp 200-209 (March 1969).
- (6) Morrow, JoDean, Wetzel, R. M., and Topper, T. H., "Laboratory Simulation of Structural Fatigue Behavior", Effect of Environment and Complex Load History on Fatigue Life, ASTM STP 462, pp 74-91 (1970).
- (7) Grosskreutz, J. C., and Shaw, G. G., "Critical Mechanisms in the Development of Fatigue Cracks in 2024-T4 Aluminum", Int. Conf. on Fracture, Brighton (England), p 620 (1969).
- (8) Grover, H. J., "Fatigue of Aircraft Structures", Navair 01-1A-13, Naval Air Systems Command, (1954, Revised 1960).
- (9) Hyler, W. S., Popp, H. G., Gideon, D. N., Gordon, S. A., and Grover, H. J., "Fatigue Behavior of Aircraft Structural Beams", NACA TN 4137 (September 1956).
- (10) Leis, B. N., and Topper, T. H., "Cyclic Deformation and Fatigue Analyses for Notched Components", Nuclear Engineering and Design, Vol 29, pp 370-383 (1974).
- (11) Leis, B. N., and Topper, T. H., "Long-Life Notch Strength Reduction in the Presence of Local Biaxial Stress", to be published in J. Matl. Engr. and Tech.
- (12) Leis, B. N., Gowda, C. V. B., and Topper, T. H., "Cyclic Inelastic Deformation and the Fatigue Notch Factor", Cyclic Stress Strain Behavior - Analysis, Experimentation and Failure Prediction, ASTM STP 519, pp 133-150 (1973).

- (13) Leis, B. N., Gowda, C. V. B., and Topper, T. H., "Some Studies of the Influence of Localized and Gross Plasticity on the Monotonic and Cyclic Concentration Factors", J. of Testing and Evaluation, JTEVA, ASTM, Vol 1, No. 4, pp 341-348 (July 1973).
- (14) Gowda, C. V. B., Leis, B. N., and Smith, K. N., "Dependence of Notch Strength Reduction Factor on Plasticity and Duration of Crack Growth", JTEVA, ASTM, Vol 2, No. 1, pp 57-61 (January 1974).
- (15) Stowell, E. Z., "Stress and Strain Concentration at a Circular Hole in an Infinite Plate", NACA TN 2073 (April 1950).
- (16) Hardrath, H. F., and Ohman, L., "A Study of Elastic and Plastic Stress Concentration Due to Notches and Fillets in Flat Plates", NACA TN 1117 (1953).
- (17) Neuber, H., "Theory of Stress Concentration for Shear Strained Prismatic Bodies With Arbitrary Nonlinear Stress-Strain Law", J. App. Mech., Trans. ASME, Vol 28, No. 4, pp 544-560 (December 1951).
- (18) Wundt, B. M., Effect of Notches on Low-Cycle Fatigue, A Literature Survey, ASTM STP 490 (May 1972).
- (19) Leis, B. N., Brophy, P. D., and Topper, T. H., "Predicting Fatigue-Life Behavior of Notched Components From Deformation Measurements", AFOSR TR, in preparation under Grant No. AFOSR 71-2120.
- (20) Leis, B. N., Topper, T. H., Gowda, C. V. B., "Cyclic Inelastic Deformation and Fatigue-Life Behavior of Notched Components", University of Waterloo, Department of Civil Engineering, Waterloo, Ontario, Canada, Interim Progress Report, Report No. AFOSR-TR-74-0869, USAF, AF Office of Scientific Research, Arlington, Virginia, Grant No. AFOSR 71-2120, AD 780 120 (April 1974).
- (21) Crews, J. H., "An Elastoplastic Analysis of An Uniaxially Loaded Sheet With an Interference Bolt", NASA TN D-7748 (October 1974).
- (22) Landgraf, R. W., Mitchell, M. R., and LaPointe, N. R., "Monotonic and Cyclic Properties of Engineering Materials", Ford Motor Company (June 1972).
- (23) Smith, K. N., Watson, P., and Topper, T. H., "A Stress-Strain Function for Fatigue of Metals, JMLSA, ASTM, Vol 5, No. 4, pp 767-778 (December 1970).
- (24) Leis, B. N., and Topper, T. H., "An Energy Based Fatigue Damage Parameter", AFOSR TR in preparation under Grant No. 71-2120.
- (25) Diciccio, V. F., Leis, B. N., and Topper, T. H., "Influence of Different Test Spectra on a Multiple Failure Mode Component", Proceedings of the 8th International Committee on Aeronautical Fatigue, Lausanne, Switzerland, Paper No. 3.3 (June 1975).

## APPENDIX A

### HOLE PREPARATION AND METROLOGY

#### INTRODUCTION

As the major portion of this program dealt with the stress-strain states around interference-fit fastener (IFF) holes, exacting control of the hole preparation process as well as precise hole metrology data was of the utmost importance. It was quickly determined that it was far easier to drill good quality holes as opposed to the task of generating poor quality holes on purpose. However, as the personnel became more experienced with the Taper-Lok system, the task became easier. In fact, after several months' experience, shop and technician personnel were able to judge hole quality with amazing accuracy just by tapping a "blueing" pin into place.

The following sections are intended to provide insights concerning hole drilling and metrology procedures used in this program.

#### HOLE DRILLING

The first step in the hole-drilling phase of the program was a 2-day visit of two Omark representatives to BCL to familiarize personnel with the Taper-Lok fastener system. During this visit, demonstrations were given of procedures set forth to insure that the finished specimen holes represented those required by specification,<sup>(1)</sup> similar to those prepared in a typical airplane structure. Such topics as feed rate, drilling speeds, and dwell time were just a few of the subjects discussed that could produce the various hole conditions desired. The visit was completed when the BCL's machinists had successfully performed the drilling of various hole conditions in both the aluminum and titanium materials. The tools used for the hole drilling procedure consisted of reamers, Taper-Lok drill reamers, microstop drill cages, and a Bridgeport vertical mill or a variable speed drill press.

The microstop drill cage (shown in Figure A-1) was employed for drill reaming to accurately controlled depths. The cage consists of a

---

(1) Omark Industries Inc., "Taper-Lok Installation Specification - BPS148".

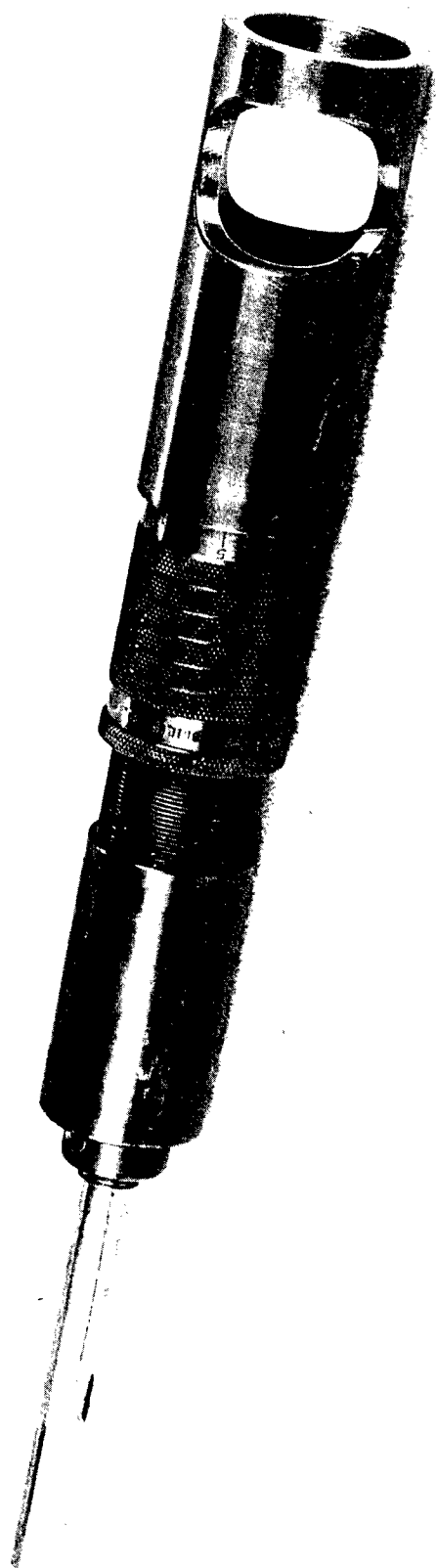


FIGURE A-1. MICROSTOP DRILL CAGE

6325

graduated indexing sleeve mounted on a drill spindle. Depth adjustment was achieved by turning the sleeve and accuracies of 0.001 inch were achieved. Once the cage was set, the hole depth and size could easily be reproduced as long as all other conditions remained the same.

Figure A-2 shows two of the Taper-Lok drill reamers used in this operation. The reamer shown in Figure A-2a is for the drilling of flush-head-type fastener holes in which both the hole drilling and countersinking are accomplished in one operation. The other reamer (Figure A-2b) is used for drilling holes for the protruding head-type fastener. In both cases, the drill cutting lips are on the end of the tool and the reaming flutes on the side. The drill reamers are categorized into nominal diameters, head types, material, and group size similar to that used for the fasteners.

The Bridgeport mill is a large nonportable unit with adjustable spindle speeds from 15 to 660 revolutions per minute. The drill press used for many of the drillings had various speeds from 230 to 2800 revolutions per minute. Prior to use, the perpendicularity of the microstop drill cage to the specimen was adjusted so that the tubular foot of the cage is held flat against the material. After the specimen was clamped to either of the drilling units, a centering of the predrilled pilot hole (approximately 1/64 to 1/32 inch undersize of the nominal hole diameter) to the drill reamer was achieved through vertical and horizontal adjustments of the table.

Generally, the Taper-Lok Reference Manual<sup>(2)</sup> gives a very accurate explanation of the drilling procedures for a normal hold condition. Once a machinist acquired the feel for the tool, hole preparation was highly successful and reproducible. For the out-of-round and fluted hole, the following items were varied from the normal operation method.

- (1) The drilling speed was increased or decreased.
- (2) The tool pressure was changed.
- (3) Dull reamers were used.
- (4) Wobble was induced in the spindle.
- (5) Dwell time was varied.

---

(2) Mead, D. R., Taper-Lok Reference Manual, Third Edition, Mead Printing Company, Inglewood, California, (April 1972).



6327

FIGURE A-2a. TAPER-LOK DRILL REAMER FOR FLUSH-  
HEAD-TYPE FASTENER HOLES

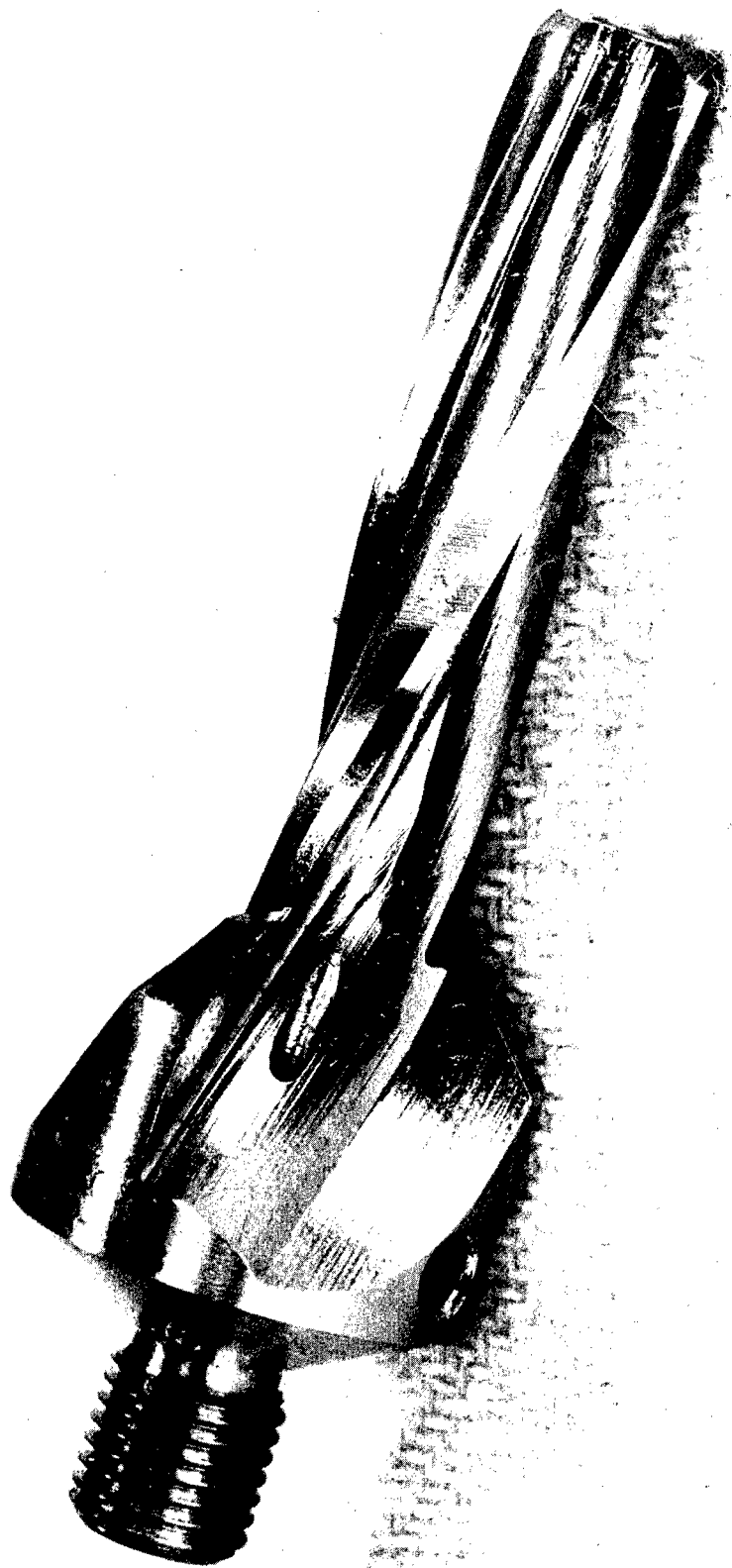


FIGURE A-2b. TAPER-LOK DRILL REAMER FOR PROTRUDING-  
HEAD-TYPE FASTENER HOLES

6326

### METROLOGY STUDY

Since a key variable of the investigation dealt with the fastener hole, an extensive metrology study was applied in that area of the specimen. Before the installation of the fastener into the specimen, each hole was studied to determine

- (1) Degree of interference, i.e., the theoretical difference between the minimum hole diameter and the maximum fastener shank diameter.
- (2) Contact area between the bolt and the hole - expressed as a percent of total surface contact between hole and fastener.
- (3) Perpendicularity of the hole centerline to its top surface.
- (4) The degree of roundness - as expressed as a percent of total indicator reading.
- (5) The amount of taper.
- (6) The surface roughness ..

In the early stages of the experimental program, a very elaborate metrology study was applied to each hole. From these studies, it was determined that a much more simplified method of hole studies could also be used to obtain necessary information. A detailed explanation of each of these methods follows.

For many of the specimens, the hole metrology was performed in BCL's controlled-environment metrology facility. A Model 51 Talyrand and a Talysurf 4 were used in this study. Traces from these instruments for each hole gave an excellent representation of the hole condition.

The Model 51 Talyrand was used to measure the degree of roundness, perpendicularity of the hole centerline to its top surface, and amount of taper. An electric displacement indicator, carried on an optically worked precision spindle, was rotated around the inside of the hole while the specimen remained stationary on the work table. The signal from the indicator was amplified and then applied to a polar coordinate recorder giving straight radial ordinates on inkless "Teledeltos" paper. The recordings were made at a range of magnification from X50 to X10,000.

The specimen was placed on the work table which provides a limited amount of movement for the initial centering of the hole. Adjustments situated around the spindle housing provided for fine centering. The initial measurement was recorded with the stylus in the upper section of the tapered hole. After the table had been raised by a known amount by use of a gage block reference, another recording was made on the same polar plot.

Figures A-3, A-4, and A-5 show typical results of the Talyrand measurements of a normal, fluted, and nonperpendicular hole, respectively. Each 1/10-inch movement in the radial direction represented 0.0005 inch change in the hole radius. The 0.350-inch spacing in Figure A-3 indicates the thickness distance between the two recordings. A description of the method used to interpret the traces follows.

Note in Figure A-3 that each of the recordings are concentric to the initial measurement (less than a 0.0005 inch change is noticed in a 0.375-inch-nominal-diameter hole). This condition is typical of the normal round-

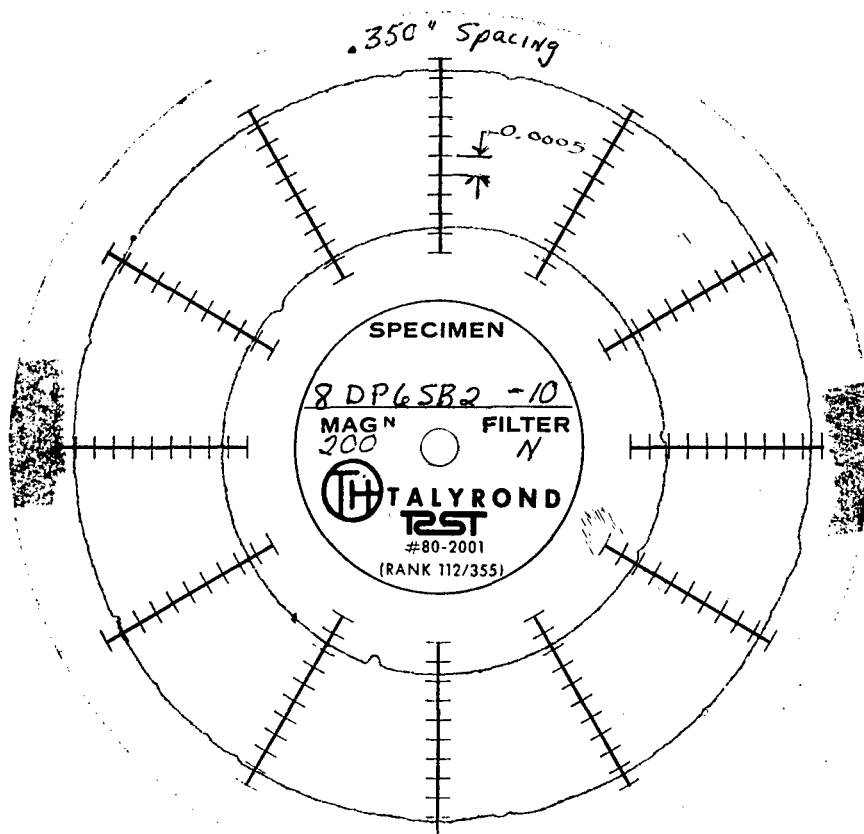


FIGURE A-3. TYPICAL TALYRAND TRACE OF A NORMAL ROUND-TAPERED HOLE

tapered hole. The taper is determined by dividing the average measured distance between recordings by the change of stylus location within the tapered hole. For example, in Figure A-3, by dividing the change in diameter (which is 0.000780 inch) by the 0.350-inch spacing, a calculated taper of 0.02229 inch per inch is determined for the hole which compares well with the theoretical value of 0.02083.

Figure A-4 shows an example of a nonperpendicular hole condition. Notice the outer circle is concentric to the center of the recording. However, in a 0.200-inch spacing, the inner circle's center is offset by 0.0015 inch. The nonperpendicularity of the hole to the surface is determined to be 0.43 degrees by computing the tangent of the angle to be the offset of innercircle divided by the spacing between recordings.

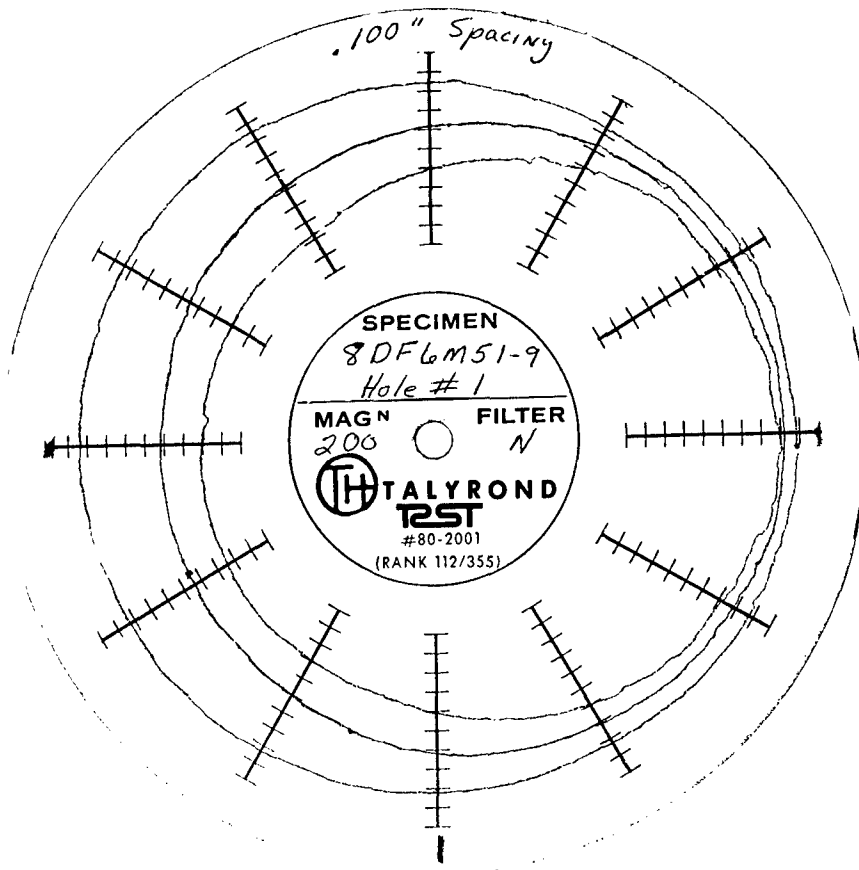


FIGURE A-4. TYPICAL TALLYRAND TRACE OF A NONPERPENDICULAR-TAPERED HOLE

A Talyrand trace of a fluted hole is shown in Figure A-5. In examining the trace, a radial change from the center of the Talyrand is observed indicating either an out-of-round or fluted hole. For this particular specimen, the difference between the maximum peak and minimum peak is 0.00135 inch. The change is divided by the nominal diameter of the hole and a percentage of 0.36 is calculated to be the out-of-roundness of the hole indicator value. It should also be noted that the maximum and minimum peaks of the inner and outer traces do not fall upon the same radial line. This effect indicates that of a fluted hole in which there exists a spiralizing effect through the hole. In an out-of-round hole (i.e., not fluted), the maximum and minimum peak would be straight through the thickness.

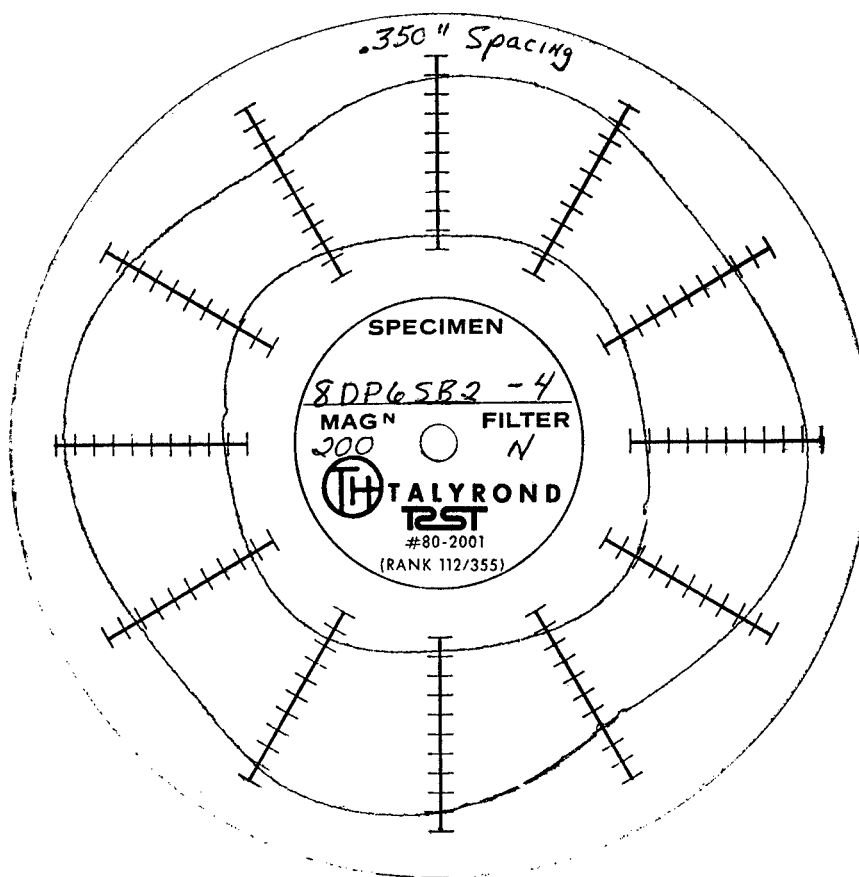


FIGURE A-5. TYPICAL TALYRAND TRACE OF AN OUT-OF-ROUND AND FLUTED HOLE

The Talysurf 4 surface-measuring instrument was employed in the determination of surface roughness within each hole. This system uses a pointed stylus to trace the profile of the surface irregularities over a section of the hole. By means of an inductive transducer activated by the stylus, its vertical movement relative to a skid which is used as a datum is converted to a corresponding change in an electric current. These changes are amplified and recorded onto the graph. Figure A-6 shows a typical section of the recording. A meter recording of the Center Line Average (CLA), an integrated measurement over a selected length of surface, provides numerical assessment and basis for comparison.

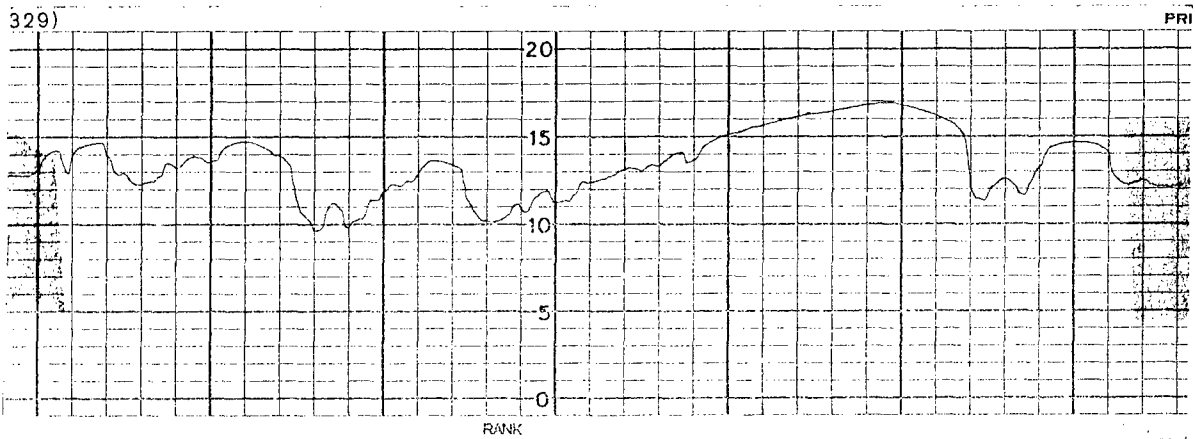
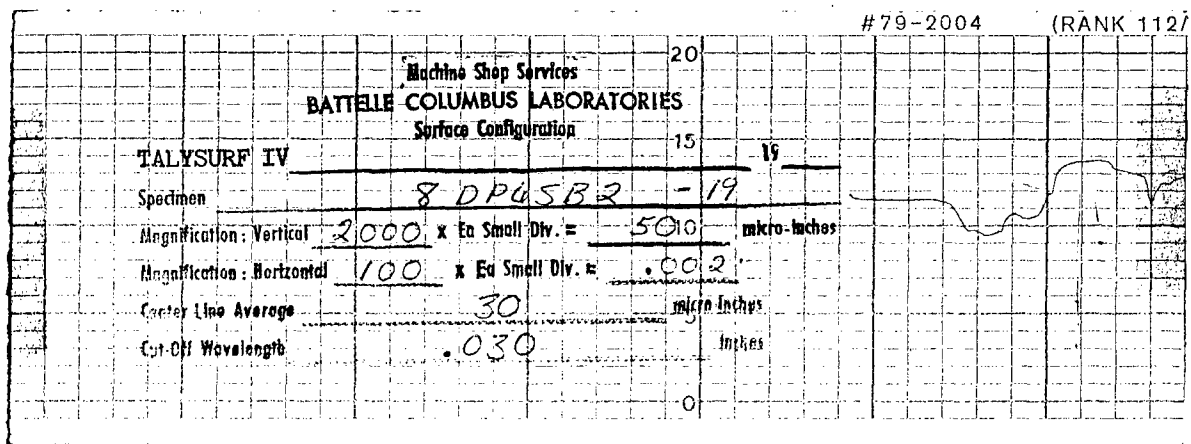


FIGURE A-6. TYPICAL TALYSURF TRACE OF TAPERED HOLE

### INTERFERENCE AND CONTACT AREA MEASUREMENT

The preceding section described the method initially used to determine the holes' perpendicularity, degree of roundness, amount of taper, and surface roughness.

The Taper-Lok TLG 5160 fastener protrusion pin was used to determine the degree of interference and contact area between the bolt and hole. The pin is categorized by nominal diameter and group sizes and is designed similarly to a protruding head taper fastener with an extended shaft length of 0.5 inch and is without threads. The pin was used in the following manner.

The hole was first cleaned and freed of any drilling chips. A thin uniform coating of nondrying prussian blue was applied to the clean protrusion pin and the pin was installed in the hole with finger pressure. The protrusion (P) from the surface of the specimen to the bottom lip of the pin's head was measured and the amount of interference (I) was determined by the sample expression

$$I = (P - 0.5)/48 \quad (1)$$

The pin was tapped into the hole until a "solid" fit was obtained. Being careful not to rotate it, the pin was then removed from the hole. After pin removal, the generated bearing pattern was examined for rifling, out-of-roundness, and percentage of contact as depicted by the amount of blueing removed from the pin at contact points. After extensive use of the pin, it was found that this method also provided excellent indications of complete hole conditions.

Flush-head type fastener holes were inspected for proper countersink depth with a TLG 5120 countersink depth gage. The gage is simply an undersized shaft pin with a very close tolerance 100-degree, flush head. The depth of the countersink is checked by placing the gage into the hole and flushness of the gage head to the specimen surface is measured.

APPENDIX B  
DISLOCATION ETCHING TECHNIQUE

INTRODUCTION

The Fe-3Si steel dislocation-etching technique (DET) is an extremely accurate means of measuring highly localized plastic strains, especially in the area of steep strain gradients. The DET has been used extensively by Hahn, Rosenfield, and coworkers at BCL<sup>(1)</sup>, as well as investigators at other facilities. DET was used in this program to establish the validity of analytical models.

The technique employs Fe-3Si steel as an elastic-plastic model material in the same way that photoelastic materials are used to model elastic behavior. In the case of DET, strain is revealed by etching the surface or an interior section after the model component has been stressed and properly treated. Because DET can reveal interior and surface strains, it was used to bridge the gap between surface strains measured with speckle photography and to verify strains predicted by analytical procedures. DET is well suited for measuring local strains generated by interference-fit fasteners for a number of reasons.

(1) DET reveals plastic strain. This is important because the localized damage caused by fasteners is associated with plastic rather than elastic deformations. Measurements of the extent of plastically deformed regions afford the most sensitive tests of the analytical methods.

(2) DET reveals strain in the interior of the metal as well as on the surface. Hence, with DET, strain distribution can be characterized in three dimensions. This is important because the interference-fit problem is a three-dimensional one.

(3) DET is very sensitive and has high resolution. It is capable of detecting plastic strains as small as  $\epsilon_p \sim 10^{-6}$ , corresponding to the operation of a single dislocation source in an isolated grain, and provides quantitative measure of plastic strain in the range of  $10^{-6} \leq \epsilon_p \leq 10^{-1}$ . DET is capable of detecting

---

(1) Hahn, G. T., Mincer, P. N., and Rosenfield, A. R., "The Fe-3Si Steel Etching Technique for Local Strain Measurement", Experimental Mechanics, June 1971.

strains on the microscopic scale over distances as small as  $5 \times 10^{-3}$  millimeters (0.0002 inches)--a resolution shown to be more than adequate for the interference-fit fastener problem.

(4) DET is highly visual; hence, simplifying communication of results to the nonspecialist.

### PHYSICAL BASIS FOR DET

#### Dislocation Generation

The plastic deformation of metals is accompanied by the generation of large numbers of crystal dislocations; typically,  $\sim 10^9$  dislocations/cm<sup>2</sup> are generated by 1 percent plastic strain. The dislocation density locally is a measure of amount of prior plastic deformation.

#### Decoration

In Fe-3Si steel a light aging treatment (i.e., 150 C for 20 minutes) permits randomly dissolved carbon and nitrogen atoms to diffuse to the cores of the dislocations.

#### Chemical Differentiation

The chemical potential difference between dislocations "decorated" with carbon and nitrogen and the dislocation-free matrix is large enough to permit a differentiation by means of a special etching procedure (electrolytic polishing and etching in a Morris solution). At the same time, localized deformation introduced by sectioning (cutting and grinding) after aging is transparent to the etchant because the dislocations are not decorated.

#### Etching Response

In well-annealed Fe-3Si steel that is lightly strained, individual dislocations produce etch pits which can be resolved with a light microscope. Since the displacement produced by a single dislocation is approximately

$10^{-9}$  mm, approximately 100 dislocations arrayed in a slip band in a 0.05-millimeter diameter grain represents a plastic strain  $\epsilon_p \approx 2 \times 10^{-6}$ . This illustrates the extreme sensitivity of the etching technique. Moderate plastic strains in the range of  $5 \times 10^{-3} \leq \epsilon_p \leq 10^{-1}$ , produce so many dislocations that they are difficult to resolve individually. The etched surface is roughened and appears dark. In heavily strained regions where  $\epsilon_p \geq 10^{-1}$  dislocation densities are so great, e.g.,  $>10^{10}$  cm/cm<sup>3</sup>, that there is not enough carbon and nitrogen atoms in solution for adequate decoration. Such regions remain smooth and light after etching.

#### MANUFACTURE OF Fe-3Si STEEL

The Fe-3Si steel used in the studies described herein was prepared from a 100-pound heat produced by induction melting and casting in air using standard practice. The charge consisted of Armco iron, ferrosilicone, and graphite. The final composition by percent weight is shown below.

Si	3.10/3.20
C	.01/.02
Mn	residual
P	residual
S	residual.

The cast ingot was reduced to workable sheet size by the following process: (1) 4 hours at 1000 C, (2) upset several times and rapidly forged to a final thickness of 1-inch in the range of 1000 to 700 C (this required two reheats to 1000 C to prevent the temperature from falling below 700 C), (3) plates annealed at 750 C for 1 hour and furnace cooled, (4) warm rolled at 400 C to a thickness of 0.6 inch using reductions of 0.015 inch per pass. An intermediate anneal at 750 C as in Step (3) above was accomplished after a 25 percent reduction in thickness. The plates were then given a stress relief treatment (1 hour at 475 C) prior to machining into final test specimens. After the test specimens were machined, they were annealed 4 hours at 780 C and forced-air cooled to room temperature to provide retention of carbon in solution and enhance etching response.

### MECHANICAL PROPERTIES

Mechanical properties of the Fe-3Si steel, obtained by using standard ASTM tensile bars, are as follows:

<u>Specimen</u>	<u>Yield Strength, psi</u>	<u>Ultimate Strength, psi</u>	<u>Preset, Strain</u>
4D-1	64,650	84,500	Fracture
4D-2	64,100	85,100	Fracture
4D-3	64,800	-	2.5
4D-4	63,500	-	1.0
4D-5	64,200	-	5.0
4D-6	62,800	-	9.0
4D-7	64,200	-	7.0
4D-8	-	-	90% of yield stress
4D-9	64,100	-	14
4D-10	68,822	86,235	Fracture

The stress-strain characteristics of the material are shown on Figure B-1 and load-deflection curves are shown in Figures B-2 and B-3.

### ETCHING RESPONSE CALIBRATION

Tensile specimens were loaded to 90 percent of yield stress and 1, 2.5, 5, 7, 9, and 14 percent plastic strain as shown in Figures B-4 through B-10. The specimens were aged for 20 minutes at 150 C and then sectioned for metallographic polishing. Polishing and etching were performed electrolytically in the Morris solution (7 cc H<sub>2</sub>O, 25 g chromium trioxide, 133 cc glacial acetic acid). The electrolytic polishing occurs in the range of 22 to 44 volts with a stainless-steel anode and a specimen-cathode separation of 1/4 to 3/4 inch in 5 to 20 minutes with the solution agitated and maintained at 20 C. Etching occurs at about 5 volts in 3 to 15 minutes without agitation. The etching response of the specimens is shown in Figures B-11 through B-16.

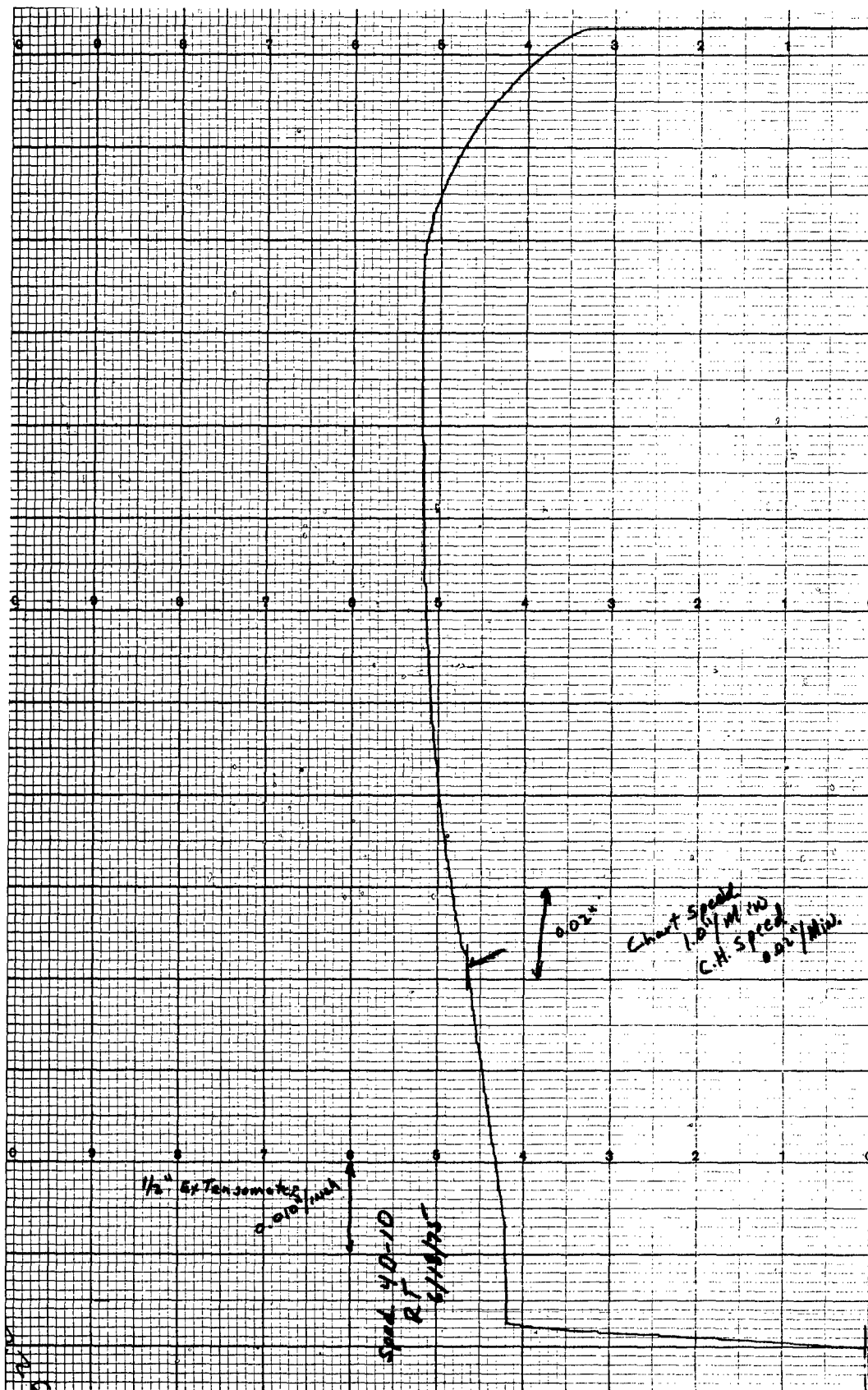


FIGURE B-1. STRESS-STRAIN CHARACTERISTICS FOR Fe-3Si Material

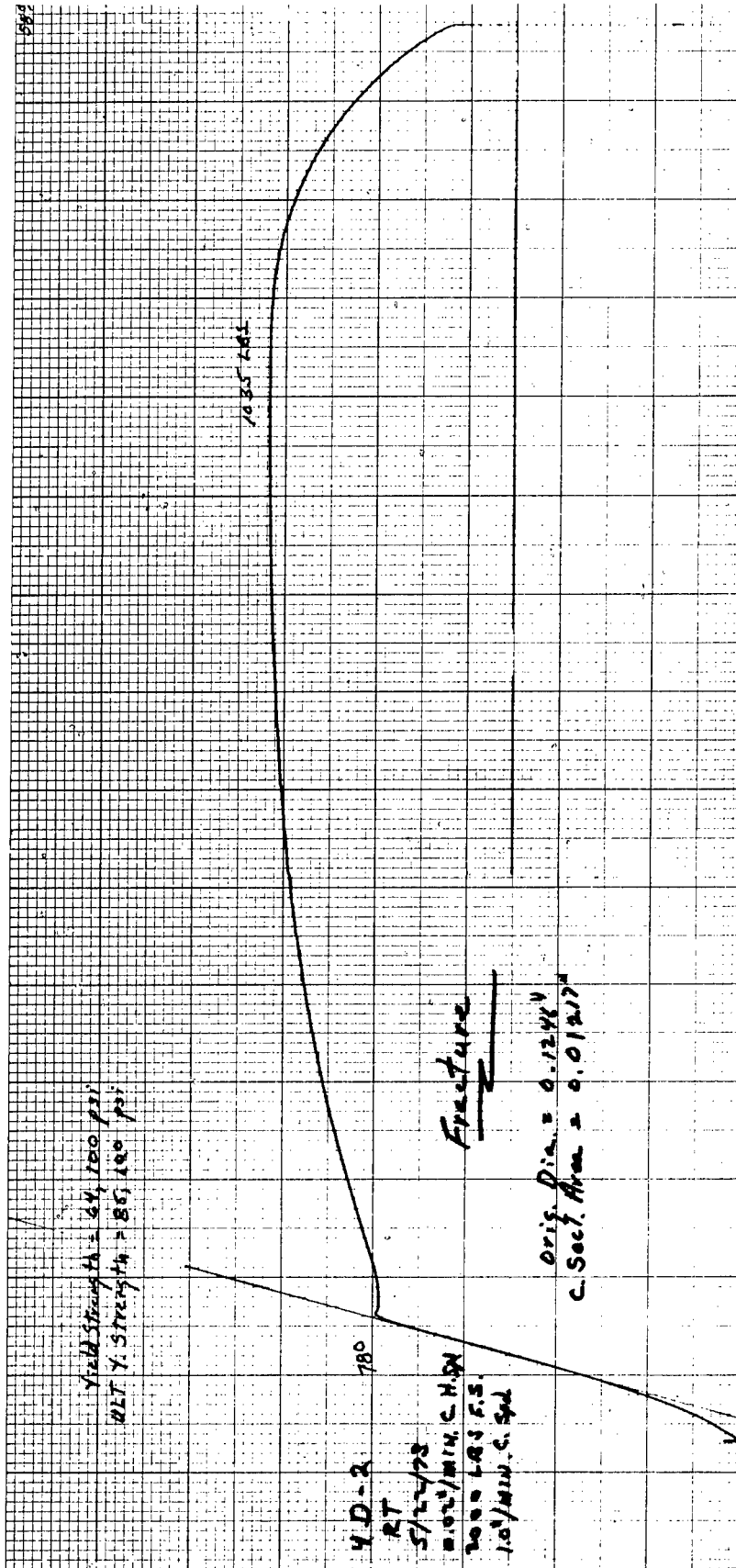


FIGURE B-2. LOAD-DEFLECTION CHARACTERISTICS FOR Fe-3Si MATERIAL

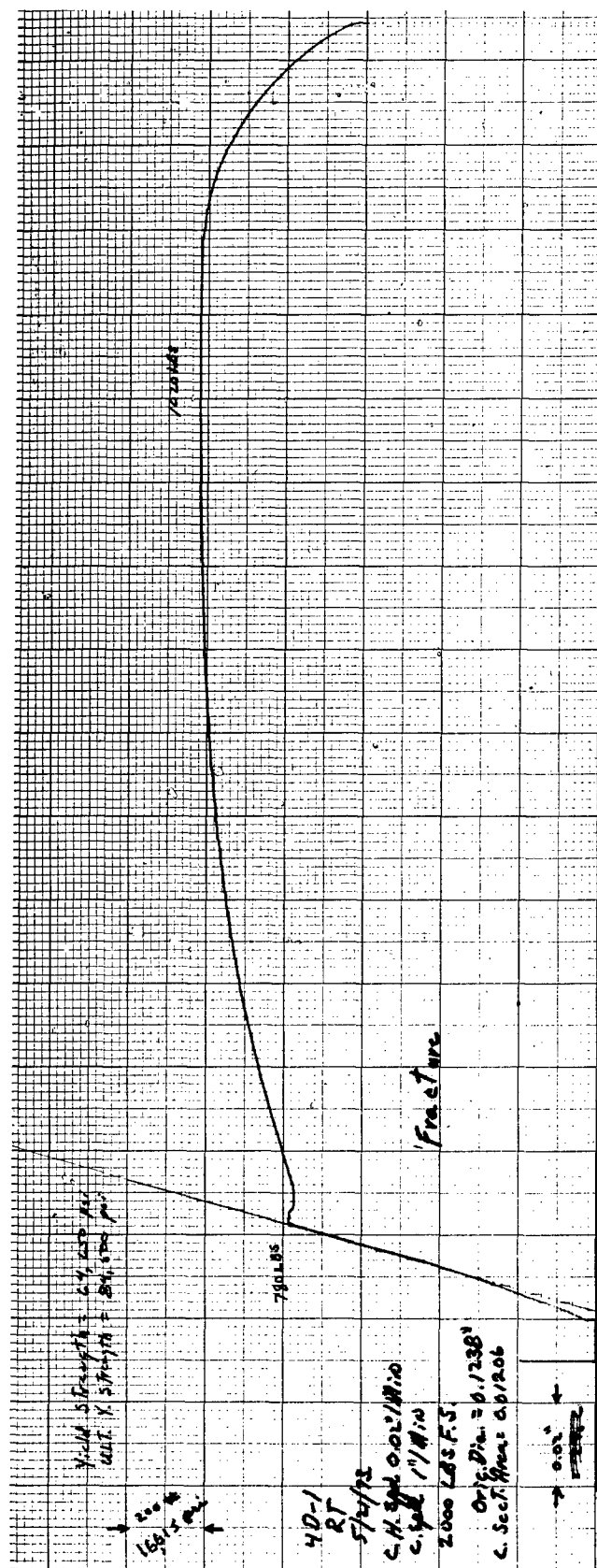


FIGURE B-3. LOAD-DEFLECTION CHARACTERISTICS FOR Fe-3Si MATERIAL

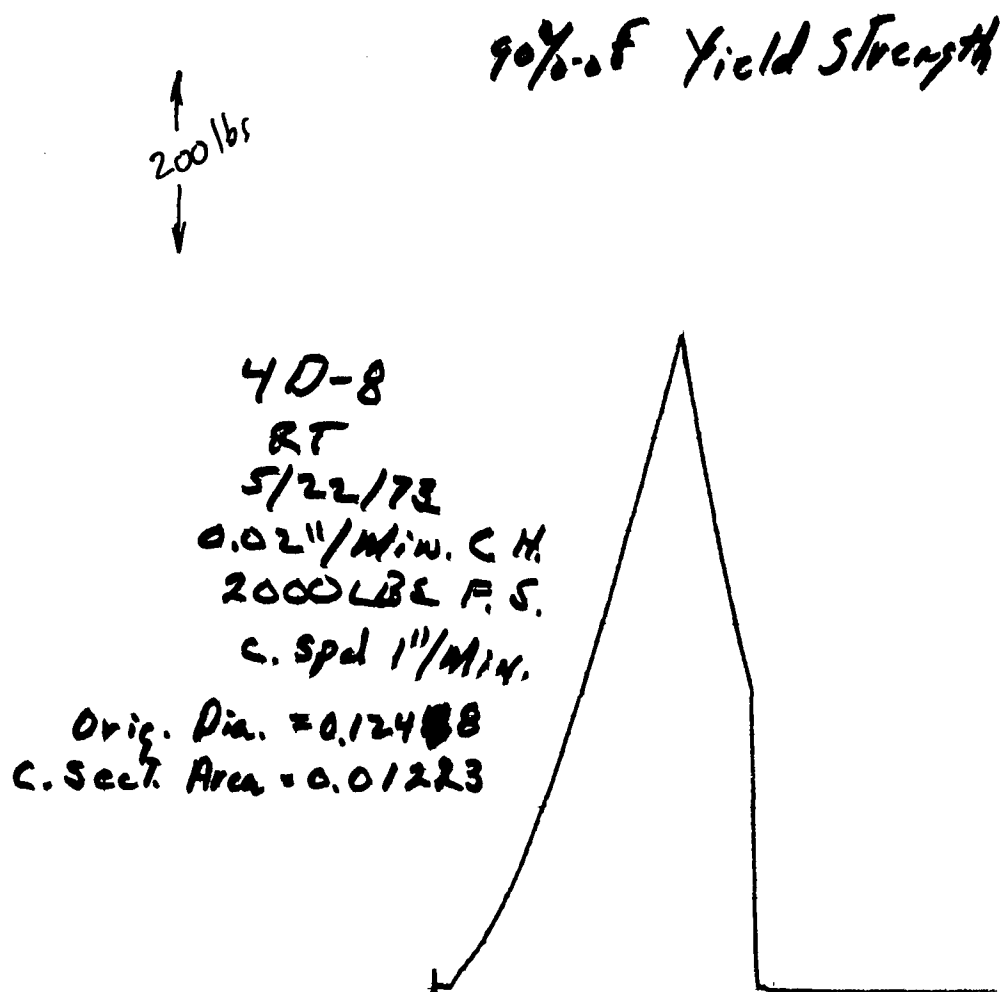


FIGURE B-4. TEST SPECIMEN STRAINED TO 90 PERCENT OF YIELD STRESS ( $\epsilon_p = 0$ )

Yield Strength = 63,500 psi

Orig. Dia. = 0.1244  
C. Sect. Area = 0.0125

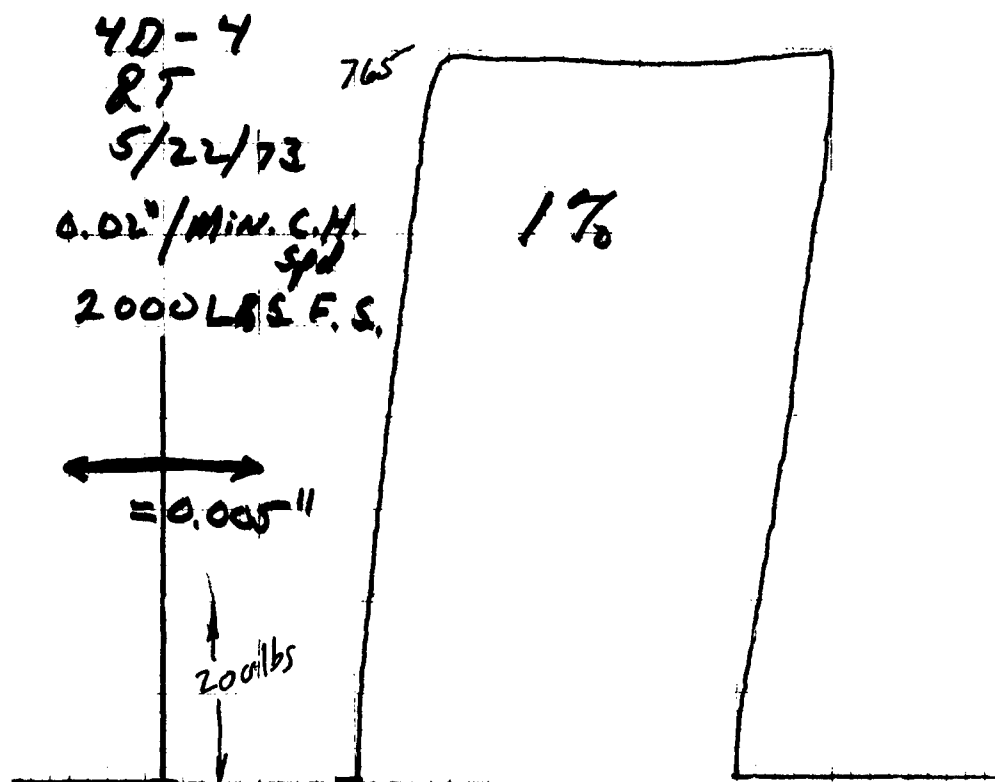


FIGURE B-5. TEST SPECIMEN STRAINED BEYOND  
YIELD STRESS,  $\epsilon_p = 1$  PERCENT

Yield Strength = 64,800 psi

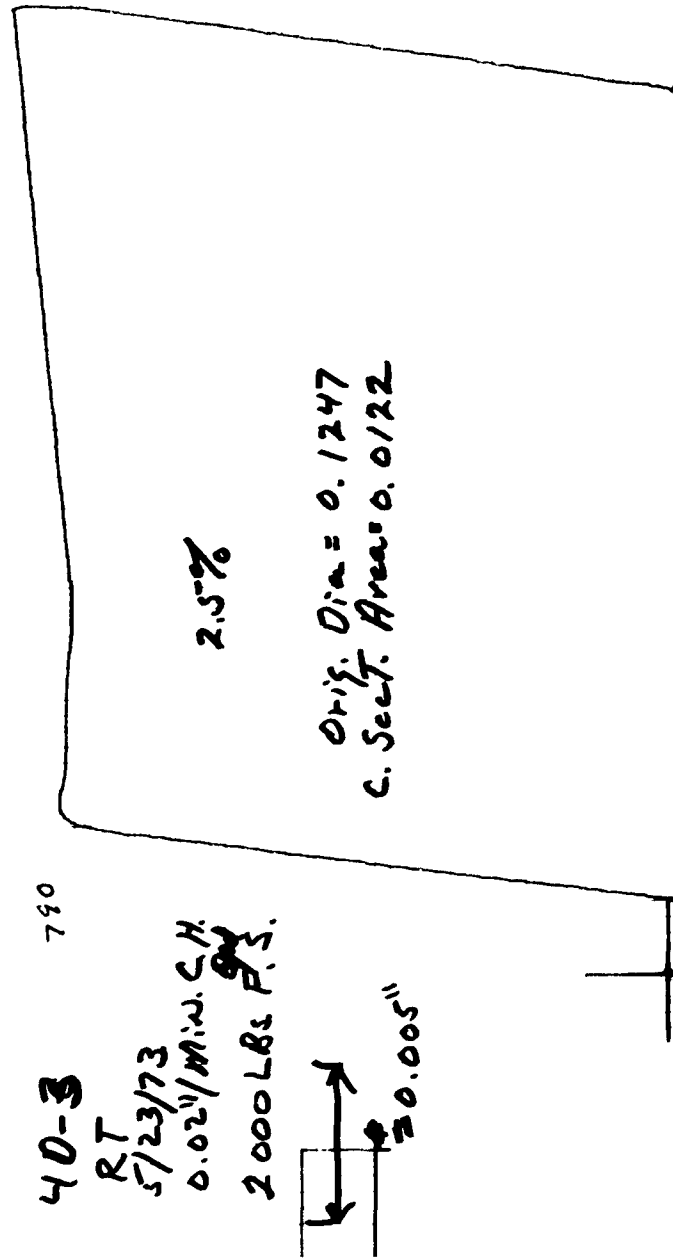


FIGURE B-6. TEST SPECIMEN STRAINED BEYOND YIELD STRESS,  $\epsilon_p = 2.5$  PERCENT

Yield Strength = 44,200 psi

4D-5

RT

5/2-173

0.02" Min. C.H.S.

2000 LBS F.S.

↔ = 0.005"

780

5%

Orig. Dia. = 0.1244  
C. Sect. Area = 0.01215

FIGURE B-7. TEST SPECIMEN STRAINED BEYOND YIELD STRESS,  $\epsilon_p = 5$  PERCENT

Yield Strength = 64,197 psi

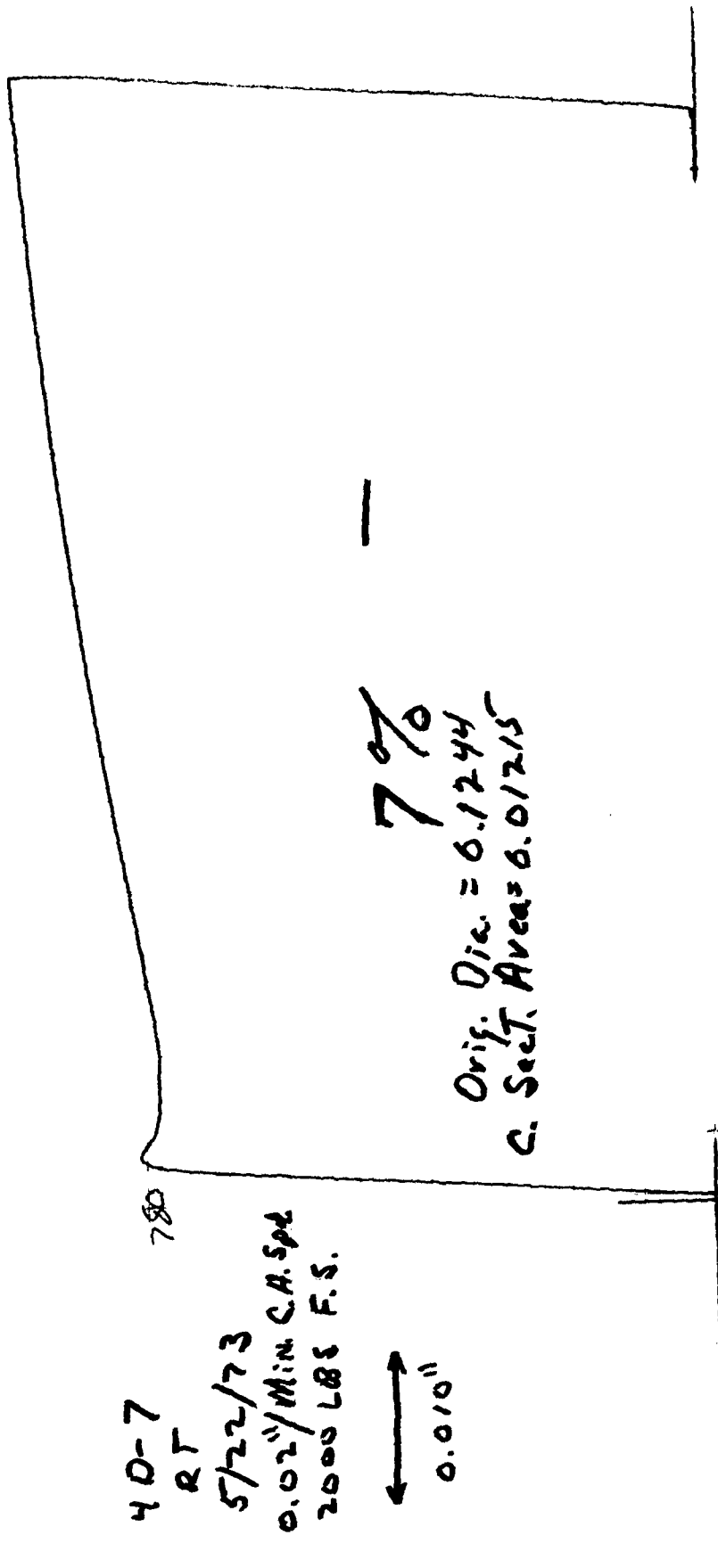


FIGURE B-8. TEST SPECIMEN STRAINED BEYOND YIELD STRESS,  $\epsilon_p = 7$  PERCENT

Yield Strength = psi

4D-6

RT

5/22/73

0.02" MIN. CH

2000 LBS F.S. (SP4)

→ = 0.010"

9%

Orig. Dia. = 0.1242

C. Sec. Area = 0.0121

FIGURE B-9. TEST SPECIMEN STRAINED BEYOND YIELD STRESS,  $\epsilon_p = 9$  PERCENT

Orig. Dia. = 0.1247  
 C. Sect. Area = 0.01222

62000 psi

4 D-9  
 RT

6/12/73

0.02"/Min. C.H.

2000 LBS FS.

↔ = 0.020"

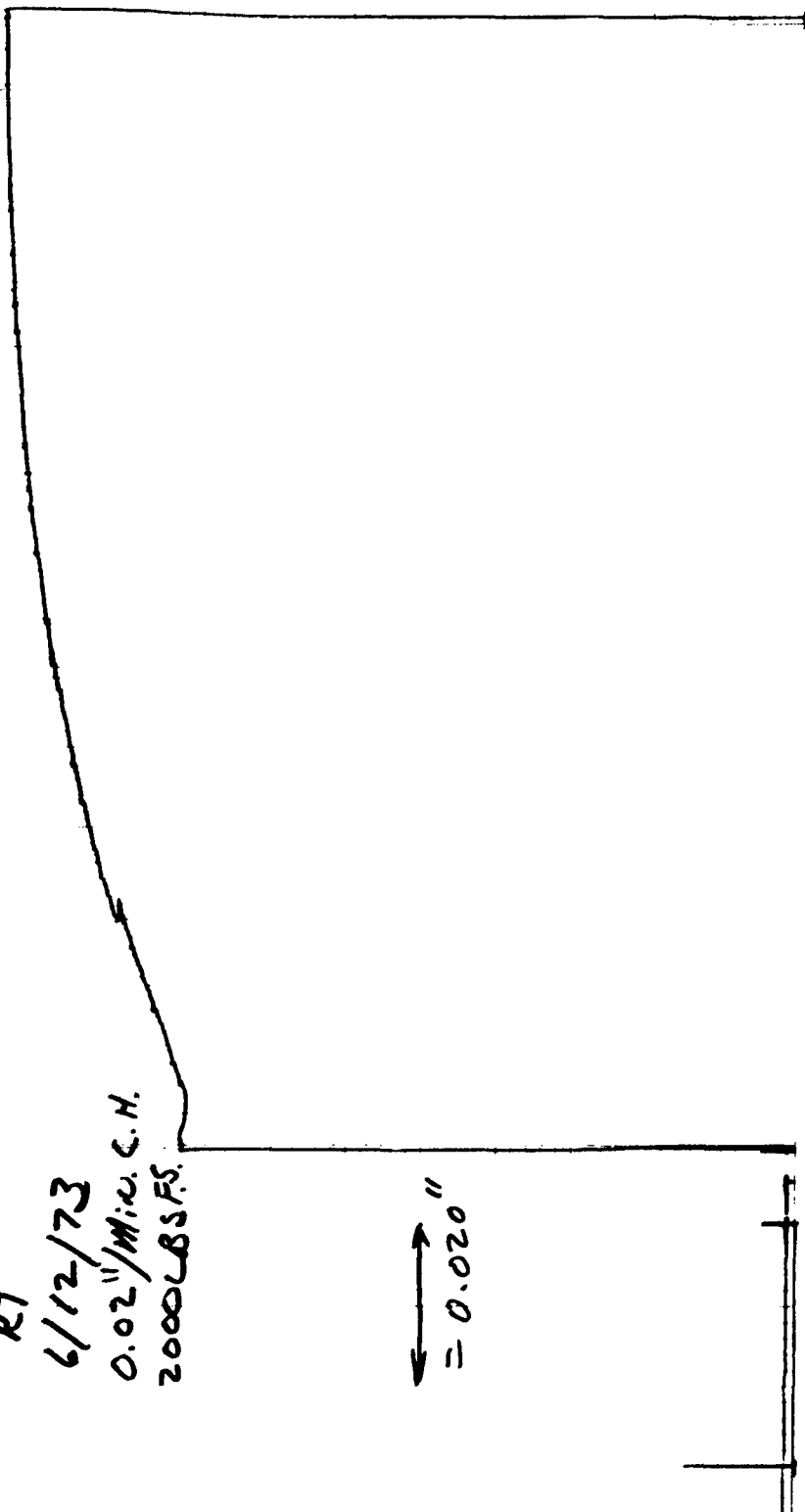


FIGURE B-10. TEST SPECIMEN STRAINED BEYOND YIELD STRESS,  $\epsilon_p = 14$  PERCENT

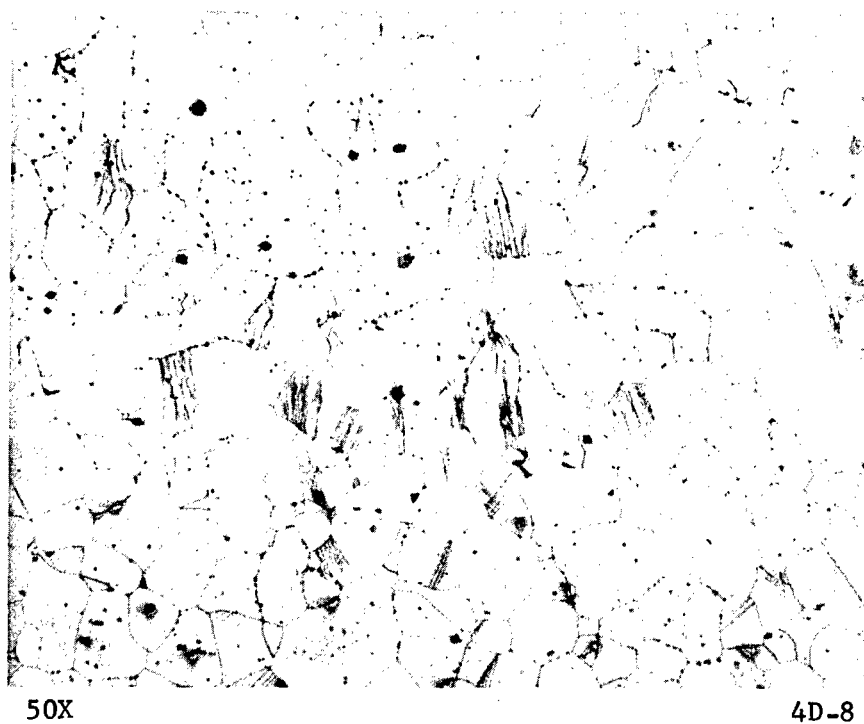


FIGURE B-11. ETCHING RESPONSES FOR SPECIMEN LOADED TO 90 PERCENT YIELD ( $\epsilon_p = 0$ )

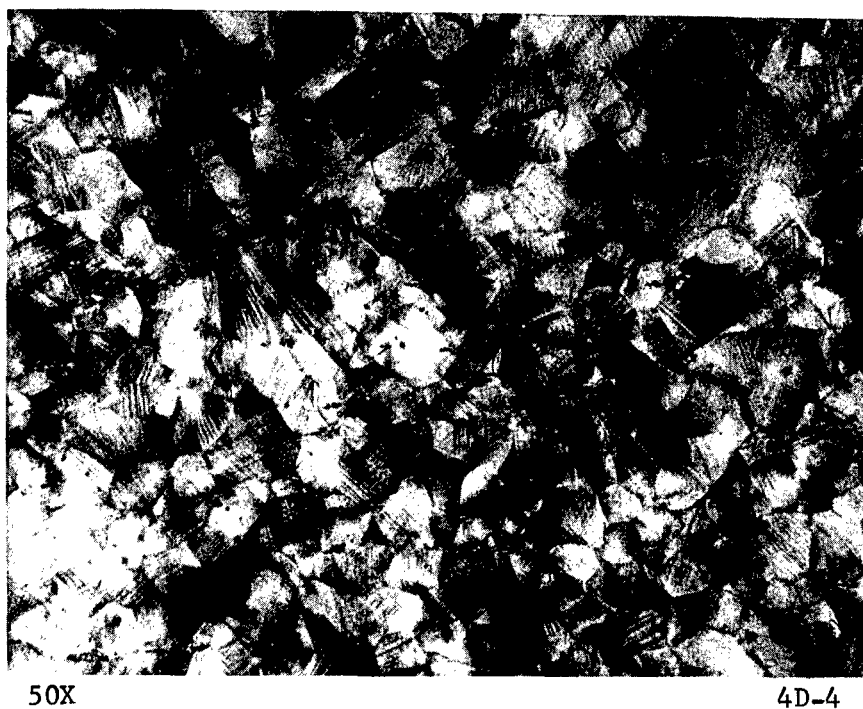


FIGURE B-12. ETCHING RESPONSE FOR  $\epsilon_p = 1$  PERCENT

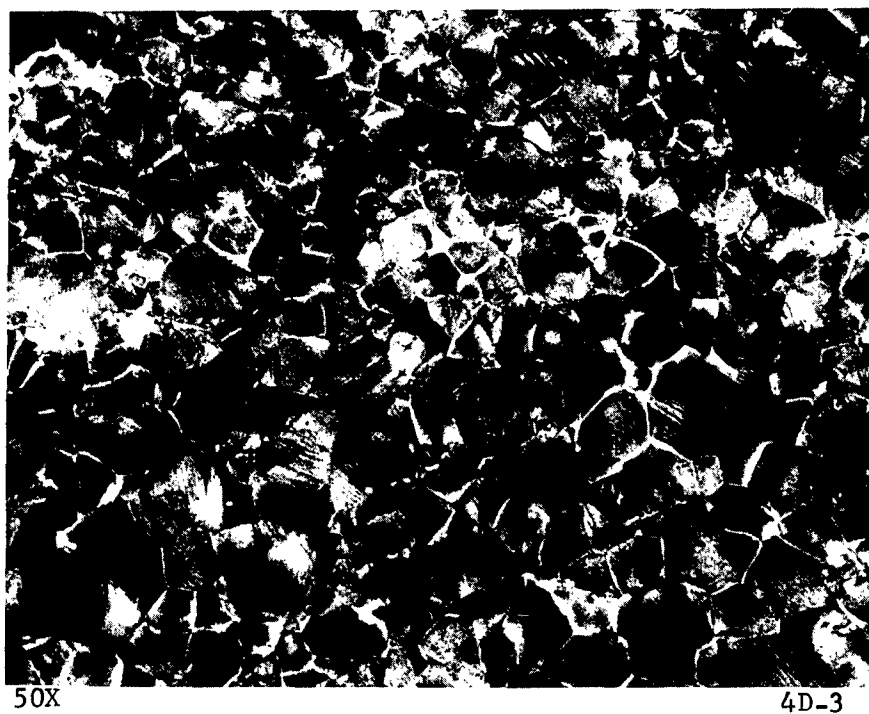


FIGURE B-13. ETCHING RESPONSE FOR  $\epsilon_p = 2.5$  PERCENT

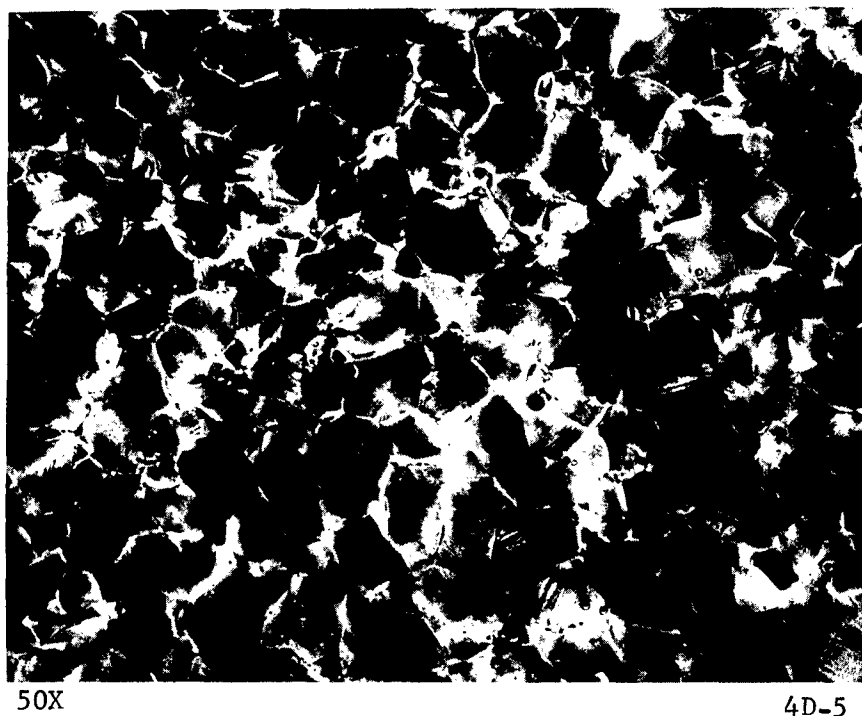
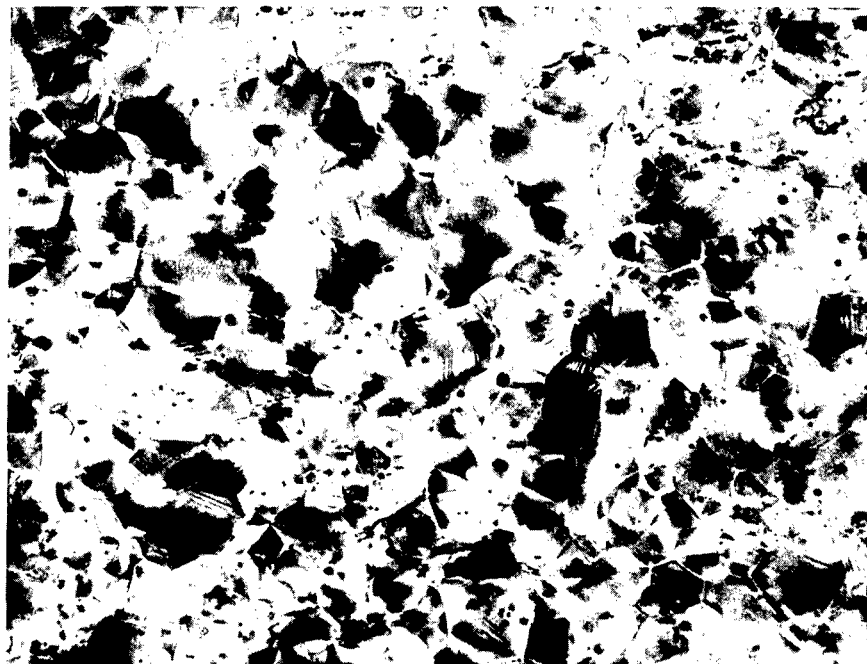


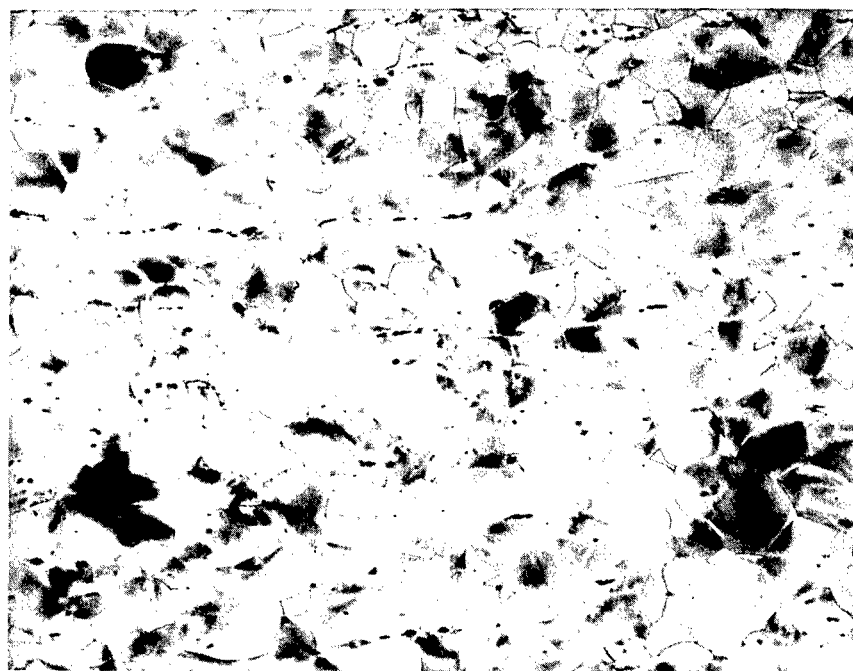
FIGURE B-14. ETCHING RESPONSE FOR  $\epsilon_p = 5$  PERCENT



50X

4D-6

FIGURE B-15. ETCHING RESPONSE FOR  $\epsilon_p = 9$  PERCENT



50X

4D-9

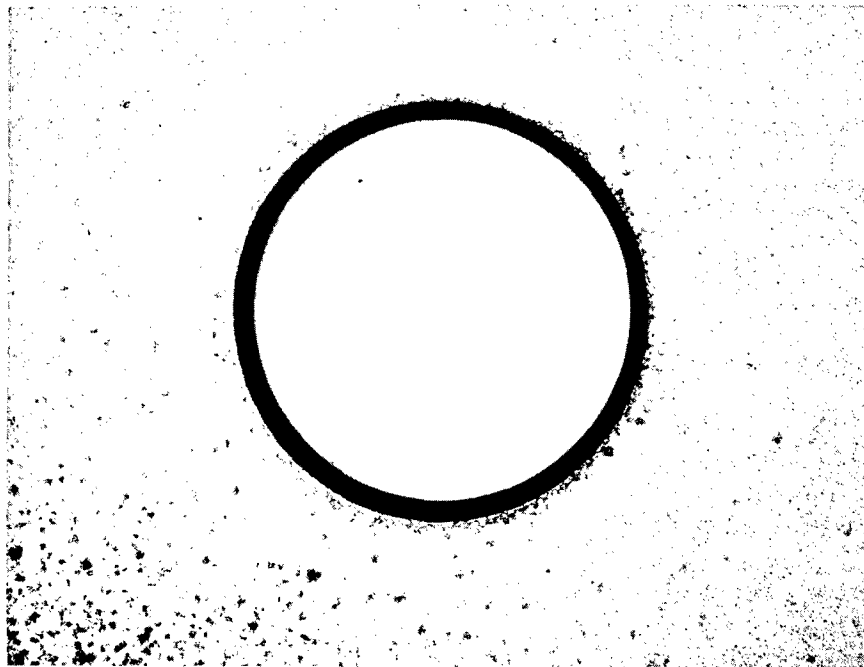
FIGURE B-16. ETCHING RESPONSE FOR  $\epsilon_p = 14$  PERCENT

## EXPERIMENTAL RESULTS

Several early experiments indicated that complete specimen preparation could not be accomplished prior to the final annealing cycle because the final cycle left scale deposits on the finished hole surface. This made determination of the fastener interference level impossible and, hence, the specimen results were of no value. In a resulting investigation, it was determined that light hand reaming of the hole after the annealing cycle produced no identifiable plastic strains. This process was used on all succeeding specimens.

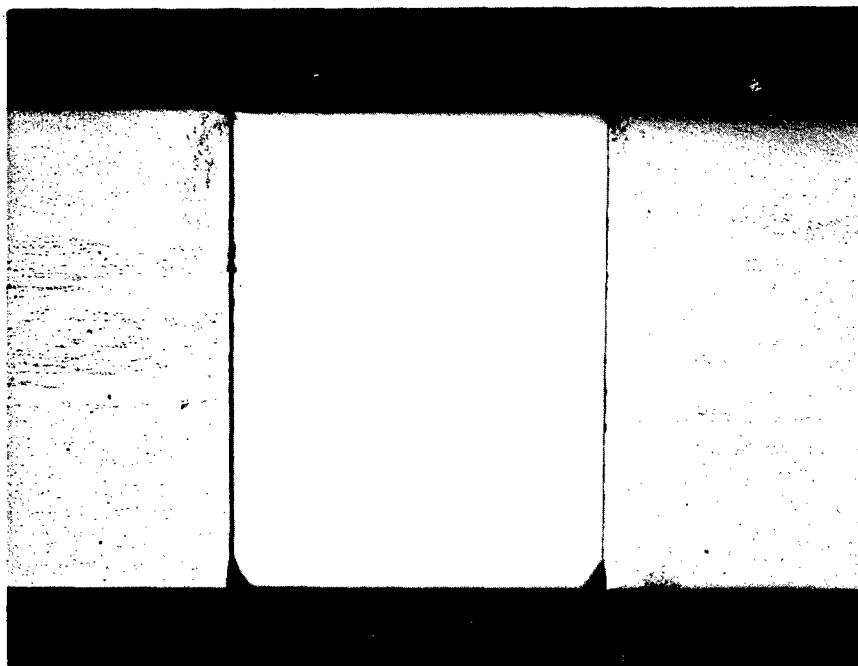
A 2-inch square by 1/2-inch-thick coupon specimen was prepared and drilled to provide 0.004-inch interference. Photographs at 5X magnification of the polished and etched specimen are shown in Figures B-17 and B-18; greater magnification photos (18X) of these same sections are shown in Figure B-19 and B-20. The maximum plastic yield zones indicate plastic yield near the top and bottom surfaces in the range of 1 percent, decreasing to approximately 0.5 percent about 0.07 inch from the edge of the hole. These values are in very good agreement with the analytically predicted values and, hence, indicate the technique is viable.

A no-load-transfer specimen was prepared for a fastener insertion at 0.003-inch interference. Etching and study of this specimen was preceded by load application to 70 percent of the material yield strength. Initial study of the etched and polished specimen was somewhat disconcerting in that the top view as seen in Figure B-21 indicated excessive yielding on one side of the specimen, implying that the specimen had been improperly gripped in the loading machine, thus, inducing bending loads instead of the desired uniaxial loads. A review of analytical results suggested that plastic strains were not adversely affected in the direction parallel to the load application and, hence, the specimen was sectioned to view the plane parallel to the direction of applied load as shown in Figure B-22. Study of the 16X magnification photographs of the sectioned specimen parallel to the load application (see Figure B-23) indicated that plastic strains beneath the head of the fastener and the nut are extremely high, in the range of 14 percent. However, these are reduced quite quickly to the analytically predicted values of 1 percent in the major portion of the through thickness. Particular note also should be taken of the high plastic



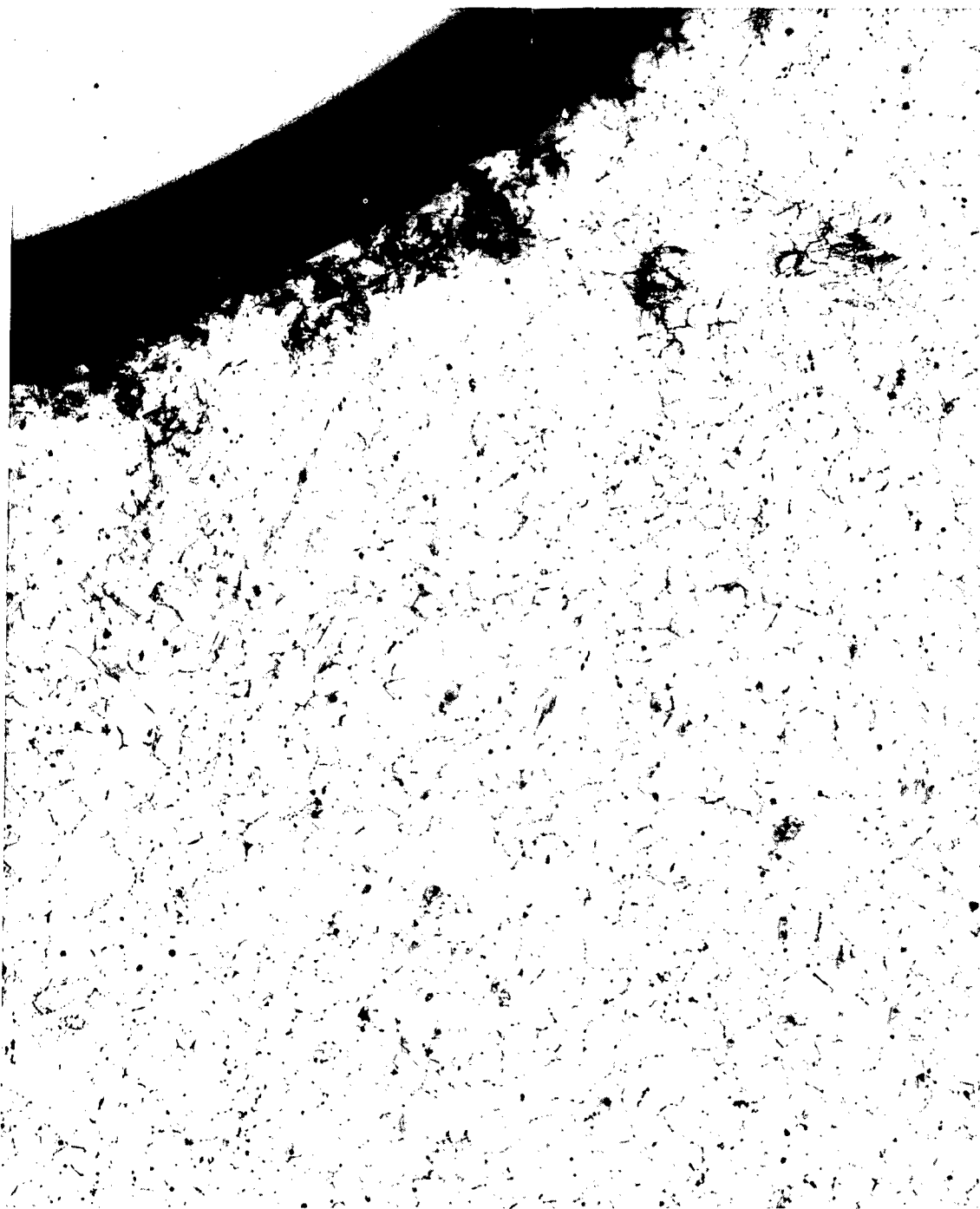
5X

FIGURE B-17. TOP VIEW OF 2-INCH-SQUARE x 1/2-INCH-THICK COUPON SPECIMEN



5X

FIGURE B-18. CROSS-SECTIONAL VIEW OF 2-INCH-SQUARE x 1/2-INCH-THICK COUPON SPECIMEN



18X

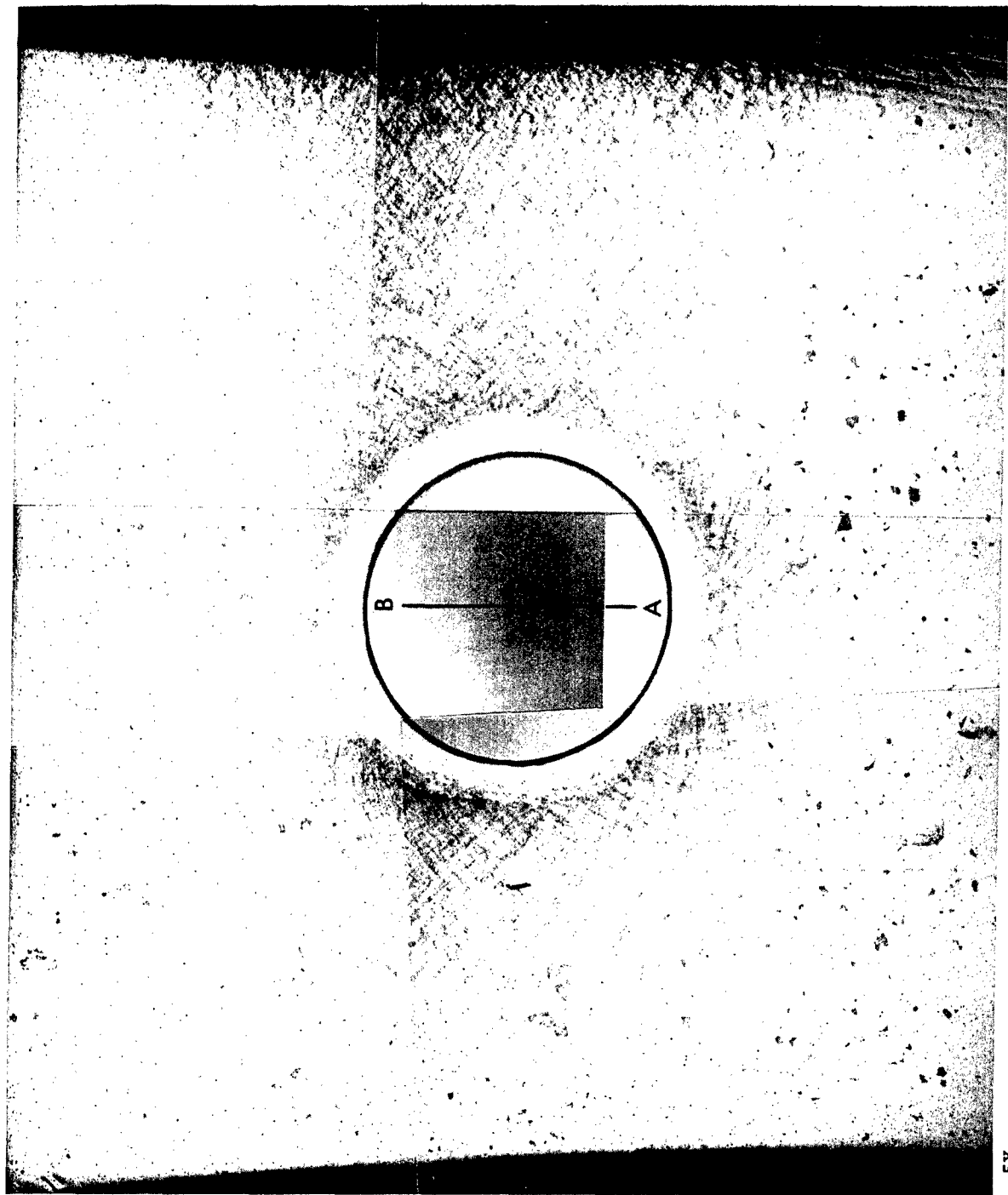
FIGURE B-19. TOP VIEW OF 2-INCH-SQUARE x 1/2-INCH-THICK COUPON SPECIMEN



18X

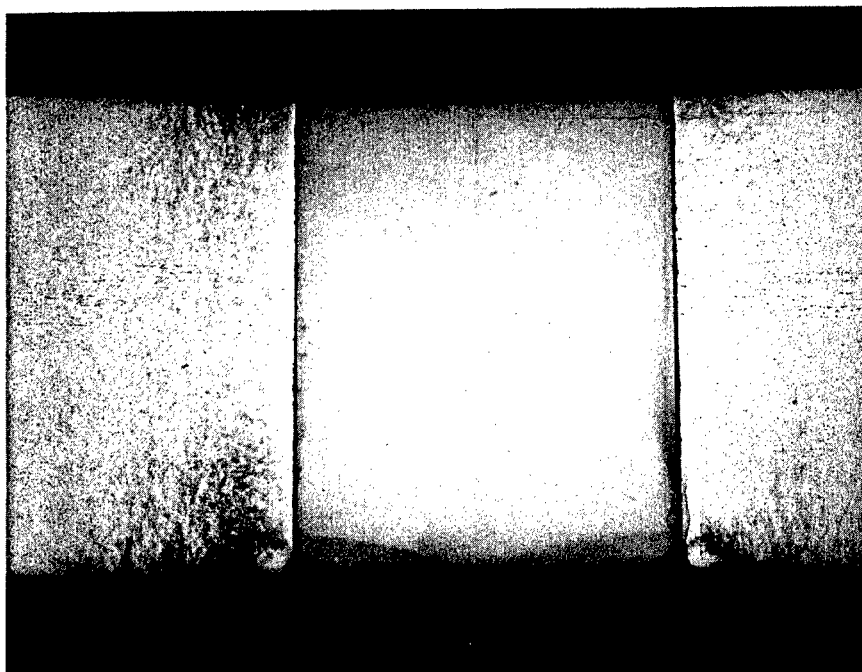


FIGURE B-20. CROSS SECTIONAL VIEW OF 2-INCH-SQUARE x 1/2-INCH-THICK COUPON SPECIMEN



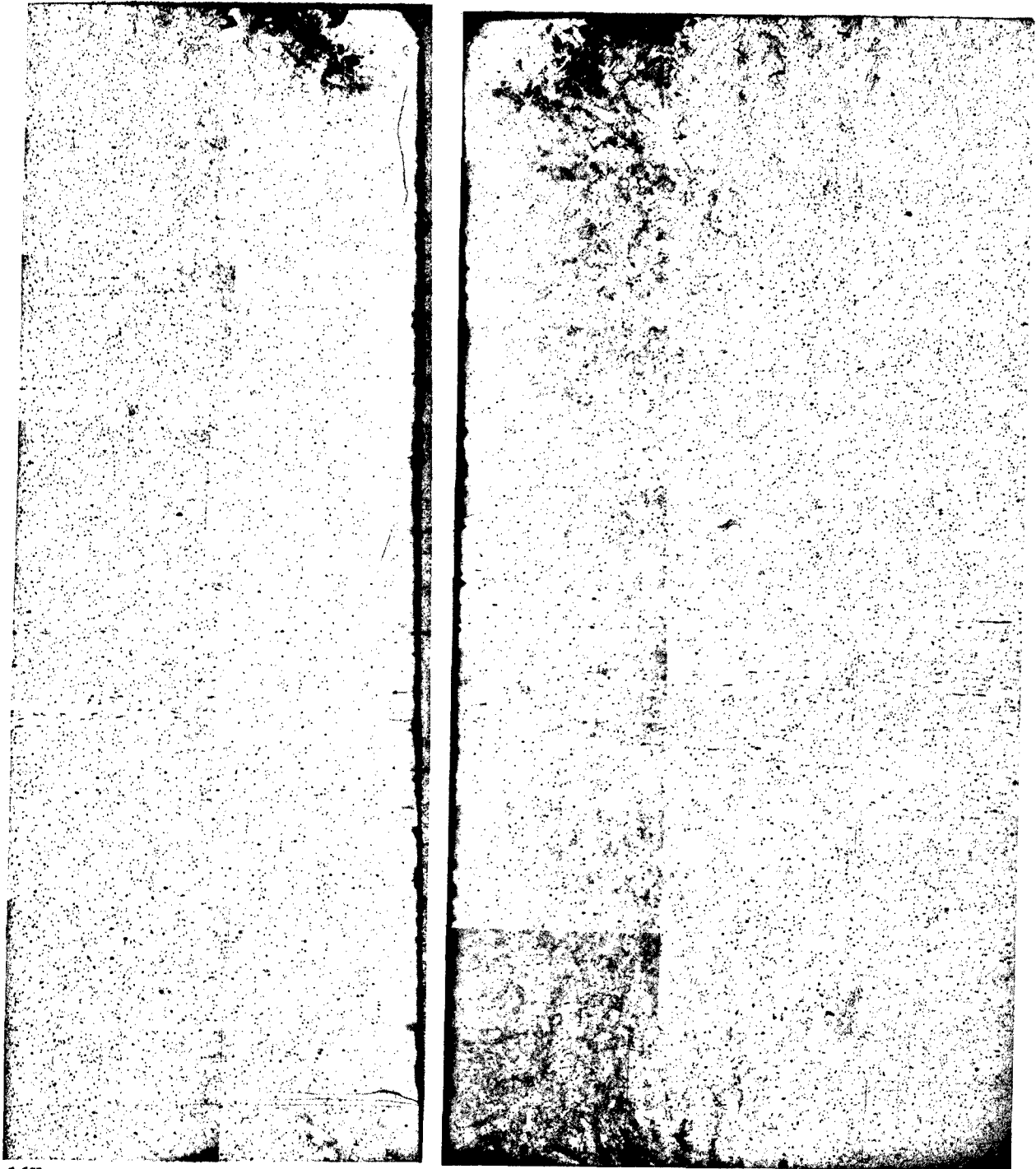
5X

FIGURE B-21. TOP VIEW OF NO-LOAD-TRANSFER SPECIMEN



5X

FIGURE B-22. NO-LOAD-TRANSFER SPECIMEN -- SECTIONED  
ALONG LINE A-B



16X

FIGURE B-23. ENLARGED VIEW OF NO-LOAD-TRANSFER SPECIMEN --  
SECTIONED ALONG LINE A-B

strains induced by the bearing stresses under the fastener head and nut. These externally applied loads should be considered in future analytical determinations.

For specimens subjected to fatigue tests, it was determined that the time duration at room temperature required to complete the fatigue test was such that aging of the Fe-3Si material occurred; hence, making it unresponsive to the etching process.

As analytical models for other geometries and loading conditions were unavailable, additional DET specimens were not sectioned and polished. However, the two examples presented above correlate very well with the analytical results presented in the finite-element-modeling portion of this report.

## APPENDIX C

### SPECKLE PHOTOGRAPHY

#### INTRODUCTION

At the inception of this program, it was intended that the speckle-correlation technique <sup>(1,2)</sup> be used to measure displacements in fastener specimens. Although the correlation technique was feasibly applicable to the interference-fit-fastener (IFF) problem, it was concluded that the speckle-photography technique would yield good results with less experimental development in the laboratory. Furthermore, the optical system for doing speckle photography is quite simple.

It is worth noting that at the time this program was beginning, speckle techniques were not well known and few, if any, real applications had been attempted by researchers. To date, most of the literature still centers around the speckle correlation technique.

This appendix will attempt to explain the fundamentals of speckle photography, the equipment developed in this program, the procedures used in the experiments, and the results obtained.

#### SPECKLE PHOTOGRAPHY TECHNIQUE

When using coherent laser light for illumination, a uniform diffuse surface has a speckled or grainy appearance. This is due to random changes

- 
- (1) Adams, F.D., "A Study of the Parameters Associated with Employing Laser Speckle Correlation Fringes to Measure In-Plane Strain", AFFDL-TR-72-20, March 1970.
  - (2) Hung, Y.Y., and Hovanesian, J.D., "Full-Field Surface-Strain and Displacement Analysis of Three-Dimensional Objects by Speckle Interferometry", Experimental Mechanics, October 1972.

in phase when the light is scattered from a diffuse surface. The eye or a photographic system produces an image in superposition with random interference. The mean size of laser speckles is proportional to the wavelength of light and the numerical aperture of the imaging lens. With f/1 optics, speckles as small as 1 micron in diameter are possible. Figure C-1 is a photograph illustrating laser speckle. An f/22 lens aperture was used to accent the speckle phenomena.

Several methods of exploiting the speckle phenomenon to measure small displacements or strains have been devised. Of particular interest is a technique called speckle photography<sup>(3,4,5)</sup>. A double exposure "specklegram" (photographic negative image) is made of the speckled surface. Exposures are made before and after a displacement has occurred. Thus, each bright speckle point is recorded on the specklegram as two dark points — one in the undisplaced position and the other in the displaced position. Conversely, each dark speckle is recorded as two clear transmission areas on the specklegram. Only knowledge of the photographic magnification factor is required to determine the local in-plane displacement vector once the length and direction of a line segment between the recorded speckle pairs are known.

A direct point-to-point measurement on a specklegram is virtually impossible or, at best, extremely tedious because of randomness in the speckle field. Fortunately, this is not necessary. If a narrow collimated laser beam (monochromatic and coherent) is directed through the specklegram, diffraction will modify the emerging light rays into a cone. This "diffraction halo" is the result of diffraction from the random distribution of small speckles. Since the speckles are recorded in pairs, however, a parallel fringe pattern (Young's fringes) also occurs in the emerging light cone.

---

(3) Archbold, E., Burch, J.M., and Ennos, A.E., Optics Acta, 17, No. 12, 883, (1970).

(4) Archbold, E. and Ennos, A.E., Optics Acta, 19, No. 4, 253, (1972).

(5) Adams, F.D., and Maddux, G.E., "On Speckle Diffraction Interferometry for Measuring Whole Field Displacements and Strains", AFFDL-TR-73-123 (December, 1973).

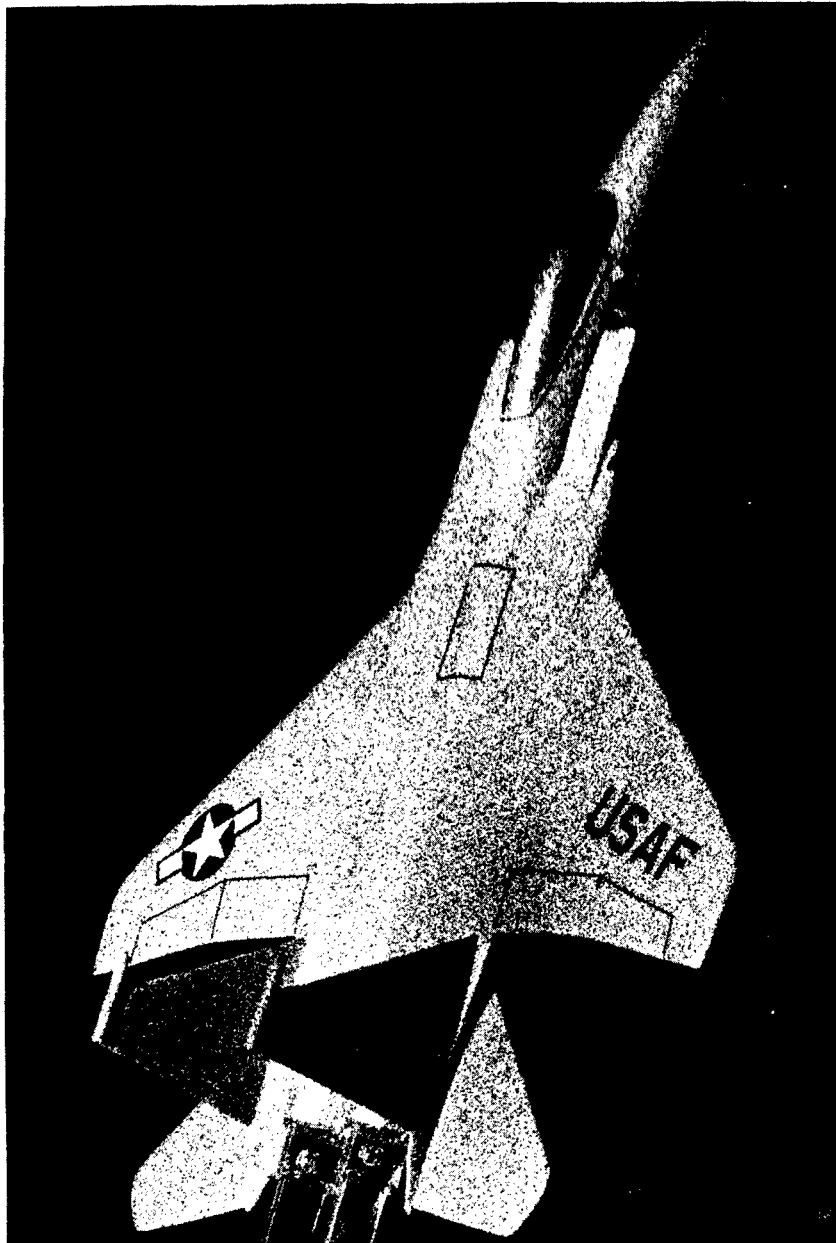


FIGURE C-1. PHOTOGRAPH OF MODEL AIRCRAFT ILLUMINATED BY LASER LIGHT

Figure C-2 is a photograph of a typical speckle diffraction halo with a displacement-induced fringe pattern.

For small diffraction angles, Young's fringes are perpendicular to the displacement vector and the spacing is inversely proportional to the displacement magnitude. This provides a measurement of local displacement since, in general, a narrow laser beam is used to interrogate only a small area of the image on a specklegram. The resolution depends on the laser beam diameter and magnification used in the photographic setup. The in-plane displacement distribution can be obtained by scanning the laser beam over the entire image area and taking measurements at selected points.

Other methods for extracting in-plane displacement data from a specklegram have been developed <sup>(3,4,5)</sup>. These provide a displacement contour fringe pattern superimposed on an optical image of the test specimen. Although such whole field methods are excellent for qualitative analyses and "quick look" at the displacement data, they do not provide the spatial resolution that can be attained using the point read-out technique. In addition, only one component of the displacement field can be contoured at one time. The point-data-acquisition method yields displacement magnitude and direction simultaneously.

Measurement accuracy is very dependent on signal-to-noise ratio in the diffraction halo. Signal amplitude is directly related to the fringe contrast. As can be seen in Figure C-2, the primary source of noise is secondary speckle in the diffraction halo. These secondary speckles are not related to the speckles which are photographically recorded on the specklegram negative, but are generated by the coherent illumination of the acquisition laser beam. This type of noise affects accuracy if the fringe spacing approaches the speckle size. With larger fringe spacing, filtering or smoothing techniques will yield an acceptable signal-to-noise figure.

There are several items which can reduce fringe contrast (signal amplitude) and thus affect measurement accuracy. These are

- (1) Insufficient isolation of the measuring apparatus and specimens from environmental vibration.
- (2) Steep gradients in the displacement field.

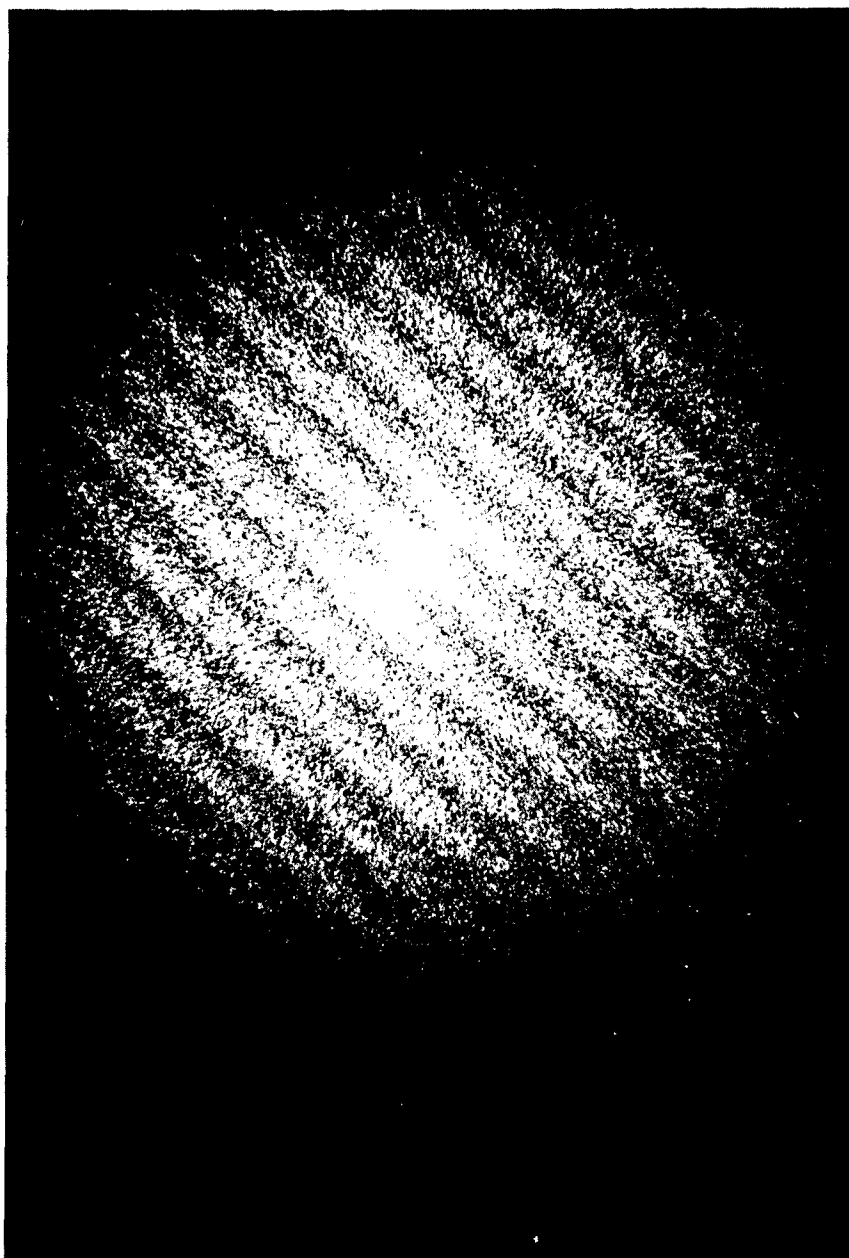


FIGURE C-2. YOUNG'S FRINGES IN THE DIFFRACTION HALO

- (3) Out-of-plane displacements or rotations of the specimen about in-plane axes.
- (4) Changes in the surface characteristics of the specimen between photographic exposures.

Each item will be discussed separately.

Relative motion between the test specimen and camera should be limited so as not to blur speckles in the film plane. When measuring very small displacements, tiny speckles are required and are generated by using a large aperture lens. Optical "stable tables" are employed for these measurements. Larger displacements allow for larger speckles which reduce the stability requirement proportionally. With a lens opening of  $f/8$  or smaller, the measurement can usually be made without a stable table.

Steep gradients in the displacement field can reduce contrast or wash out Young's fringes. This usually occurs when there is a significant change in displacement across the diameter of the readout laser beam. Since this diameter cannot be reduced to less than about 1 mm, it is necessary to use larger photographic magnification when this problem is encountered.\*

Out-of-plane displacements and rotations of the specimen about in-plane axes which take place between double exposures will tend to wash out Young's fringes. This occurs because speckles are three-dimensional entities. Although a laser illuminated object "appears" to have a speckled surface, these speckles are, in reality, generated in the scattered light field. For most lens systems, the speckle is very much elongated in a direction parallel to the optical axis. This allows some out-of-plane displacement to occur with no effect on the Young's fringes. However, out-of-plane displacements which are many times larger than the in-plane displacements being measured will destroy speckle correlation between exposures. In such cases, speckle pairs are not recorded and Young's fringes cannot be produced. Lenci<sup>(6)</sup> performed

---

\* Secondary speckle size is inversely proportional to the diameter of the readout laser beam. Also, edge diffraction becomes a problem with very small diameter laser beams.

(6) Lenci, M. R., "Investigation of Displacement Limitations for Laser Speckle Photography", TM-74-144-FBR, July 1974.

a series of experiments which measured the effect of various amounts of out-of-plane displacement and specimen rotation.

Changes in surface characteristics which occur between exposures can also reduce or wash out fringe contrast. This is also a type of decorrelation in the speckle pattern which is independent of in-plane translation. The primary cause is usually local plastic yielding of the material which upsets the surface. Fortunately, this is not a "go or no-go" situation. A small amount of plastic yielding will partially upset the surface and cause some reduction in fringe contrast. As loading and yielding are increased, the transition to complete fringe washout is not gradual, but neither is it sudden. As a result, it is possible to use speckle photography to study plastic yielding if measurements are obtained for small load increments. The resultant total displacement field is obtained by superposition of the incremental data.

For the investigation of IFFs reported herein, Item (1) above was not a problem since the specklegrams were recorded on an optical stable table. Item (2) was controlled by using magnification factors of unity or larger. Item (3) presented no problem with the testing of the coupon specimens (interference only). These problems became severe, however, when tensile loads were also applied. Incremental loading was used to control Item (4), since plastic yielding usually does occur when IFFs are installed in joints. Details are discussed in the next section.

#### APPARATUS AND PROCEDURE FOR TESTING COUPON SPECIMENS

The basic arrangement of apparatus required to record a specklegram is diagrammed in Figure C-3. A 50-milliwatt helium-neon laser was used to illuminate the test specimen. A microscope objective lens and a 25-micron pinhole were employed to expand and filter the laser beam.

A rather massive fixture was fabricated to hold the test specimen and camera. This was done to minimize whole body displacements of the specimen relative to the camera which might occur during torque up of a fastener. Figure C-4 is a photograph of the test fixture with a 2-inch by 6-inch

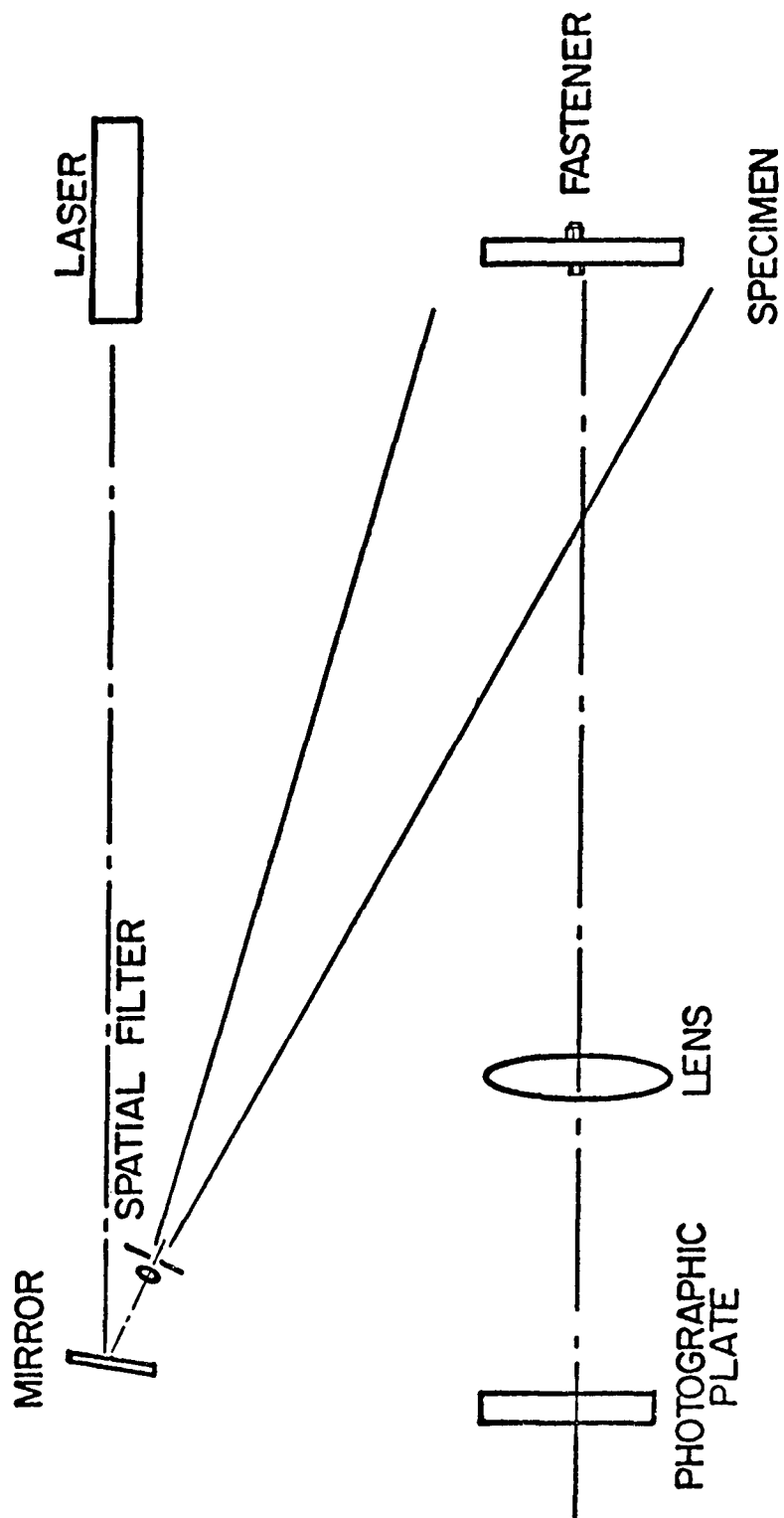


FIGURE C-3. SPECKLEGRAM RECORDING PROCEDURE

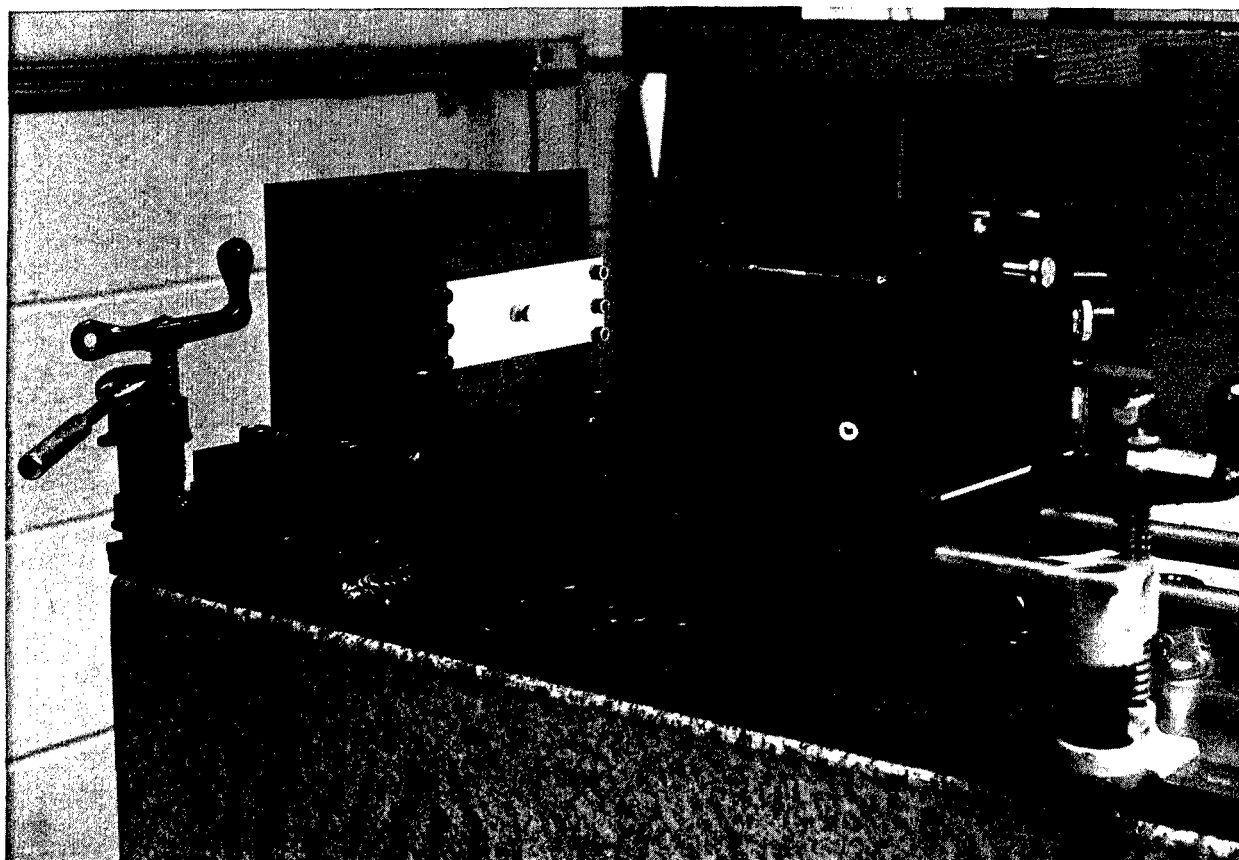


FIGURE C-4. PHOTOGRAPH OF THE LOADING FIXTURE AND CAMERA

aluminum coupon test specimen bolted to the box frame. A single 3/8-inch tapered IFF was installed in the center of the coupon. The front surface of all test specimens was grit blasted to insure a diffuse scattering of the laser light.

The speckle camera, especially designed and fabricated for this program, incorporated a high-quality half-silvered mirror in order to permit two film plates to be exposed simultaneously. Figure C-5 is a diagram of this camera. The horizontal film plate holder was equipped with a "dark slide". This provided the use of the vertical image plane for making several specklegrams of small incremental displacements while recording the total displacement on the horizontal film plate. The small incremental specklegrams provided good data in the plastic yield zone very near the fastener. Smaller displacements in the far field elastic zone were easier to obtain on the total incremental specklegram.

In practice, the following procedure was used. Both film plates were exposed with an IFF placed in the specimen hole but not torqued up. The dark slide was then used to shield the horizontal image plane. Twenty to thirty percent of the recommended interference was then achieved by torquing the IFF. In order to record this increment, a second exposure was made in the vertical film plane only. This film was then replaced with a fresh plate and a new exposure made. A second increment was recorded by further torquing of the fastener followed by exposing the vertical film plate. The process was repeated until the total interference recommended by the fastener manufacturer was obtained. The final exposure was made with the dark slide removed to record the total displacement increment.

Once specklegrams were obtained, the next step was to acquire and reduce data. As discussed in a previous section, the point-acquisition technique was found to be most acceptable for our purposes. This yielded displacement magnitude and direction as a function of coordinate position. Figure C-6 is a drawing of the basic configuration used for data acquisition.

Young's fringe formula states that the distance,  $D$ , between fringe minimum is approximately

$$D \approx L\lambda/d \quad , \quad (1)$$

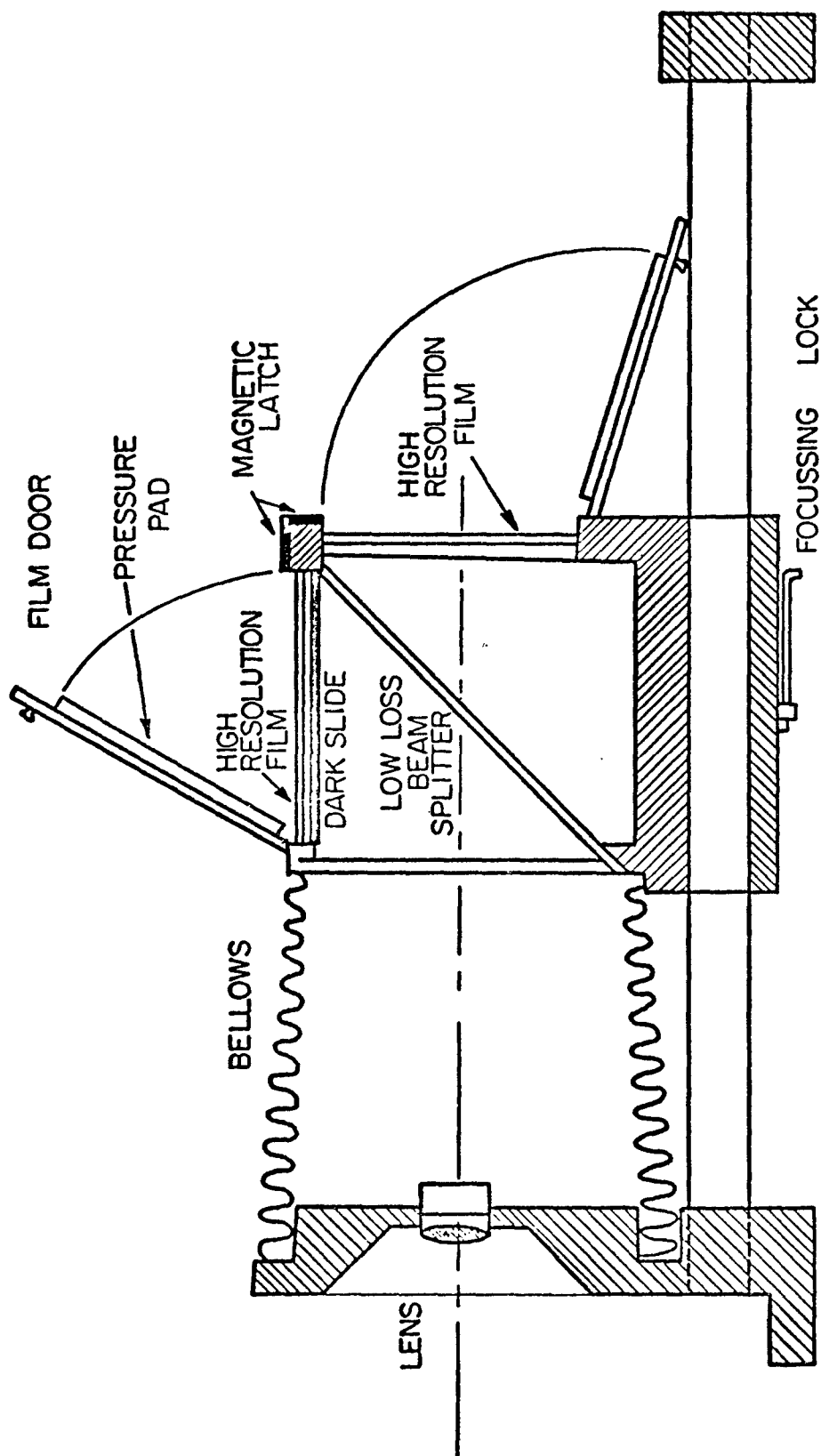


FIGURE C-5. CROSS SECTION OF CAMERA

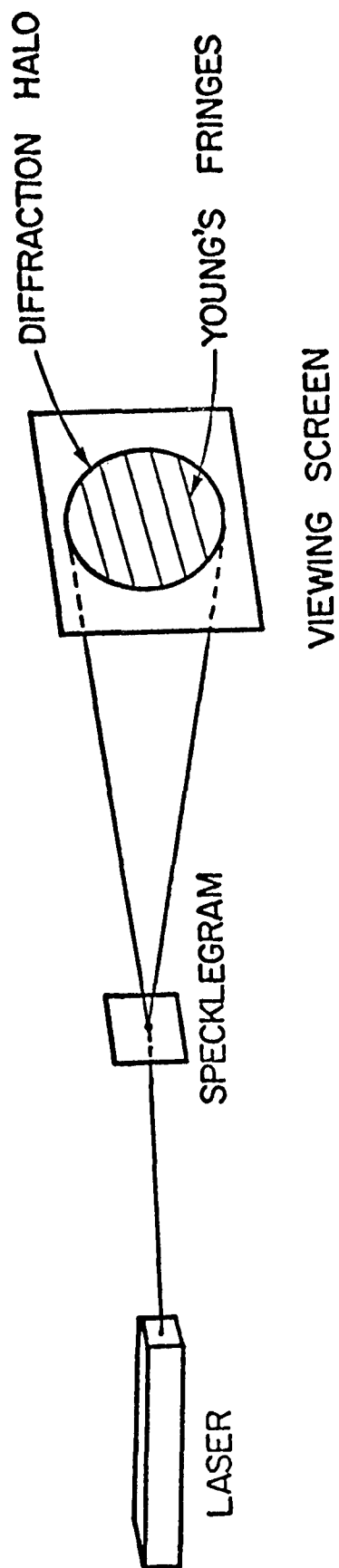


FIGURE C-6. DATA ACQUISITION PROCEDURE

where  $L$  is the distance from the specklegram to the viewing plane,  $\lambda$  is the wavelength of light, and  $d$  is the separation distance of speckle pairs. Young's fringes are, of course, perpendicular to the displacement direction.

The mechanics of measuring the fringe spacing are somewhat more difficult than it appears. This is particularly true if high accuracy is required. Attempts to physically measure the fringe spacing with scales on a translucent view screen produced data scatter of 5 percent or more. Therefore, a scanning device was designed and fabricated which employed a Bell and Howell Type 509 photodetector to plot light intensity in the diffraction halo.

Figure C-7 is a photograph of the optical bench used for data acquisition readout. The major components are a 5-milliwatt laser, an X-Y positioner to locate the specklegram, a photodetector scanning device, and a translucent view screen. The scanner and view screen were attached in a rotatable mount. This allowed the operator to position the scanner such that the fringes were traversed in a perpendicular direction. The angular orientation of the fringe pattern was measured in "degrees" from a scale attached to the 18-inch-diameter view screen. The scanning aperture was a 4-inch slit. This slit aperture was very effective in smoothing out speckle noise in the diffraction halo.

An X-Y recorder was used to plot light intensity versus scanner position. A typical plot is shown in Figure C-8. Some further noise reduction was accomplished by drawing a smooth curve over the recorded data. The distance between minimum light intensity locations was determined by direct measurement with scales.\* The distance between speckle points was obtained by solving Young's fringe equation [Equation (1)] for  $d$ . Finally, the final displacement magnitude,  $\delta$ , was calculated by dividing  $d$  by the camera magnification factor,  $M$ . Thus,

$$\delta = \frac{L\lambda}{DM} . \quad (2)$$

The displacement magnitude  $\delta$ , the displacement direction  $\theta$ , and the X-Y coordinate at the point on the specklegram image which was interrogated were tabulated for each measurement.

---

\* The average intensity distribution in a diffraction halo is not uniform and falls off rapidly with distance from the center. This can cause a shift in the distance between maxima in a fringe pattern. For this reason, the distance between minima was always measured.

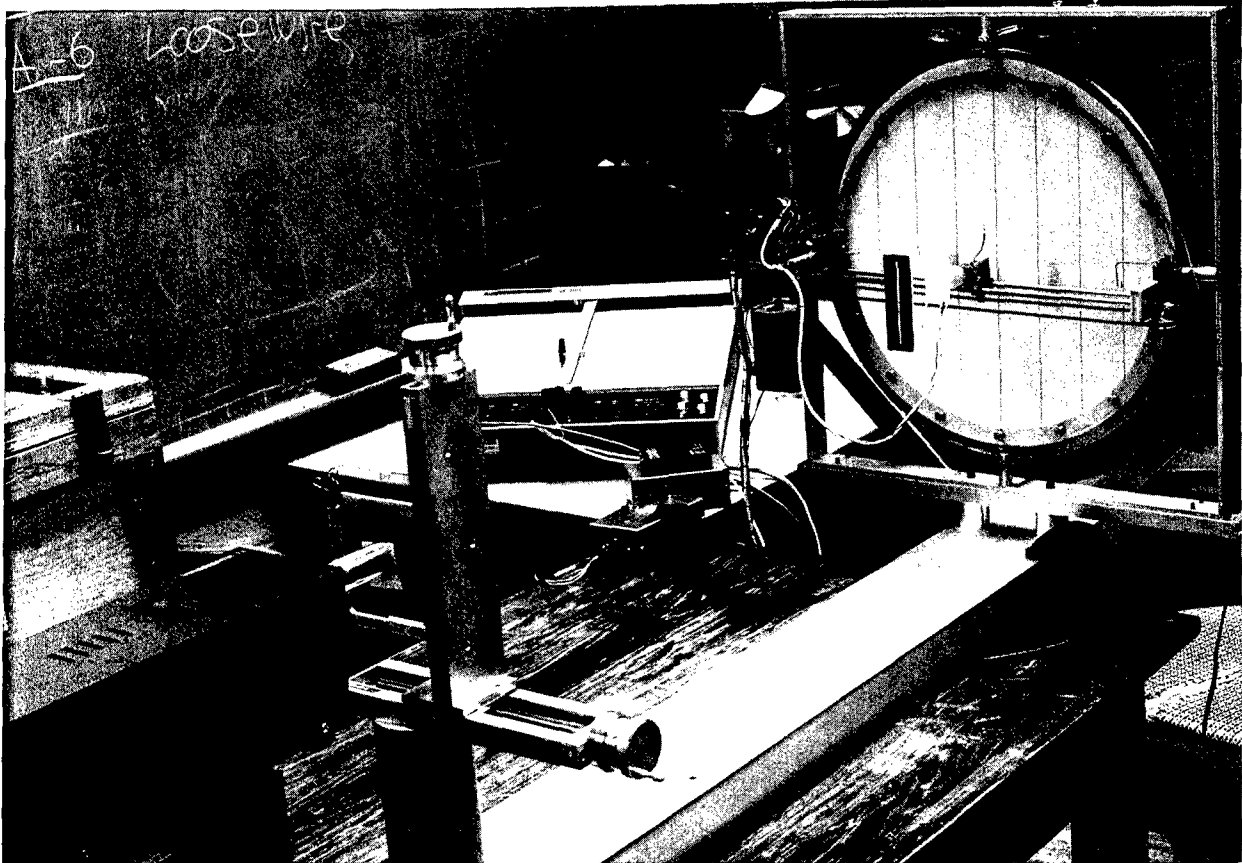


FIGURE C-7. PHOTOGRAPH OF THE DATA ACQUISITION SCANNING DEVICE

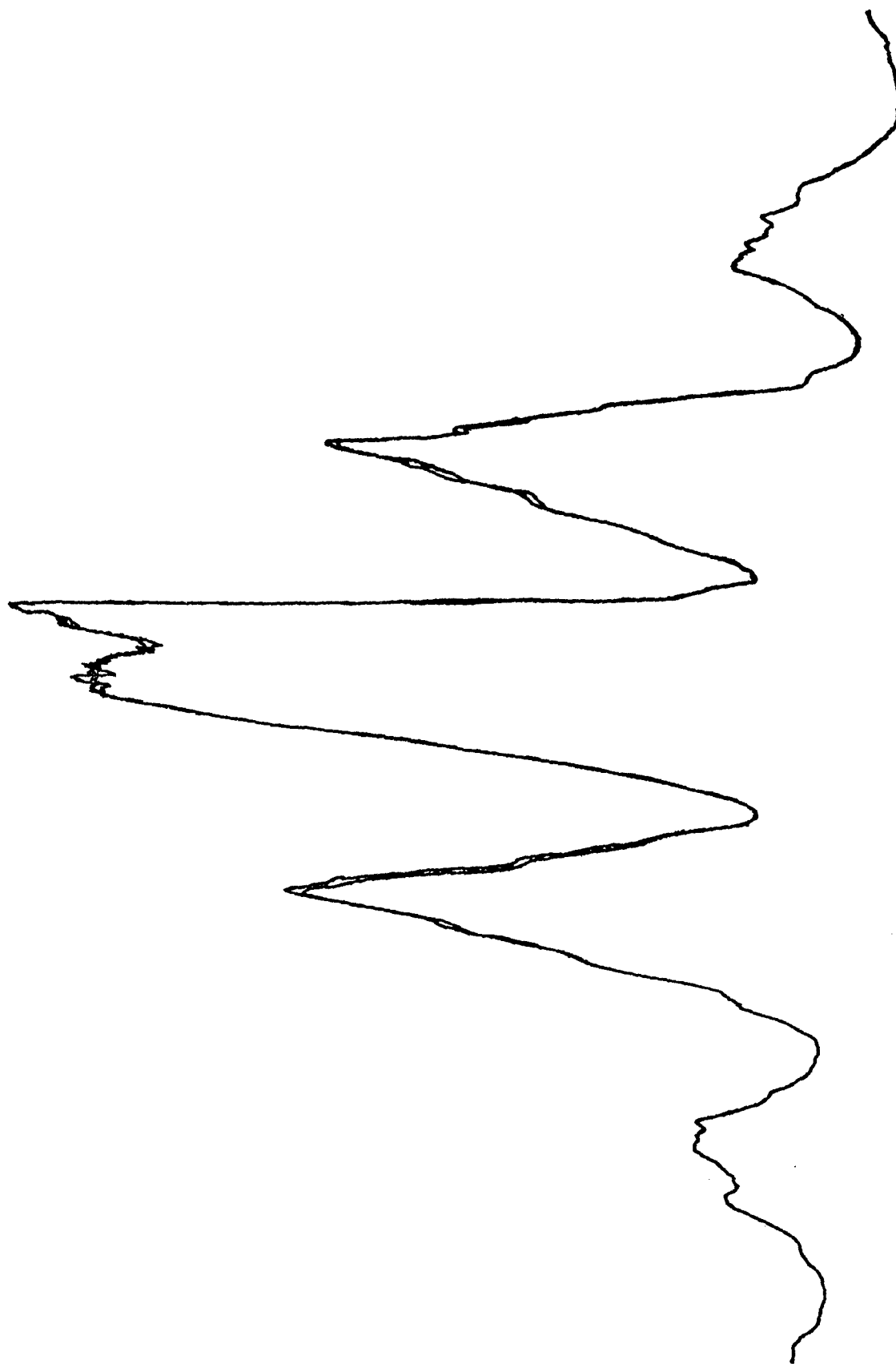


FIGURE C-8. A TYPICAL PLOT OF THE DIFFRACTED HALO WITH YOUNG'S FRINGES

## RESULTS AND DISCUSSION FOR COUPON SPECIMENS

Speckle photography measurements were made on a 6 x 6 x 0.5-inch 7075-T6 aluminum coupon specimen with a 3/8-inch steel Taper-Lok\* fastener installed with a diametral interference of 0.00368 inch. This value of diametral interference was determined by measuring the fastener protrusion before and after installation. Since the shank taper is 1/4 inch per foot, diametral interference is the protrusion difference divided by 48. The results obtained from four different radial traverses out from the hole edge are shown in Figure C-9. It can be seen from this figure that the radial displacement patterns from all four traverses have an 1/r type of distribution and are in good agreement with one another.

Radial displacements obtained from a finite-element analysis\*\* are also plotted in Figure C-9 and appear as a solid line. These results follow the shape of the experimental data points but are larger by approximately 30 percent. To explain this discrepancy, three incremental exposures were examined in detail. This examination revealed that the first load increment, which should have produced a radial edge displacement of about 0.0006 inch (diametral interference of 0.0012 inch), caused an edge displacement of less than 0.0001 inch. The second and third increments produced the expected displacements. Thus, the effective interference was lower than that calculated by the protrusion method. If it is assumed that the second and third increments each force an edge displacement of 0.0006 inch, then a total displacement of 0.0013 inch at the edge of the hole would seem reasonable. Figure C-10 is a comparison of the interference of 0.0026 inch.

To determine the cause of this "slack" interference, metrological measurements taken before the specimen was loaded were examined. A portion of these measurements are shown in Figure C-11. The polar plot, Plot A, reveals that the hole was perpendicular and of uniform taper. Variations of up to 0.0007 inch, however, are discernable. Plot B is only a portion of the plot obtained from the hole surface in the longitudinal direction of the

---

\* Trade name for tapered bolt fastener manufactured by Omark Industries, El Segundo, California.

\*\* All finite-element calculations are presented in a separate section.

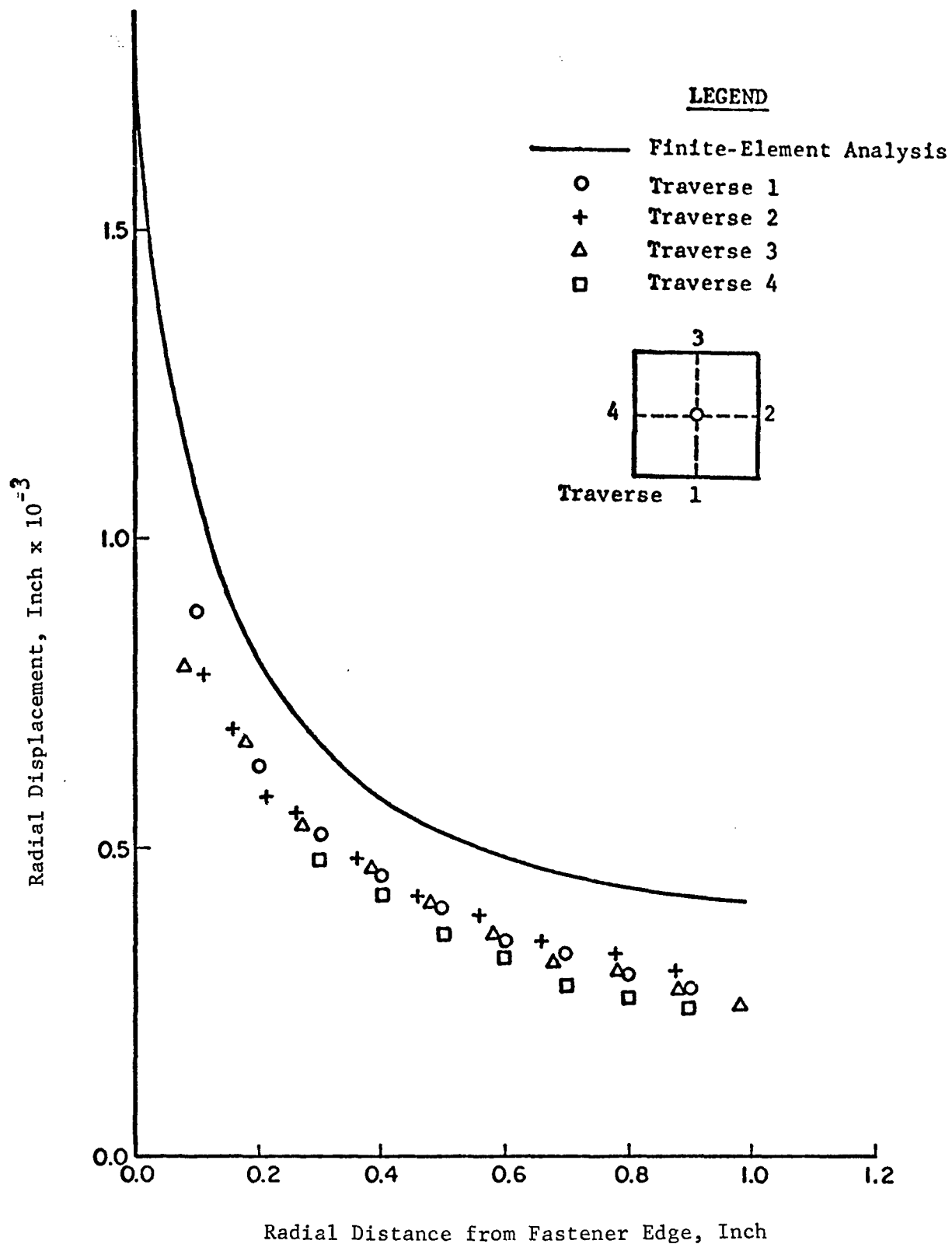


FIGURE C-9. RADIAL DISPLACEMENT VERSUS RADIAL POSITION FOR A 6 X 6 X 0.5-INCH 7075-T6 ALUMINUM SPECIMEN WITH 0.00378-INCH INTERFERENCE

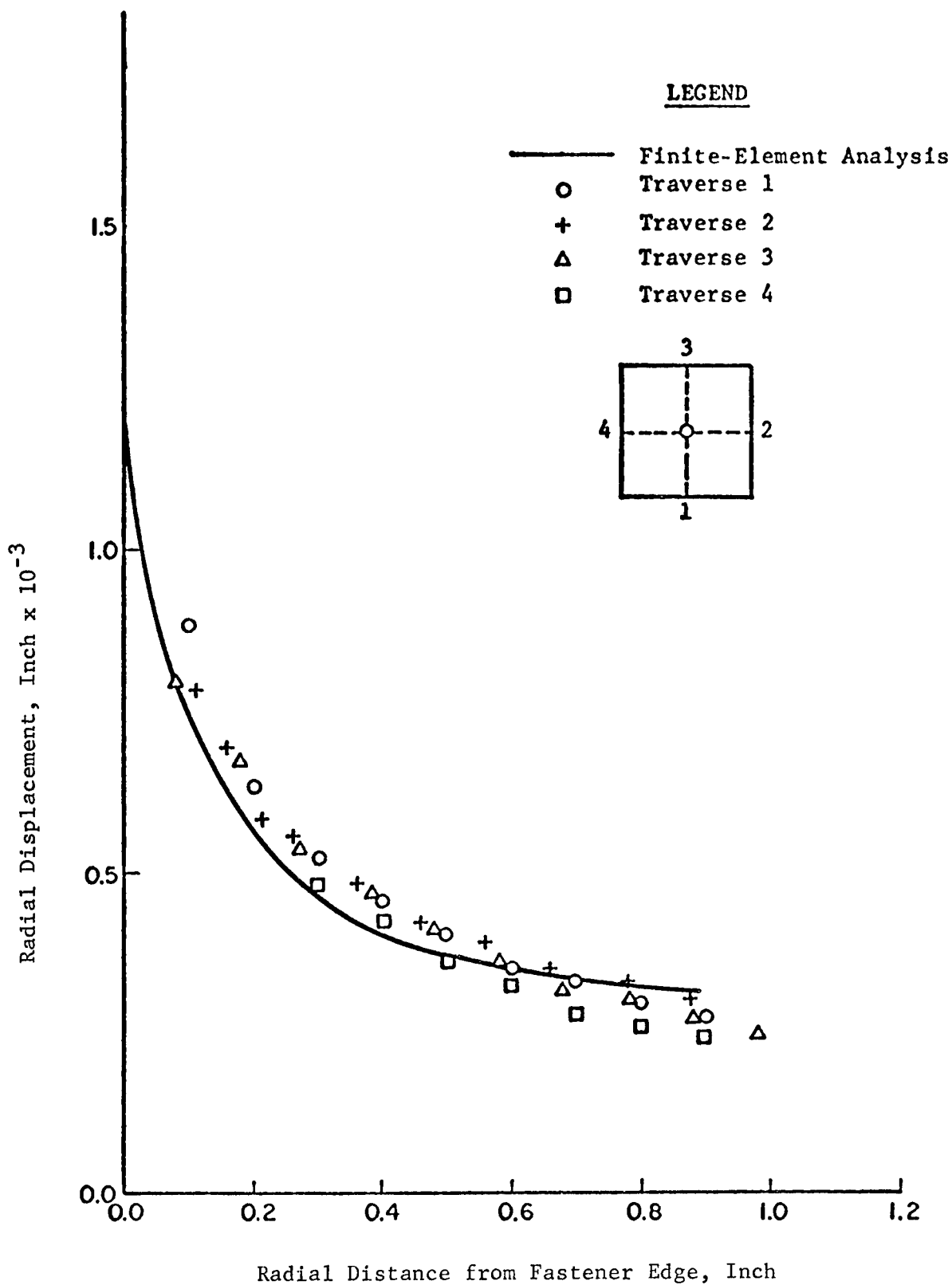
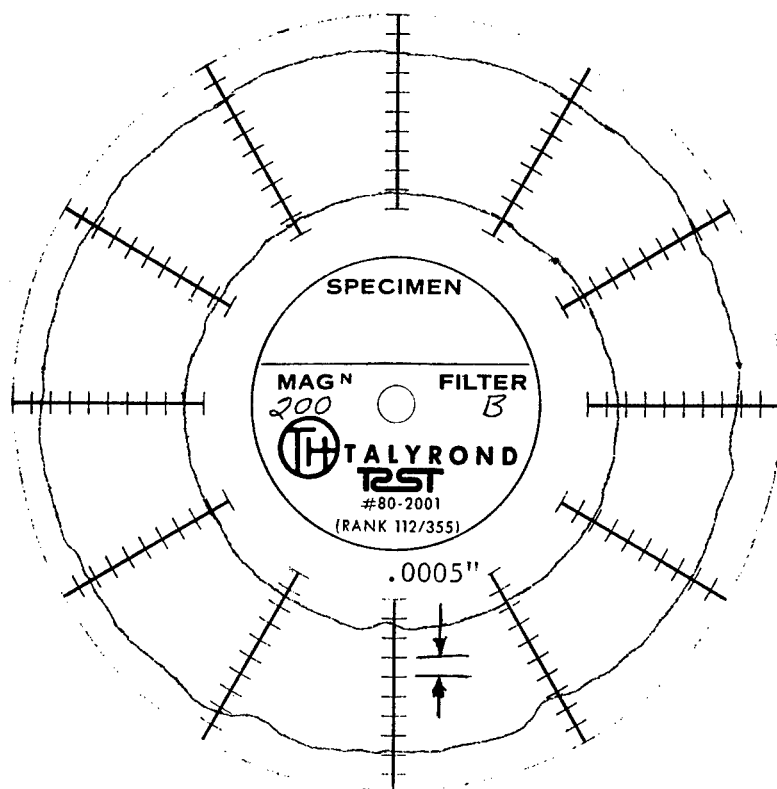
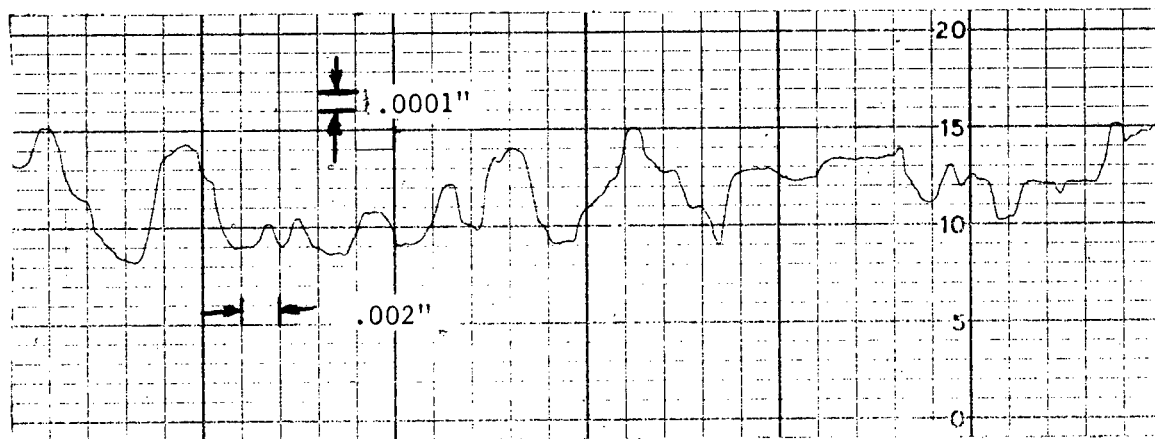


FIGURE C-10. RADIAL DISPLACEMENT VERSUS RADIAL POSITION FOR A  
6 X 6 X 0.5 INCH 7075-T6 ALUMINUM SPECIMEN WITH  
0.0026-INCH INTERFERENCE



PLOT A



PLOT B

FIGURE C-11. METROLOGICAL DATA FOR AN ALUMINUM COUPON SPECIMEN

hole. Variations in this plot are again seen to be about 0.0007 inch. The above-mentioned irregularities required that local smoothing be accomplished during the first increment before complete interference could be obtained.

Speckle-photography measurements were also made on a 2 x 2 x 0.5-inch silicon iron coupon specimen fitted with a 3/8-inch steel Taper-Lok fastener. This specimen was included in the test matrix so that eventually a comparison could be made between measurements obtained by speckle photography and the dislocation etching technique. Data from the dislocation etching technique were not available as the time required to complete the speckle photography work induced aging to the material such that it did not respond to the etching process. However, a comparison between finite-element predictions and speckle photography measurements was accomplished.

Measured displacements are plotted in Figure C-12. Also, presented are two theoretical curves obtained by finite-element analysis. The dashed curve shows the displacements resulting from a "protrusion determined" interference of 0.00243 inch. The solid line shows the predicted displacements for an interference level that best fits the experimental data, which is 0.00175 inch or 72 percent of the above value.\*

Two equal incremental exposures were made for this specimen. These were again examined to see if the "slack" interference could be accounted for. Measured displacements in the first increment were only  $\frac{1}{2}$  of those found in the second. This would indicate that the total effective interference should be about 75 percent of the protrusion determined interference. This is quite close to the 72 percent value obtained by best fitting the data. Metrology of the steel hole is presented in Figure C-13 and is consistent with these results.

The data presented in Figure C-12 exhibit less symmetry in comparison to the measurements made on the aluminum specimen (Figure C-10). Some of this is due to simple difference in the hole geometries. However, a steel-in-steel installation requires relatively high torque and some movement of the coupon could have occurred. The measured displacements would

---

\* It should be noted in Figure C-12 that the theoretical displacement at the edge of the fastener hole is not equal to  $\frac{1}{2}$  the diametral interference. This is due to compression of the fastener which is much greater with a steel specimen as compared to aluminum due to the difference in Young's modulus.

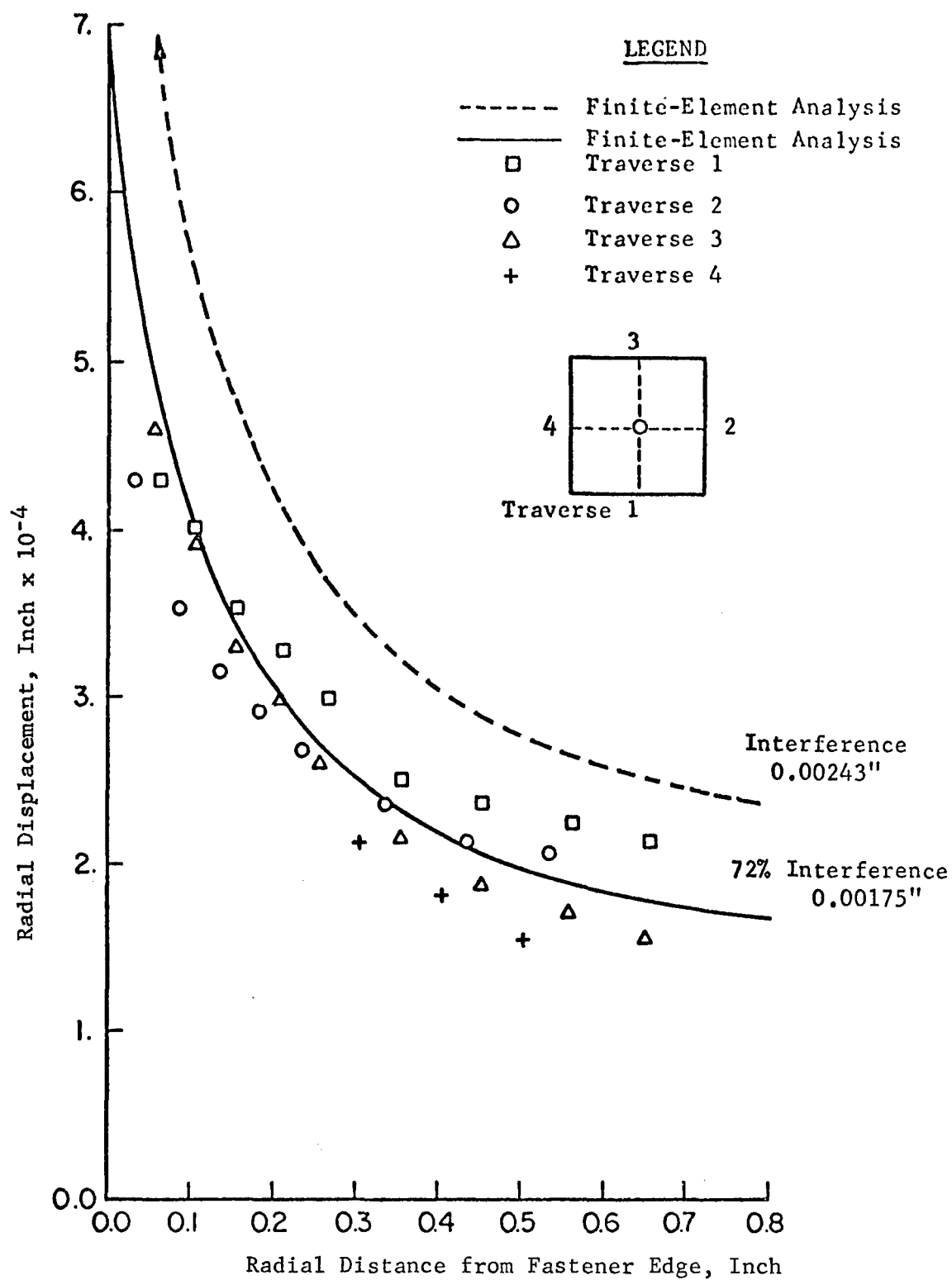
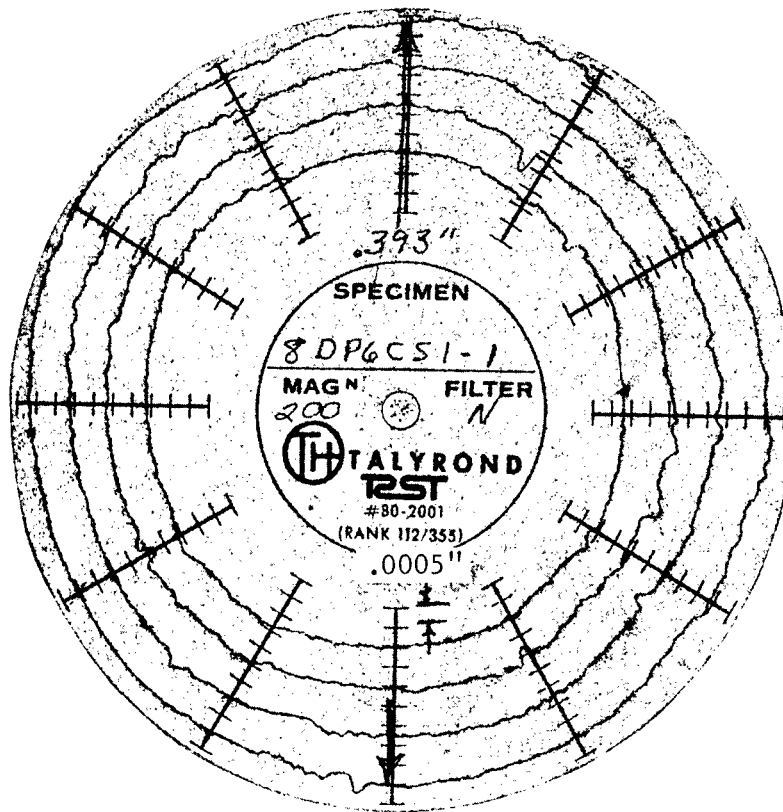
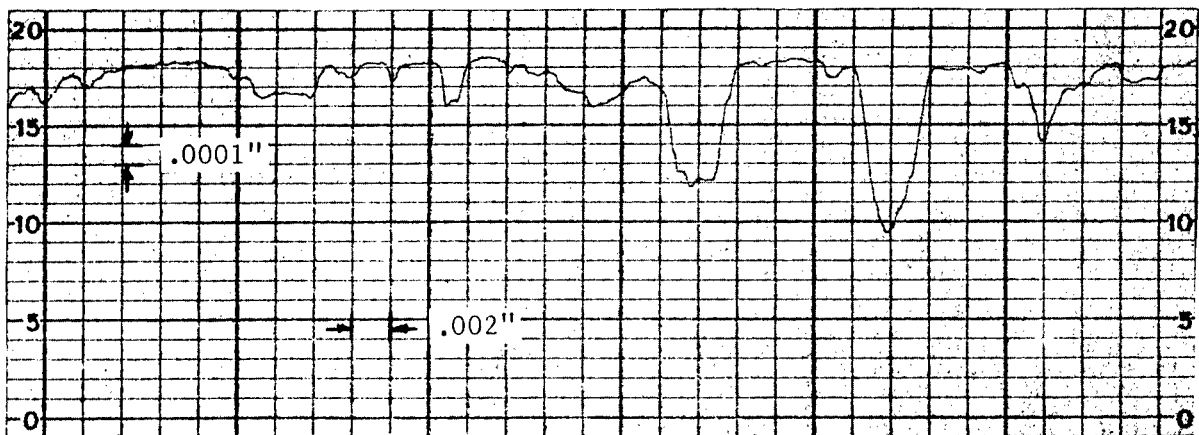


FIGURE C-12. RADIAL DISPLACEMENT VERSUS RADIAL POSITION FOR A 2 X 2 X 0.05-INCH SILICON-IRON SPECIMEN WITH 0.00243-INCH INTERFERENCE



Polar Plot



Longitudinal Plot

FIGURE C-13. METROLOGICAL DATA FOR A STEEL COUPON SPECIMEN

then have a component of rigid body translation or rotation superimposed on the interference-induced displacement.

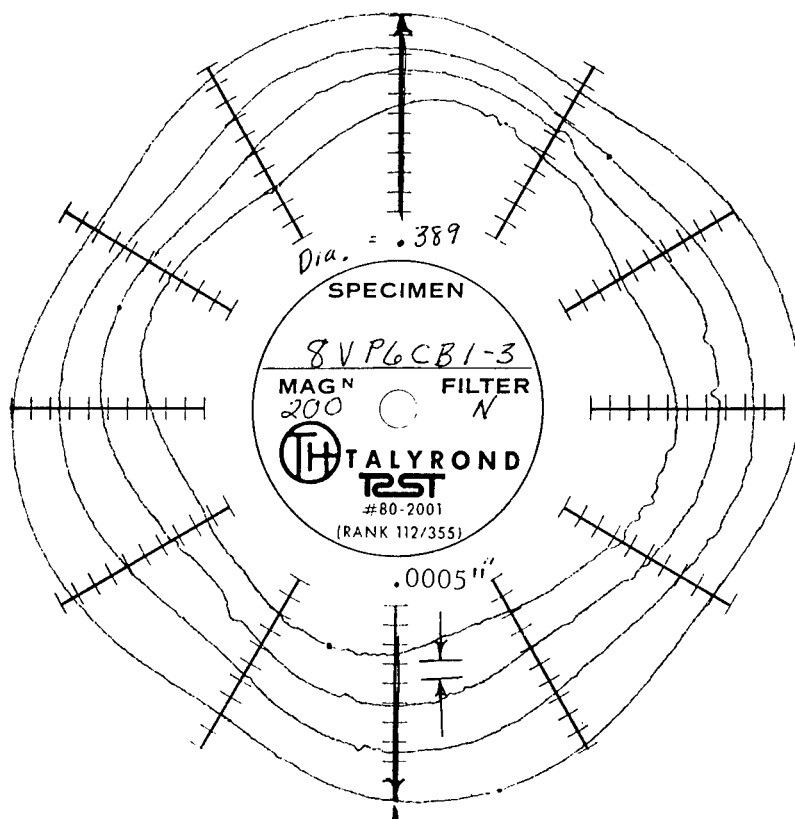
Finally, measurements were obtained on a 6 x 6 x 0.5-inch aluminum coupon specimen which had a 3/8-inch tapered hole that was 0.5 percent out-of-round. Metrological data for this hole are presented in Figure C-14. An interference of 0.00366 inch was applied to the specimen with a steel Taper-Lok fastener.

Out-of-round IFF holes are not an uncommon occurrence. They are often caused by high feed rates and/or dull reaming drills. When an out-of-round hole condition exists, the fastener shank is not initially in contact over its entire surface area. As the fastener is drawn into the hole, a greater portion of its shank contacts the specimen. For small amounts of out-of-roundness, the fastener will eventually make total contact. Additional interference will cause deformations similar to the "round hole" case, except that the strain field will lack symmetry.

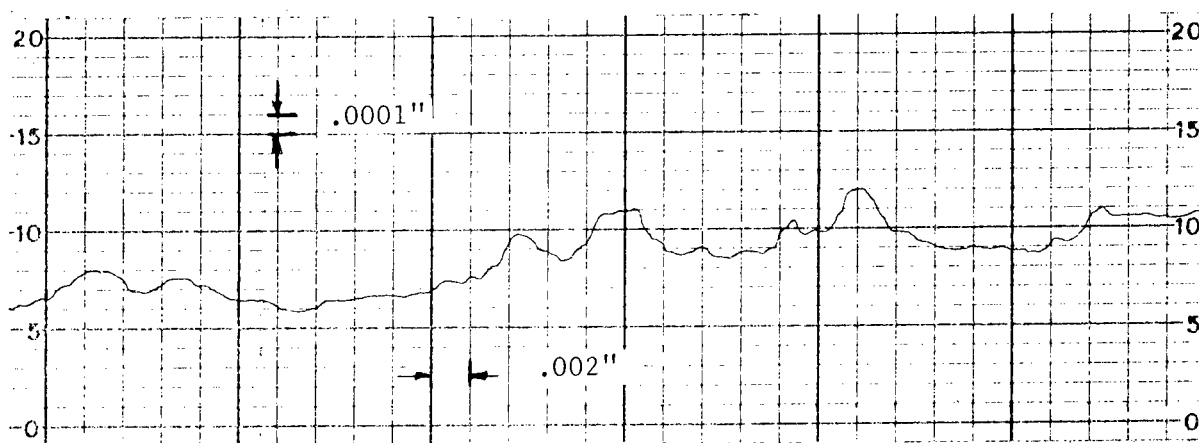
Measured displacements are plotted in Figure C-15. In addition, results obtained from a plane-stress finite-element analysis are also plotted. The dashed line shows the displacements corresponding to the axis of maximum deformation (initial contact). The solid line represents the displacements along the axis of minimum deformation (largest gap). Data points from traverse 2 at the 45 degrees correspond to the dashed line. Data from traverses 1 and 3 relate to the solid line.

The experimental data are in good agreement with the finite-element analysis. However, there are several features worth examining in great detail. In Figure C-15, the measurements along traverse 2 fell below the theoretical curve. The hole metrology, as presented in Figure C-14, helps explain this discrepancy. The orientation of out-of-roundness varied by about 30 degrees through the thickness of the specimen. This "spiraling" pattern effectively broadened the region of initial contact and had an attenuating influence on the displacement along traverse 2.

It is also interesting to note that this specimen appeared to have an absence of slack interference. Incremental exposures also confirmed this. The first increment showed relatively large displacements in the area of initial contact and little elsewhere. The first incremental exposure for the round hole specimens revealed generally small but symmetrical displacements. This difference probably resulted from the positive initial contact



Polar Plot



Longitudinal Plot

FIGURE C-14. METROLOGICAL DATA FOR AN OUT-OF-ROUND ALUMINUM COUPON SPECIMEN

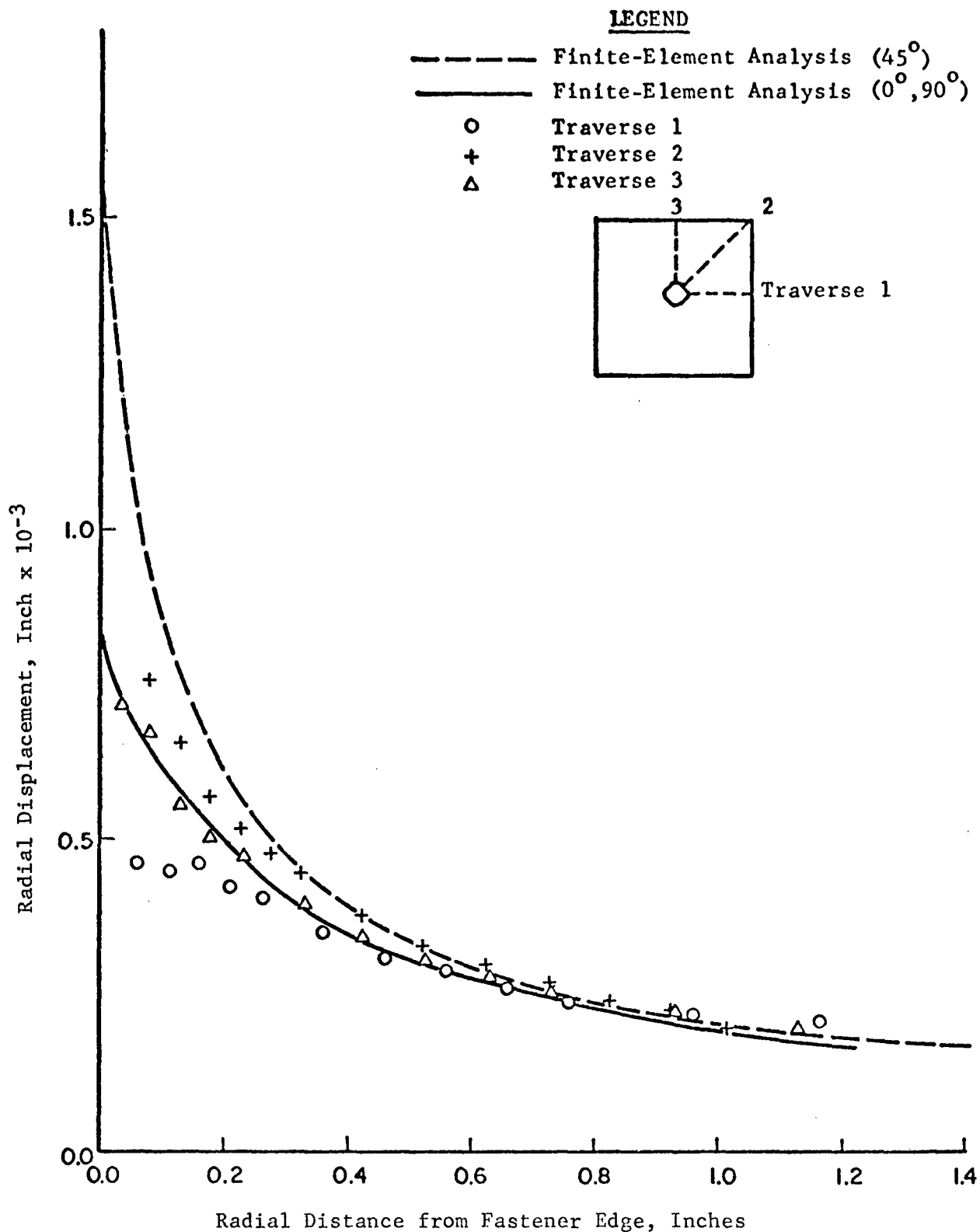


FIGURE C-15. RADIAL DISPLACEMENT VERSUS RADIAL POSITION FOR A 6 X 6 X 0.5-INCH ALUMINUM SPECIMEN WITH A 0.5 PERCENT OUT-OF-ROUND HOLE AND 0.00366-INCH INTERFERENCE

due to the out-of-roundness. The finite-element model for the out-of-round condition was constructed from the hole metrology. The spiraling effect, however, could not be included in the model since the analysis was performed under the assumption of plane stress.

Measurements were also attempted on ten additional specimens. These data were unfortunately invalidated by a number of causes which include specimen rotation, film plate motion, and inadequate fringe visibility. Because data from these specimens cannot be interpreted, they are not presented here.

#### APPARATUS, PROCEDURE, AND RESULTS FOR AXIALLY LOADED JOINT SPECIMENS

It was initially intended that a number of axially loaded fastened joint specimens would be tested. However, difficulties with the technique unfortunately reduced the number of specimens to one.

The specimen that was tested was a no-load-transfer 7075-T6 aluminum specimen. Before loading, eight electrical resistance strain gages with a gauge length of 0.015 inch were applied to the specimen as shown in Figure C-16. A compensating gage was mounted on a similar piece of material.

In order to apply the interference loading, the specimen was first installed in the test fixture that was previously used with the coupon specimens. All mating surfaces were grit blasted to reduce the possibility of relative motion. An interference of 0.00338 inch was applied using a 3/8-inch-diameter Taper-Lok fastener.

The speckle camera was used to obtain a single double exposure specklegram. No incremental specklegrams were made. The eight strain gages were read before and after the loading was applied. Figure C-17 is a plot of the displacements obtained from the specklegram compared with displacements predicted by the finite-element method. It is interesting to note that in this case no "slack interference" was present. Examination of the hole metrology shown in Figure C-18 provides no clue as to why this is so. It is believed that the lack of "slack interference" is a direct result of a dry graphite lubricant and higher torque being applied to the fastener when it was initially installed. Unfortunately, the displacements determined from the specklegram were highly affected by the initial installation and,

GAGE	DIST. IN INCHES TO GAGE CENTER FROM CENTER OF FASTENER	ORIENTATION
1	.750	AXIAL
2	.375	AXIAL
3	.210	RADIAL
4	.208	CIRCUMFERENTIAL
5	.206	CIRCUMFERENTIAL
6	.208	RADIAL
7	.500	AXIAL (TOP)
8	.500	AXIAL (BOTTOM)

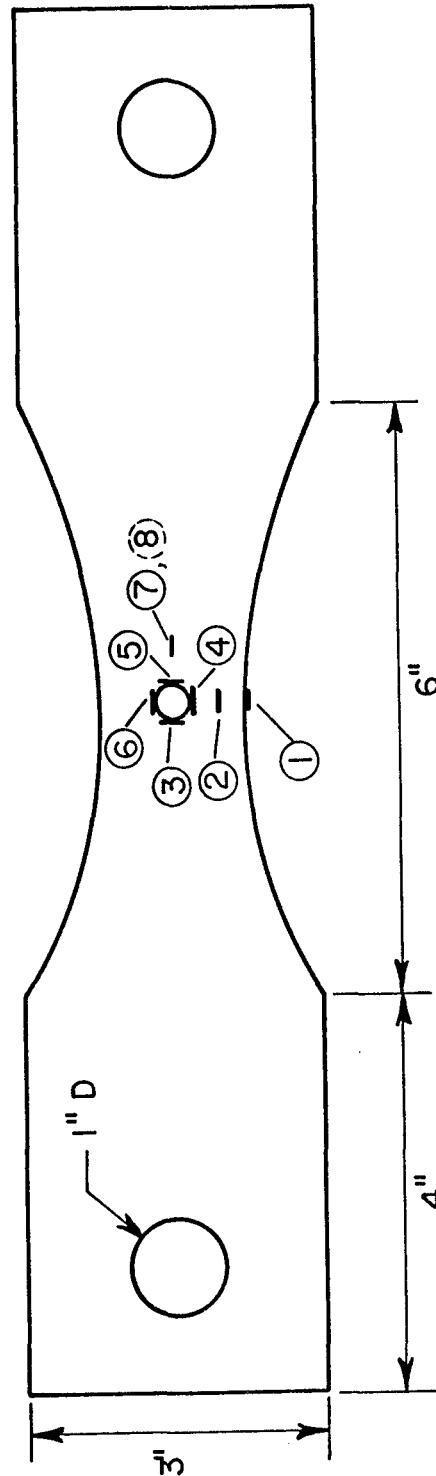


FIGURE C-16. STRAIN GAGE LOCATIONS ON A 7075-T6 ALUMINUM NO-LOAD SPECIMEN

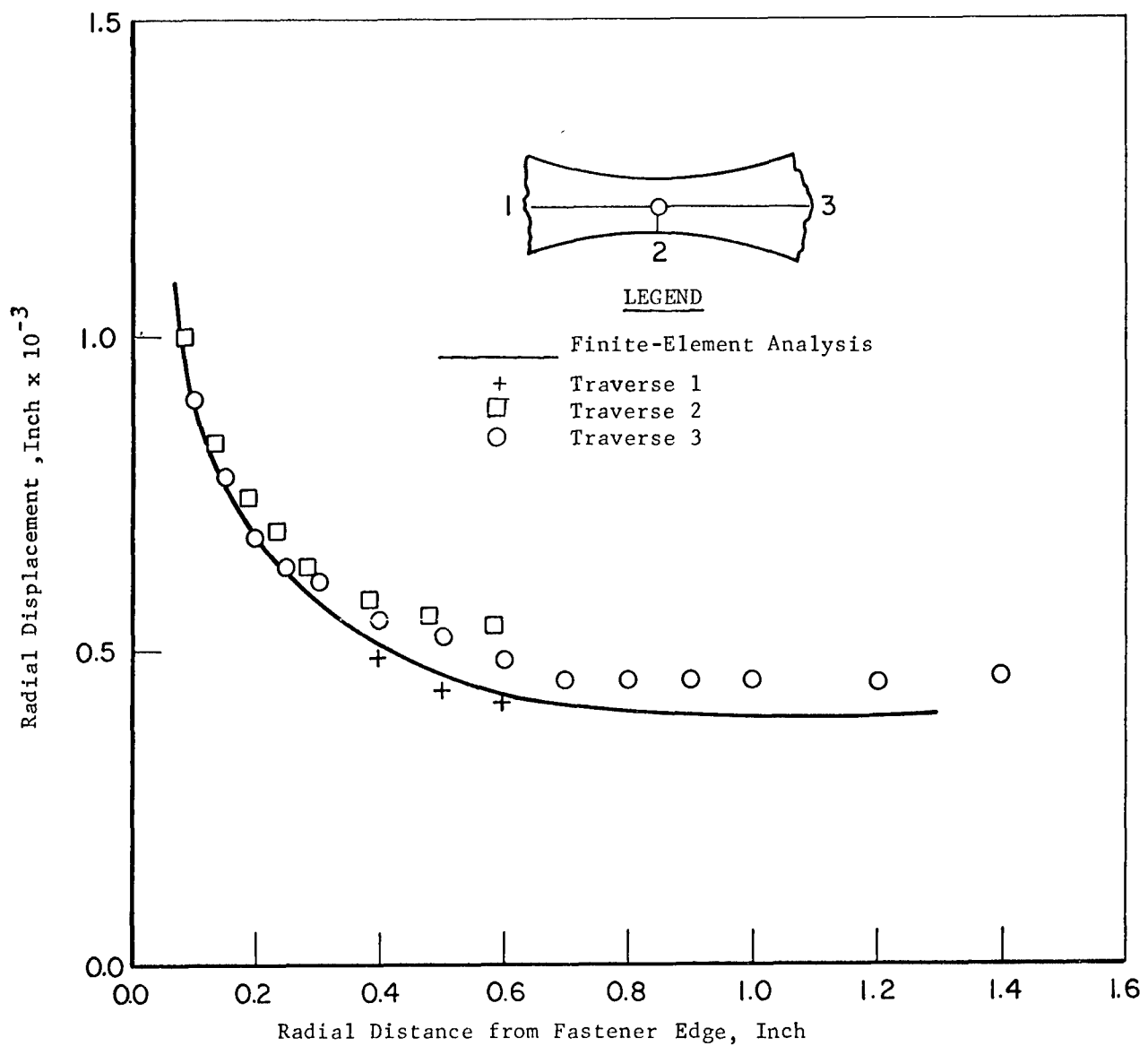
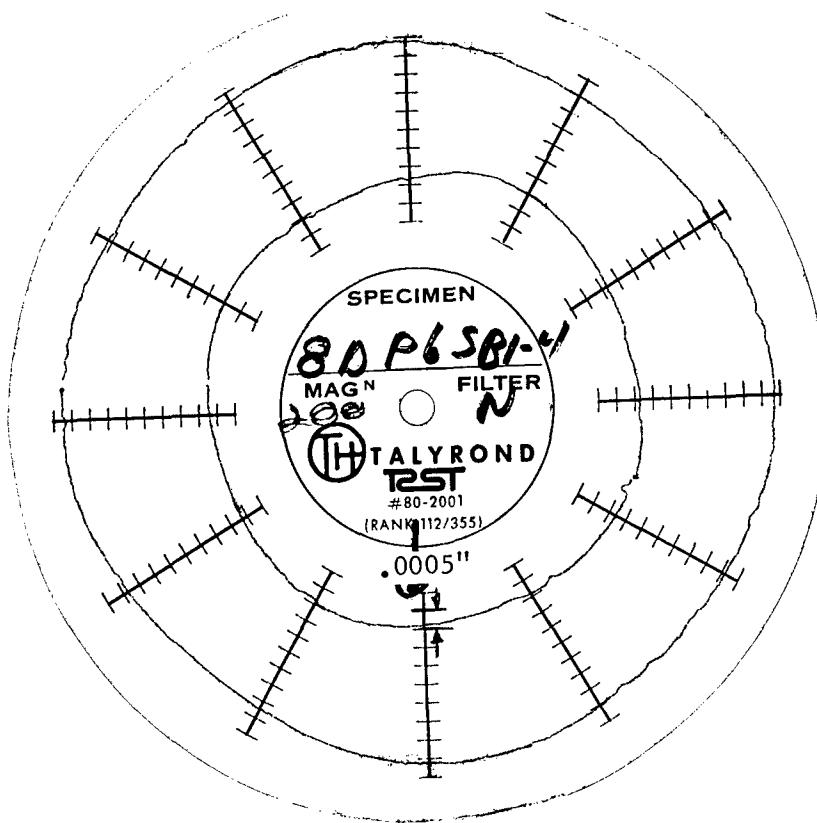
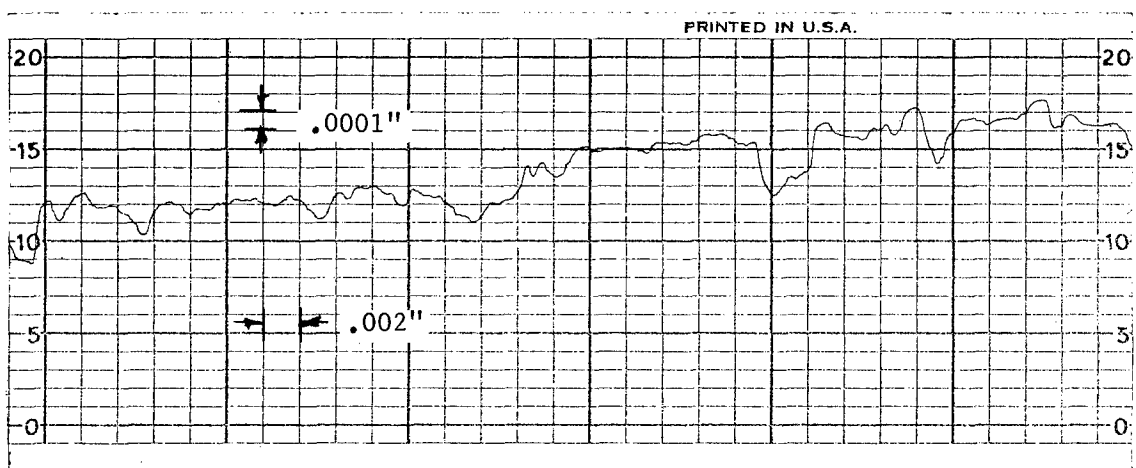


FIGURE C-17. RADIAL DISPLACEMENT VERSUS RADIAL POSITION  
FOR A NO-LOAD 7075-T6 ALUMINUM SPECIMEN  
WITH 0.00338-INCH INTERFERENCE



POLAR PLOT



LONGITUDINAL PLOT

FIGURE C-18. METROLOGICAL DATA FOR AN ALUMINUM NO-LOAD-TRANSFER SPECIMEN

furthermore, the experimenter's knowledge of the "slack interference" phenomenon may have biased the initial installation. Regardless, good agreement is seen between the experimental points and the finite-element results.

The strain gage readings and strains obtained from the finite-element analysis for the center of each gage are shown in Table C-1. The strain gage readings agree reasonably with the predicted strains at locations well away from the hole; i.e., gages 1, 2, 7, and 8. However, poor agreement was obtained at locations near the hole. The reasons for such poor agreement are not known at this time. It is understood that slight inaccuracies in gage placement and high strain gradients may be responsible for some error. However, it seems doubtful that errors of this magnitude could be caused by either of these factors. In fact, similar data obtained from four fatigue specimens and reported in Appendix E agree very well with these data and suggest modification of the finite-element model may be necessary.

After applying the interference load, an elaborate high-precision hydraulic-loading fixture was used to apply axial loads to the specimen. Specklegrams were obtained from exposures taken before and after loading. It was determined from the specklegram that even low values of load produced sufficient rigid body motion to make data reduction impossible by regular techniques. In some instances, speckle correlation was completely lost and in others the desired data were buried in a high-density family of rigid body fringes when the specklegram was interrogated. This problem precluded any opportunity to obtain meaningful data at that time. Work done since that time by Adams and Maddux<sup>(7)</sup> indicate that a new two-plate technique may be the key to solving the common problem of rigid body motion in specklegrams. It was anticipated that the problems just described would make meaningful measurements difficult for the loaded specimens. This problem was the primary impetus for the installation of the strain gages. The strain gage readings are compared to strains predicted by the finite-element analysis in Table C-2. Again, readings from gages away from the fastener were in good agreement with the predicted strains, while readings from gages adjacent to the fastener were in poor agreement. Although several explanations for minor variations can be offered, it is still unknown why the measured strains near the hole were so much less than indicated by the finite-element analysis.

---

(7) Adams, F. D. and Maddux, G. E., "Dual Plate Speckle Photography", AFFDL-TM-75-57-FBR, April 1975.

TABLE C-1. COMPARISON OF STRAIN GAGE READINGS WITH STRAINS PREDICTED BY FINITE-ELEMENT ANALYSIS FOR AN INTERFERENCE LOAD OF 0.00338 INCH IN AN ALUMINUM NO-LOAD-TRANSFER SPECIMEN

Gage Location(a)	Strains x 10 <sup>6</sup> in./in.	
	Gage	Finite-Element Analysis
1	969	1240
2	1247	1690
3	-3767	-8550
4	4037	6940
5	4201	7180
6	-2271	-7970
7	-660	-893
8	-660	-893

(a) Reference Figure C-16 for gage location.

TABLE C-2. COMPARISON OF STRAIN READINGS WITH STRAINS  
PREDICTED BY FINITE-ELEMENT ANALYSIS FOR AXIAL  
LOADS IN AN ALUMINUM NO-LOAD-TRANSFER SPECIMEN

Load Gage Location(a)	2000 lb		3000 lb		4000 lb	
	Strain x 10 <sup>6</sup>		Strain x 10 <sup>6</sup>		Strain x 10 <sup>6</sup>	
	Gage	FEM <sup>(b)</sup>	Gage	FEM	Gage	FEM
1	269	263	404	394	541	526
2	237	241	361	361	481	482
3	105	307	181	460	276	613
4	171	245	268	368	384	491
5	-24	-57	-58	-85	-164	-114
6	-53	-131	-93	-197	-150	-263
7	240	250	362	375	476	499
8	255	250	388	375	512	499
Avg 7 & 8	248	250	375	375	494	499

(a) Reference Figure C-16 for gage locations.

(b) FEM refers to strains from the finite-element analysis.

## SUMMARY AND CONCLUSIONS

Speckle photography has been demonstrated as a useful technique for measuring in-plane displacements produced by the installation of IFFs. Although axially loaded specimens were not analyzed successfully, it is believed that further work with techniques to eliminate rigid body motion will eventually produce a reliable technique for use with axially loaded joint specimens. New techniques may still be prone to errors caused by specimen rotation about an in-plane axis and out-of-plane specimen movement; therefore, special attention will have to be given to test fixture and specimen design so that these motions may be minimized.

Further conclusions are summarized briefly as follows:

- (1) It is believed that the development of the incremental form of speckle photography is a significant advance for determining displacements in areas of high strain gradient and local plasticity. Additional verification of the reliability of the technique is warranted, however, since the sum of the incremental displacements does not always add up to the displacement indicated by the total displacement specklegram.
- (2) While the point-by-point data reduction technique does exhibit some definite advantages, it is still somewhat slow and time-consuming with the semi-automated equipment developed in this program. It is definitely worthwhile to simplify and further refine this portion of the technique as much as possible.
- (3) When comparing measured displacements with those determined by analytical means, care must be used so that any effects of "slack interference" are considered. It has been demonstrated that the effects of "slack interference" are not always predictable. Further work is warranted to determine a reliable method of establishing the initial

fastener-hole relationship that is called zero interference.

- (4) Although only one test was performed, it appears that data obtained near a fastener with short gauge length strain gages may be inaccurate.

APPENDIX D  
FINITE ELEMENT METHODS

INTRODUCTION

A major objective of this program was to develop finite-element techniques whereby stress-strain states around interference-fit fasteners (IFF's) could be analytically predicted. These data were then to be used to develop fatigue prediction techniques for IFF joints. This section of the report describes the analysis of techniques used in this effort and presents the results of those cases studied.

ANALYSIS TECHNIQUES

Finite-Element Program - AXISOL

The finite element computer program AXISOL has been used to solve several problems pertinent to the determination of stress and strain fields in IFF problems. The capabilities of the AXISOL computer program are described in this subsection.

Program AXISOL is a versatile tool for analysis of two dimensional, plane or axisymmetric, elastic or elastic-plastic deformations in finite-element models. The finite element is of the constant strain type. A triangular element is used with the displacement field prescribed in the form

$$\begin{aligned}U_x &= \alpha_1 + \alpha_2 x + \alpha_3 y \\U_y &= \alpha_4 + \alpha_5 x + \alpha_6 y\end{aligned}$$

The  $\alpha$ 's can be replaced by the values of the displacement components at the three vertices or nodal points of the triangular element, where in matrix form

$$\{d\} = [A]^{-1} \{V\} \quad (D-1)$$

The V vector contains the displacements at the nodal points and the A matrix is a function only of the nodal point coordinates. The elemental strains are

$$\epsilon_x = \frac{\partial u_x}{\partial x} = \alpha_2 ,$$

$$\epsilon_y = \frac{\partial u_y}{\partial y} = \alpha_6 , \quad (D-2)$$

$$\gamma_{xy} = \frac{\partial u_x}{\partial y} + \frac{\partial u_y}{\partial x} = \alpha_3 + \alpha_5 ;$$

the strains being constant through the element and expressed as a function of the displacements of the vertices. The stresses are written as a function of the strains by way of the following matrix equation:

$$\begin{Bmatrix} d\sigma_x \\ d\sigma_y \\ d\gamma_{xy} \end{Bmatrix} = [D] \begin{Bmatrix} d\epsilon_x \\ d\epsilon_y \\ d\gamma_{xy} \end{Bmatrix} , \quad (D-3)$$

where the incremental form appropriate to elastic-plastic analysis is taken. For elastic problems, the D matrix is composed of the elastic constants for plane-stress states. In the plastic range, AXISOL uses the form due to Yamada for the von Mises yield criteria, and the Reuss flow law,

$$[D] = \frac{E}{Q} \begin{Bmatrix} \sigma_y'^2 + 2P & & \text{SYM.} \\ -\sigma_x'\sigma_y' + 2\nu P & \sigma_x'^2 + 2P & \\ -\frac{\sigma_x' + \nu\sigma_y'}{1+\nu} \tau_{xy} - \frac{\sigma_y' + \nu\sigma_x'}{1+\nu} \tau_{xy} & \frac{R}{2(1+\nu)} + \frac{2H'}{9E} (1-\nu)\bar{\sigma}^2 & \end{Bmatrix} \quad (D-4)$$

$$\text{where } P = \frac{2H'}{9E} \bar{\sigma}^2 + \frac{\tau_{xy}^2}{1+\nu}, \quad Q = R + 2(1-\nu^2)P, \quad R = \sigma_x'^2 + 2\nu\sigma_x'\sigma_y' + \sigma_y'^2, \\ \frac{2}{3} \bar{\sigma}^2 = \sigma_x'^2 + \sigma_y'^2 + 2\gamma_{xy}^2, \quad H' = d\bar{\sigma}/d\bar{\epsilon}_p .$$

The primes indicate the deviatoric components of stress. The plastic strain increment,  $d\bar{\epsilon}_p$ , and the transverse strain,  $d\epsilon_z$ , are given by

$$\begin{aligned}
d\bar{\epsilon}_p &= \frac{2\bar{\sigma}}{3Q} [\sigma'_x + \nu\sigma'_y] d\epsilon_x + (\sigma'_y + \nu\sigma'_x) d\epsilon_y + (1 - \nu) \tau_{xy} d\gamma_{xy} \\
d\epsilon_z &= -\frac{\nu}{E} (d\sigma_x + d\sigma_y) - \frac{d\bar{\epsilon}_p}{2\bar{\sigma}} (\sigma_x + \sigma_y)
\end{aligned}
\tag{D-5}$$

With the above relations, the stresses in the element can be related to the nodal point displacements. The stresses acting across the sides of the element are replaced by equivalent nodal force vectors,  $\{f\}$ , so that

$$\{f\} = [F] \{\sigma\}, \tag{D-6}$$

where the matrix  $F$  is a function only of the nodal point coordinates. The net result of the above is a relationship between nodal displacements and forces by an elemental stiffness matrix  $[k]$ ,

$$\{f\} = [k] \{v\}. \tag{D-7}$$

The element force-displacement equations for all of the elements are combined to give a set of linear equations with the nodal point displacements as unknowns.

In treating the transition of element response from elastic to plastic behavior, the "partial stiffness" approach of Marcal and King<sup>(1)</sup> is utilized. Loadings may be applied in an arbitrary sequential fashion to represent loading cycles imposed on fasteners under service conditions. This general capability required modification of an existing elastic-plastic finite-element program to permit specification of multiple load states as input data. For each load state, an incremental procedure is followed to follow the course of plastic deformation from one load state to the next. Special numerical procedures were developed to perform appropriate checks at the onset of each change in load state to determine which elements undergo elastic unloading and which elements continue to yield. The procedure applies a small perturbation to the loading and an elastic analysis is performed to determine whether the von Mises effective stress increases or decreases as a result of the load change.

A second special feature of the computer program allows simulation of the contact conditions along surfaces such as a fastener-hole interface. The technique involves the use of a special type of element to represent the desired type of contact condition. In modeling the region of contact, pairs

---

(1) Marcal, P. V., and King, I. P., "Elastic Plastic Analysis of Two-Dimensional Stress Systems by the Finite Element Method", Int. J. Mechanical Sciences, Volume 9, 1967, pp. 143-155.

of nodal points are designated along the interface, with one node in each of the contacting materials. The coordinates of the paired nodal points are identical. These superimposed points, however, are in general allowed to displace independently, with the contact condition being imposed as a constraint through the stiffness characteristics of the special element. Thus, relative displacements normal to the contact surface can be maintained as zero, with the nodal point pairs being allowed to displace freely in the direction tangent to the contact surface. This procedure has been extended to also allow an initial clearance or interference between the contacting surfaces as well as frictional stresses along the surface.

The interfacial node and element configuration is shown in Figure D-1 along with the interaction forces. If  $u_1$  and  $u_2$  are the displacement components normal to the contact surface of adjacent nodes, the equal and opposite forces acting between these nodes are given by

$$F_n = k(u_2 - u_1) - ku_0 \quad , \quad (D-8)$$

where  $u_0$  is the initial clearance between the surfaces. The stiffness,  $k$ , is assigned by the computer program to be much larger than the nodal stiffness contributions of the adjacent elements.

The frictional forces,  $F_t$ , between adjacent nodes are treated as external loads and are determined by an iterative procedure. On the first iteration, these forces are taken to be zero. On the second and successive iterations, these forces are taken as

$$F_t = \mu F_n \quad , \quad (D-9)$$

where  $F_n$  is the normal force from the previous iteration and  $\mu$  is the coefficient of friction. This procedure was found to converge rapidly. It should be noted that the conditions of Equation (D-2) could be imposed directly on the system of equations for the nodal point displacements and the iteration process could be avoided. However, this would introduce nonsymmetric terms into the system of equations and thereby prevent the use of the highly efficient solution methods which apply to symmetric systems of linear algebraic equations.

### Three-Dimensional Finite-Element Program — MARC-CDC

Finite-element techniques for general three-dimensional problems have recently been developed to the point that computer programs can be used

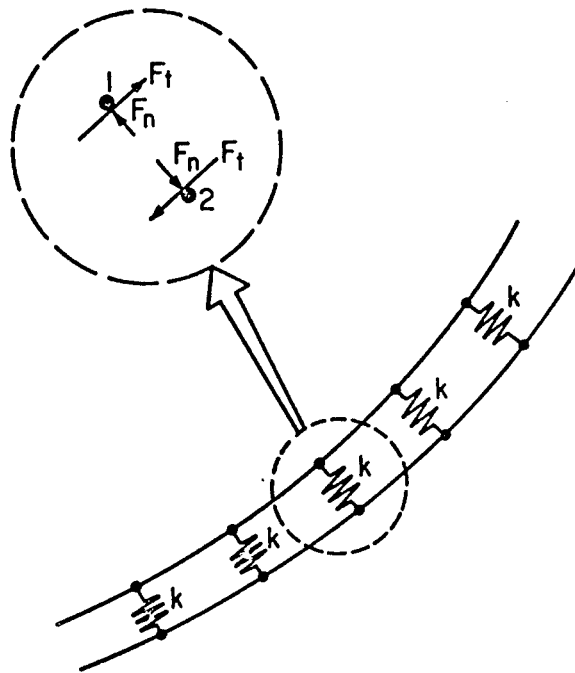


FIGURE D-1. LINEAR STIFFNESS ELEMENTS AND FRICTIONAL FORCES ACTING ON INTERFACE

to solve problems of practical importance. The code used at BCL for the analysis of three-dimensional models involving IFF's is MARC. MARC is a general purpose computer code with large finite-element libraries capable of performing linear or nonlinear analysis of structures. In particular, the 20-node isoparametric three-dimensional solid element in which the displacements are approximated by a quadric function generates highly accurate answers and may be profitably used for the analysis of three-dimensional configuration.

In MARC, plasticity is accounted for through the use of the tangent modulus incremental approach. This method is accurate when extensive deformations within the structure might arise due to the loads. The program accepts the input of experimentally derived stress-strain data in the approximate forms of either multilinear segments or power law functions like the Ramberg-Osgood representation. In the MARC code, the user can also exploit to advantage linear material behavior at the onset of load reversals by taking judiciously chosen large load increments. The program accommodates either isotropic or kinematic strain hardening. Oak Ridge National Laboratories (ORNL) constitutive

theories may also be used through a user-coded routine. This technique may also be used for cyclic-load analysis.

Restart capability is provided by the code which makes it convenient for close examination of results throughout the load incrementation process. The provision of equilibrium check is also offered by the program. Further, the program offers the multipoint constraint feature. This feature facilitates simulation of unzipping of nodes modeled along the path of a propagating crack.

MARC has efficient assembly and solution procedure choices. A block overrelaxation equation solver is also available.

### FINITE-ELEMENT MODEL STUDIES

#### Steel Fastener in 2 x 2-Inch Plate

The case of a 3/8-inch steel fastener inserted in a coupon specimen was analyzed, using the AXISOL code, for three different plate material cases. An elastic interference due to fastener insertion was modeled. Analyses for several load increments into the plastic range were performed to reach the assumed fastener interference of 0.005 inch.

In order to limit the size of the problem, the three-dimensional configuration was approximated successively by a plane model and an axisymmetric finite-element model. Preliminary results using the plane stress condition for a square coupon provided encouragement for modelling the plate by an axisymmetric grid because the edges of the plate had a negligible effect on the uniformity of stresses and strains in the circumferential direction in the vicinity of the fastener. The axisymmetric model took into account the taper of the fastener and provided valuable insight into the through-the-thickness variation of stress.

The finite-element grid for the plane stress model of the coupon consisted of 163 nodes and 141 elements and is shown in Figure D-2. The coupon was assumed to be a 2 x 2-inch plate. Due to symmetry, only one quarter of the geometry was modelled. The outer edge of the plate was assumed to be free of any restraints. Two sets of nodes on the interface were used in the model to represent the fastener and the plate and to allow relative sliding between them. The interference load was applied incrementally with the first increment corresponding to incipient yield in one of the elements around the fastener.

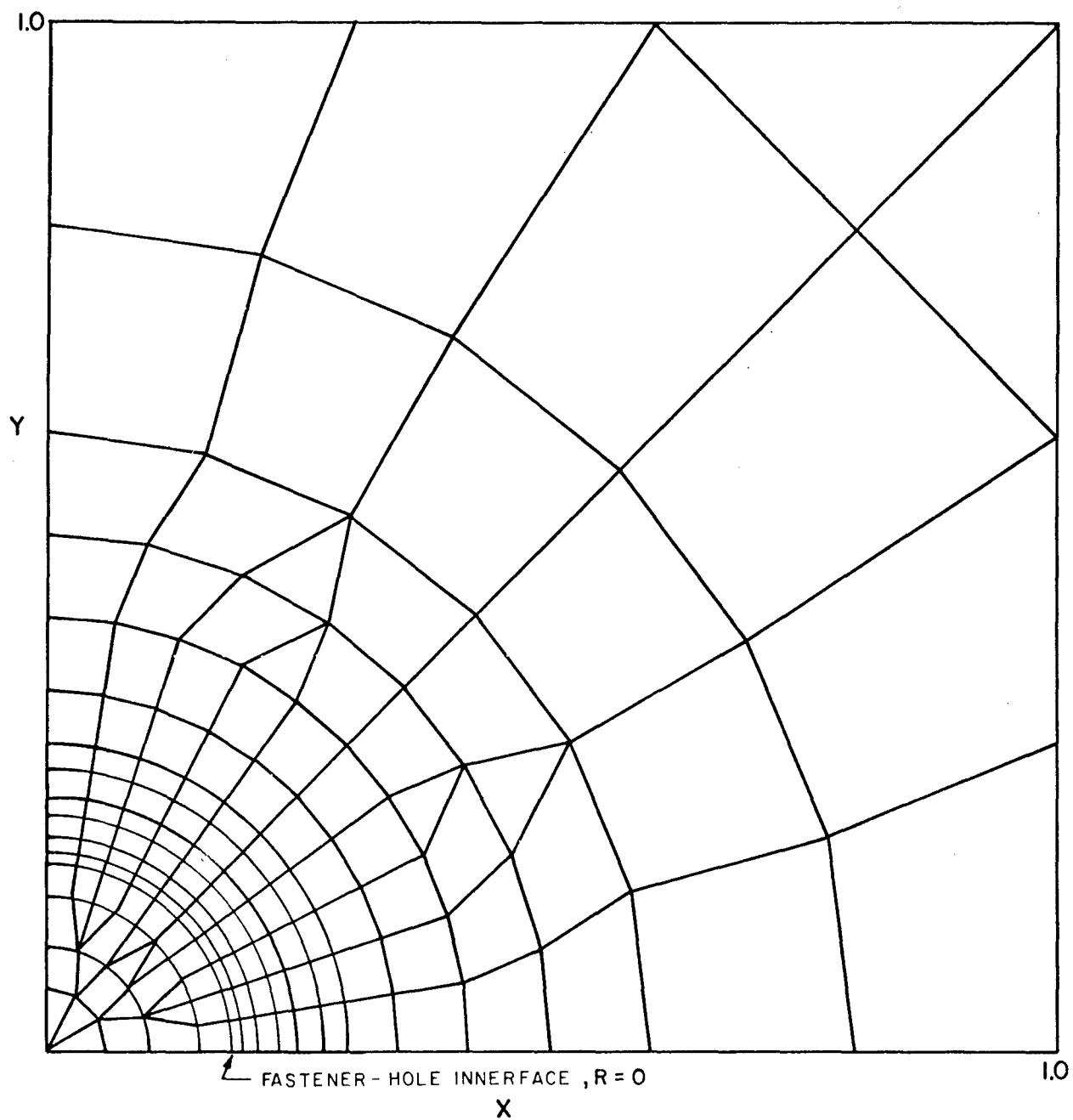


FIGURE D-2. FINITE-ELEMENT GRID OF ONE QUARTER OF A 2 x 2-INCH PLATE

Thereafter, the load was incremented in steps up to a maximum value corresponding to a diametral interference of 0.005 inch.

The material properties of the plate were successively assumed as those corresponding to 7075-T6 aluminum alloy, Fe-3Si silicon steel, and 6Al-4V titanium alloy. The stress-strain curves for the materials were assumed as bilinear. The yield stress values for these three materials were assumed to be 69,800, 62,000 and 134,000 psi, respectively. Correspondingly, the ratios of the plastic modulus divided by the elastic modulus, which are measures of the strain hardening of the materials, were assumed as 0.011, 0.0073, and 0.012.

The variations of von Mises stresses and the equivalent plastic strains as a function of distance along R (see Figure D-2) from the fastener-plate interface obtained for the plane stress model have been plotted in Figures D-3, D-4, and D-5, respectively, corresponding to the three material cases.

#### Edge Effects

In order to evaluate the interaction of the plate edges and the localized high stress region around the fastener, a 6 x 6-inch plate was modelled in a plane stress condition. The AXISOL finite-element mesh consisted of 208 nodes and 180 elements--constructed by adding nodes and elements in the expanded region of the mesh shown in Figure D-2. The plate material was 6Al-4V titanium. Two cases of elastic-plastic analyses were performed for this geometrical and material configuration. In the first case, the outer boundary of the plate was assumed as unconstrained. The stress and strain values for increasing distance from the fastener interface is shown in Figure D-6 for various interference load values. As before, these values have been plotted along one of the principal axes of the plate.

Figure D-7 shows the effect of clamping the outer edges of the (6 x 6-inch) 6Al-4V titanium plate with a steel fastener. Comparison of Figures D-5, D-6, and D-7 indicates that the stress and strain distribution around the fastener in a coupon specimen is local in character and rather insensitive to external boundary conditions or the size of the square plate.

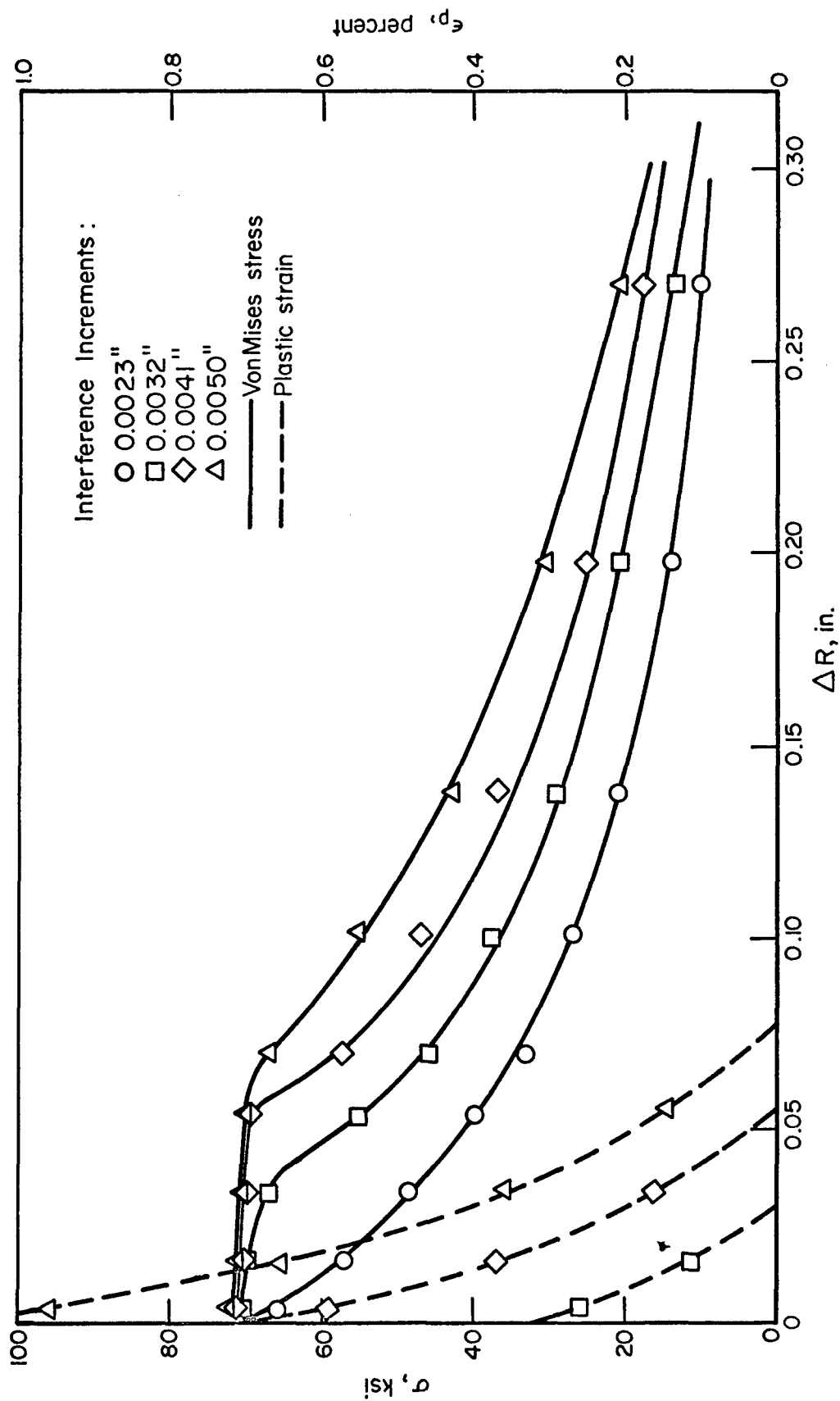


FIGURE D-3. 3/8-INCH-DIAMETER STEEL FASTENER IN 2x2x1/2-INCH ALUMINUM PLATE

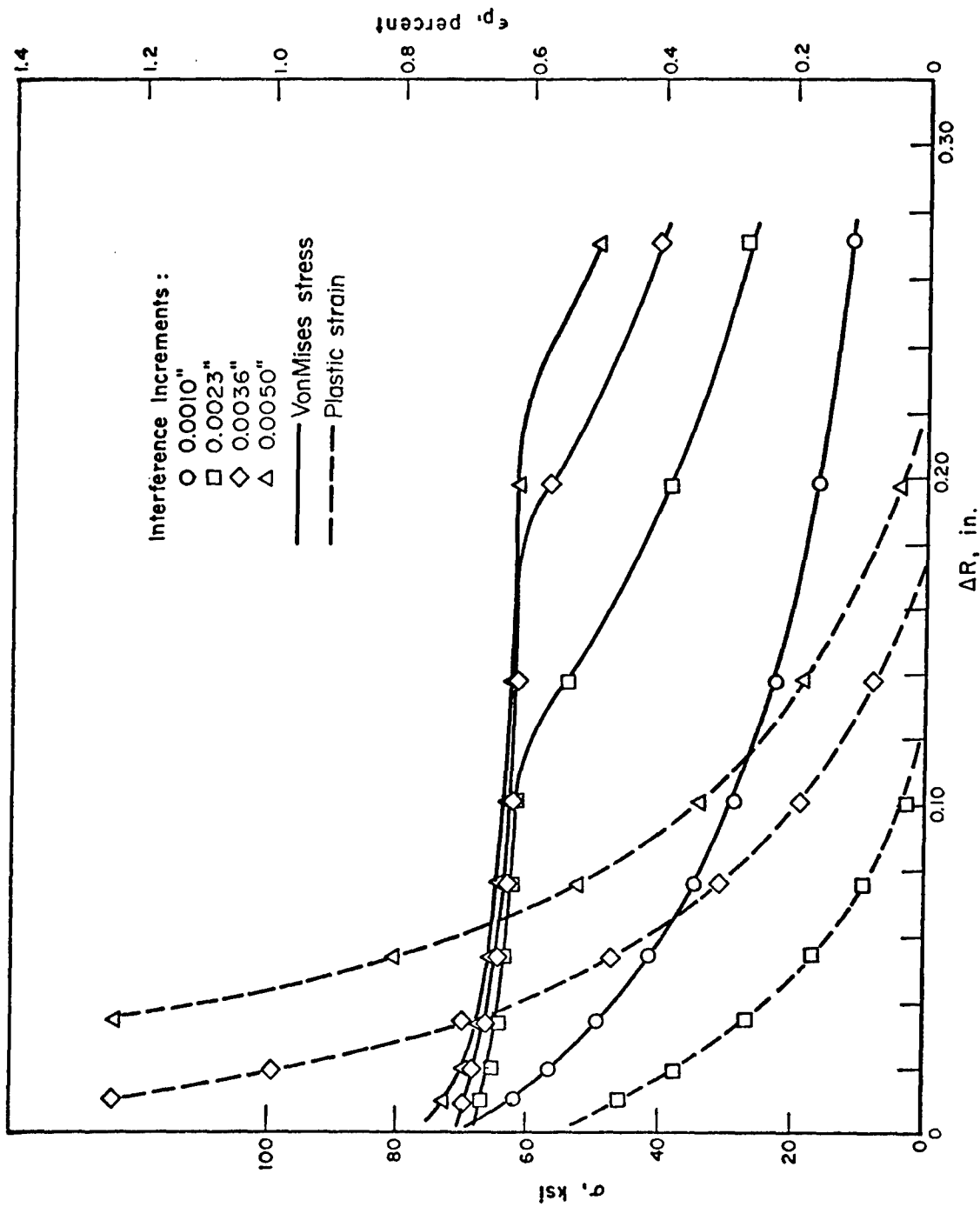


FIGURE D-4. 3/8-INCH-DIAMETER STEEL FASTENER IN 2x2x1/2-INCH Fe-3Si PLATE

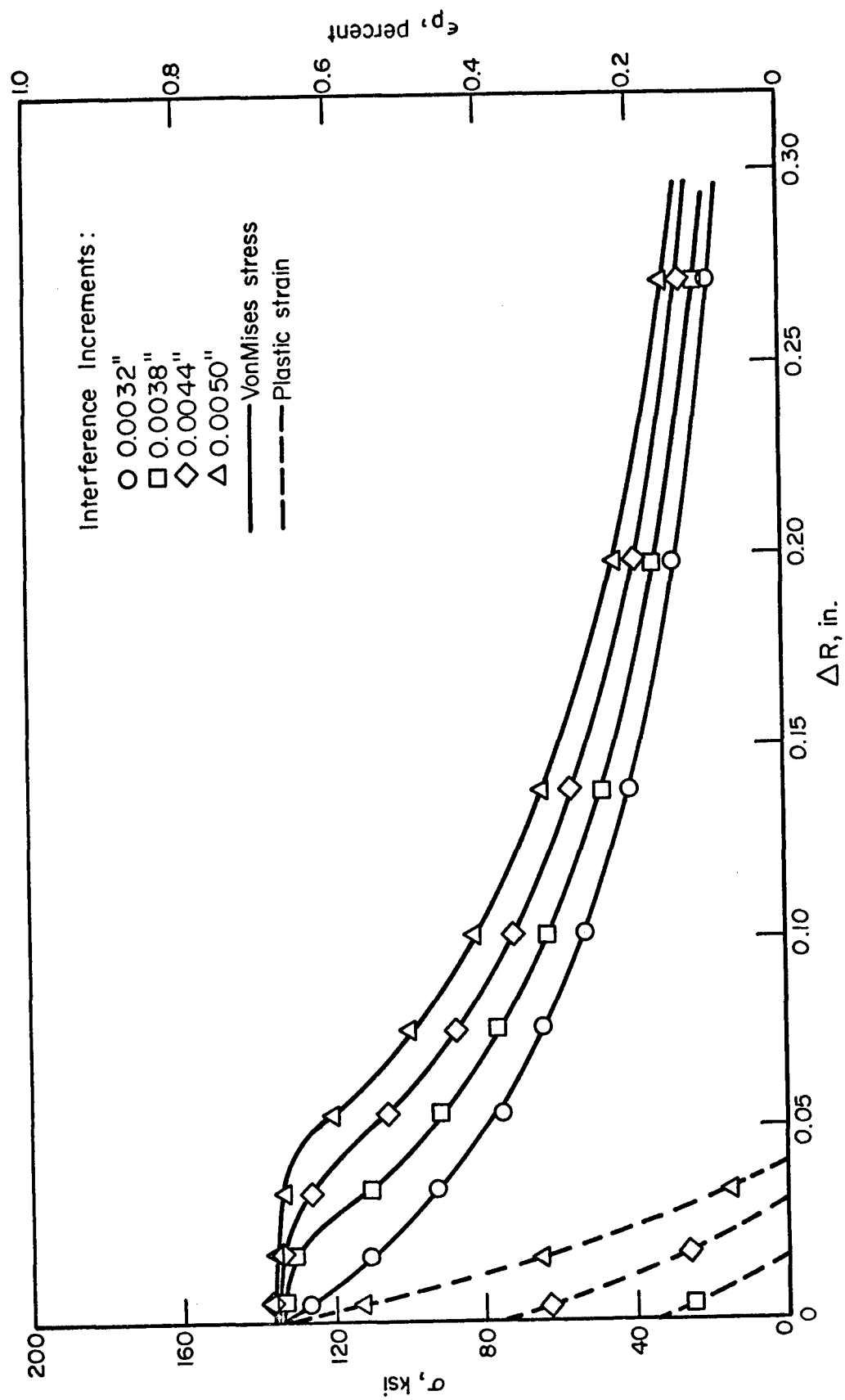


FIGURE D-5. 3/8-INCH-DIAMETER STEEL FASTENER IN 2x2x1/2-INCH TITANIUM PLATE

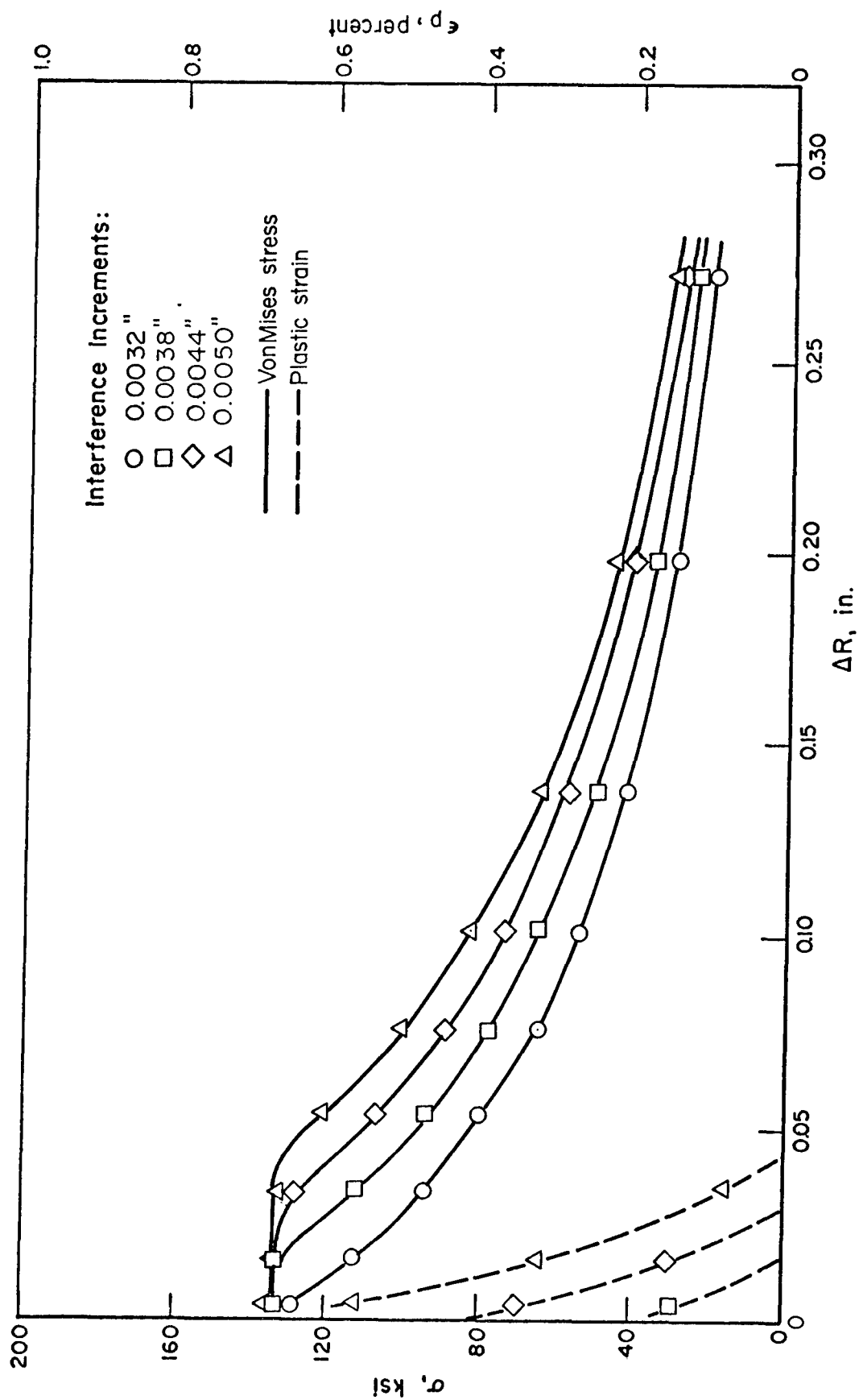


FIGURE D-6. 3/8-INCH-DIAMETER STEEL FASTENER IN 6x6x1/2-INCH TITANIUM PLATE - EDGES FREE

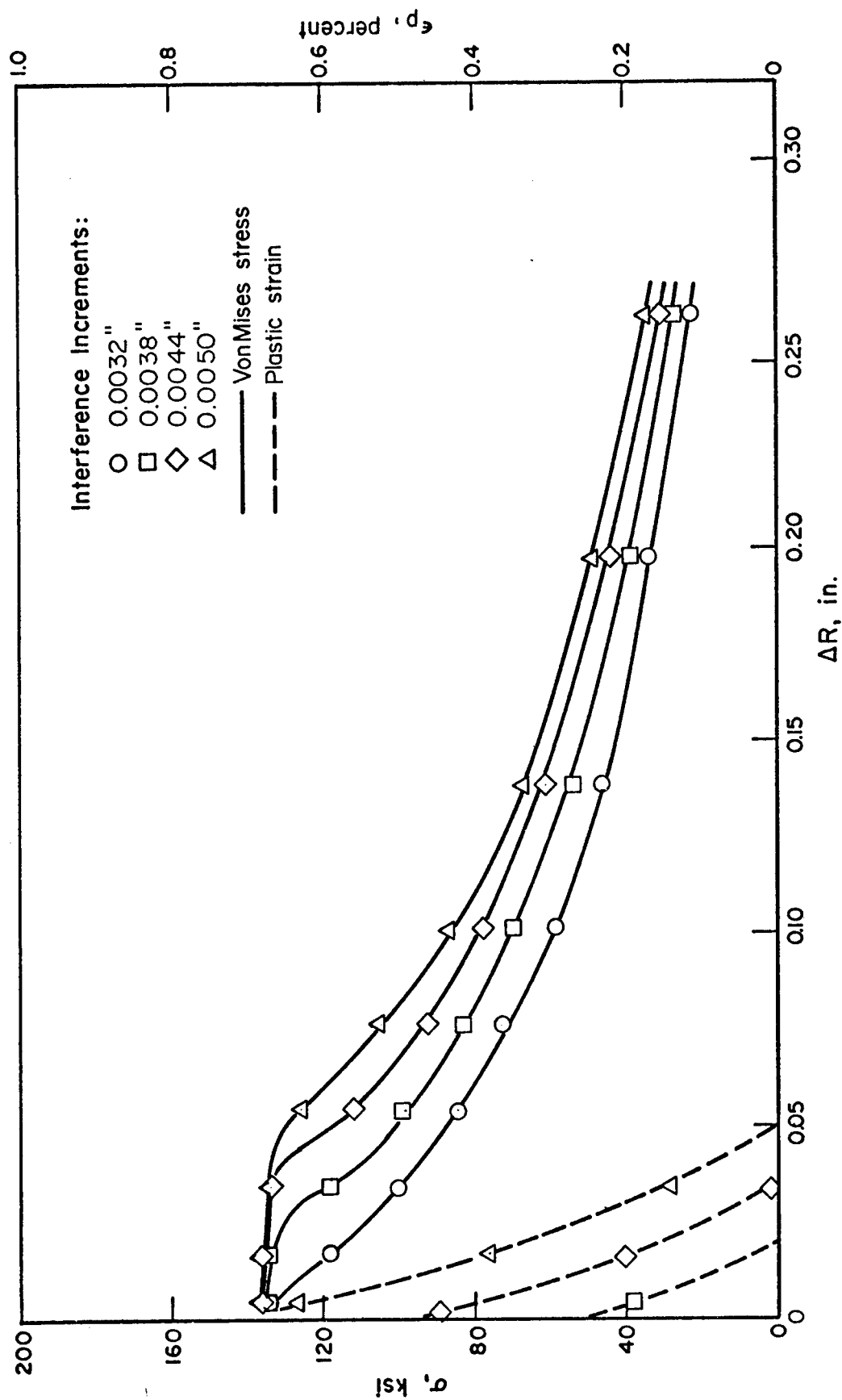


FIGURE D-7. 3/8-INCH-DIAMETER STEEL FASTENER IN 6x6x1/2-INCH TITANIUM PLATE - EDGES CLAMPED

### Axisymmetric Disk

Based on the above conclusion, the coupon specimen was also modelled as an axisymmetric disk in order to study the variation of stress through the thickness of the plate. The AXISOL finite-element grid consisted of 312 nodes and 275 elements as shown in Figure D-8. The fastener was assumed to have a taper of 1/50 along its length with the hole in the plate having a matching taper. Dual nodes were modelled on the hole-fastener interface to allow for tangential displacements between the fastener and the hole surface. Similar to the plane stress case, the load was due to fastener interference of 0.005 inch in the diametral direction.

The three different plate material cases (7075-T6, Fe-3Si steel, and 6Al-4V titanium) were analyzed. The steel fastener size was 3/8 inch and the plate thickness 1/2 inch. Figures D-9, D-10, D-11, and D-12 show the results obtained for the 7075-T6 plate case. Figure D-9 shows the stress distribution along the thickness of the plate in the elements interfacing the fastener. These values have not been extrapolated to the interfacial boundary but, due to the refined mesh in this vicinity, the plotted values are nearly equal to the peak values. It can be seen that the strains are greatest at or near the top of the plate, while at mid-thickness the stress is lower due to hydrostatic action. Figures D-10, D-11, and D-12 are plotted to show the variation of the von Mises stress and the equivalent plastic strain for increasing radial distance from the fastener interface. Figure D-10 shows the stresses in the elements at the bottom of the plate; Figure D-11, the stresses at mid-thickness of the plate; and Figure D-12, the stresses at the top surface of the plate.

Similarly, Figures D-13, D-14, D-15, and D-16 and Figures D-17, D-18, D-19, and D-20 have been plotted for the Fe-3Si steel and 6Al-4V titanium plate cases, respectively.

It should be noted that the plastic strains near the top of the plate are substantially higher for the aluminum and titanium specimens than for the Fe3Si steel specimen. This may be explained by the fact that the Fe-3Si specimen has a modulus of elasticity equal to the fastener whereby the aluminum and titanium specimens have moduli substantially lower than the fastener, thus causing larger displacements at the free surface.

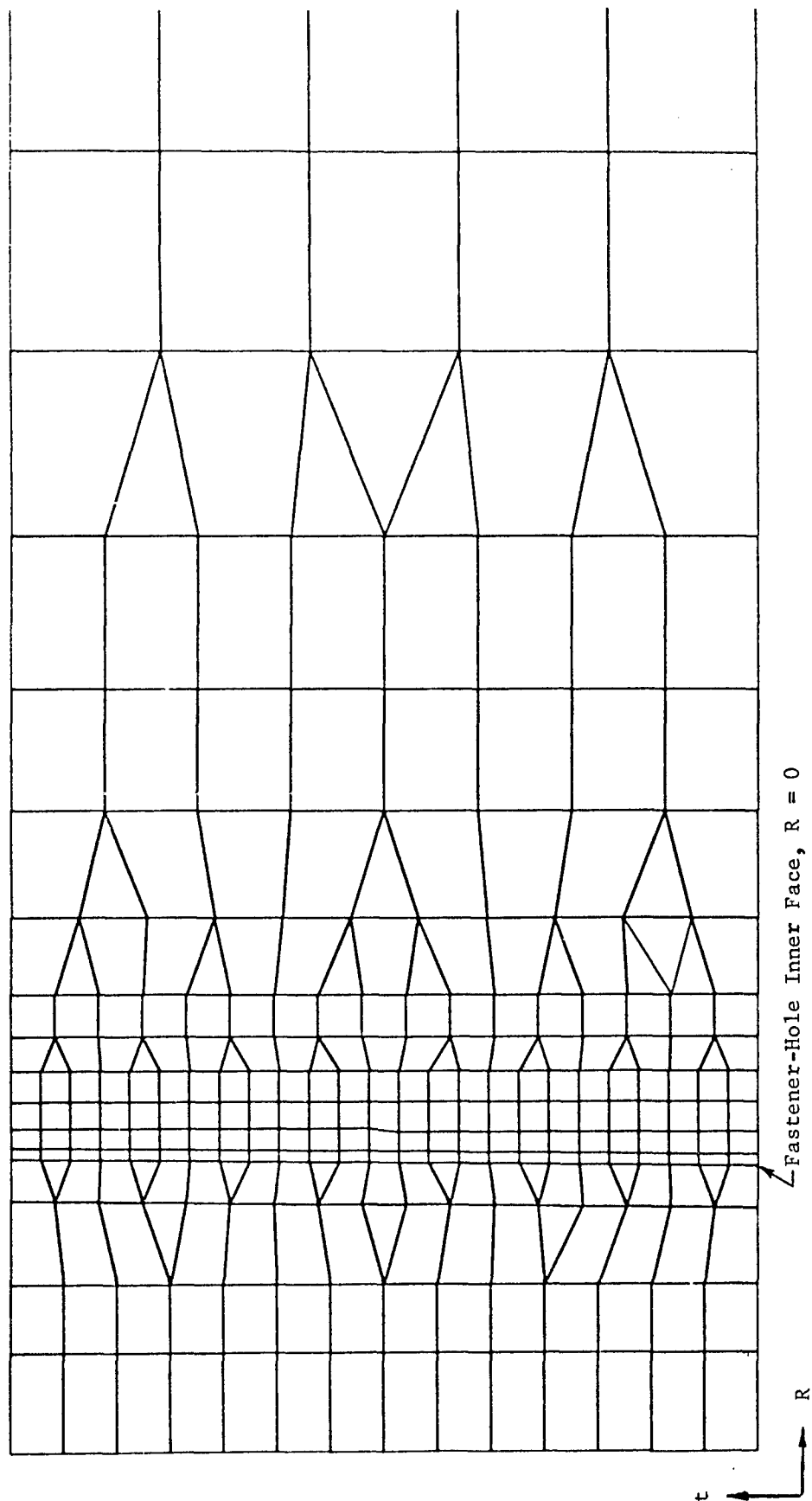


FIGURE D-8. FINITE-ELEMENT GRID THROUGH THE THICKNESS OF AXISYMMETRIC DISK

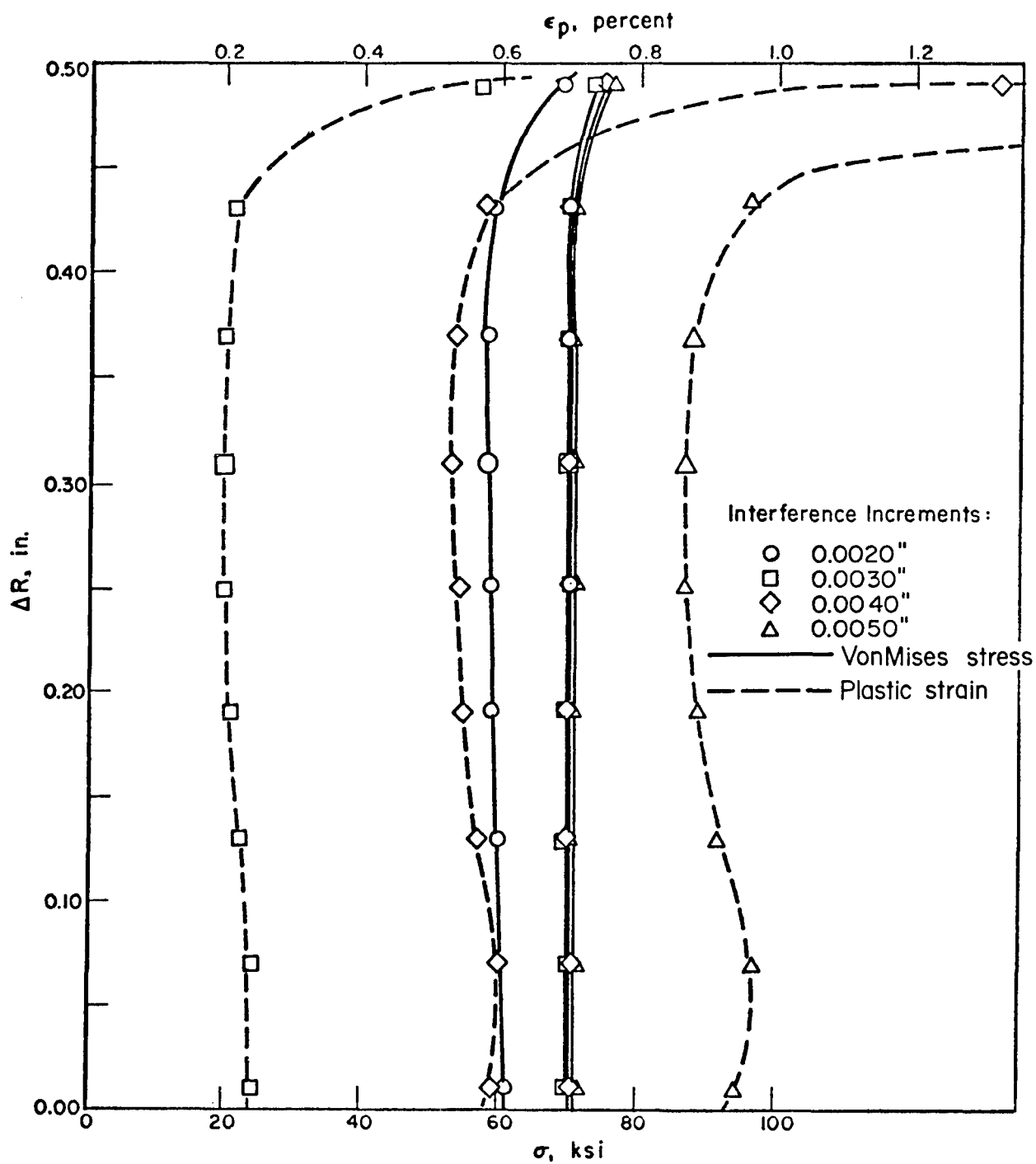


FIGURE D-9. 3/8-INCH-DIAMETER STEEL FASTENER IN 2-INCH-DIAMETER ALUMINUM DISK — STRESS AND STRAIN AT FASTENER AT HOLE INTERFACE

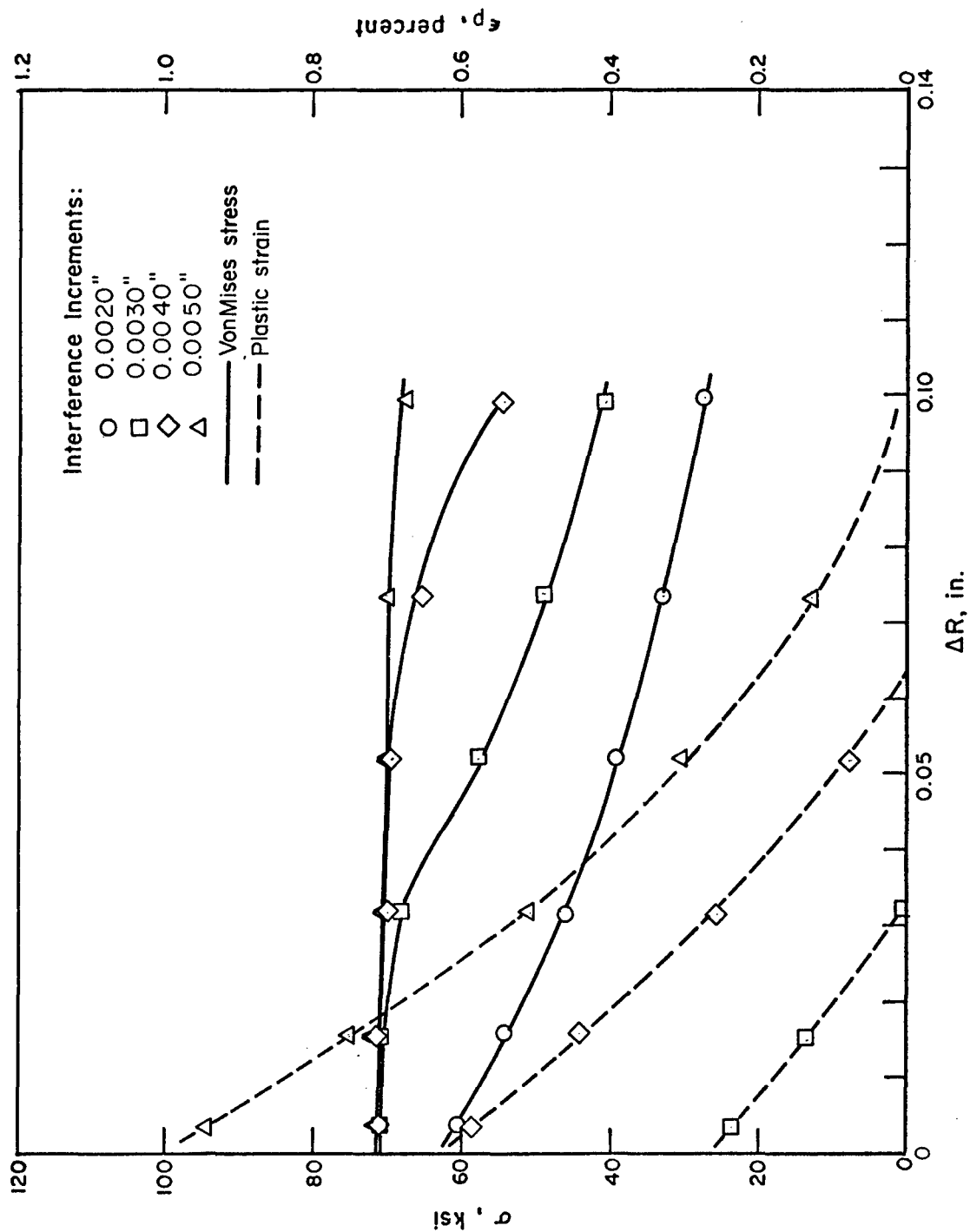


FIGURE D-10. 3/8-INCH-DIAMETER STEEL FASTENER IN 2-INCH-DIAMETER ALUMINUM DISK - STRESS AND STRAIN ALONG BOTTOM SURFACE

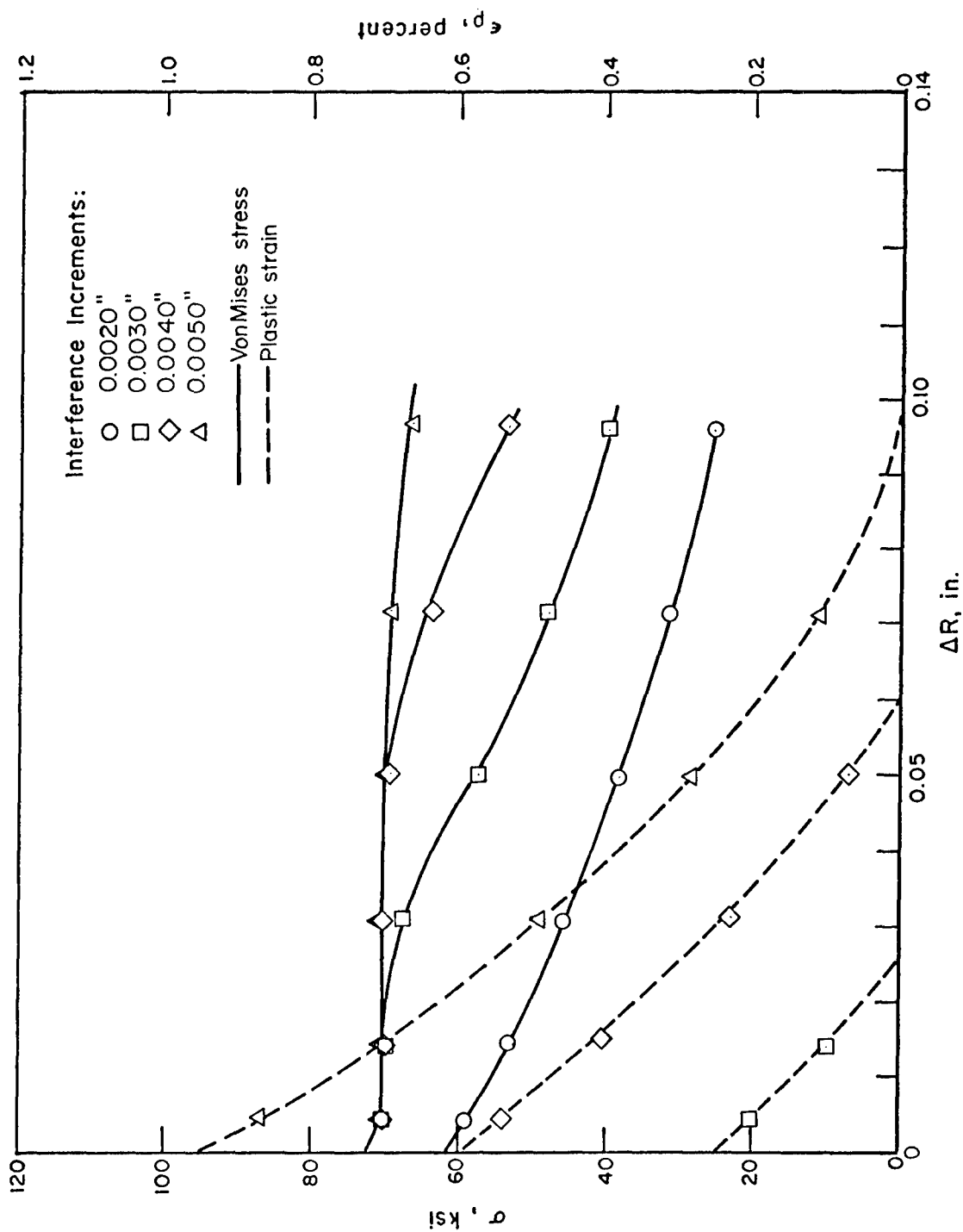


FIGURE D-11. 3/8-INCH-DIAMETER STEEL FASTENER IN 2-INCH-DIAMETER ALUMINUM DISK - STRESS AND STRAIN AT MID-THICKNESS

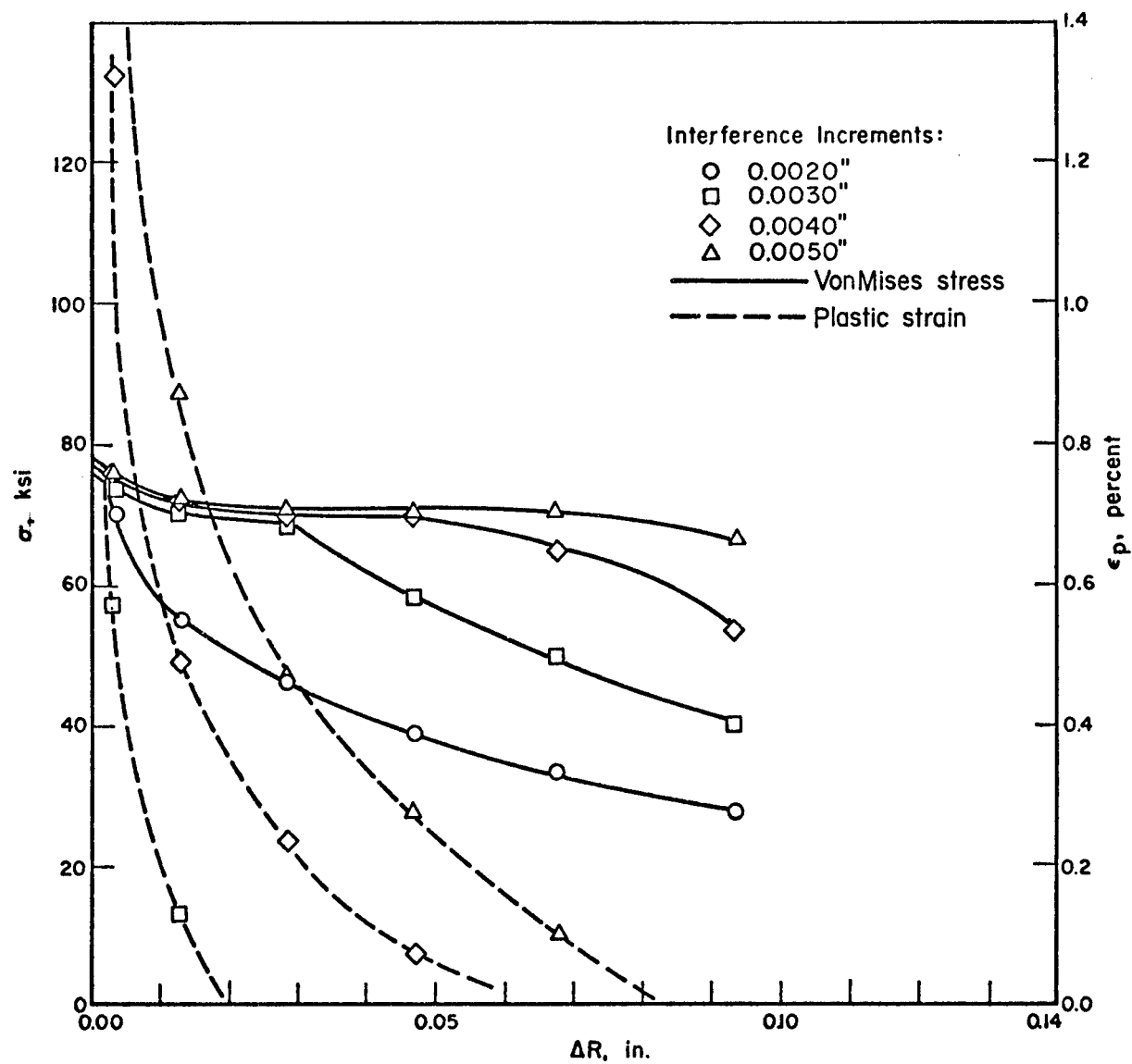


FIGURE D-12. 3/8-INCH-DIAMETER STEEL FASTENER IN 2-INCH-DIAMETER ALUMINUM DISK - STRESS AND STRAIN ALONG TOP SURFACE

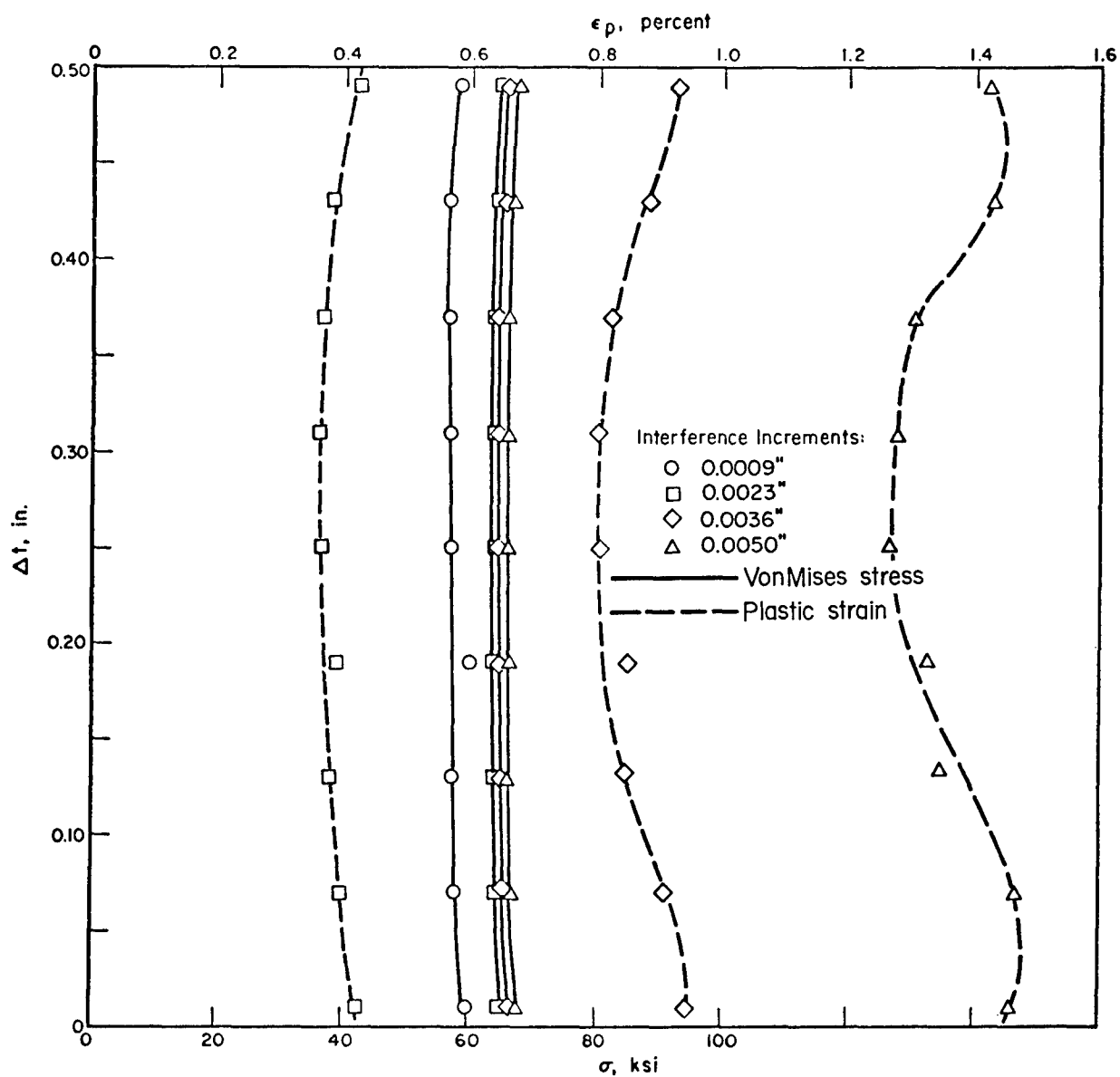


FIGURE D-13. 3/8-INCH-DIAMETER STEEL FASTENER IN 2-INCH-DIAMETER Fe-3Si DISK — STRESS AND STRAIN AT FASTENER-HOLE INNERFACE

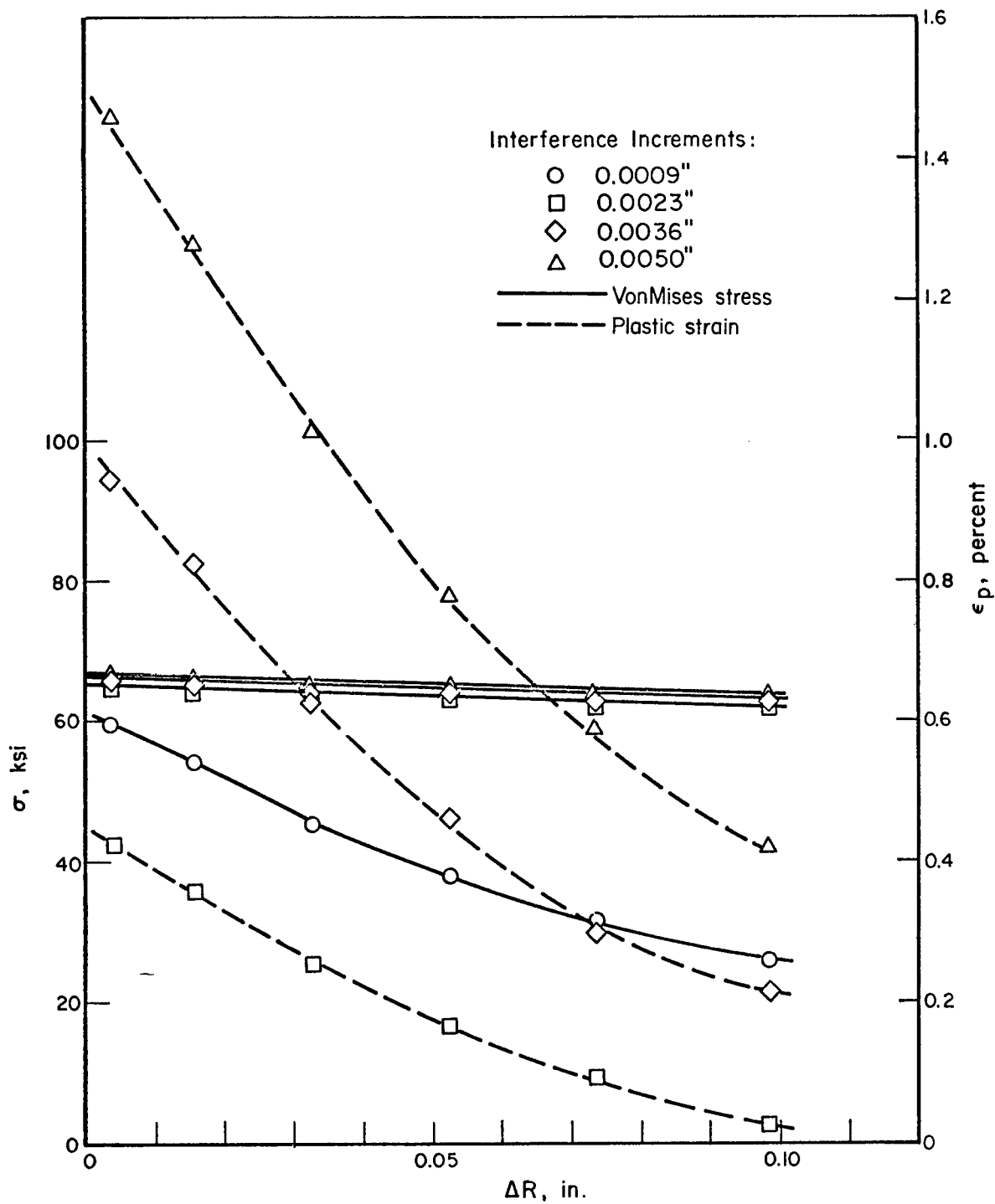


FIGURE D-14. 3/8-INCH-DIAMETER STEEL FASTENER IN 2-INCH-DIAMETER Fe-3Si DISK - STRESS AND STRAIN ALONG BOTTOM SURFACE

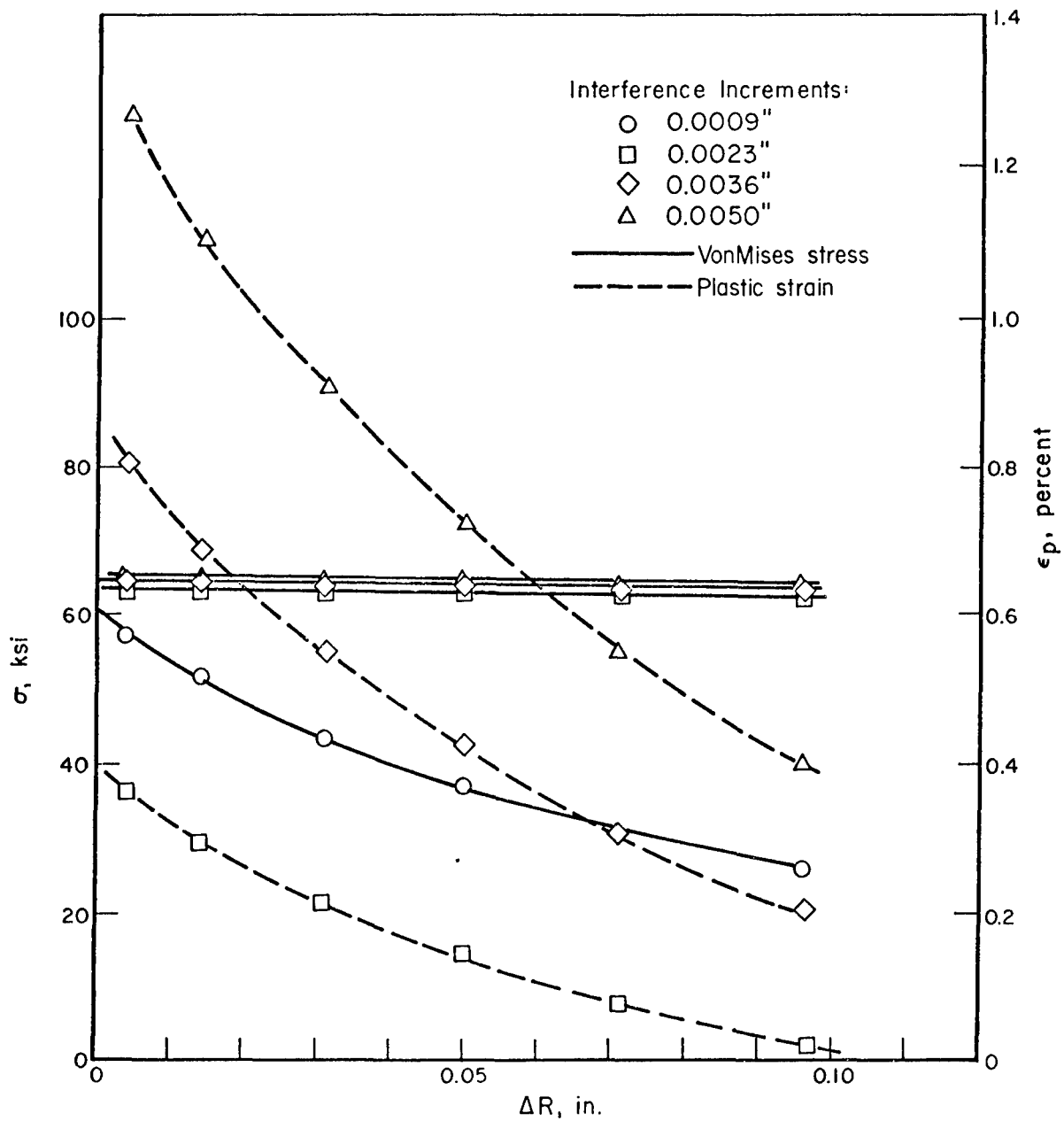


FIGURE D-15. 3/8-INCH-DIAMETER STEEL FASTENER IN 2-INCH-DIAMETER Fe-3Si DISK -- STRESS AND STRAIN AT MID-THICKNESS

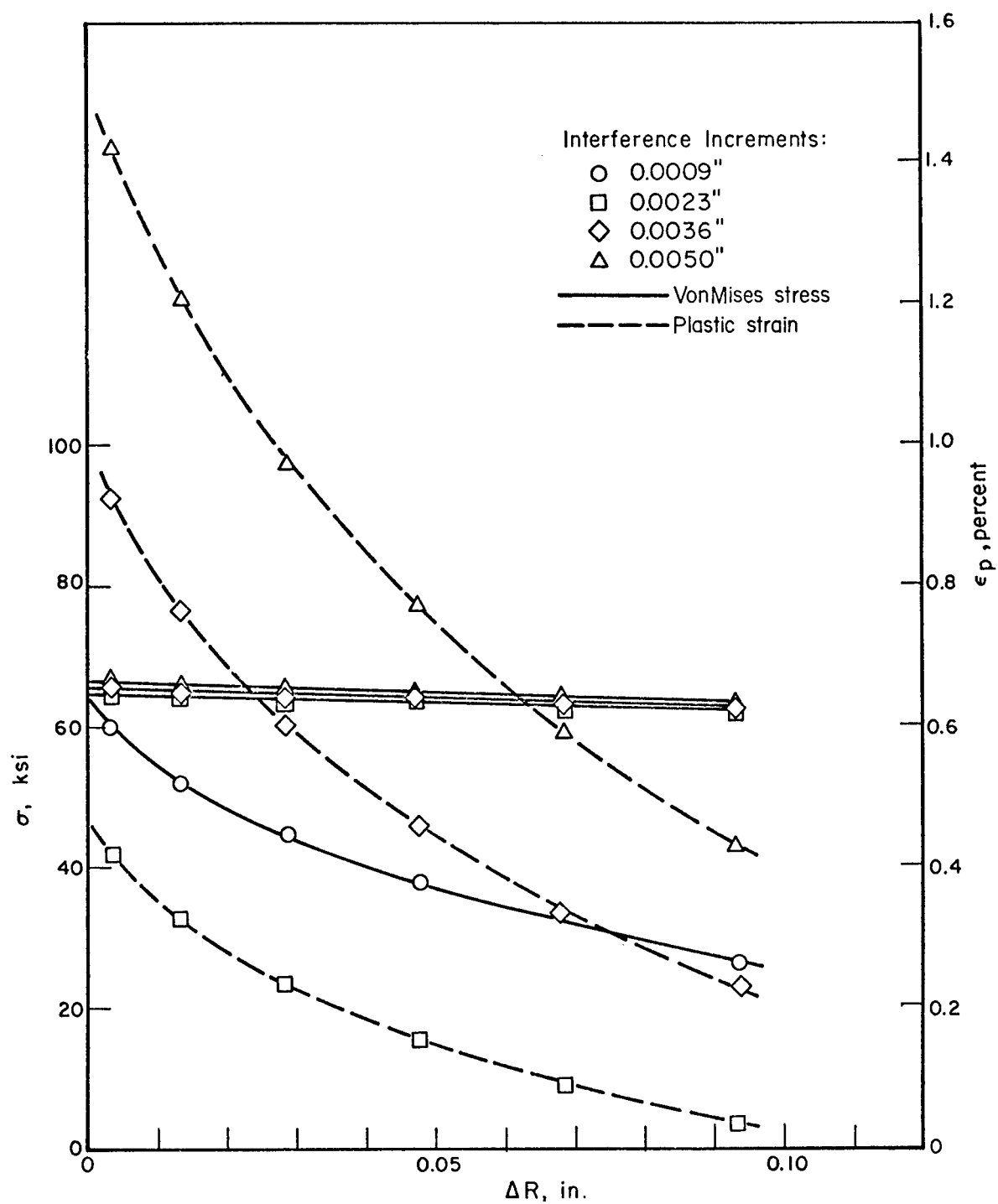


FIGURE D-16. 3/8-INCH-DIAMETER STEEL FASTENER IN 2-INCH-DIAMETER Fe-3Si DISK - STRESS AND STRAIN ALONG TOP SURFACE

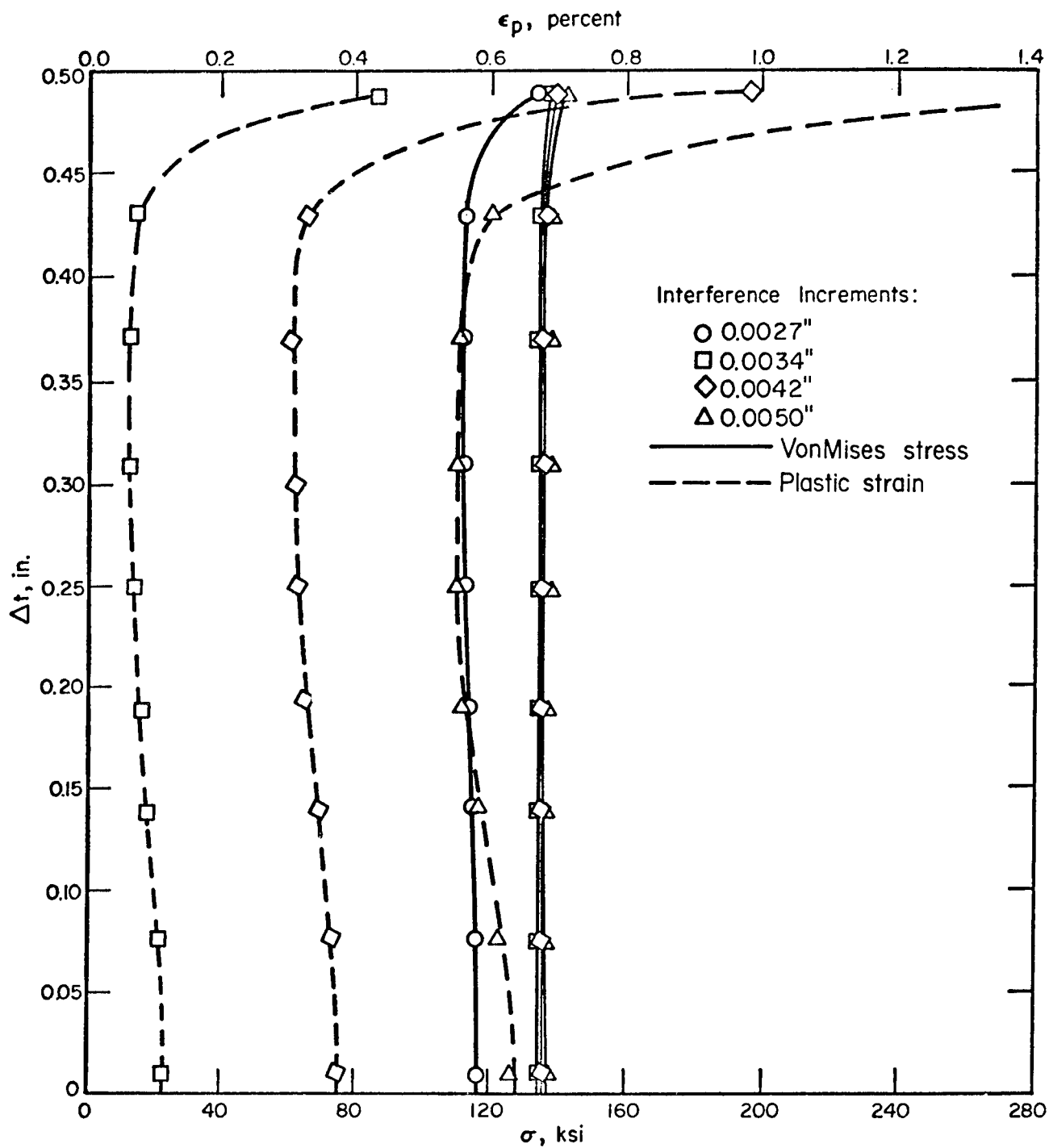


FIGURE D-17. 3/8-INCH-DIAMETER STEEL FASTENER IN 2-INCH-DIAMETER TITANIUM DISK - STRESS AND STRAIN AT FASTENER-HOLE INNERFACE

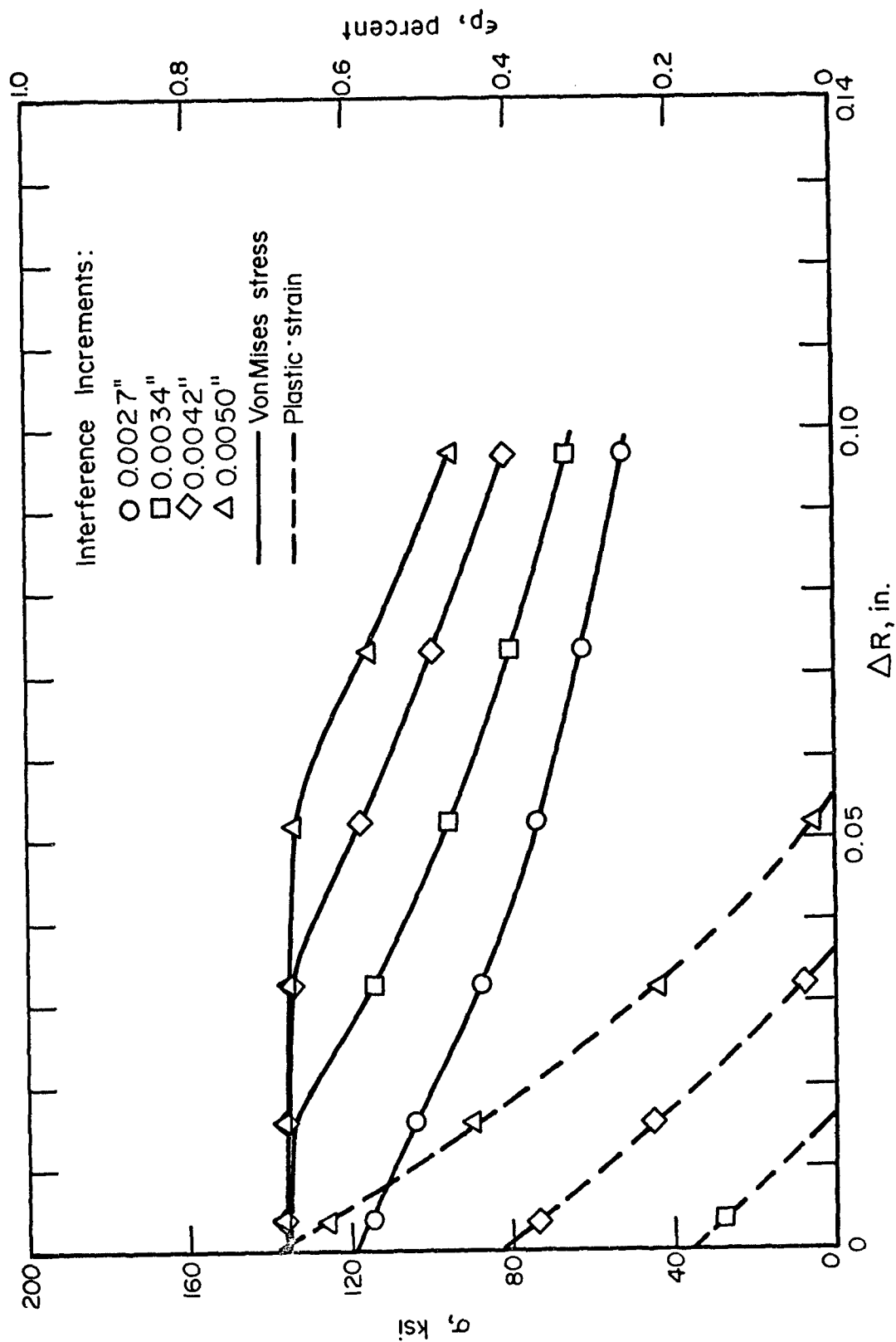


FIGURE D-18. 3/8-INCH-DIAMETER STEEL FASTENER IN 2-INCH-DIAMETER TITANIUM DISK - STRESS AND STRAIN ALONG BOTTOM SURFACE

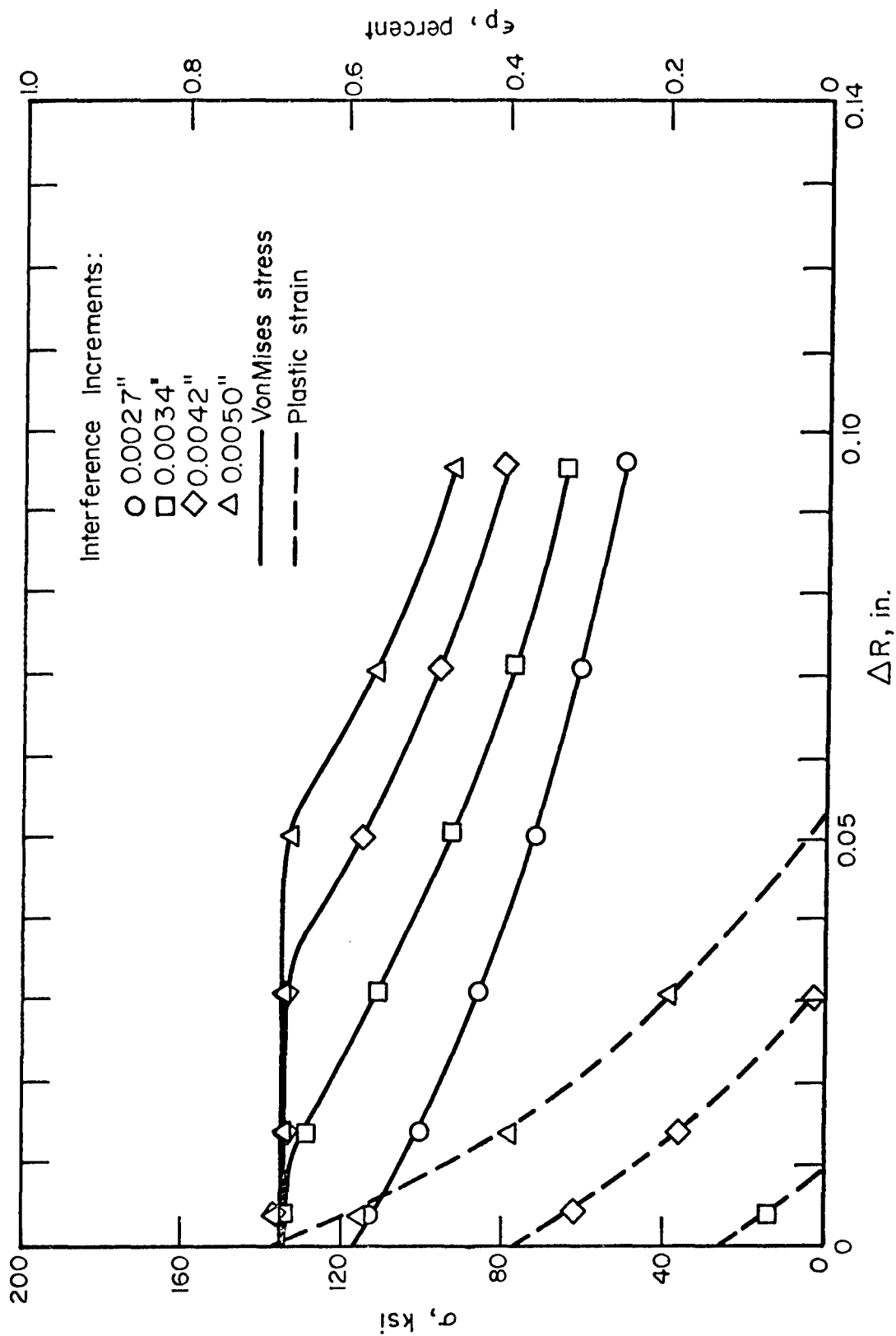


FIGURE D-19. 3/8-INCH-DIAMETER STEEL FASTENER IN 2-INCH-DIAMETER TITANIUM DISK - STRESS AND STRAIN AT MID-THICKNESS

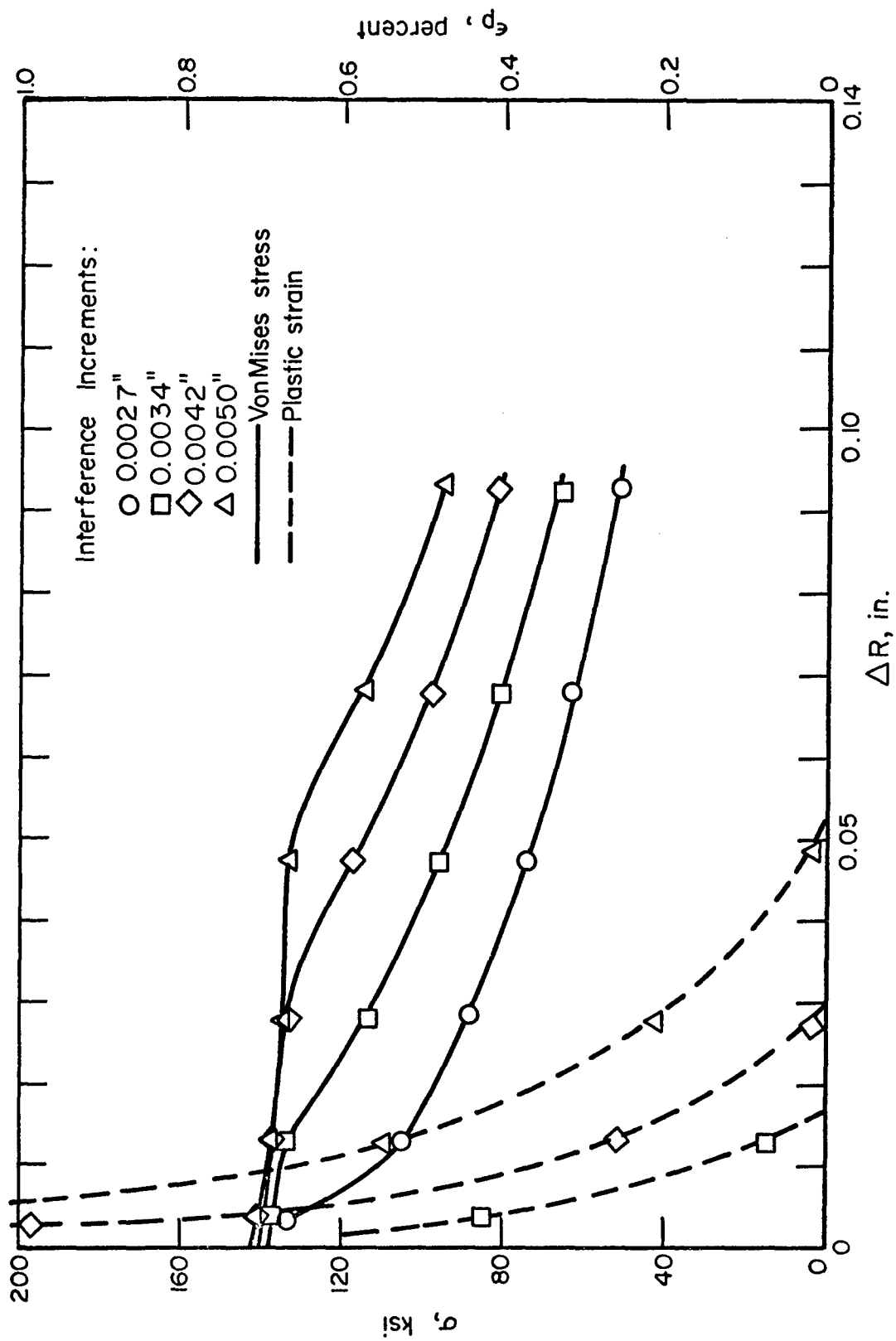


FIGURE D-20. 3/8-INCH-DIAMETER STEEL FASTENER IN 2-INCH-DIAMETER TITANIUM DISK — STRESS AND STRAIN ALONG TOP SURFACE

### MARC Elastic Plate Analysis

A fully three-dimensional elastic analysis was conducted on a 4 x 4 x 3/8-inch 7075-T6 coupon specimen with a steel fastener, using the MARC computer program. The model consisted of 450 nodes and 285 isoparametric brick elements. Due to symmetry, only one quarter of the planform of the plate was modelled. The fastener was assumed to have a taper of 1/50. The results of the analysis indicated that the stresses in the plate around the fastener are fairly constant in the circumferential direction and vary a negligible amount through the thickness of the plate. Figure D-21 shows the von Mises stresses obtained for a fastener interference of 0.0025 inch along the principal direction of the plate in the layer of elements edging the bottom, top, and mid-thickness surfaces of the plate.

### Out-of-Round Hole

The case of an elliptical hole in a square aluminum plate specimen with a 3/8-inch round oversized fastener inserted in the hole has been investigated using the node coupling capability of the AXISOL code. A plane stress condition was assumed. Due to symmetry, only one quarter of the fastener plate configuration was modelled. The finite-element grid consisted of 163 nodes and 141 elements (Figure D-2). Two sets of nodes on the interface were used in the model to represent the fastener and the plate and to allow the two surfaces to separate. The out-of-roundness of the hole was assumed to be 4 percent of the fastener diameter. Very small load increments were applied. Following each load increment, coupling of the nodes in the radial direction was made in the area where newly formed contact between the fastener and the hole was indicated. As before, the interference load was modelled by assuming thermal expansion of the fastener. The thermal load was incremented until a value corresponding to a diametral interference of 0.008 inch was reached. The growth of the contact area round one quadrant of the fastener-plate interface is shown in Figure D-22. As the figure shows, contact is achieved over an angle of approximately 45 degrees only, in spite of the high value of interference imposed. Since fastener designs usually assume a contact area of around 90 percent, control of out-of-roundness in fabrication is seen to be a very sensitive factor in fastener performance. In Figure D-23, the radial stress and the equivalent plastic strain around the

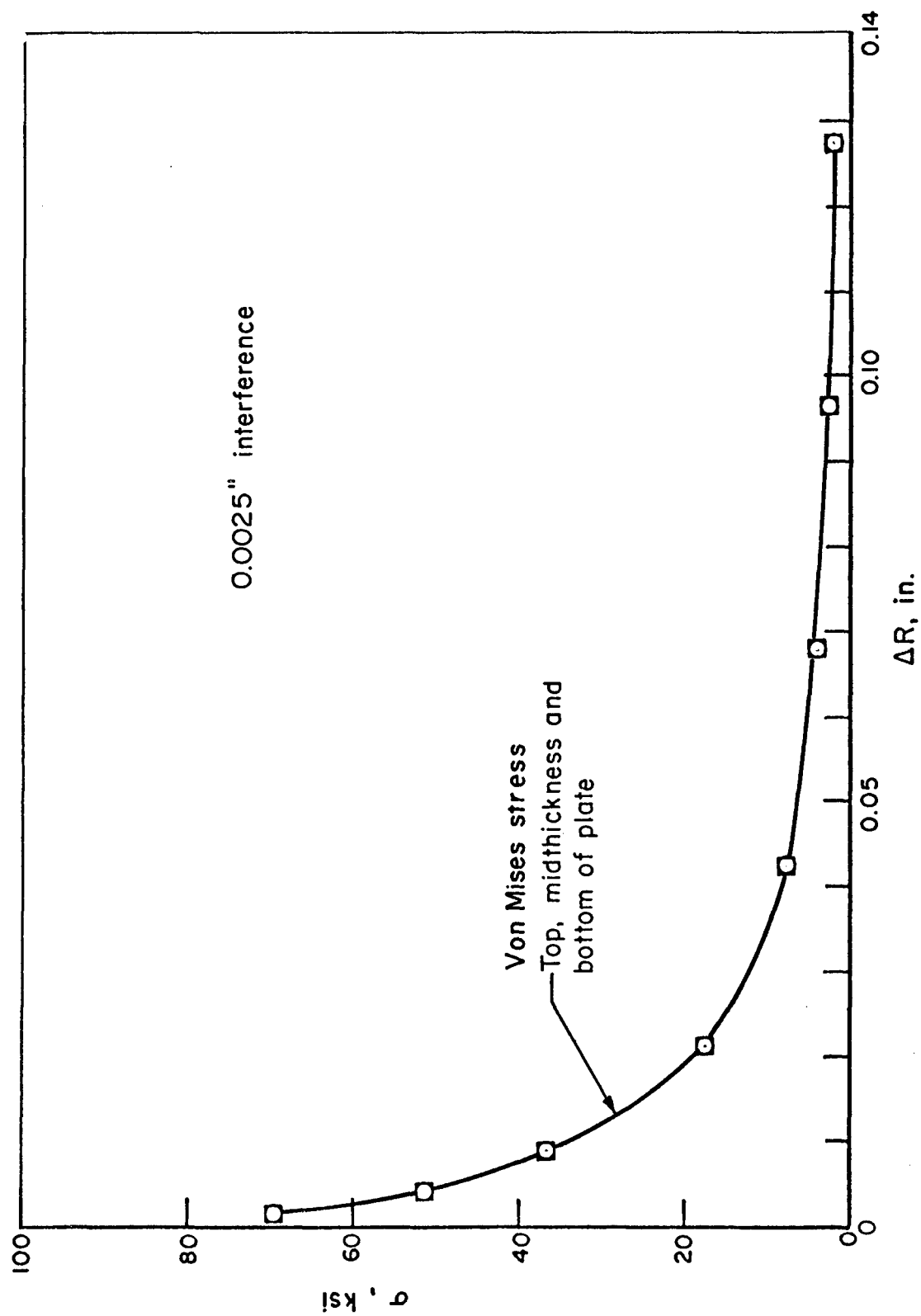


FIGURE D-21. 3/8-INCH-DIAMETER STEEL FASTENER IN 4x4x3/8-INCH ALUMINUM PLATE - 0.0025-INCH INTERFERENCE

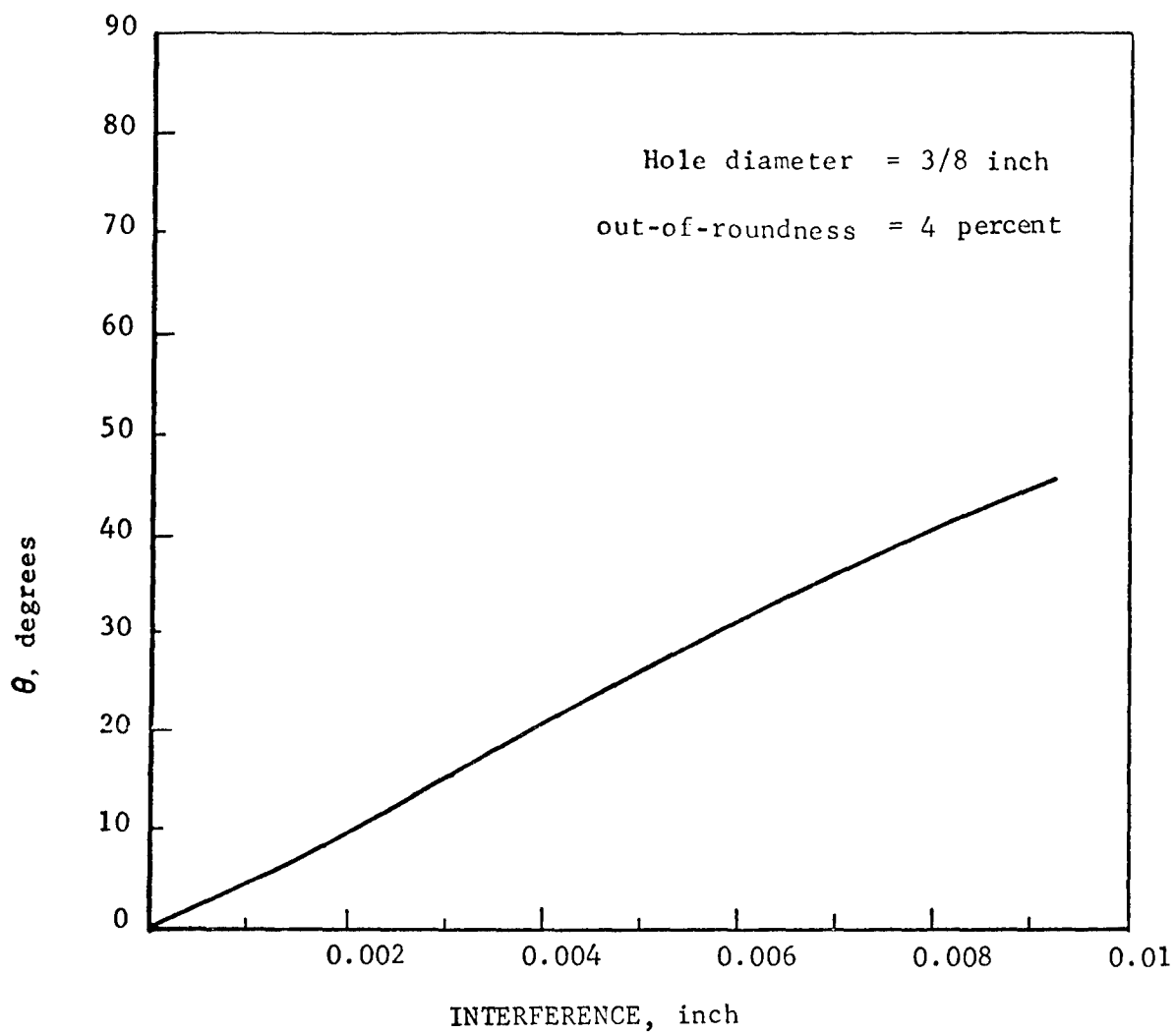


FIGURE D-22. CONTACT ANGLE ACHIEVED BETWEEN FASTENER AND OUT-OF-ROUND HOLE SURFACES FOR VARIOUS INTERFERENCES

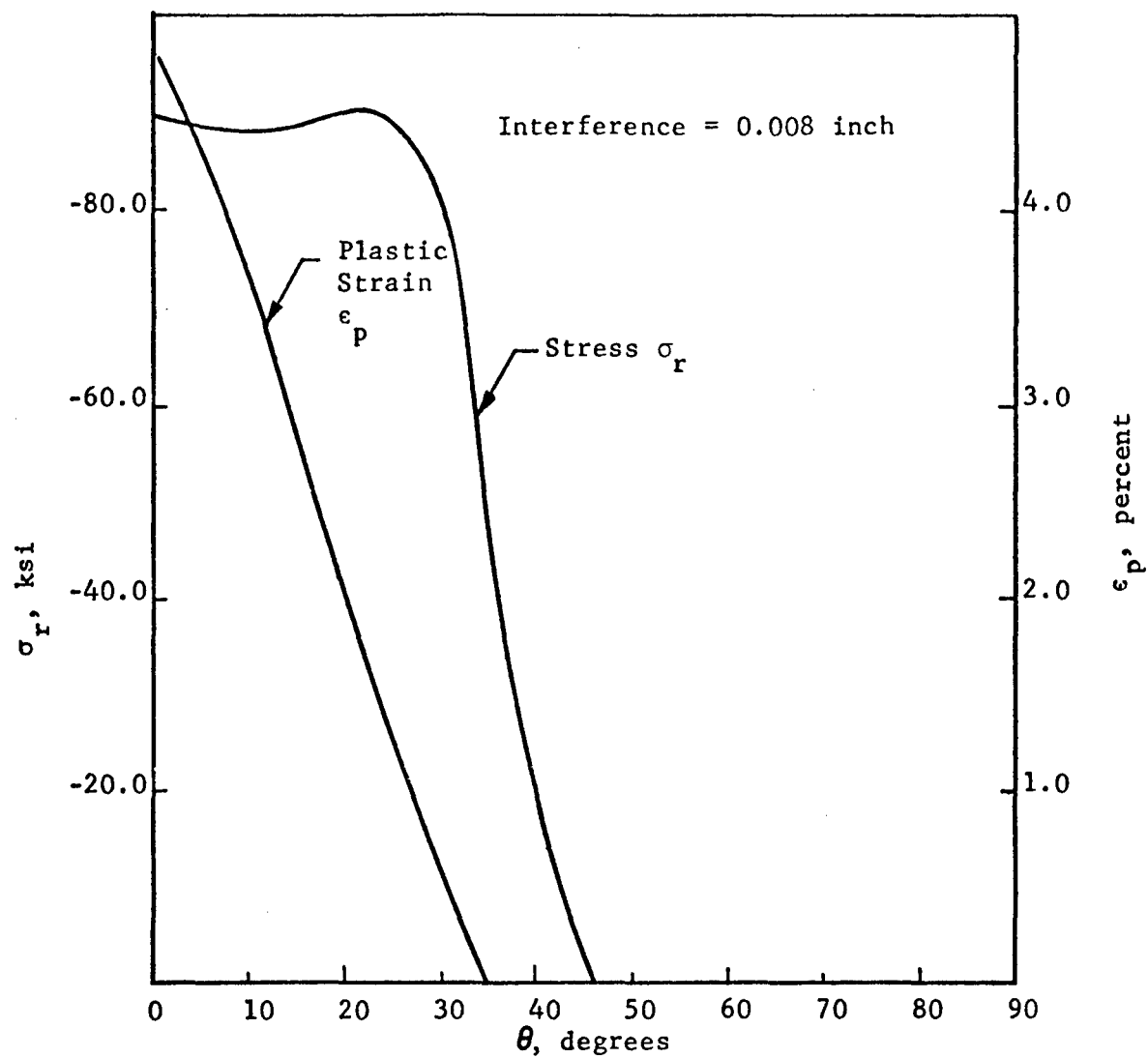


FIGURE D-23. RADIAL STRESS AND EQUIVALENT PLASTIC STRAIN AROUND EDGE OF OUT-OF-ROUND HOLE

edge of the hole in the plate have been plotted for the maximum interference value of 0.008 inch. Again the high values of stress and strain in the contacting region stem from the low area of contact.

A second case of a round fastener in an out-of-round hole was analyzed to determine the stresses and the accompanying plastic strains when the fastener interference was greater than the out-of-roundness, resulting in a snug fit of the fastener in the hole. The geometrical data for this case was drawn from metrology performed on the hole in a certain coupon specimen. The experimentally observed slight asymmetry of the hole periphery was neglected in the analytical model, so that the hole in the finite-element model had fourfold symmetry. The 6 x 6-inch coupon was assumed to be under a plane stress condition. The outer edges of the plate were assumed as clamped. The finite-element model consisted of 208 nodes and 180 elements. Figures D-24 and D-25 depict the stresses around the edge of the hole for two levels of fastener interference. The out-of-roundness of the hole is also shown in the two figures by plotting the difference between the fastener size and the value of the hole radius. As before, high local stresses and plastic strains were indicated. It is interesting to note in Figure D-24 that at the point with the least radial contact stress the von Mises stress is still high due to a large circumferential stress.

#### No-Load-Transfer Specimen, Sequentially Loaded

The case of a 3/8-inch steel fastener installed in a 1/2-inch-thick 7075-T6 aluminum alloy no-load-transfer specimen which is subsequently subjected to axial tension has been studied. A plane stress condition was assumed. Due to symmetry, only one quarter of the geometry needed to be modeled. The MARC finite-element model consisted of 287 nodes and 259 elements. Figure D-26 shows the finite-element grid in a limited region of the specimen model. Due to symmetry and the low value of axial load, a nonsliding condition was assumed at the interface of the fastener and the plate. An elastic interference (as opposed to a rigid interference) due to fastener insertion was modeled by artificially ascribing a thermal expansion to the fastener region. The first increment is the interference load which causes the specimen to reach yield. Analyses for several load increments into the plastic range were performed to reach the assumed fastener oversize of 0.005 inch. The stresses were found to be fairly constant

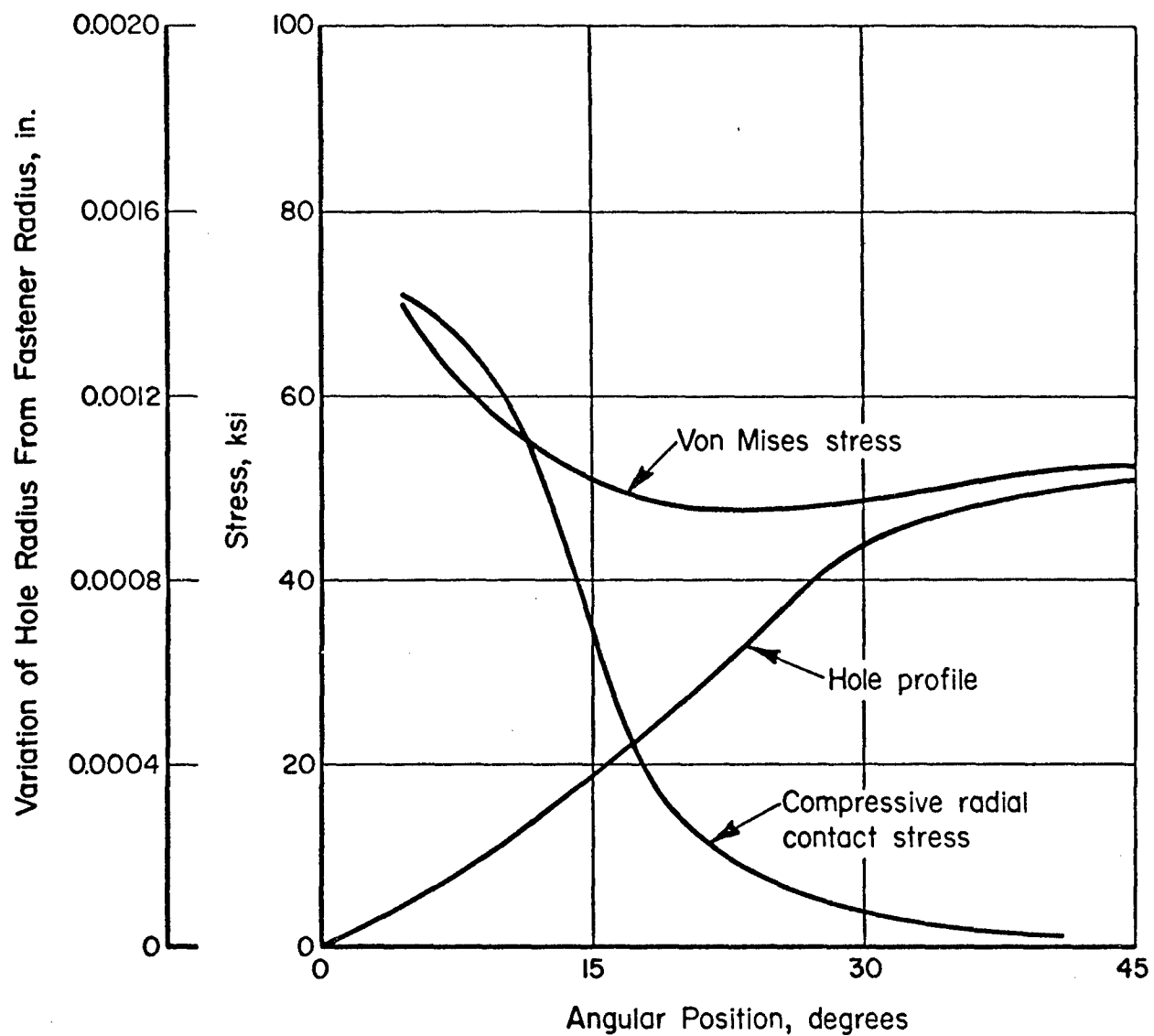


FIGURE D-24. GEOMETRY OF OUT-OF-ROUNDNESS OF HOLE AND CONTACT STRESS DISTRIBUTION AROUND THE EDGE FOR INTERFERENCE LOAD WHICH CAUSES INITIAL YIELD IN SPECIMEN; DIAMETRAL INTERFERENCE = 0.00271 INCH

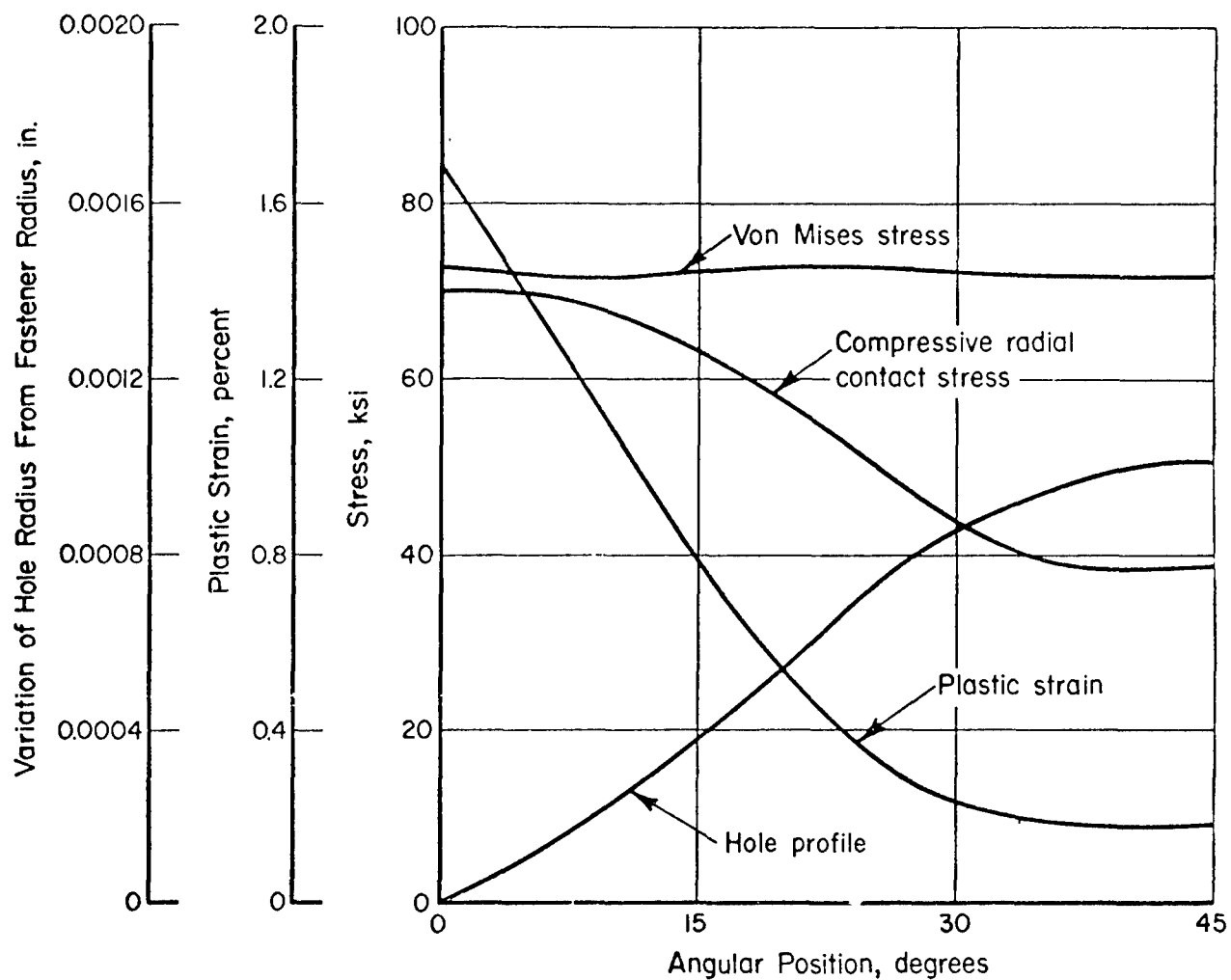
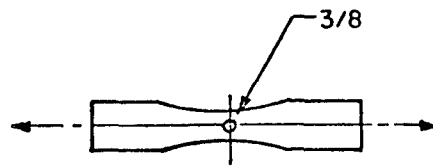


FIGURE D-25. STRESS AND PLASTIC STRAIN DISTRIBUTION AROUND THE EDGE OF OUT-OF-ROUND HOLE FOR MAXIMUM INTERFERENCE;  
DIAMETRAL INTERFERENCE  $\approx$  0.005 INCH



NO LOAD TRANSFER SPECIMEN

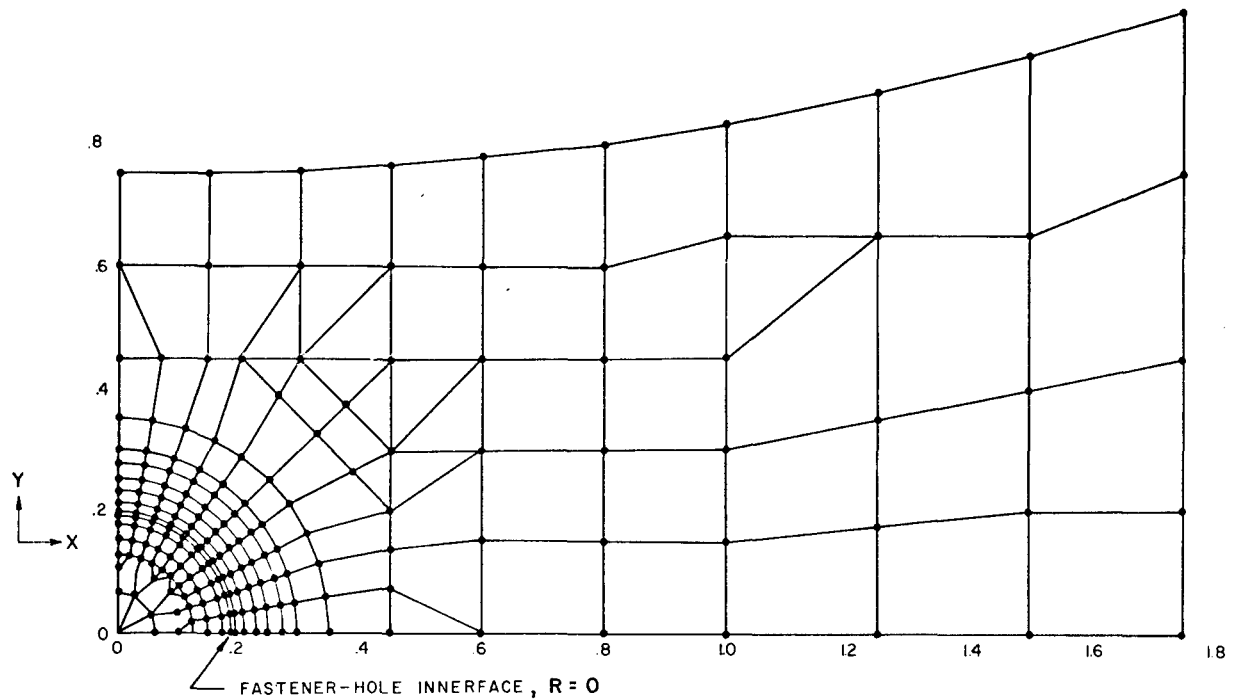


FIGURE D-26. FINITE-ELEMENT GRID OF A QUARTER SECTION OF A NO-LOAD-TRANSFER SPECIMEN

around the periphery of the hole, but the plastic strains showed a greater variation. The width of the yield zone was found to be approximately 0.08 inch for the interference of 0.005 inch. The von Mises stresses and the equivalent plastic strains have been plotted in Figures D-27 and D-28 for various levels of fastener interference.

An axial tensile stress of 12,200 psi was then applied incrementally to the ends of the specimen model. The nominal stress at the minimum cross-section corresponding to this axial loading was 32,500 psi or 47 percent of the yield stress of the material. The von Mises effective stresses and the equivalent plastic strains are plotted in Figures D-29 and D-30 as a function of the radial distance from the hole edge.

Figure D-31 shows the striking difference between the results of a sequential load type of analysis and one in which the loads are applied simultaneously. In Figure D-31, the stresses and strains in the plate are shown around the fastener interface for the two types of analyses. It is evident that the latter type of solution can grossly underestimate the residual plastic strains.

### CONCLUSIONS

The results of this portion of the program have shown that it is possible to analytically predict the stress-strain states around IFF's. However, it has also been determined that the extension from coupon specimens to fastened joints is a difficult one. In particular, node and element quantity restrictions frequently make it impossible to construct three-dimensional grids of adequate "resolution" to properly handle high gradient regions within complex models. Additionally, as reported herein, there is evidence that the finite-element results for no-load-transfer joints (and therefore, probably other more complex joints) are not in agreement with experimental data. It is conjectured that this disagreement may be due to modeling deficiencies, element shapes, the effects of compound loading, or a combination of all three.

It was intended to perfect the analytical model for the no-load-transfer joint and then extend the analysis to model both specimen loading and unloading. As noted in the body of the report, the first loading cycle appears to provide the critical data pertinent to fatigue prediction. However,

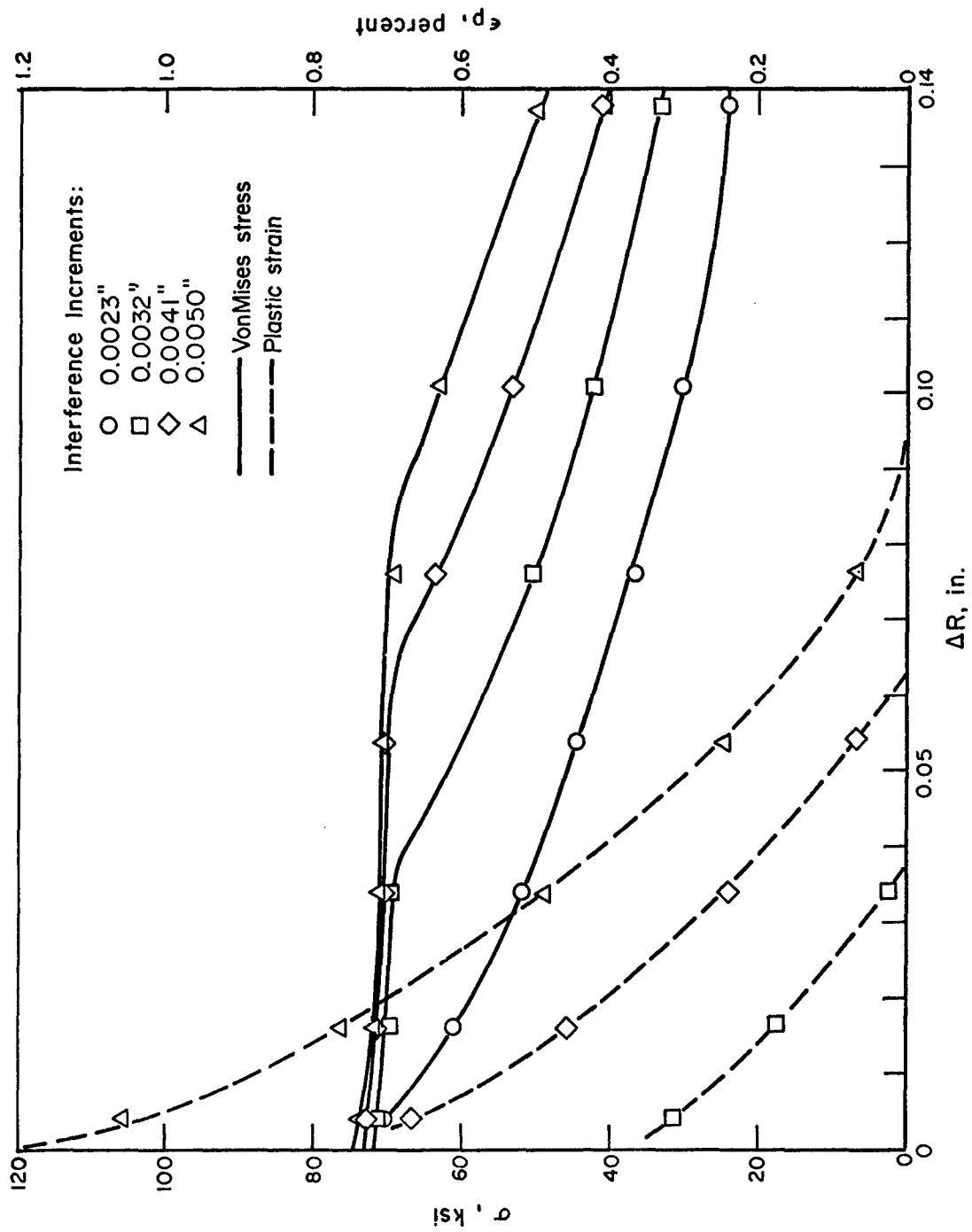


FIGURE D-27. 3/8-INCH-DIAMETER STEEL FASTENER IN ALUMINUM NO LOAD TRANSFER SPECIMEN - STRESS AND STRAIN PARALLEL TO LOADING DIRECTION DUE TO FASTENER INSTALLATION

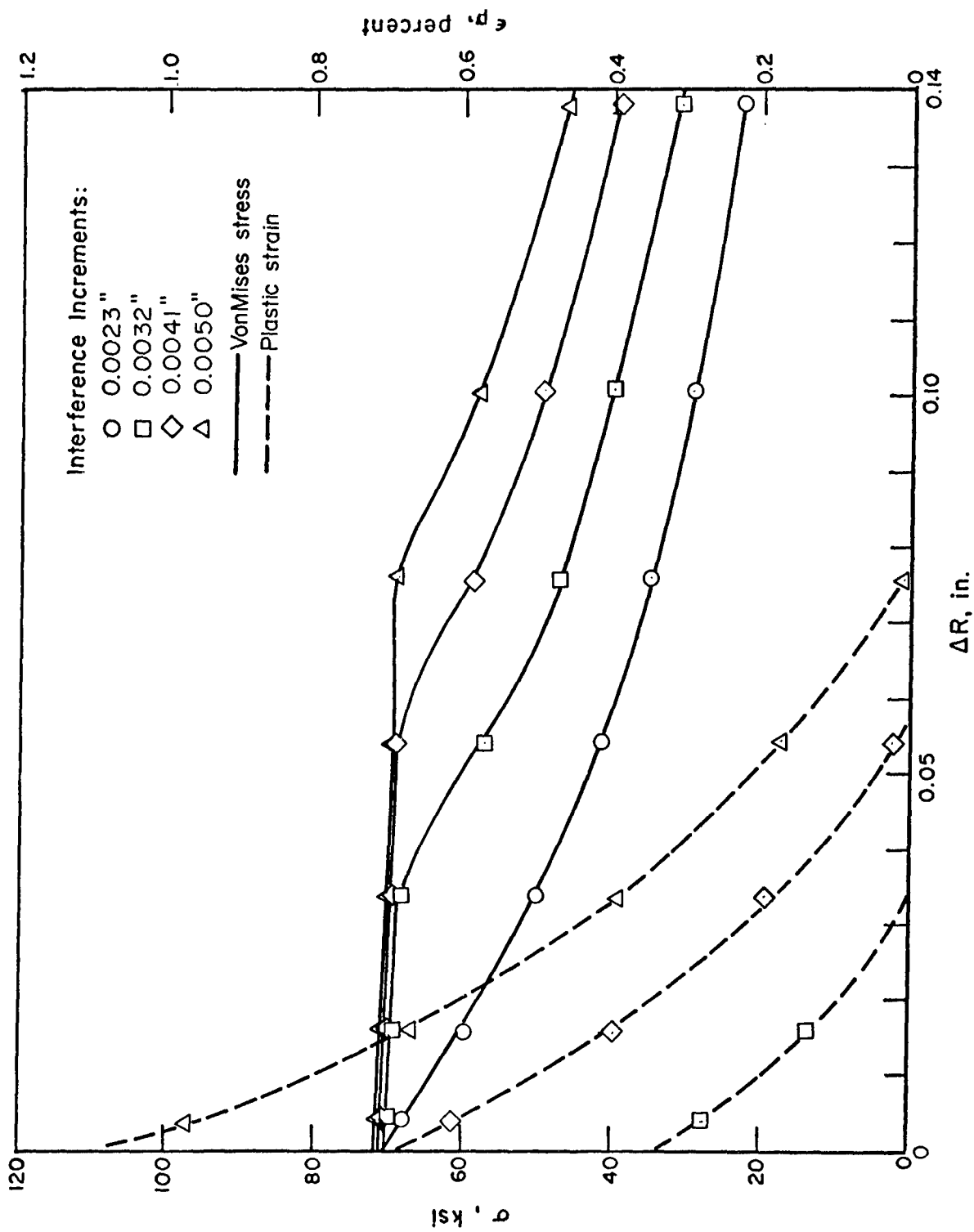


FIGURE D-28. 3/8-INCH-DIAMETER STEEL FASTENER IN ALUMINUM NO LOAD TRANSFER SPECIMEN - STRESS AND STRAIN NORMAL TO LOADING DIRECTION DUE TO FASTENER INSTALLATION

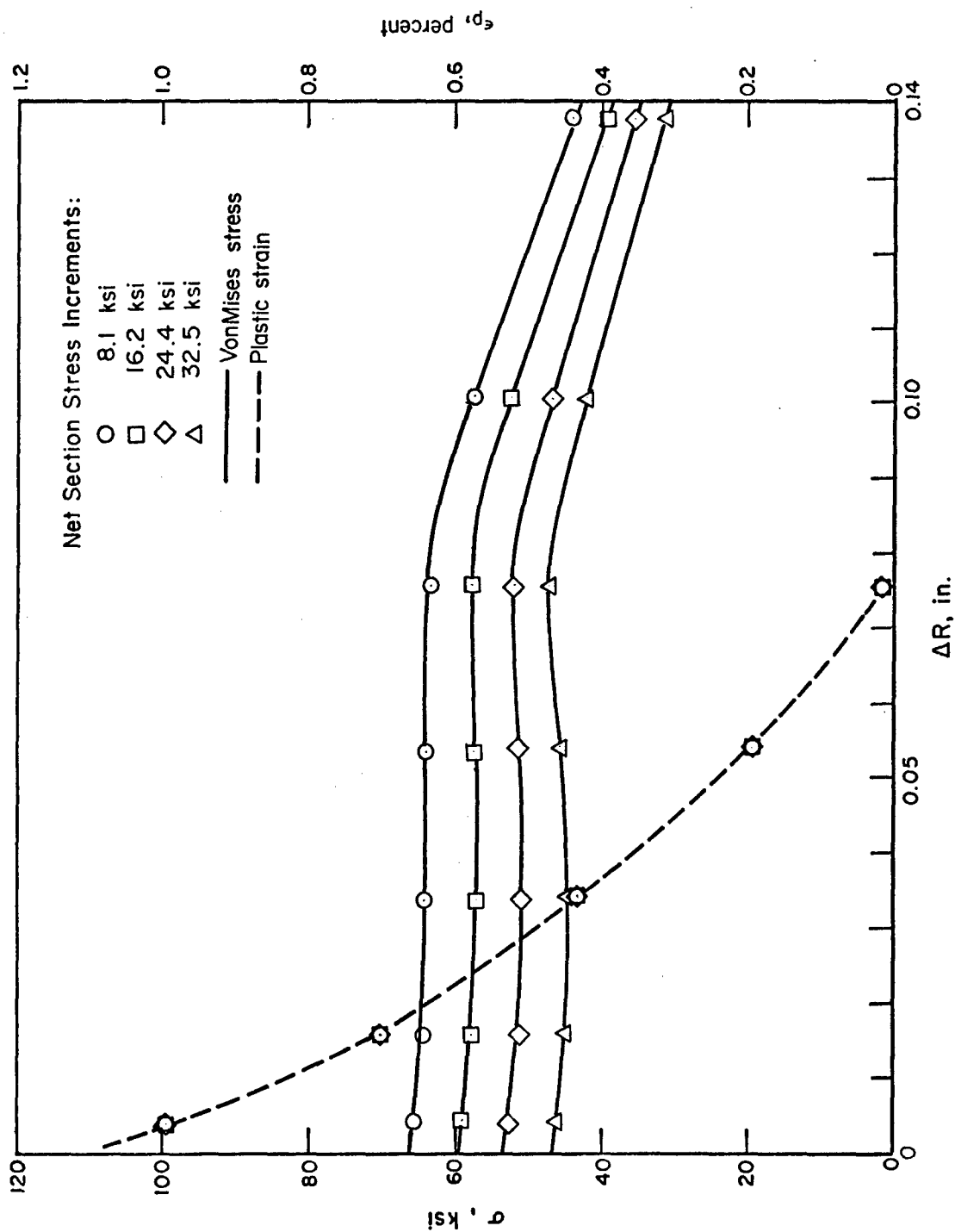


FIGURE D-29. 3/8-INCH-DIAMETER STEEL FASTENER IN ALUMINUM NO LOAD TRANSFER SPECIMEN - STRESS AND STRAIN PARALLEL TO LOADING DIRECTION DUE TO AXIAL LOAD

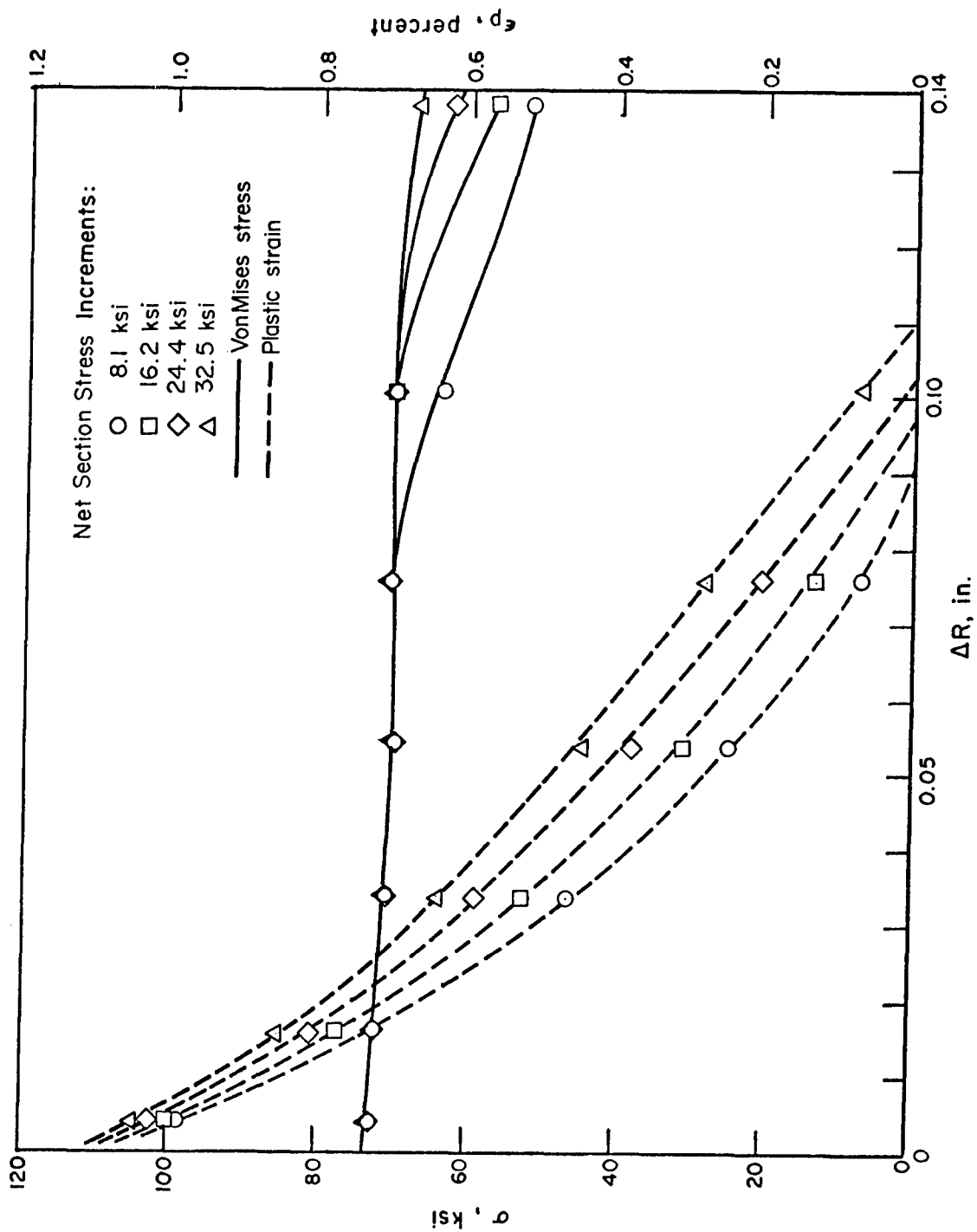


FIGURE D-30. 3/8-INCH-DIAMETER STEEL FASTENER IN ALUMINUM NO LOAD TRANSFER SPECIMEN - STRESS AND STRAIN NORMAL TO LOADING DIRECTION DUE TO AXIAL LOAD

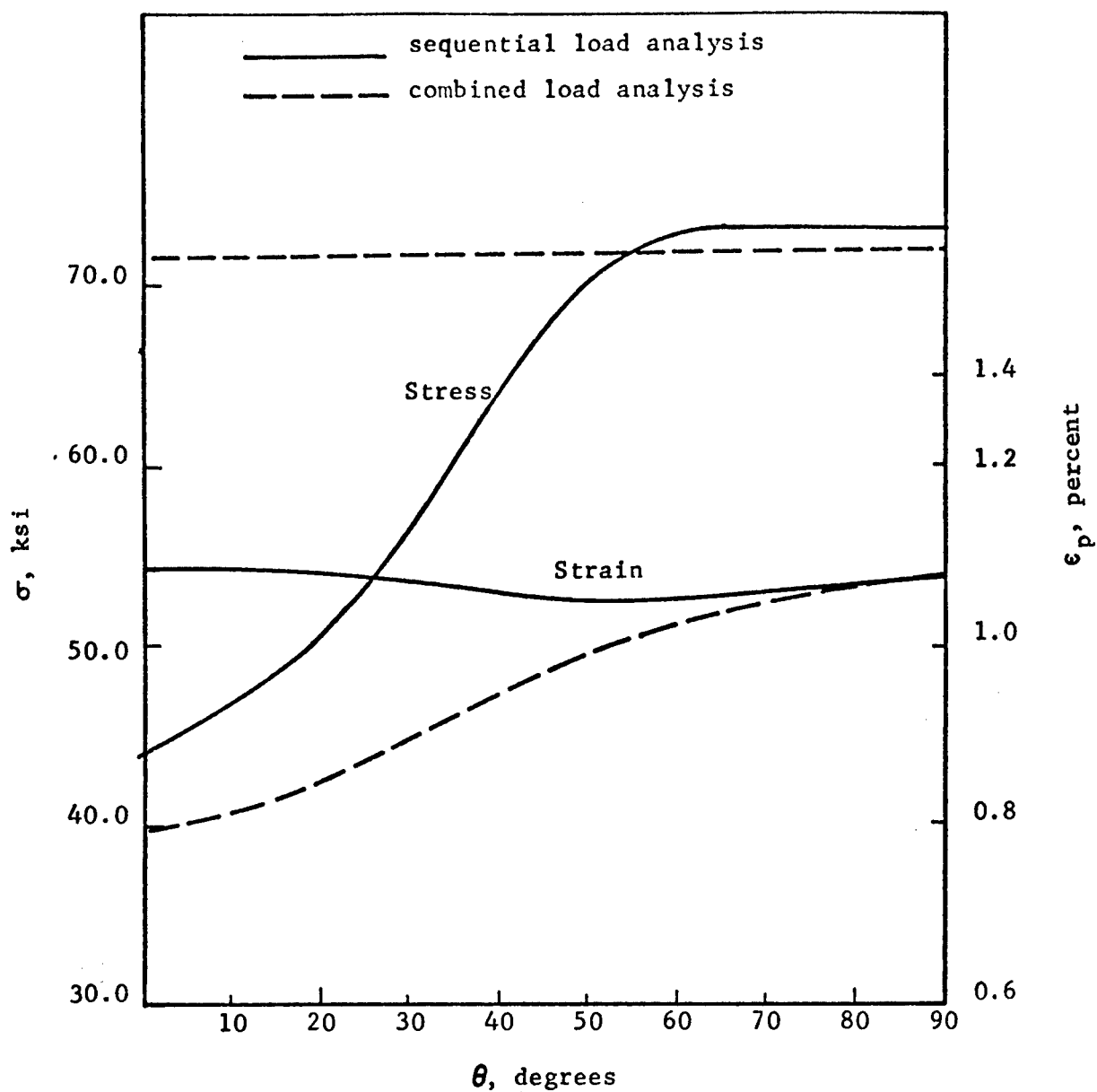


FIGURE D-31. VON MISES STRESS AND EQUIVALENT PLASTIC STRAIN AROUND THE HOLE EDGE: COMPARISON BETWEEN SEQUENTIAL AND COMBINED LOAD ANALYSIS

difficulties were encountered in obtaining completed computer runs at the AFFDL facility. These difficulties, coupled with time and funding limitations, made it impossible to complete the intended model analysis of low-load and high-load transfer joints.

It should be noted, however, that considerable success has been achieved in this portion of the program. This, coupled with the successes experienced by other investigators, should provide continued impetus to the finite-element modeling of fastened joints, but not without continued experimental verification.

## APPENDIX E

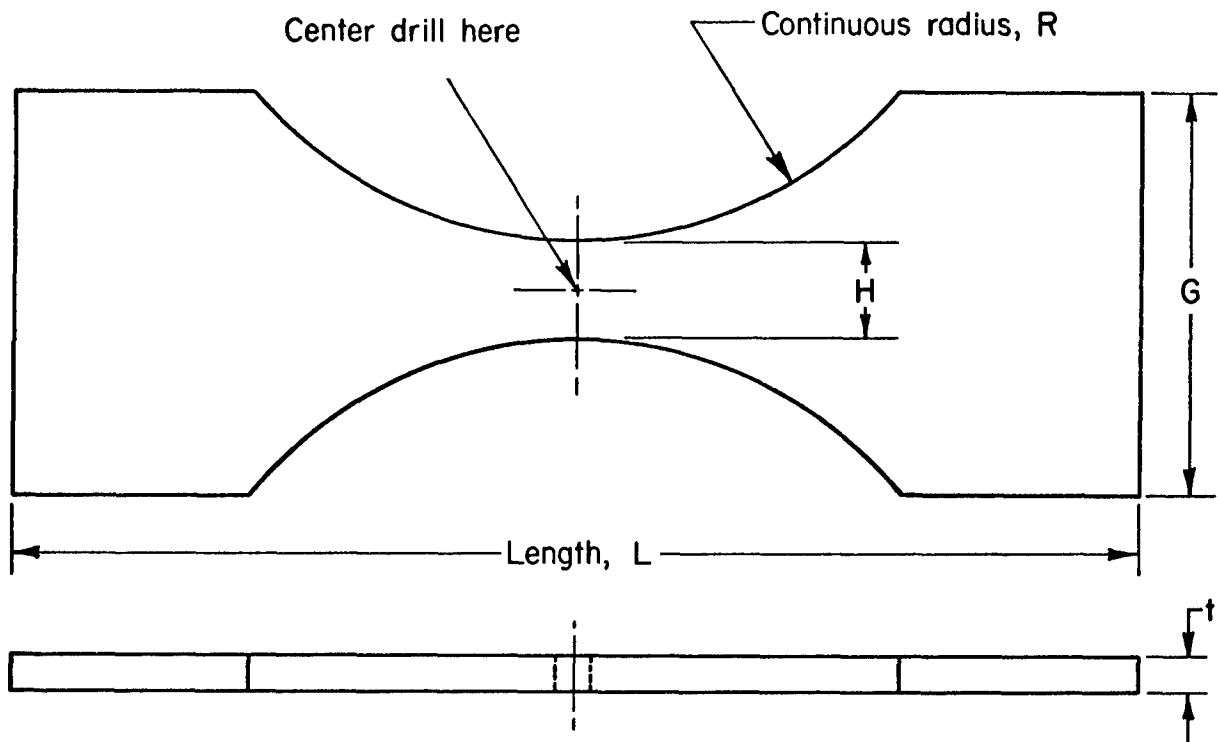
### EXPERIMENTAL ASPECTS OF THE FATIGUE PROGRAM

#### INTRODUCTION

The experimental fatigue program was designed to provide data to prove, and make it possible to refine, where necessary, the fatigue prediction techniques evolved throughout the program. Three different fatigue specimens were used, namely, no-load, low-load and high-load transfer configurations. Both constant-amplitude and spectrum-load experiments were conducted. In addition, such parameters as thickness-to-diameter ratio ( $t/D$ ), edge distance ( $e/D$ ), and hole conditions were varied. Initially, it had been proposed to conduct experiments using both 7075-T6 aluminum and mill-annealed 6Al-4V titanium joints. However, it was determined relatively early in the program that the material properties of titanium are highly dependent upon grain orientation, thus making the finite-element analysis impractical. As a result, tests were not conducted on titanium material joints. Specific details of the experimental fatigue program are outlined below.

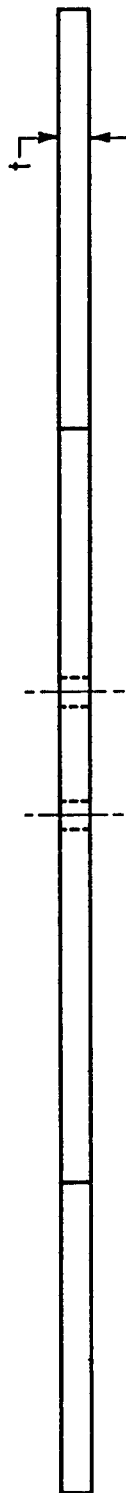
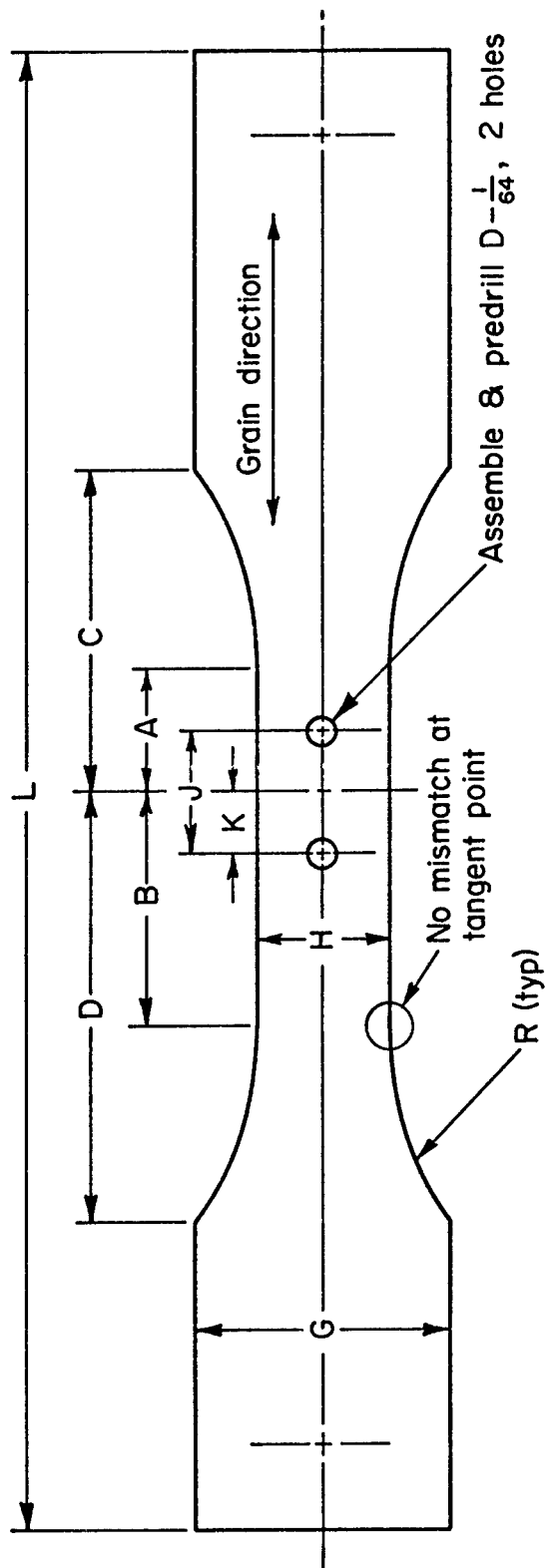
#### SPECIMEN DESCRIPTION

As noted above, three specimen configurations were used in the experimental fatigue program. They were fabricated from 7075-T6 aluminum alloy in accordance with Figures E-1, E-2 and E-3. Upon completion of the fabrication operation, specimen numbers were assigned to facilitate data logging during metrology studies, specimen assembly, and testing. The specimen identification code is explained as follows.

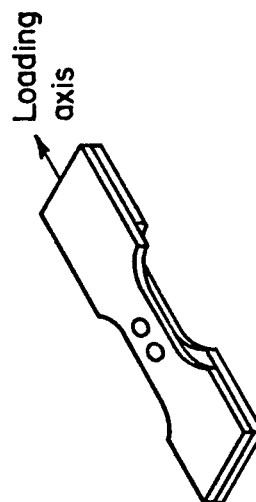


NOMINAL D	$\pm .020$ L	$\pm .010$ G	$\pm .005$ H	$\pm .020$ R	THICKNESS t
3/8	16.0	3.50	2.250	12.0	.375, .500

FIGURE E-1. NO-LOAD-TRANSFER JOINT SPECIMEN

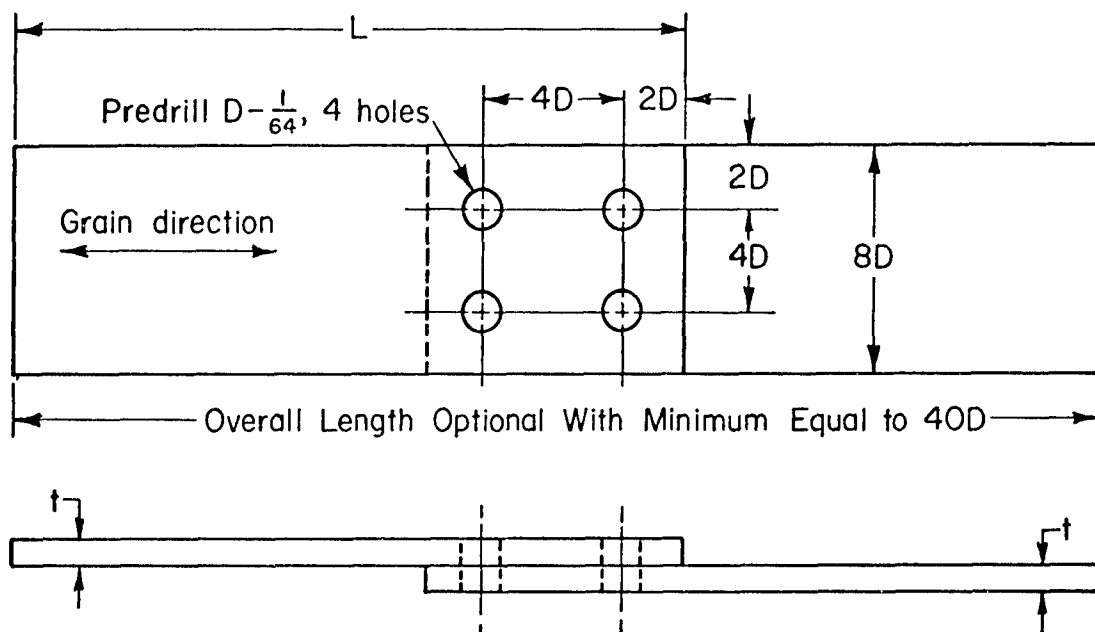


NORMAL FASTENER SIZE-D	THICKNESS															
	L	G	H	D	C	B	A	R	J	K	t					
3/8	19.00	3.500	2.250	6.116	4.916	3.450	2.250	6.000	1.500	.750	.375 .500					



Assembly - reverse or  
offset dogbone specimen

FIGURE E-2. SPECIMEN DETAIL, REVERSE DOGBONE - LOW-LOAD-TRANSFER TEST SPECIMEN



NOMINAL FASTENER SIZE - D	$\pm .005$ 2D	$\pm .005$ 4D	$\pm .005$ 8D	$\pm .010$ L	THICKNESS t
3/8	.750	1.500	3.000	11.000	.190, .375, .500

FIGURE E-3. SIMPLE LAP JOINT SPECIMEN - SINGLE SHEAR,  
100 PERCENT LOAD TRANSFER

		Identification Code							
		X	X	X	X	X	X	-	X
Material Thickness (in 1/16's)	0.190	3							
	0.375	6							
	0.500	8							
Bolt Material									
Alloy Steel			D						
Titanium			V						
Bolt Head Type									
Flush Head				F					
Protruding Head				P					
Bolt Diameter (in 1/16's)	0.250			4					
	0.375			6					
	0.500			8					
Joint Configuration									
No-Load Transfer					S				
Low-Load Transfer					D				
Modified 1½ Dogbone					L				
High-Load Transfer					M				
Joint Material									
Clad 7075-T6 Aluminum						B			
6Al-4V Titanium						T			
Test Series								1-9	
Specimen Number									1-99

Hence, for example, 8DP6MB2-7 describes a specimen made up of a 3/8-inch diameter, protruding head alloy steel fastener installed in a high-load-transfer joint made of 7075-T6 aluminum, 1/8-inch thick. The specimen is to be used for the seventh experiment of test series number 2.

#### EQUIPMENT

The BCL Structural Fatigue Laboratory is an air-conditioned, humidity-controlled area housing several closed-loop servocontrolled systems (see Figure E-4). For the purposes of this program, systems with dynamic load capabilities of 50,000 and 130,000 pounds were used. Programming equipment was selected to provide for either constant-amplitude or spectrum-load control.

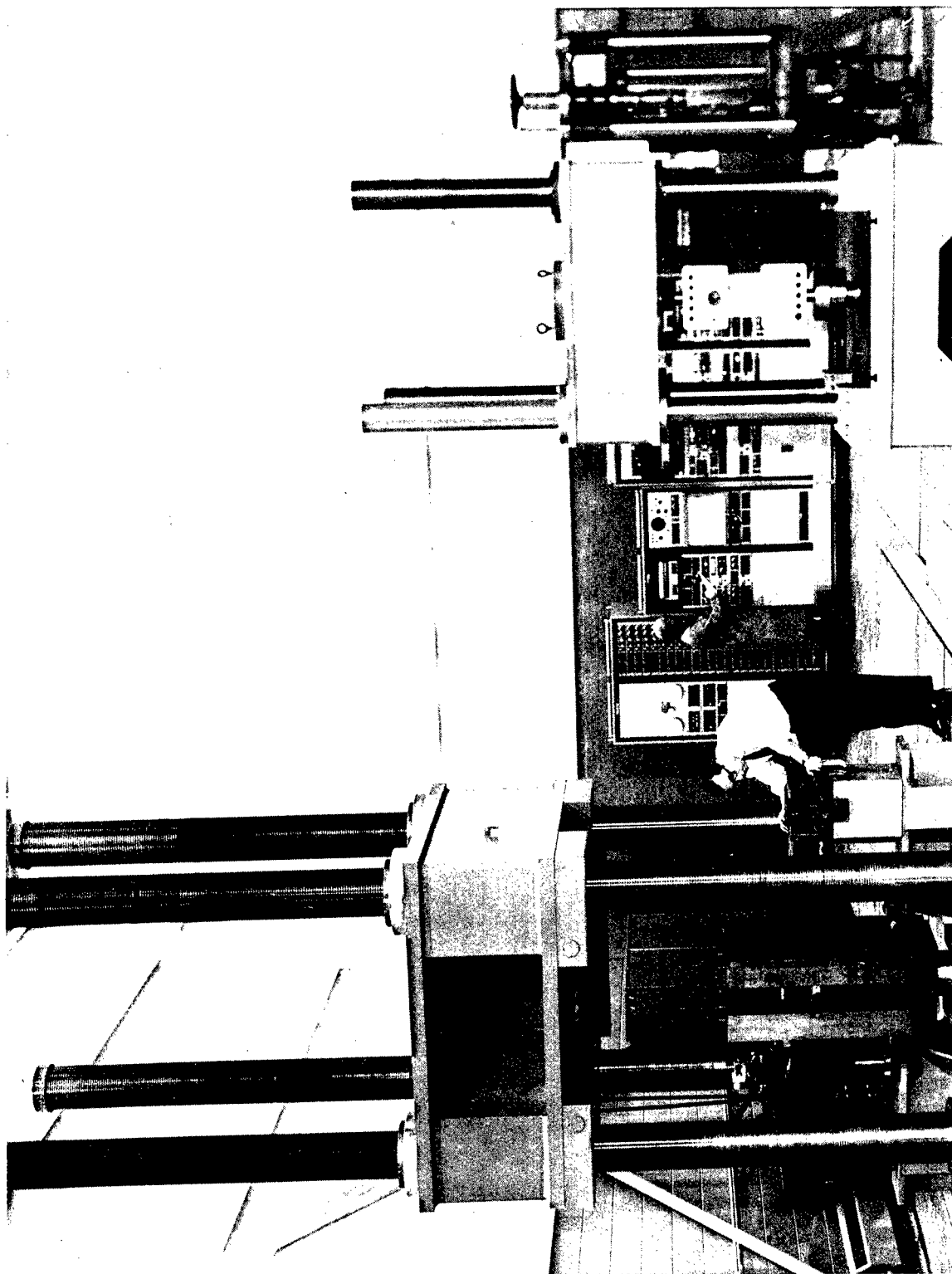


FIGURE E-4. STRUCTURAL FATIGUE LABORATORY

Specimens were mounted in the fatigue test equipment using either pin or wedge grid fixtures as shown in Figures E-5 and E-6. In addition, high-load transfer joints were restrained from bending as recommended in MIL-STD-1312, Proposed Test 21<sup>(1)</sup>.

#### LOAD LEVELS

Fatigue life data were generated for three types of loading conditions.

- Constant Amplitude, Stress Ratio = 0
- Spectrum 1, Constant Stress Ratio
- Spectrum 2, Constant Mean Stress

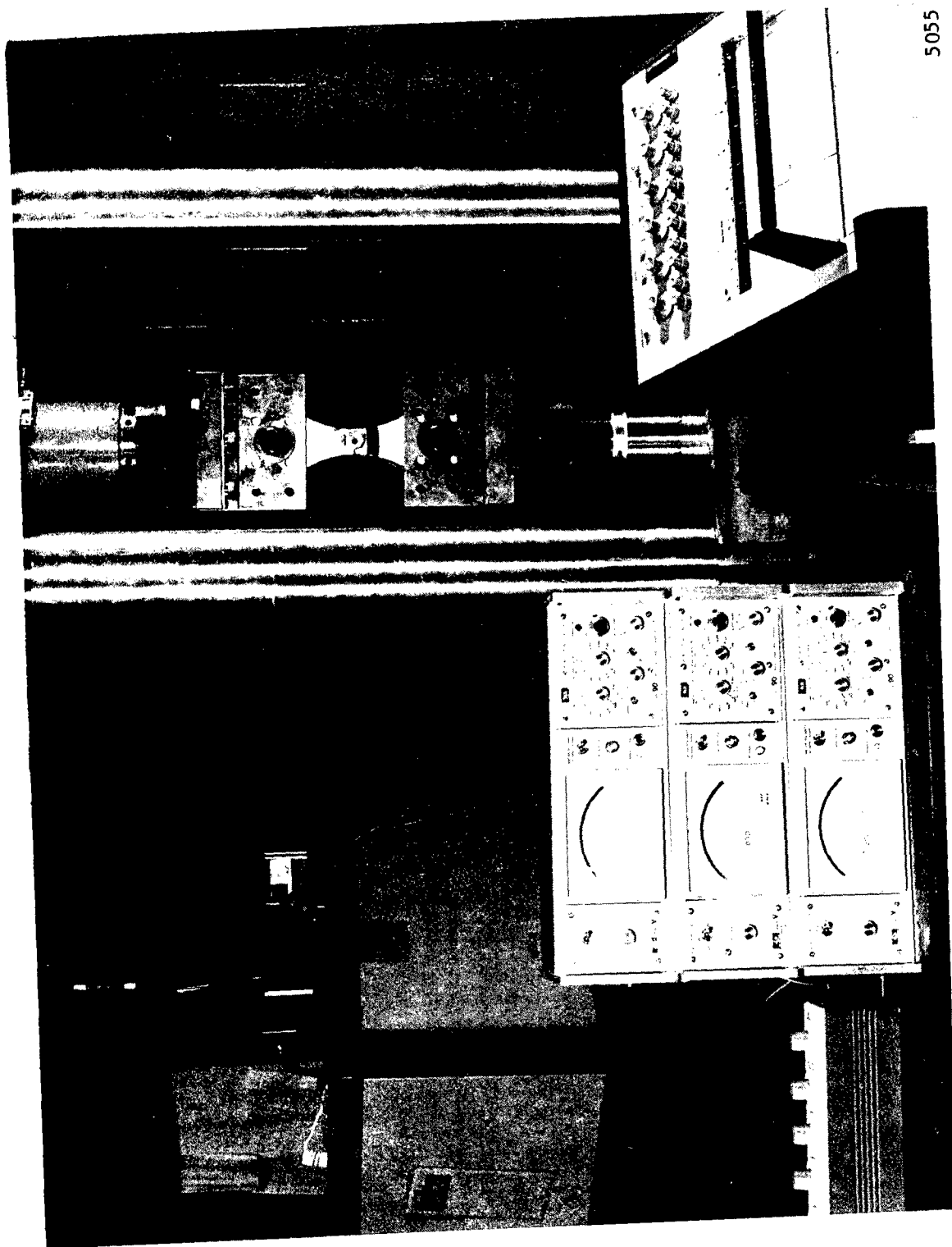
The initial experiments on each specimen configuration were conducted at net section stress levels equivalent to 35 and 70 percent of the specimen material yield strength. Later experiments dealing with installation variables, as noted in Tables E-1, E-2, and E-3, were conducted at other levels. Stress levels for each of the load conditions are listed below.

<u>Load Level, percent yield</u>	<u>Net Section Stress, psi</u>
25	17,500
35	24,500
50	35,000
70	49,000
75	52,500
100	70,000

Relatively simple repeated load spectra were selected to provide data for spectrum fatigue prediction. Those experiments indicating spectrum number 1 (Spec 1) were designed to provide data at a constant R ratio. Thus, the spectrum was set up to repeat the following sequence: 2,000 cycles at a maximum stress of 70 percent of yield and a stress ratio of zero followed by 6,000 cycles at a maximum stress of 35 percent of yield and a stress ratio of zero. The second spectrum (Spec 2) was selected to provide constant mean stress data whereby the spectrum was laid out to provide 2,000 cycles at a mean stress of 35 percent of yield and an alternating stress of 35 percent of

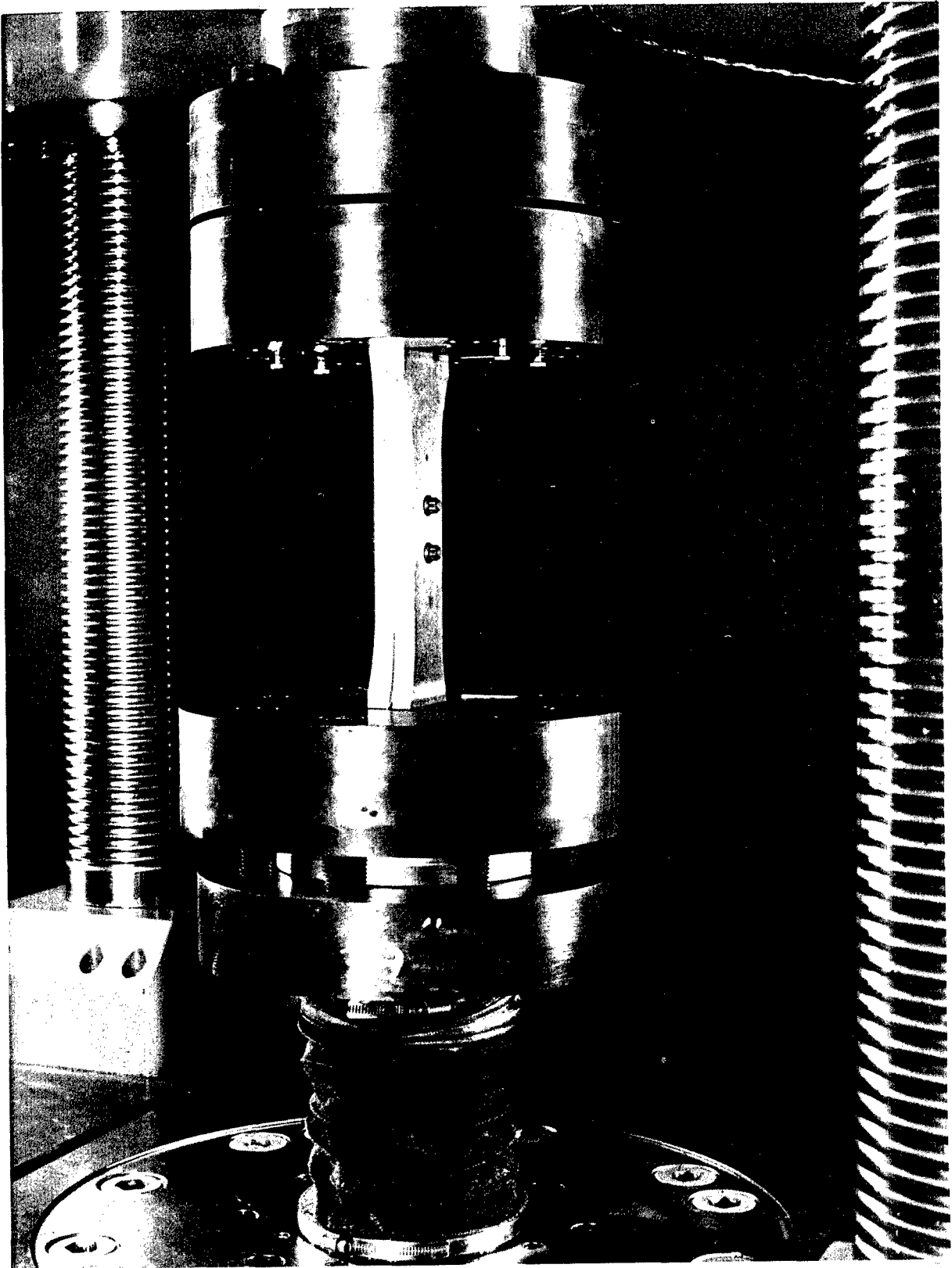
---

(1) MIL-STD-1312, Fastener Test Methods. Proposed Test 21, Shear Joint Fatigue - Constant Amplitude.



5055

FIGURE E-5. STRAIN GAGED FATIGUE SPECIMEN MOUNTED IN FATIGUE MACHINE USING PIN GRIPS



5053

FIGURE E-6. FATIGUE SPECIMEN MOUNTED IN FATIGUE MACHINE USING WEDGE GRIPS

yield followed by 6,000 cycles at a mean stress of 35 percent of yield and an alternating stress of 17.5 percent of yield. These blocks were repeated until the specimen failed. All fatigue experiments were conducted at a cycle rate ranging from 1 to 35 Hz dependent upon the test load and specimen compliance.

#### EXPERIMENTAL RESULTS AND CONCLUSIONS

The experimental fatigue results for 3/8-inch-diameter steel fasteners installed in 7075 aluminum no-load-transfer specimens are presented in Table E-1. The experimental fatigue test results for 3/8-inch-diameter protruding-head steel fasteners installed in 7075 aluminum high-load-transfer specimens are presented in Table E-2 and the results for 3/8-inch-diameter protruding head steel fasteners in aluminum low-load-transfer specimens are presented in Table E-3. Photographs of typical failed specimen surfaces are shown in Figures E-7 through E-9. Data obtained as a part of the strain gage investigation of fastener installation effects are shown in Figure E-10 and discussed in the section of the report entitled "Analysis Framework for No-Load-Transfer Specimens Subjected to Constant-Amplitude Loading" (Section 2.2.4).

Consideration of the fatigue life data listed in Table Nos. E-1, E-2, and E-3 leads to the following conclusions.

- (1) Independent of specimen configuration, the presence of fluted or out-of-round holes causes, at best, only minor reductions in fatigue life as compared to well-prepared holes.
- (2) There appears to be no significant difference in the fatigue life behavior of low-load-transfer joints as compared to no-load-transfer joints. The same conclusion might well be expected in regard to high-load-transfer joints, if bending stresses were not present.

TABLE E-1. ALUMINUM NO-LOAD TRANSFER SPECIMEN FATIGUE RESULTS -  
3/8-INCH-DIAMETER STEEL FASTENERS

Specimen Number	t/D	Head	Interference	Hole Condition	Load Level, % Yield	Cycles to Failure	Failure Mode
8DP65B2-14	1.3	No Fastener		Good	70	4,153	B
- 3	1.3	None	.002	Good	35	146,850	C
- 1	1.3	None	.002	Good	35	451,380	A,C
-17	1.3	None	.002	Good	35	390,290	A
-12	1.3	None	.002	Good	70	16,440	C
-22	1.3	None	.002	Good	70	32,340	A
- 7	1.3	None	.004	Good	35	1,566,690	D
- 8	1.3	None	.004	Good	35	432,715	A(1)
-20	1.3	None	.004	Good	70	25,833	C
-18	1.3	None	.0045	Good	35	638,300	D
- 9	1.3	None	.005	Good	35	685,400	D
-16	1.3	None	.005	Good	70	70,321	D
-19	1.3	None	.0055	Good	70	63,150	D
-11	1.3	None	.004	Out of Round	70	8,700	A,C
-13	1.3	None	.004	Out of Round	70	11,510	A,C
-15	1.3	None	.004	Fluted	70	22,220	C
- 4	1.3	None	.004	Fluted	70	23,180	A
- 6	1.3	None	.004	Good	70	80,220	D (2)
- 5	1.3	None	.004	Good	70	67,290	D (2)
-10	1.3	Prot	.002	Good	70	56,530	D
- 2	1.3	Prot	.0031	Good	70	53,820	C (3)
-21	1.3	Prot	.004	Good	70	29,790	C (3)
-23	1.3	Prot	.004	Good	70	36,160	C (3)
-24	1.3	Prot	.005	Good	70	63,170	A
- 1	1.3	Prot	.005	Good	70	72,650	A
6DP6SB2- 1	1.0	Prot	.004	Good	70	58,850	D
- 2	1.0	Prot	.004	Good	70	73,110	D
- 3	1.0	Prot	.004	Good	70	48,130	D
6DP6SB4-37	1.0	Prot	.005	Good	25	11,000,000+	DNF
-38	1.0	Prot	.005	Good	25	10,273,970+	DNF
-39	1.0	Prot	.005	Good	50	197,280	D
-41	1.0	Prot	.005	Good	75	46,820	D
-42	1.0	Prot	.005	Good	75	31,160	D
-40	1.0	Prot	.005	Good	94	24,140	D
-43	1.0	Prot	.005	Out of Round	25	13,546,920+	DNF
-44	1.0	Prot	.005	Out of Round	50	149,750	C
-45	1.0	Prot	.005	Out of Round	75	15,210	C
-46	1.0	Prot	.005	Fluted	25	14,613,180	A
-47	1.0	Prot	.005	Fluted	50	88,930	C
-48	1.0	Prot	.005	Fluted	75	14,140	B
-21B	1.0	Prot	.004	Good	Spec. 1	301,630	B
-23B	1.0	Prot	.004	Good	Spec. 2	168,250	B
-23i	1.0	Prot	.005	Good	Spec. 1	217,310	D
-24i	1.0	Prot	.005	Good	Spec. 2	96,320	D
-25j	1.0	Prot	.005	Out of Round	Spec. 1	200,060	D
-26j	1.0	Prot	.005	Out of Round	Spec. 2	152,010	C
-27k	1.0	Prot	.005	Fluted	Spec. 1	225,110	D
-28k	1.0	Prot	.005	Fluted	Spec. 2	169,380	D

Failure Mode -

A - Edge of Hole at Head  
B - Inside Hole

C - Edge of Hole at Nut  
D - Away From Hole

DNF - Did Not Fail

- (1) Initiated at clearance radius of hole - no contact.  
(2) e/D = 1.25.  
(3) Poor contact at bottom of hole.

TABLE E-2. ALUMINUM HIGH-LOAD TRANSFER SPECIMEN FATIGUE RESULTS - 3/8-INCH DIAMETER PROTRUDING HEAD STEEL FASTENERS

Specimen Number	t/D	Interference	Hole Condition	Load Level, % Yield	Cycles to Failure	Failure Mode
8DP6MB2- 6	1.3	.004	Good	35	154,030	D
- 5	1.3	.004	Good	35	142,760	C
- 4	1.3	.005	Good	35	171,370	C
- 2	1.3	.005	Good	35	107,670	D
-10	1.3	.004	Out of Round	35	140,300	C
8DP6MB1- 2	1.3	.004	Out of Round	35	149,490	D
8DP6MB2-16	1.3	.004	Fluted	35	126,870	D
-15	1.3	.004	Fluted	35	137,600	C
6DP6MB4- 1	1.0	.005	Good	25	333,660	B
- 2	1.0	.005	Good	25	350,560	B
- 3	1.0	.005	Good	50	22,370	D
- 4	1.0	.005	Good	50	68,690	C
- 8	1.0	.005	Good	75	2,090	B
- 7	1.0	.005	Good	75	7,740	B
-16	1.0	.005	Out of Round	25	390,910	C
-17	1.0	.005	Out of Round	50	54,240	B
-18	1.0	.005	Out of Round	75	4,360	B
- 9	1.0	.005	Fluted	25	285,190	B
- 6	1.0	.005	Fluted	50	60,430	B
- 5	1.0	.005	Fluted	75	1,950	B
-21	1.0	.0025	Good	25	330,770	B
-23	1.0	.0025	Good	50	58,490	B
-29	1.0	.0025	Good	75	8,750	B
-1a	1.0	.005	Good	Spec. 1	105,870	C
-2a	1.0	.005	Good	Spec. 1	113,770	B
-11c	1.0	.004	Out of Round	Spec. 1	24,150	B
-13d	1.0	.004	Fluted	Spec. 1	57,070	B
-31	1.0	.0025	Good	Spec. 1	72,600	C
- 3a	1.0	.005	Good	Spec. 2	56,640	C
- 4a	1.0	.005	Good	Spec. 2	51,740	A
-12c	1.0	.004	Out of Round	Spec. 2	25,430	D
-14d	1.0	.004	Fluted	Spec. 2	33,350	B
6DP6MB2- 1	1.0	.0025	Good	Spec. 2	49,670	A
3DP6MB2- 1	0.5	.005	Good	25	318,580	C
- 2	0.5	.005	Good	50	58,260	C
3DP6MB4- 7	0.5	.005	Good	75	34,800	B
3DP6MB2- 3	0.5	.005	Good	Spec. 1	73,460	C
3DP6MB4- 1	0.5	.005	Good	Spec. 2	16,130	C

Failure Mode -

A - Inside Hole-Head Side

B - Inside Hole-Fay Side

C - Away From Holes-Fay Surface  
in Line with Holes

D - Away From Holes-Fay Surface  
at Edge of Specimen

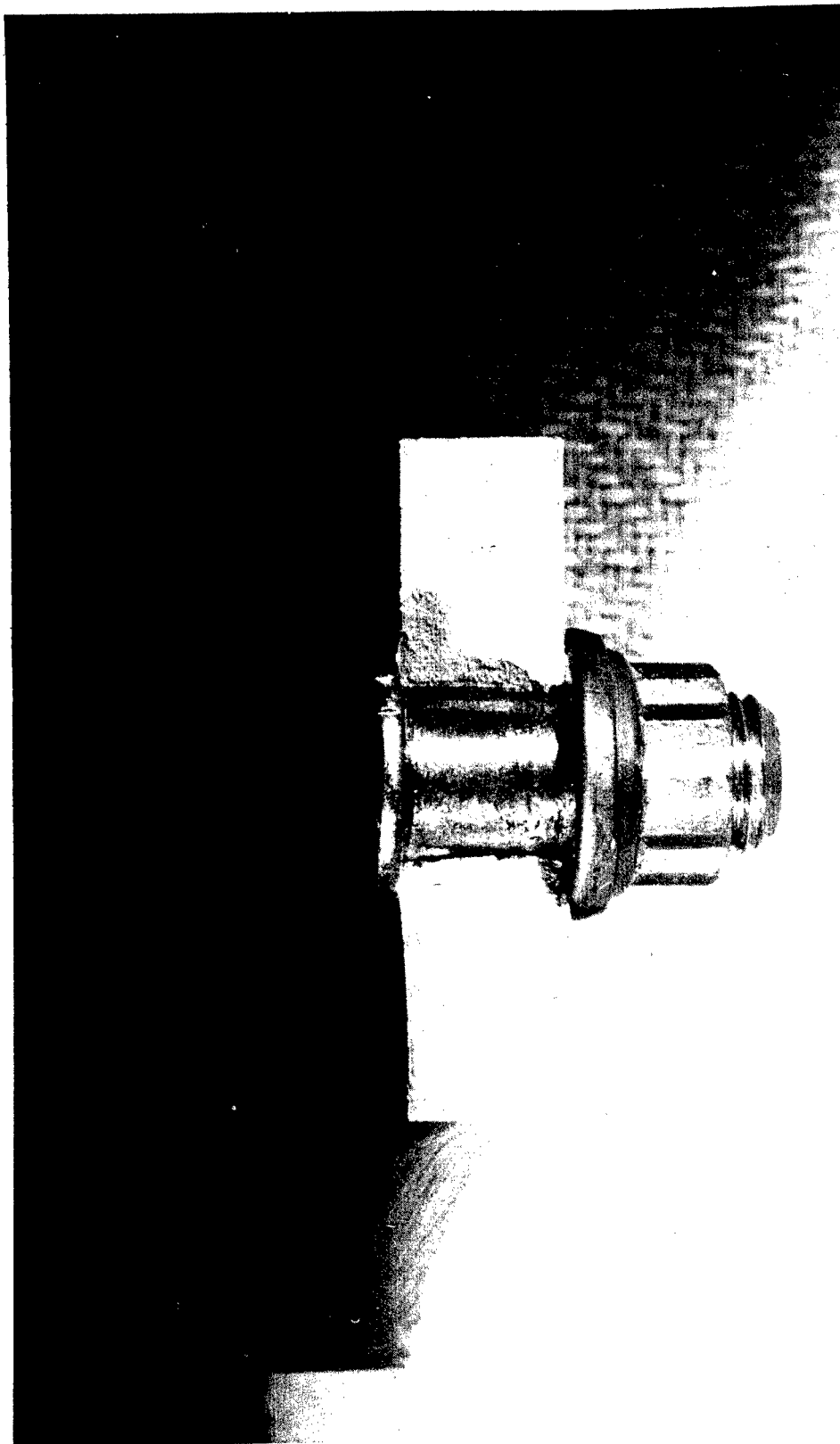
TABLE E-3. ALUMINUM LOW-LOAD-TRANSFER SPECIMEN FATIGUE RESULTS - 3/8-INCH-DIAMETER PROTRUDING-HEAD STEEL FASTENERS

Specimen Number	t/D	Interference	Hole Condition	Load Level, % Yield	Cycles to Failure	Failure Mode
8DP6DB1- 6	1.3	.004	Good	70	14,730	A
6DP6DB4-25	1.0	.005	Good	25	1,311,380	D
-10	1.0	.005	Good	50	85,330	D
-28	1.0	.005	Good	50	121,620	E
-26	1.0	.005	Good	50	143,670	D
-30	1.0	.005	Good	75	24,290	D
- 9	1.0	.005	Good	75	35,580	D
-31	1.0	.004	Out of Round	25	902,470	B
-32	1.0	.004	Out of Round	50	96,120	C
-33	1.0	.004	Out of Round	75	14,360	C
-34	1.0	.005	Fluted	25	10,000,000+	DNF
-35	1.0	.005	Fluted	50	124,290	E
-36	1.0	.005	Fluted	75	19,990	D
-17f	1.0	.005	Good	Spec. 1	136,820	E
-19g	1.0	.004	Out of Round	Spec. 1	33,490	B
-21h	1.0	.005	Fluted	Spec. 1	128,230	E
-18f	1.0	.005	Good	Spec. 2	110,670	E
-20g	1.0	.004	Out of Round	Spec. 2	27,700	B
-22h	1.0	.005	Fluted	Spec. 2	129,230	D

Failure Mode -

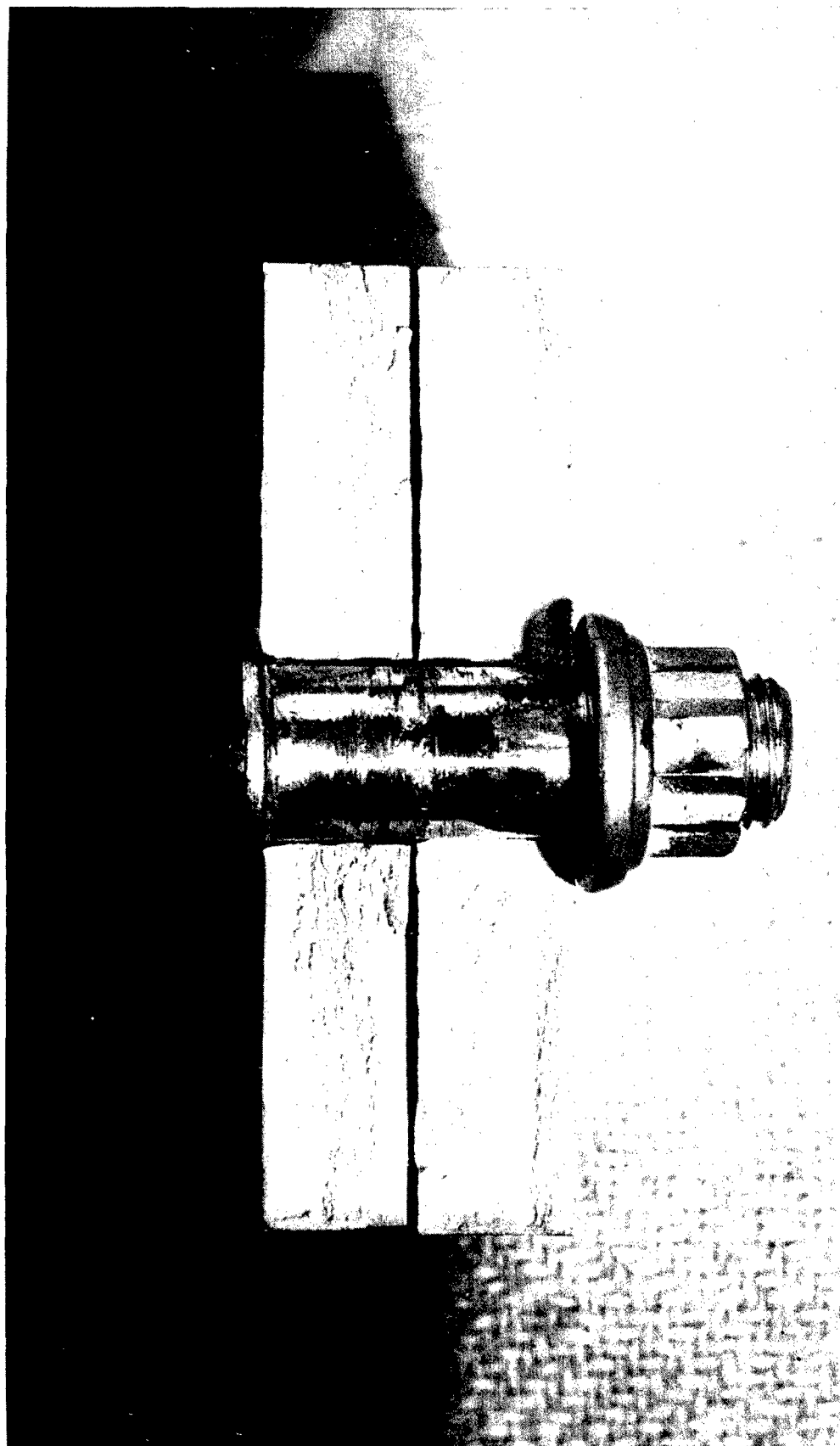
A - Inside Hole-Head Side  
 B - Inside Hole-Nut Side  
 C - Edge of Hole at Nut

D - Away From Hole-Fay Surface  
 E - Away From Hole-Nut Surface  
 DNF - Did Not Fail



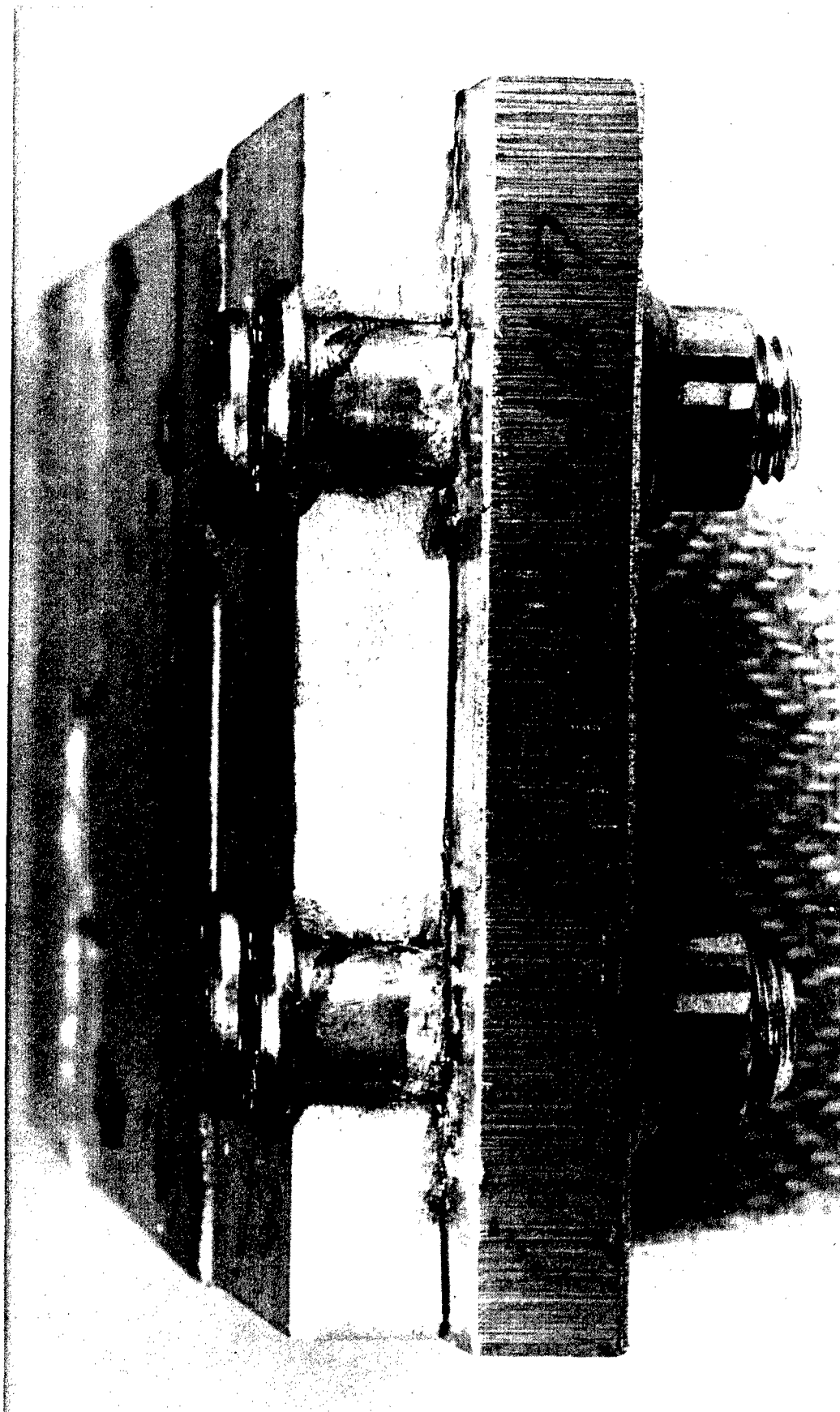
6327

FIGURE E-7. FAILED NO-LOAD-TRANSFER SPECIMEN



6321

FIGURE E-8. FAILED LOW-LOAD-TRANSFER SPECIMEN



6323

FIGURE E-9. FAILED HIGH-LOAD-TRANSFER SPECIMEN

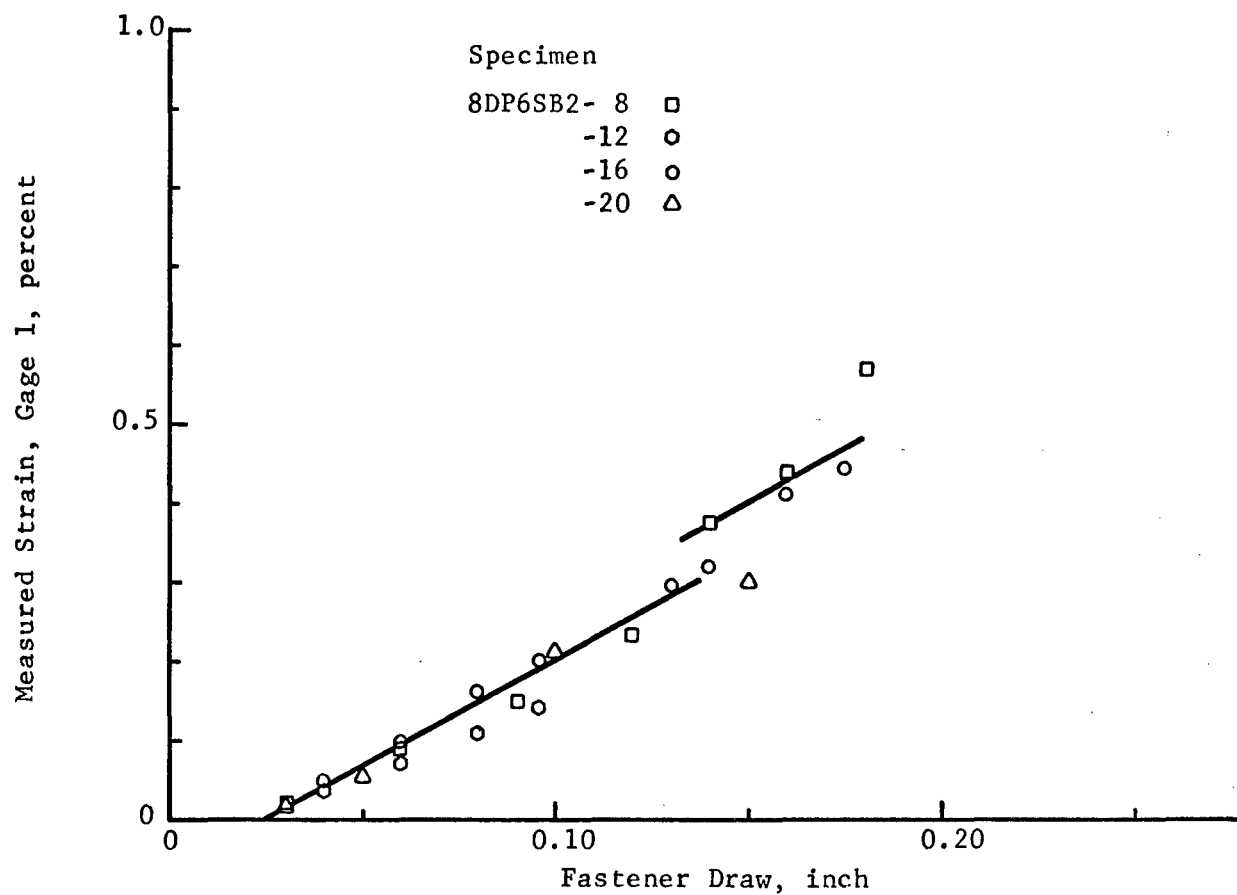


FIGURE E-10. SURFACE STRAIN AS A FUNCTION OF FASTENER DRAW